Size-dependent High-Temperature Behavior of Bismuth Oxide Nanoparticles

Größenabhängiges Hochtemperaturverhalten von Bismutoxid Nanopartikeln

Zur Erlangung des Grades eines Doktors der Naturwissenschaften (Dr. rer. nat.)
genehmigte Dissertation von Gerrit Günther (Dipl.-Ing. (FH)) aus Frankfurt a.M.
Februar 2013 — Darmstadt — D 17

TECHNISCHE
UNIVERSITÄT
DARMSTADT

Material- und Geowissenschaften
Nichtmetallisch - Anorganische
Werkstoffe

Size-dependent High-Temperature Behavior of Bismuth Oxide Nanoparticles
Größenabhängiges Hochtemperaturverhalten von Bismutoxid Nanopartikeln

Genehmigte Dissertation von Gerrit Günther (Dipl.-Ing. (FH)) aus Frankfurt a.M.

1. Gutachten: Olivier Guillon
2. Gutachten: Horst Hahn

Tag der Einreichung: 10. Oktober 2012
Tag der Prüfung: 14. Dezember 2012

Darmstadt — D 17

Contents

1 Introduction

A new branch that spans fields of physics, chemistry and materials science is nanoscience. Vast applications exist e.g. in electronics, catalysis, sensors and coatings but also reach into environmental sciences, biotechnology and medicine. “Nano” designates the size dimension of 10^{-9} meters (nm). Atomic bonds are on the scale of 10^{-10} meters (Å). The special properties of nanomaterials arise from their size which is between 1 and 100 nm per definition. Objects in this mesoscopic region consist of several hundred to a few thousand arranged atoms. This is too large for molecular behavior but small enough that bonds and the atomic arrangement diverge from regular ones in infinitely expanded materials (bulk). All material properties (e.g. mechanical, electrical, optical, thermal, etc.) ultimately result from the constituing atoms as well as their bonds and their arrangement. Hence the properties change by altering the size and shape of nano-objects. This means that well established constant material properties as tabulated in text books and material databases actually change at the nanoscale. The aim of nanoscience is therefore to control and take advantage of novel material properties. To achieve this three serial steps can be identified:

1. Produce nano-objects of defined size and shape in a controllable and reproducible way
2. Measure and understand the properties
3. Tune these properties in a desired way for application

An example for phenomena at the nanoscale is the size-dependent change of the melting point: The melting temperature is usually regarded as one of the fundamental material properties. At the nanoscale, however, it changes with decreasing dimensions of the melting object. Several metals in the form of nanoparticles have been proven become liquid at lower temperatures than known for the bulk. As many size-dependent effects at the nanoscale the melting temperature depends reciprocally on the size; thus it drops smoothly with decreasing size. The melting point of a 5 nm gold particle is, for example, decreased by 20 % [1, 2] and other materials and phase transitions exhibit even stronger changes. Another phenomenon is nano phases which have a different structure and properties than the bulk phase. Zirconium dioxide, for example, adopts a tetragonal structure in the nano phase [3]. Direct applications of size-dependent phase transformations can be conceived e.g. for stabilization of special structures with desirable properties or for liquid phase sintering with a lower melting, nano-sized additive.

Historically metals and semiconductors have been a major scope of nanoscience largely because production and investigation are easier to accomplish for such materials. On the other hand size-effects depend on the bond-strength and bond-nature which are stronger in inorganic compounds with their covalent-ionic bonds. A systematic investigation of phase transitions in separated particles of such a material is not known in literature, except for a structural transition in PbS_2 last year [4]. Therefore such a study would be desirable and the findings could shed new light on the topic. Above all, this will be an experimental challenge because the currently known investigation methods are not well suited for compounds such as oxides.

In this thesis the focus is on the experimental investigation of size-selected, spherical nanoparticles of bismuth(III) oxide (Bi_2O_3). The changes of phase transformations with size will be shown and compared to the existing models for metals. The results will be used to outline a size-dependent phase diagram for Bi_2O_3. Furthermore a thorough comparison of existing melting models as well as a developed high-temperature chip calorimeter capable of characterizing nanoparticles under various atmospheres, will be presented. The structure of this thesis is as follows: It begins with an explanation of ambiguous yet important terms. Then the state of knowledge about phase transitions and reactions in nanoparticles in general is described, followed by inorganic compounds and bismuth oxide in particular (chap. 2). Then, the various models describing size-dependent melting will be tested on the experimentally well investigated material gold. Several findings concerning meaning, use and application of the models will be given (chap. 3). It follows the

experimental part which deals with the phase transformations of bismuth oxide nanoparticles. The three different transformations solid-state, evaporation and melting are treated in separate chapters (chap. 4 to 7). In the subsequent chapter 8 the size-dependent transformations are combined to draw a schematic stability diagram of Bi_2O_3 at the nanoscale. A separate chapter presents high-temperature chip calorimetry as a promising method for investigating inorganic nanoparticles. The setup and mode of operation of the developped device are described and the experiments show its potential for future works (chap. 9). The conclusion summarizes the findings of chapters 3 to 9 to obtain a conclusive picture of the size-dependent phase transformations in bismuth oxide. Finally, future developments of experimental techniques as well as sensible material scientific investigations will be outlined.

2 Background

Thermodynamic effects like melting, evaporation, structural phase transitions and redox-reactions as well as related properties like morphology, density and surface energy of bismuth oxide nanoparticles are in the scope of this thesis. No magnetic, spin electronic or other types of transitions will be treated.

2.1 Surface energy and surface stress

As it will be seen in the following chapters, surfaces play a key role in the unusual behavior of nanosized materials. There are different methods and vocabulary used throughout the literature to describe them. For this reason this chapter shall introduce and clarify this field as it is indispensable for the following description of phase transitions in nanoparticles. In the next section 6 the problems and limits of the approach are outlined.

Two terms are frequently used to describe borders of particles: Interface and surface. Interface is the more general expression which also incorporates surfaces. It refers to the boundary between two phases regardless of their aggregate state. The most common case when describing particles is the interface between a condensed phase with the surrounding gas atmosphere. This special kind of interface is called a surface. Any other case, where two condensed phases meet is termed 'interface'

The structure, bond strength and bond length at and close to an interface is different compared to the bulk constellation which affects quantities like the local density and entropy. For metals these differences occur approx. 1-3 atomic layers below the surface, but could be higher for materials with covalent bonds [5, 6]. Ergo, an interface has a small, but non-zero depth and the quantities change continuously (or in steps of atomic layers) across the interface region. Additionally, differences near the interface can have a considerable influence on the (small) volume of nanoparticles. The traditional framework of thermodynamics deliberately ignores these details. They are summarized in excess quantities which are completely ascribed to the border between the phases, without any volume. The thermodynamic behavior of interfaces is described by two quantities: Surface/interface energy γ and surface/interface stress σ. Much confusion and inaccurate use of terminology can be found concerning the use of these two terms (see discussions in references [7, 8, 9]). Especially because a third term, surface tension, is in use for both meanings. Surface tension was first used by J. W. Gibbs to describe the surface of liquids. Confusion began when Gibb's derivations were transferred to solids.

The meaning and relationship will be explained now for the isotropic case of a surface. γ is the specific surface excess free energy and has units of energy per area. γ times the area is the total excess energy of a particle which is wholly attributed to the surface; it is the energy required to create a new surface. It can be thought of as the energy of the unsatisfied (dangling) bonds on the surface, but it also includes disorder, reorganization and strain-induced excess. σ is the scalar of stress in plane of the surface and also has units of energy per area. This is the work required to alter a given surface by elastically deforming it. Surface stress imposes a pressure onto the interior of the particle [10]. These two surface quantities are related via the Shuttleworth equation *[11]*: σ describes the change of the total surface energy γA for an infinitesimal change in its area, e.g. when the surface tangentially strains:

$$\sigma = \frac{d(\gamma A)}{dA} = \gamma + A\frac{d\gamma}{dA} \tag{1}$$

The molecules of a liquid are free to move and therefore cannot sustain a bond stress. Thus, the second term in equation 1 is zero and the surface stress is equal to the surface energy (e.g. > 0). Solids can sustain stresses. Thus, the second term is significant. Depending on its sign, σ can be either positive or negative, whereas the surface excess energy remains always positive.

The tangential stress on the surface causes a pressure change $\triangle p$ in the volume of particles, which is reflected in the capillary equation for a spherical particle of diameter D:

$$\triangle p = \frac{4}{D}\gamma \tag{2}$$

For a liquid particle this is the capillary pressure (Young-Laplace) equation and $\triangle p$ is always positive. Analogously the equation also helps to imagine that for a solid particle the internal pressure can be either positive (compressive) or negative (tensile), depending on the sign of σ. The volume of the solid reacts on such a pressure like any solid material by (lattice) contraction or expansion. The amplitude of the strain depends on the particle size with an $1/D$ dependence [10]. But the use of equation 2 for solids is wrong (section 2.1), because it is a stress and not a pressure that causes this strain in the lattice. In nanoparticles of noble metals the lattice is long known to contract. The atomistic explanation is as follows: On the surface the bond order and consequently the electron density is reduced. The surface atoms attempt to level this by reducing their interatomic distance. The contraction causes the surface atoms to be in positive surface-stress. In many oxides and compounds the lattice has been reported to expand, which is caused by a negative surface-stress. The reasons for such negative values are related to a more complex (and anisotropic) surface structure and can not be generally answered. For more information see reference [12, 13].

Following the outlined derivation into the other direction makes it possible to calculate the mean surface stress and the surface energy from the measured lattice contraction in nanoparticles [14, 12, 15].

$$\frac{\triangle V}{V} = -4\frac{\sigma}{E\,D} \tag{3}$$

E is the bulk modulus and V is determined by the lattice constants a, b, c. This method is sometimes called the size-dependent lattice parameter (SDLP) method. The surface excess free energy can be calculated from enthalpies of drop-solution calorimetry measurements and thermodynamic cycles [16]. Which quantity is to be used depends on whether a new surface is being created (γ) or an existing surface is being modified (σ). For high temperature phase transitions of nanoparticles we assume an equilibrated state without external stresses. The relevant quantity for describing the size-dependent change of the state variables is thus the surface energy γ.

Limitations

Except for bulk single-crystal studies the common experimental data provides only scalar averages of strain and stress and averages of energy. That's why mean surface energy and mean, isotropic surface stress will be used throughout this work. Though scalar values are used one should not mistake this (like it has happened in the past) with the correctness of the capillary equation for liquids in solid particles (compare eq. 2). As explained by Weissmüller [6], the pressure jump inside a liquid is caused by the local curvature r which is absolutely constant in a droplet, just as γ. This is not the case for a crystalline, faceted particle. It consists of many different planes as well as edges and corners. So $\triangle P$ would be locally different. In fact a surface plane i has a specific γ_i and no curvature, so $\triangle P$ would be zero. Furthermore the stress in a solid can not be explained by the scalar γ. In contrast to γ the surface stress is a second rank tensor (for a plane surface[10]) and it is different for every surface plane. So it is more sensible to work with a balance of surface stress σ and volume stress to describe lattice changes in nanoparticles. Another point made by Weissmüller [6] is that γ determined via the SLDP method from the lattice change in nanoparticles (as done in [15]) gives the energy which is only related to the surface. This is different to the usual surface excess energy determined with calorimetry data which incorporates any excess energy of a nanoparticle, not only the one from the surface.

Another problem is that equation 2 would describe the crystal size by a single value r. The equilibrium shape of a small crystallite is faceted, i.e. it deviates from the ideal sphericity. Each facet has a different surface and thus different

γ_i. Only the Curie-Wulff theorem can justify the use of an equivalent radius to describe the size of a solid crystal. It establishes the relation of the surface energy of separate facets γ_i to the mean value of the entire particle γ [17]:

$$\frac{\gamma_i}{h_i} = \frac{\gamma}{r} \tag{4}$$

where h_i is the distance from the center of an equilibrium shaped crystal to its i-th facet. The radius r is the one of a sphere with the same volume as the crystal. Equation 4 makes it possible to describe a crystal with only the dimension r and an average surface energy but it requires the particle to have the equilibrium shape. All the thermodynamic models which were and will be presented make use of this theorem.

The limit of this approach to describe surfaces is actually reached within the nanoscale for several reasons: Closer consideration shows that many nanoparticles (especially those synthesized by wet-chemical routes near room temperature) do not posses the required equilibrium shape. So the total surface energy will be higher and Wulff theorem can not be applied. What is more, the surface regions of nanosized particles are only nanometers apart, so the influence from the surface (e.g. surface-induced volume stress) affects the entire interior. Consequently, the free energy state of the interior is higher than the known bulk reference value. When the surface excess energy over the bulk reference of such particles is measured (usually by calorimetry), it will be (a) higher and (b) incorporate contributions from the surface and from the interior. This is one reason for frequent discrepancies between different studies and sizes.

Another reason are surface adsorbates or surface defects. Under ambient conditions this can change the surface properties completely. For oxides dissociatively adsorbed water reduces γ [18] and causes more compressive σ. CO_2 has a similar effect. Oxides which can form carbonates tend to build a surface carbonate layer [13]. Superficial reduction and oxygen vacancy formation is another effect which alters the surface regions of oxides [19]. Less is known for metals, but as they are prone to oxidation most experiments with metal nanoparticles take place under high vacuum where such problems are minor.

Another inferiority of the thermodynamic approach originates from ascribing the surface excess energy to a surface without any depth. The position of the artificial surface should be chosen correctly within the real surface region in a way that it correctly reproduces the particle's behavior. In other words: The size and all depending parameters can have an error which is as big as thickness of the surface region - typically around ± 1 nm. This error becomes the more important the smaller the particles are. Below a certain size the continuous regime ends and any thermodynamic description fails. This is the size region of clusters which display a molecular-like behavior. Such clusters are not addressed in this work.

While the uncertainty of γ in liquid droplets is less than $\pm 0.5\,\%$, Lee et al. estimated the range for solid γ to be $\pm 10\,\%$ around the determined value for gold [20] and Zhang et al. [15] used error bars of approx. $\pm 15\,\%$.

2.2 Phenomenology of size effects

Two kinds of size-dependent effects exist in small systems: Firstly, smoothly scaling effects related to the fraction of low-coordinated atoms at the surface and secondly, quantum effects due to the completion of shells which show discontinuous behavior (steps). The latter case can occur in particles < 10 nm. An illustrative example is the size dependent fluorescence effect due to quantum confinement in silicon or CdSe nanocrystals [21, 22]. In the scope of this work is the former kind which occurs in phase transformations of nanomaterials. The surface energy adds a total excess energy to a nano-object that is proportional to the surface area. With that in mind, the principle of smoothly scaling size effects can be understood by a simple geometric consideration. Figure 1(a) shows cubes which consists of atoms symbolized by spheres. The edge length a is measured in number of atoms and the total number of atoms in the cube is $a^3 = N$. The surface area is $6a^2$ and the surface/volume ratio, e.g. the fraction of atoms at the surface is

$$\frac{A}{V} = \frac{6}{a} = \frac{6}{N^{1/3}} \tag{5}$$

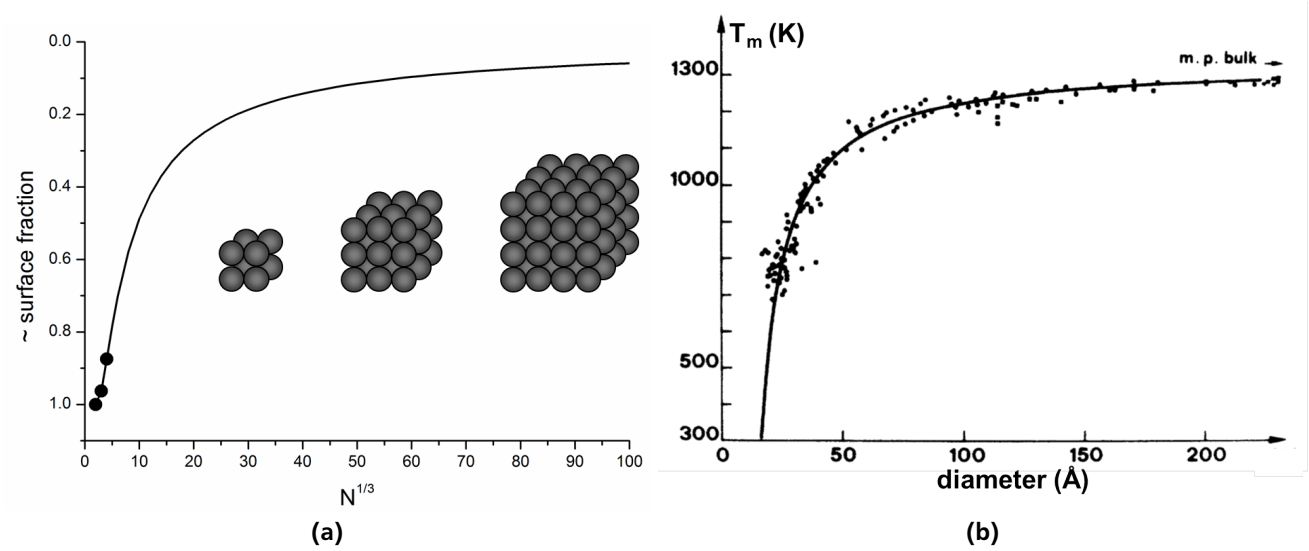

Figure 1: (a) The surface fraction in cubic particles made up of atoms. The atoms are symbolized by spheres. The fraction of atoms at the surface is plotted over the edge length of the cube, which is the 'total number of atoms$^{1/3}$'. The three smallest cubes are depicted and the corresponding points in the plot are marked with solid circles. One can easily count the number of atoms exposed to the surface. The fact that atoms on edges and corners are even more exposed is not considered. (b) Melting point depression of gold nanoparticles, measured by Buffat and Borel [1]. The points are measured melting temperatures and the solid line comes from a model describing the melting point reduction. The identical shape of the curves in (a) and (b) testifies the dependency of the melting point on the surface/volume ratio (surface fraction).

The respective curve can be seen in figure 1(a). It shows how the fraction of atoms at the surface increases proportionally to $1/a$. This proportionality holds for every shape; merely the proportionality factor changes (e.g. 3 for a sphere).

$$\frac{A}{V} \propto \frac{1}{r} \propto N^{-1/3} \tag{6}$$

A material property which is influenced by the surface excess energy must follow this dependency. As can be seen in figure 1(b) this is exactly the case for the depression of the melting point of gold nanoparticles. The excess contribution adds to the total free energy of the nanosized object. Therefore, less additional, thermal energy is needed to reach the melting point. The relative change of the melting temperature follows a $1-1/r$ dependency. In the following chapter the models for describing size-dependent phase transformations will show that the same relationship holds for other types of transformations as well.

2.3 Phase transformations in nanoparticles

Knowing about the properties of surfaces and understanding the size-effect the peculiarities of phase transitions in surface-dominated materials - e.g. nanoparticles can be described. As the heading of this work implies small particles are the objects under investigation, not thin films, rods or tubes. Even if such structures often behave in similar ways with rather quantitative than qualitative differences.

A phase transition is a change from one stable state to another when changing the state variable like pressure and temperature. The most common phase transitions are changes in the aggregate state: Melting and freezing as well as evaporation and condensation. But also structural solid-solid, magnetic, electronic state or superconducting transitions are possible. When the temperature is increased, the entropy rises. In ordered solids this change is much stronger than in a disordered gas and liquids are between these extremes. Therefore, at a certain point (T,P) the total free energy of the solid (liquid) state exceeds the one of the liquid (gaseous) state. Hence a phase transition takes place. The regions

of stability of the different phases, spanned by T and P, are graphically displayed in phase diagrams. The basis for describing the properties and stability of phases in a thermodynamic way is Gibbs free energy G or the molar Gibbs free energy, the chemical potential μ .

$$\mu = \left(\frac{\partial G}{\partial n}\right)_{T,p} \tag{7}$$

Here n is the number of moles of the pure substance.The boundary line of two adjacent, stable phases in a phase diagram marks the phase transition. Along this line the two phases are in equilibrium with each other, which means that their chemical potentials equal:

$$\left(\mu(s \dot{\vee} l)\right)_{T_0,P_0} = \left(\mu(l \dot{\vee} g)\right)_{T_0,P_0} \tag{8}$$

Here s, l and g denote the solid, liquid and gaseous aggregate state, respectively and $\dot{\vee}$ is the mathematical sign for 'exclusive or'. When describing phase transitions of nanoparticles the principles remain the same, but for a condensed phase an additional term for the surface excess free energy γ on the surface A is added to G. At constant temperature and pressure one finds

$$(G)_{P,T} = \frac{V}{v_m}\mu + A\gamma \tag{9}$$

The first summand is the usual volume (bulk) term, the second summand describes the surface free energy. For a bulk material the second term is negligibly small. But as the surface-volume ratio increases for small particles (see chapter 2.2) the surface term contributes more and more to G. As $G(s)$ and $G(l)$ change ($G(g) = const.$) relative to each other, the regions of phase stability and thus the phase transition temperatures change. So in addition to the usual variables P, T and N the surface area A enters the equations and the free energy and chemical potential become area-dependent (size-dependent). Note that the surface energy as it is described here is only correct if the surface excess only depends on the amount of surface A while γ is constant. If γ was variable itself because it depended on the global or local curvature (e.g. at an edge or corner), equation 9 would not be correct anymore. What is more, this thermodynamic description breaks down at a certain size: Phase transitions are collective phenomena. One makes use of thermodynamics to phenomenologically describe the behavior of a system comprised of a large number of identical parts (atoms or molecules). With a lower number of atoms in a cluster a phase transition is less well defined. It is therefore no longer sharp. Small clusters behave more like molecules than like bulk matter. Thus, the definition of a phase and hence a transition temperature is not correct anymore. This is similar to the limit of the formalism to describe the surface energy from chapter 2.1 on page 5. At the limit of the continuous regime the thermodynamic models, the desciption of surfaces as well as the theory of phase transformations break down. Below that size a thermodynamic description fails because the contribution of every atom is important to describe the cluster behavior. Such clusters are not addressed in this work.

In practice working with nanoparticles evokes a lot of problems. Peculiarities of different syntheses often cause the size-dependent properties to be superimposed by other factors like residual stresses, interface segregations, size-distribution, non-equilibrium phases, impurities and surface adsorbates. Characterization in the nanoscale is also challenging and many details remain hidden. The view on size-dependent behavior is therefore often blurred by several parasitic effects. In the following sections the relevant phase transformations for this work: Evaporation, melting and solid state transformations in oxides will be elucidated. We will start with the liquid-vapor phase transition, since the isotropic properties of melts make the models simpler and more accurate than in the melting case. Emphasis is put on melting as the most common, most investigated and most discussed phase transformation. Finally, we will introduce the transformations of different modifications in solid nanoparticles.

2.3.1 Evaporation

In evaporation and also in melting the surface plays a decisive role because it is the surface from where condensed species enter the gas phase. So it is always a process that depends on the surface properties, even if it is treated as a bulk property in thermodynamics. This fact is independent of the particles size.

For a single component, two-phase system such as a liquid and a vapor of the same substance the phase boundary curve is equivalent to the vapor pressure of the condensed phase (function of temperature). To calculate the phase boundary one makes use of the Clapeyron equation which gives the slope of the vapor pressure p_s.

$$\frac{dp_s}{dT} = \frac{\triangle_{tr}H}{T\,\triangle_{tr}v_m} \tag{10}$$

Here $\triangle_{tr}H$ and $\triangle_{tr}v_m$ are the phase transition enthalpy and molar volume change during the transition, respectively. With $\triangle_{tr}H = \triangle_{v}H$ the heat of vaporization and the assumption $\triangle_{tr}v_m \approx v_m(v) = RT/p$ the Clausius-Clapeyron equation follows. It describes the temperature dependence of the vapor pressure:

$$\frac{d\,ln(p_s)}{dT} = \frac{\triangle_{v}H}{RT^2} \tag{11}$$

$R = 8.31447$J/mol K is the gas constant. Evaporation is a first order phase transformation, so $\triangle v_m$ and $\Delta_v H$ ($\Delta_v S$) show a gap at the transition temperature. If done by calorimetry, where the enthalpy of vaporization (DSC) or the heat capacity C_p (AC- or modulated calorimetry) can be directly measured, T_v can be accurately determined. Because the heat of vaporization is approximately constant over a wide range of temperatures one receives by integration from pressure p_1 at T_1 to pressure p_2 at T_2

$$p_2 = p_1\,exp\left[-\frac{\triangle_{v}H}{R}\left(\frac{1}{T_2}-\frac{1}{T_1}\right)\right] \tag{12}$$

If a p_1, T_1 point is known, e.g. at a phase transition in ambient pressure, one can calculate the vapor pressure/phase boundary curve for the system.

The same considerations also apply to solid-vapor equilibria. A solid phase also has a vapor pressure which is not always negligible. However, many oxides decompose prior to reaching the melting point, even under atmospheric pressure. This rather has to be described by redox-reactions than physical phase transformations (see chapter 2.4 on page 18).

After deriving the vapor pressure of bulk materials size-dependent changes for nanoparticles will be elucidated. If a spherical nanoparticle with radius r, liquid or solid, is in equilibrium with its vapor, the vapor pressure is greater than the same pressure of a planar surface. This was theoretically stated by Lord Kelvin in 1871 [23] and found repeated experimental validation starting in the middle of the 20th century [e.g. 24]. It was initially derived for a liquid droplet for which the condition of constant curvature and γ are always fulfilled. The so called Kelvin equation describes the increase in vapor pressure of small droplets compared to the planar surface of the bulk.

$$\ln\frac{p_p}{p_s} = \frac{2\gamma v_m}{rRT} \tag{13}$$

So the logarithm of the vapor pressure of the droplet p_p shows a reciprocal size dependence. Again, as described in section 2.1 for the Young Laplace equation (2) the thickness of the surface is non-zero, but expands over a few atomic distances. When the droplet becomes sufficiently small compared with the actual thickness of the surface, the use of classical thermodynamics and bulk γ become inaccurate. Hence the Kelvin and the Young-Laplace equation no longer apply. For reasons also explained in the same chapter, the Kelvin equation can be equally applied to solids if one can assume equilibrium shape. Sambles et al. [24] performed a TEM study of evaporating gold nanoparticles. They confirmed the validity of the Kelvin equation for liquid and with less accuracy also for solid nanoparticles down to 10 nm. The history

of other confirmations of the Kelvin equation can also be found in this article. Nanda et al. [25, 26, 27] presented a method for measuring the size-dependent evaporation of free nanoparticles in a gas stream. Similar like determining the onset of an event in a DSC they determined an onset temperature for evaporation which changed with initial size. With help of the Kelvin equation (13) and a bulk reference they determined a mean value for γ of PbS, Ag and Au.

In aerosol science nucleation theory is an approved tool [28]. The inverse case of heterogeneous condensation can be used to calculate the rate of evaporation of a substance from its vapor pressure. Free, levitating particles are considered. When the concentration of particles is low, so that the size of the particles is much smaller than the mean free path, the evaporation rate can be calculated from kinetic theory. In this case the Hertz-Knudsen equation gives the condensation / evaporation rate F (number of molecules per unit time) for a component [29].

$$F = \frac{dn}{dt} = \frac{\alpha(p - p_p)}{\sqrt{2\pi m_m RT}} A \tag{14}$$

α, the accommodation coefficient, is often set equal to unity, but can be different, especially for a solid. A different rate between solid and a liquid particles comes either from a different vapor pressure or $\alpha < 1$ in the solid. m_m is the molar mass and A the surface from where evaporation can take place. The $p - p_p$ term is the driving force for nucleation or evaporation. In the condensation case $p - p_p > 0$ and gas molecules deposit on the surface (thus slowly increasing the size and surface). In the case of evaporation $p - p_p < 0$. Therefore $F < 0$ and molecules leave from the surface and the particle shrinks. To describe the shrinkage one can change equation 14 to the following form [30].

$$\frac{dv}{dt} = \frac{v_m \alpha(p - p_p)}{\sqrt{2\pi m_m RT}} A \tag{15}$$

For very small particles $p_p \neq p_s$ and p_p has to be corrected by the Kelvin equation (13).

2.3.2 Melting

In melting, the surface plays a decisive role because it is the surface where the melting process is initiated. In a similar way, defects and impurities in solids can also facilitate melting by serving as disturbances of the crystalline order - just like a surface. This fact is independent of the particle size.

In analogy to evaporation, the first-order phase transformation from solid to liquid state in bulk happens at $\mu(s) = \mu(l)$ and can be described by the Clapeyron equation for the slope of the phase boundary.

$$\frac{dp}{dT} = \frac{\triangle_m H}{T \triangle v_m} \tag{16}$$

As the heat of fusion (enthalpy of melting) $\triangle_m H$ is always positive and the molar volume change $\triangle v_m$ is also usually positive and very small, the slope is steep. This means on the other hand that the differential quotient $\frac{dT}{dp}$ is small, thus the pressure dependence of the melting transition is weak.

The intrinsic mechanism of melting is in many respects still unsolved and various melting theories exist [31]. For quite successful quantitative description, Christian [32] defined melting as a nucleation and growth phenomenon: Formation of liquid is followed by a movement and growth of the solid-liquid interface through the sample. For this endothermic process it is known that it is normally initiated at solid surfaces, interfaces or defects. Once the heterogeneous nucleation of the melt has started at a disturbance site, the liquid phase expands throughout the sample. Because the surface always serves as seed for melting, it is hardly possible to overheat a substance. On the other hand, supercooling during crystallization is common for the reason of lacking seeds in the homogeneous liquid. In some cases the surface can be melted long before melting of the bulk takes place. Thermodynamically complete surface melting will occur whenever

the solid surface is able to lower its free energy by turning into a sequence of two separate solid-liquid plus liquid-vapor interfaces [33]. Thus when the following condition is fulfilled:

$$\gamma_{sv} > \gamma_{sl} + \gamma_{lv} \tag{17}$$

Typical materials exhibiting surface melting are lead and tin. Since the γ values depend on the crystal plane, the condition 17 actually has to be met separately for every surface. Hence it varies not only from material to material but also from surface to surface [34]. For many materials and surfaces the inequality in equation 17 is not true and either a very thin quasi-liquid layer retaining a certain amount of order from the solid underneath or only a certain amount of disorder appears close to the surface [35, 36, 37].

As expected, changes occur at the nanoscale. The phenomenon called melting point depression was theoretically predicted by Pawlow in 1909 [38, 39] and experimentally shown in 1956 by Takagi and Mieko [40]. Since then numerous experimental and theoretical studies have dealt with this topic. By now, it has become a well known phenomenon - at least for metals. Figure 1(b) shows the values of the famous study on gold nanoparticles by Buffat and Borel [1]. The reason for the decreasing melting temperature is the increasing relative amount of surfaces with low-bound atoms in its vicinity. As illustrated in chapter 2.2 all such effects roughly follow a $1/D$ behavior. The confirmation of such behavior is the representation as a straight line in a plot of T_m over the reciprocal size. Deviations from this straight line can have several reasons which will be treated in the discussion of this work. There are a number of different models, most of them based on an assumption of the melting process and then derived by the laws of thermodynamics. They all, thermodynamic or not, share a basic form of the equation for the size-dependent melting temperature T_m

$$T_m = T_0 \left(1 - \frac{X}{D}\right) \tag{18}$$

T_0 is the melting temperature of the bulk, and X has to be substituted depending on the model. The $1/D$ dependence is visible. All the current models haven been developed for metallic nanoparticles.

In the following sections several outstanding models will be described. They were all developed for metallic systems with an assumed proportionality between the surface to volume ratio and the cohesive energy of a particle. A thorough comparison on a test-system with several conclusions for their validity and use is performed in chapter 3.

Homogeneous growth model (HOG)

The simplest way of describing melting of nanoparticles is by taking the convention $\mu_s = \mu_L$, using chemical potentials accounting for bulk and surface and introducing a size-dependence: The Gibbs free energy of fully solid or liquid nanoparticles which are modeled as perfect spheres can be described by a usual bulk term and an additional term for the surface energy (see eq. 9):

$$\begin{aligned} G(s) &= \frac{4}{3}\pi r^3 \frac{\mu(s)}{v_m} + 4\pi r^2 \gamma_{sv} \\ G(l) &= \frac{4}{3}\pi r^3 \frac{\mu(l)}{v_m} + 4\pi r^2 \gamma_{lv} \end{aligned} \tag{19}$$

where μ is the chemical potential, v_m the molar volume, r the radius of the sphere and the letters s, l and v denote the solid, liquid and vapor phase. For the case of a nanoparticle

$$\mu(r) = \left(\frac{\partial G(r)}{\partial n}\right)_{T,p} = \mu^{\infty} + \frac{2\gamma v_m}{r} \tag{20}$$

This equation was derived using the Young-Laplace equation for the pressure increase in a droplet. In thermodynamics, melting is defined as the temperature where the chemical potential of the solid and the liquid phase equal ($\mu_s - \mu_l = 0$). A 1st-order Taylor expansion around the bulk melting temperature T_0 with $P = const.$ is

$$\mu(T)_P = \mu_0 + \frac{\partial \mu}{\partial T}(T - T_0) = \mu_0 - s_m(T - T_0) \tag{21}$$

s_m is the molar entropy. With $\triangle s_m\, T_0 = -\triangle_m H$ we get

$$\mu(s) - \mu(l) = -\triangle_m H(T_0 - T)/T_0 \tag{22}$$

With equation 20 for size-dependent μ_s and μ_l this yields

$$T_m = T_0 \left(1 - \frac{2\triangle\gamma_{sl}\, v_m}{\triangle_m H\, r}\right) \tag{23}$$

The term $\triangle\gamma_{sl} = \gamma_{sv} - \gamma_{lv}$ was used. This is the well known Gibbs Thomson equation applied for a solid-liquid transition. It describes the 1/r dependence of the melting temperature that all thermodynamic models have in common. Of course the assumption that v_m is the same in the solid and the liquid phase is a crude approximation. Introducing different volumes (or densities) and using separate γ_{sv} and γ_{lv} results in the slightly more complicated formula. It is the first model for describing the melting temperature of a small, solid particle which was derived by Pawlow in 1909 [38].

$$T_m = T_0 \left(1 - \frac{2v_m(s)}{\triangle_m H\, r}\left(\gamma_{sv} - \gamma_{lv}\left(\frac{v_m(l)}{v_m(s)}\right)^{2/3}\right)\right) \tag{24}$$

The radius is the one from the solid phase. It shows that the larger ratio of v_m(or ρ) between the liquid and the solid phase the lower the degree of melting point depression. Furthermore the condition $\gamma_s > \gamma_l \left(v_m(l)/v_m(s)\right)^{2/3}$ must be fulfilled for a reduction of the melting point.

Alternatively one could assume equality of the size-dependent Gibbs free energies (eq. 19) at a certain temperature. Using the relation in equation 22 results in the formula

$$G_s(r) - G_l(r) = \frac{4}{3}\pi r^3 \frac{\triangle_m H(T_0 - T)}{v_m T_0} + 4\pi r^2 \triangle\gamma_{sl} \tag{25}$$

Assuming $G_s(r) - G_l(r) = 0$ instead of $\mu_s - \mu_l = 0$ and rearranging to T gives the result

$$T_m = T_0 \left(1 - \frac{3\triangle\gamma_{sl}\, v_m}{\triangle_m H\, r}\right) \tag{26}$$

Using the Gibbs free energy instead of the chemical potential has the consequence that the size-dependent transition temperature according to equation 26 is lower than according to equation 23 because of the factor *3* instead of *2*. So two different size-dependent melting temperatures exist. All advanced models are based on the Gibbs-Thomson equation and therefore involve factor *2*. The two equations are used as upper and lower limit in the liquid nucleation and growth (LNG) model (chap. 2.3.2).

These thermodynamic considerations only give the size-dependent limit of stability. They do not consider changes at an atomic level and do not give any hint on how the process of melting actually takes place. One could also say that in these thermodynamic models the entire particle transforms instantly at a given temperature. It has to be emphasized that the derivations above come from a 1st-order approximation in equation 21. Buffat and Borel [1] performed the

same derivation for a 2nd-order expansion, thus introducing linearly temperature-dependent and pressure-dependent terms (thermal expansion, etc.). Furthermore the temperature-dependence of $\triangle_m H$ is usually small. Thus, most models refer to the bulk value at T_0. Possible changes of any parameter with decreasing particle size are neglected. Nevertheless, formulas 23, 24 and 26 are a reasonable basis for discussing the size dependence of the melting behavior of nanoparticles.

Heterogeneous growth model (HEG)

This model, developed by Lee et al. in 2007 [41] is a very recent model. Like the HOG, it does not presume a process of melting but uses only the thermodynamic requirement $\mu_s - \mu_l = 0$ for melting. A main difference is that it considers that in most experiments the particles lie on a carrier film made of different materials. Hence, not only a surface but also a particle-substrate interface exists and in terms of nucleation theory this would be a heterogeneous melting process. Depending on the surface energies of substrate and particle and the contact angle, the shape of the particle changes. This in turn changes the surface area and the interface area. The describing function is

$$\mu(r) = \mu^{\infty} + \frac{C_1 \gamma_{sv} v_m}{r} + \frac{C_2 \gamma_{sc} v_m}{r} \tag{27}$$

C_1 and C_2 are geometric factors for describing the particle shape and interface area. They depend on the contact angle Θ which is considered to be constant in this model. γ_{sc} is the interfacial energy between the particle and the carrier film. The lower the contact angle the higher the influence of the interface region. At $\Theta = 0$ the material would wet completely and interface and surface would have the same area, thus the same influence. For $\Theta < \pi/2$ the sphere-fraction starts to shrink. Hence, the equation only works for contact angles greater than 0 [41].

Another feature of this model is, that it does not simplify the $\mu(s) - \mu(l) = 0$ relation by assuming a constant $\triangle_m H = (s(l) - s(s))T_0$ but the correct, tabulated, temperature-dependent functions (from SGTE) of $\mu^{\infty}(s)$ and $\mu^{\infty}(l)$ are used. This gives higher accuracy and can be especially useful if multi-component materials are treated.

Liquid shell model (LSM)

The so called liquid shell model was proposed by Reiss and Wilson in 1948 [42] and further modified by Curzon [43], (cf. also Hanzen [44]). From the understanding that melting is initiated on the surface (by pre-melting) the assumption was made that a thin liquid shell of thickness t surrounds the solid particle close to the melting temperature. The size-dependent melting temperature is then

$$T_m = T_0 \left(1 - \frac{2 v_m(s)}{\triangle_m H} \left(\frac{\triangle \gamma_{sl}}{r - t} - \frac{\gamma_{lv}}{r} \left(1 - \frac{v_m(l)}{v_m(s)}\right)\right)\right) \tag{28}$$

where γ_{sl} is the solid-liquid interfacial energy. For this equation the radii of a solid and the liquid particle are assumed to be equal at the transition temperature. This is the same rough approximation like in the Gibbs-Thomson equation (23). Calculating the size difference by using mass conservation and the difference in the molar volumes the equation changes slightly.

$$T_m = T_0 \left(1 - \frac{2 v_m(s)}{\triangle_m H\, r} \left(\frac{\triangle \gamma_{sl}}{r - t} - \frac{\gamma_{lv}}{r} \left(1 - \left(\frac{v_m(l)}{v_m(s)}\right)^{2/3}\right)\right)\right) \tag{29}$$

When the liquid shell thickness approaches zero, e.g no surface melting occurs then the inequality 17 should become an equality. In that case equation 29 is equal to Pawlows HOG model (24).

Liquid nucleation and growth (LNG)

The temperatures in the models above are purely derived from thermodynamics. They do not imply anything about the process of transformation but only state the temperature for switching from one (equilibrium) state to the other. For nucleation problems the nucleation theory has shown to be very efficient, even for smallest particles [28]. Hence, the inverse process, melting of nanoparticles, was described based on nucleation theory as well: The nucleation of a solid-

liquid interface is followed by propagation into the core of the particle over time (not instantly). The theory requires the liquid to wet the solid, e.g. $\gamma_l < \gamma_s$ and also $\gamma_{sv} \geq \gamma_{sl} + \gamma_{lv}$ (eq. 17) so that it is energetically favorable to form a molten surface layer. If that is not the case a melting surface would not cover the solid core and no predictions about the growth process could be made [45].

According to the theory, a critical radius r^* for the inner, solid core r_c exists which depends on the temperature

$$r^* = \frac{2\gamma_{sl}\nu_m T_0}{\triangle_m H\,(T_0 - T)} \tag{30}$$

A temperature of unstable equilibrium is reached at $r = r^*$ (eq. 30) where $\mu_s = \mu_l$ with zero driving force in either direction. This marks the upper limit where every particle, at latest, must transform. The difference of the molar volumes is generally neglected and so the limit is the Gibbs-Thomson equation (eq. 23). The lower boundary was proposed by Couchman and Jesser *[46]*

$$T_m = T_0\left(1 - \frac{3}{\triangle_m H\, r}\left(\frac{\gamma_{sv}\nu_m(s)}{r(s)} - \frac{\gamma_{lv}\nu_m(l)}{r(l)}\right)\right) \tag{31}$$

It was derived from equating the Helmholtz free energies of the solid and the liquid phase to find the lowest temperature where a transition would be possible. Under the assumption that the radii of the solid and liquid particles are close to each other, $r(s) \approx r(l)$, and when the ν_m-difference is neglected again, this analogously corresponds to equation 26. Important consequences of the LNG were that a free energy (nucleation) barrier exists between a local minimum (liquid state) and a global minimum (solid state with liquid surface layer) as soon as the temperature is higher than the lower limit. The barrier is at the critical radius $r*(T)$. Process-wise this means that around the lower limit a liquid surface layer nucleates. It steadily grows into the solid core with rising temperature. When the core gets smaller than the critical radius ($r_c \leq r^*$), the remaining solid core will melt almost instantaneously. This can happen by fluctuations at every temperature between the lower and the upper limit and the event becomes the more likely the higher the temperature is. Hence, the melting rate rises when the temperature approaches T_m of the upper limit and the majority of an ensemble of particles melts below the upper limit. That is why the LNG model predicts a transition range. This transition range is in accordance with latest experimental observations and simulation results which do not report a clear size-dependent melting temperature but rather a coexistence range (see chapter 3.2). The melting range of separate particles should be underneath the thermodynamic equilibrium of equations 23 and 24. A nucleation rate which predicts the speed of the transformation process can also be calculated. For melting to take place at a reasonable, laboratory time-scale it was defined that the nucleation rate ought to be larger than one nucleation per second . This can be used as melting-criterion and the melting temperature can be iteratively approached by varying T until the nucleation rate equals 1 nucleus/s. This rate is more easily reached by larger particles [28, 45].

The equations for the limits of the LNG were not new. But the concept of explaining the melting as a nucleation and growth process by means of the kinetic nucleation theory rationalized the liquid surface and gave meaning to how the melting of a particle actually takes place. Compared to the LSM, the model does not simply postulate a liquid surface layer of constant thickness.

Bond-order-length-strength model (BOLS)

This model differs considerably from the previous ones because it is based on atomistic rather than thermodynamic considerations. It was established and descried by Sun et al. [47, 48, 5] for metals. It links classical thermodynamics with an atomistic approach to describe the effect of size-dependent melting and evaporation. The underlying bond-order-length-strength correlation is derived from the correlation of atomic-coordination number and atomic-radius noted by Pauling [49]: A reduction of the coordination number happening to atoms at the surface or at sites surrounding defects causes a contraction of the remaining bonds of the atom. The spontaneous bond contraction is associated with an increase of the bond energy near the disturbance site. Since Goldschmidt [50] it is known that the radii in ionic crystals regularly decrease with decreasing coordination number, so a similar behavior can be anticipated for such materials. The physical ground of the model is that if one wishes to loosen (melting) or remove (evaporation) atoms or ions in a solid material

one needs to overcome the energy of all their bonds (cohesive energy, E_{coh}). For melting E_m and for evaporation $E_v = 0$ (work function) has to be reached. It is assumed on empirical basis that this energy, supplied in form of thermal energy (E_{therm}), is proportional to the melting temperature of the material. This is necessary for comparison with experiments since T_m is the traceable quantity.

$$E_{coh} - E_m = E_{therm} \propto T_m \tag{32}$$

Other atomic models with a similar line of arguments are from Nanda et al. [51] and Qi et al. [52]. Based on observations BOLS presumes that the under-coordinated atoms with changed bond-strength in the surface region of 2-3 atomic layers dictate the T_m change of nanostructures, yet atoms of the interior remain as they are in the bulk.

The derivation of the model is as follows [5]: Starting with the coordination deficiency z and z_i are the coordination number in a bulk (usually 12 in dense packing) and in the i-th atomic layer counted from the surface. Experience showed that z_i approximately takes the values in equation 33 for a curved surface [53] where layers bigger than 3 are considered to be bulk-like. This is the point where the reciprocal size enters the model, just like in the thermodynamic models.

$$\begin{aligned} z_1 &= 1-(0.75/K_j) \\ z_2 &= 6 \\ z_3 &= 8\dot{\vee}12 \\ z_{>3} &= 12 \end{aligned} \tag{33}$$

The dimensionless form of the size is K_j (being the number of atoms lined along the radius of a sphere) of particle j.

$$K_j = r_j/d_0 \tag{34}$$

Now d_0 is the mean bond length of an atom in the bulk. Depending on z_i in the i-th layer the bond length of an atom changes to d_i which will be shorter according to the BOLS theory. It is given by

$$d_i = c_i d_0 \tag{35}$$

where c_i describes the imperfection by including the coordination number z_i of the specific atom. c_i is the heart of the BOLS model. It can also be called the normalized cohesion energy of a surface atom in i-th layer[47].

$$c_i(z_i) = \frac{2}{1+exp\left[\frac{12-z_i}{8z_i}\right]} \tag{36}$$

The consequence of the bond contraction is an increase in bond energy from the usual bulk value E_B (counted from the the work function = 0) to E_b in the respective layer.

$$E_b(d_i) = c_i^{-m} E_B \tag{37}$$

m is the only adjustable parameter in the model. It is used to represent the bond nature. For most metals it is 1 which means that E_b and c_i are linearly correlated. For alloys and compounds m is around 4, for C and Si, the m value has been optimized to be 2.56 [54] and 4.88 [53], respectively. Though m is a constant in the model, it was shown that it may vary if the bond nature evolves with atomic coordination number [55].

The single bond energies ($E_b\dot{\vee}E_B$) of an atom are summed up to the cohesive energy of an atom ($\sum_{z_i} E_b(d_i)\dot{\vee}12\,E_B$). The sum of all atoms' cohesive energy gives the total cohesive energy of an entire particle. This total cohesive energy

indicates how strongly the atoms hold together, e.g. how much thermal energy is required to loosen the bonds and reach E_m or E_v. While the surface bonds become slightly stronger the total number of bonds is decreased at the surface. The net total cohesive energy of a particle E_{coh} decreases for particles with many surface-atoms. This total cohesive energy is divided into the bulk contribution, $E_{coh}^{\infty}(N)$, and the surface excess contribution as the sum of the first three layers:

$$E_{coh}(K_j) = E_{coh}^{\infty}(N) + \sum_{i=1}^{3} N_i \left(\sum_{z_i} E_b(d_i) - 12\, E_B \right) \tag{38}$$

N is the total number of atoms in the particle and N_i the number of atoms in the i-th layer. To achieve melting of a particle, the constant energy level E_m has to be reached by additional thermal energy. The difference between the cohesive energy of the particle and the constant melting level gives the required thermal energy.

$$E_{therm} = E_{coh}(K_j) - E_m \tag{39}$$

For a given solid material only the surface layers with their changed BOLS influence the thermal energy required for evaporation/melting. Thus, it suffices to look at the relative change of energy.

$$\frac{\triangle E_{therm}}{E_{therm}^{\infty}(N)} = \frac{E_{therm} - E_{therm}^{\infty}(N)}{E_{therm}^{\infty}(N)} = \sum_{i=1}^{3} \varsigma_i \left(\frac{z_i}{z_{bulk}} c_i^{-m} - 1 \right) \tag{40}$$

ς_i is the surface layer to volume ratio (or the atomic portion of the i-th atomic shell) calculated by the formula

$$\gamma_i = \frac{N_i}{N} \simeq \frac{\tau c_i}{K_j} \tag{41}$$

and τ is the dimensionality of the solid. It is used to describe different structures like rods or plates. For a particle $\tau = 3$. Up to here only the cohesive energy on an atomic level was considered. With equation 32 the chain of arguments is linked to temperature as the traceable quantity. It follows the size dependent melting temperature calculated by the BOLS model:

$$\frac{\triangle T_m(Dp)}{T_m(\infty)} = -\sum_{i=1}^{3} \varsigma_i \left(\frac{z_i}{z_{bulk}} c_i^{-m} - 1 \right) \tag{42}$$

This equation links classical thermodynamics with an atomistic approach to describe the effect of size-dependent melting and evaporation. But the assumption of equation 32 requires the heat capacity of the nanoparticles to be the same as the one of the bulk. This surely introduces an error which was estimated to be $\leq$5% [5]. This error is said to be acceptable, especially because it causes quantitative but no qualitative errors. BOLS is basically also able to model the existing case of negative surface stress, where the surface bonds expand instead of contract. Then c_i has to be > 1 and m has to be negative instead of positive. Moreover the $c_i(z_i)$ value is a mean for all atoms in the i-th layer, but actually it would be anisotropic and dependent on the effective coordination number of every atom. Especially the surface plane, as well as edge- and corner sites, would have a strong influence.

The two main effects in the BOLS model are (a) the interatomic interactions near the surface from which the name is derived and (b) the geometric result of increasing surface area with decreasing particle size, which it shares with all the thermodynamic models. The latter effect causes a usual $1/D$ dependence. The differences of this model, which will be demonstrated in chapter 3.2, result from the former effect which changes the way the surface region is described: The surface has a constant thickness of three atomic layers (similar to t in the LSM). While the thickness is constant, equation 33 incorporates a variable coordination number which decreases in small particles due to higher curvature. This has the same effect like a decreasing γ would have in the thermodynamic models. The bond energy which the BOLS model

is based on is a very basic physical quantity. Deriving size-dependent changes like this seems sensible as it avoids any material parameters except T_0 for scaling reasons and only relies on the average atomic bond distance. Appealingly this leads to a model with few assumptions and only one adjustable parameter, m, which is not used for fitting or deriving physicochemical quantities. As the thermodynamic models, BOLS has been developed mainly with regard to metallic systems. According to Sun [5] it can be applied to other material systems as well.

2.3.3 Structural solid state transitions

Temperature induced size-dependent solid state transitions have been reported rarely because inadvertent particle reorganization, sublimation or sintering change the dispersion and obstruct the experimental observation. Rivest et al. recently reported the size-dependent solid-solid transition of low chalcocite to high calcocite copper(I) sulfide nanorods scattered on a substrate [4]. They found a similar $1/D$ dependence of the transition temperature like in melting of nanoparticles. Suresh et al. studied nanoparticles and sintered briquettes with nanocrystallites of yttria stabilized zirconia [56]. They found a size dependency of the solid-solid phase transformation from the tetragonal to monoclinic form and brought forward a model. The principles of size dependent chemical potentials were taken from the melting of nanoparticles. Yet, heating alters the size-distribution. So it is difficult to measure the transition temperature and it is more convenient to calculate the critical size (D_c) for a phase transformation at a given temperature.

$$\frac{1}{D_c} = \frac{\triangle_{tr}H}{6\triangle\gamma}\left(1 - T/T_0\right) \tag{43}$$

In analogy to the size-dependent melting $\triangle_{tr}H$ and T_0 are the bulk enthalpy and temperature of transformation. $\triangle\gamma$ is the difference between the interfacial energies of the two phases. In the case of free particles this corresponds to γ_{sv} but for sintered crystallites in a nanostructured material it changes to the grain boundary energy. In the latter case an additional term to account for the deformation energy involved in the transformation has to be added. Apparently a mayor difference between free particles, a more or less compacted powder and a dense, polycrystalline material are their surface states: Single particles have free surfaces, agglomerated ones have a mixture of surfaces and interfaces to their neighbors and a dense body solely consists of grain boundaries. As interfaces rule the properties at the nanoscale such differences have decisive consequences.

Navrotsky et al. [18, 57, 58, 59] quantitatively showed the size-dependent polymorphism and drew phase diagrams of several oxides like alumina, titania and zirconia. They also measured the impact of hydrated surfaces and of shape on the surface energy and stability. A summary of unusual phase compositions caused by nanometer-size was given by Andrievskii and Khachoyan [60].

2.4 Size-dependent chemical reactions

The size-dependent change of the free energy in nanoparticles, as noted in equation 9 on page 9 has another consequence: the shift of reaction-equilibria. In the context of this work about oxide nanoparticles especially redox equilibria are important. Navrotsky et al. [61] showed for nanoparticles of several transition metal oxides how the changes of chemical potentials can affect the stability fields. The ranges of stability of the metal and the oxide forms shift and some phases may even become completely unfavorable. Other hints in literature are that easier reduction of oxides to metal in vacuum has been observed for several nanosized oxides [62]. A higher reactivity of many materials in the nanoscale is exploited for catalysts. The reasons are not a sheer increase of surface area but also shifted bond length and strength [63].

In the course of this work a differentiation between size-dependent melting and size-dependent chemical reactions will be important. For this reason the described principles of size-dependent chemical potentials will be applied to model a size-dependent redox-reaction equilibrium now. Similar calculations with constant, measured enthalpies can be found in Navrotsky et al. [61].

In the following a size-dependent chemical reaction equilibrium will be derived. Similar calculations can be found in Navrotsky et al. [61]. Assuming that the chemical potential of a nanoparticle can be described by a constant volume term with bulk properties, μ^{∞}, and a size-dependent surface term then the chemical potential is written as in equation 20

$$\mu = \mu^{\infty} + \frac{2\gamma v_m}{r} \tag{44}$$

Generally for a simple redox reaction of a metal oxide, where M is the metal component

$$M_{n_M}O_{n_O} \rightleftharpoons n_M\, M + \frac{n_O}{2}\, O_2(g) \tag{45}$$

the Gibbs energy balance is

$$\triangle_r G_m = n_M \mu(M) + \frac{n_O}{2}\mu(O_2) - \mu(M_{n_M}O_{n_O}) \tag{46}$$

and with $-RT\, ln(k) = \triangle_r G$ and

$$k = \frac{a(M)^{n_M} \cdot p(O_2)^{n_O/2}}{a(M_{n_M}O_{n_O})} \approx p(O_2)^{n_O/2} \tag{47}$$

the phase diagram for p(O_2) - T can be calculated:

$$ln(p(O_2)^{n_O/2}) = -\frac{\triangle_r G}{RT} \tag{48}$$

The same is true for a reducing oxide nanoparticle but a size-dependent term enters. For the oxide and the metal the chemical potentials are as follows

$$\mu(MO) = \mu^{\infty}(MO) + \frac{2\gamma(MO)v_m(MO)}{r} \tag{49}$$

$$\mu(M) = \mu^{\infty}(M) + \frac{2\gamma(M)v_m(M)}{r} \tag{50}$$

As approximation the equations neglect the difference in r for respective particles with the same amount of n_M, just as the Gibbs-Thomson equation (23) in the HOG model and equation 28 in the LSM model did. These chemical potentials substituted in equation 46 render

$$\begin{aligned} \triangle_r G_m &= n_M \left(\mu_{\infty}(M) + \frac{2\gamma(M)v_m(M)}{r}\right) + \frac{n_O}{2}\mu_{\infty}(O_2) - \left(\mu_{\infty}(MO) + \frac{2\gamma(MO)v_m(MO)}{r}\right) \\ &= \triangle_r G_m^{\infty} + \frac{2}{r}\left(n_M\, \gamma(M)\, v_m(M) - \gamma(MO)\, v_m(MO)\right) \end{aligned} \tag{51}$$

$\triangle_r G_m^{\infty}$ includes all bulk terms and the difference in the brackets determines the extent of size-dependence. As all values are approximately constant, it can be substituted by X for ease of reading. The new expression for the Gibbs energy of the reaction is inserted in equation 48.

$$ln(p(O_2)^{n_O/2}) = -\frac{1}{RT}\left[\triangle_r G_m^{\infty} + \frac{2}{r}(X)\right] \tag{52}$$

From equations 51 on the previous page and 52 on the preceding page it is clear that the Gibbs energy of such a reaction follows a $1/r$ dependence, just like the melting temperature. Also the logarithm of $p(O_2)$ depends on the inverse of r as well as the inverse of T. Hence the size-dependence enters as a further variable to describe the redox reaction equilibrium with the same qualitative dependence as the melting temperature of nanoparticles.

Under common experimental conditions with a small sample in a huge reservoir, pO_2 can be considered as being constant. That enables to calculate the size-dependent reaction-equilibrium temperature

$$T = -\frac{1}{R\,ln(p(O_2)^{n_O/2})}\left[\triangle_r G_m^{\infty}(T) + \frac{2}{r}(X)\right] \tag{53}$$

Not to forget that $\triangle_r G_m^{\infty}(T)$ is actually a function of temperature which can be calculated from the Gibbs free energies of substances in the SGTE tables [64] or obtained from experimental data about the respective redox reaction.

2.5 Non-metallic materials

The majority of studies have been performed on different metals, especially gold and lead. The only non-metallic materials in the continuous regime were PbS [25] for evaporation, CdS [65] for melting and Cu_2S [4] for a solid-state transition. The present study deals with oxide particles which possess a covalent-ionic bonding character. The few insights into materials with such bonds are summarized here.

Studies about sintering of ceramic materials are quite common. Here an enhanced sinterability at lower temperature was observed repeatedly [66]. This could be a sign for size effects in ceramics. However, these effects have multiple factors. Two very important ones are that (a) the driving-force for sintering is greatly enhanced due to the small curvature and (b) very short diffusion distances facilitate early sintering. These observations are therefore no unambiguous sign for the change of phase transition temperatures.

On a thermodynamic basis there is no reason why materials with covalent or ionic bonds should behave in a qualitatively different manner than described in the above models. But this is because thermodynamics has no means to differ between atomic bond types. On an atomic level more sophisticated considerations come into play. Farell and Siclen [67] made density functional theory calculations on group IV elements. Their covalent bonds posses the possibility of re-hybridization to compensate for the loss of nearest neighbors at the surface. Therefore, the degree of bonding of surface atoms is higher than the sheer number of nearest neighbors would predict. The consequence is a change of the size-dependence for e.g. melting and evaporation which is better described by a square of the reciprocal radius ($1/r^2$) dependence. For other materials with covalent bonds such a dependence was prognosticated as well. However, Farell and Siclen only simulated particles consisting of 1 to 100 atoms (< 1.5 nm diameter) which is clearly below the continuous regime and falls into the category of clusters. The experimental study of Goldstein et al. [65] found no deviation from the typical $1/r$ behavior for CdS between 2.4 and 7.6 nm which weakens the theory. A likely explanation for the inconsistency is that the number of nearest neighbors of surface atoms only changes notably beyond the continuous regime. Down to that point the surface energy of particles with covalent bonds would be as constant as the one of metallic particles. That would mean, that the thermodynamic models would hold for covalently bound materials in the continuous regime. Diehm et al. reviewed the surface stress of oxides and other inorganic compounds [13]. They noted that ionic bonds, like metals, do not have an angular dependency and no possibility for re-hybridization. Ergo, despite the different nature of the bonds a principally similar behavior concerning surface stress and surface energy is expected. Considering all information at hand, one can expect a qualitatively similar, yet quantitatively different size-dependent behavior of inorganic compounds like bismuth oxide.

2.6 The Bismuth Oxygen system

The material under investigation in this work is mainly bismuth(III) oxide (Bi_2O_3). It was chosen because of its low melting temperature combined with good crystallinity and a stable melt - at least under atmospheric conditions. Fur-

thermore, a low $\triangle_m H$ promised a pronounced melting point depression at the nanoscale. The important structural and thermodynamic properties, as reported in literature, are summarized here.

2.6.1 Polymorphism

In the pure binary oxide the common oxidation state of Bi is +III, but in mixed valent Bi(III,V) oxides (e.g. Bi_2O_5 [68]) and in ternary oxides (e.g. $KBiO_3$ [69]) the +V state has also been reported. Also subvalent bismuth oxides (e.g. BiO [70]) are known. However, most of the work on bismuth oxides concentrates on Bi_2O_3. The proportion of covalency in the bonds is approx. 60%. A number of different polymorphs is known and only the most important ones are mentioned here. They are summarized in figure 2 together with the approximate transition temperatures. The stable structures occurring in every study are monoclinic α-Bi_2O_3 (P21/c (14)) which transforms at 1002 - 1008 K to cubic δ-Bi_2O_3 (Fm-3m(225)). Melting takes place from the δ-structure at 1077 - 1098 K (most often 1097 K) and boiling the point is 2163 K (in air). Two alternatively occurring, metastable phases are reported during cooling, the tetragonal β-Bi_2O_3 (P-421c (114)) or the b.c.c. γ-Bi_2O_3 (I23 (197)). The process is difficult to control and is strongly influenced by the presence of trace amounts of metal impurities and the texture of the sample. The conditions under which the phases form also seem to differ depending on the history of treatment: heating rate, cooling rate, maximum temperature and atmosphere. Furthermore β-Bi_2O_3 can be directly produced at RT by quenching from the melt, by decomposition of $(BiO)_2CO_3$ in air or bismuth oxalate in vacuum or by additions of e.g. CeO_2 or CeO_2 [71, 72]. Similarly γ-Bi_2O_3 can persist down to RT and can be directly prepared from α-Bi_2O_3 by tempering with an addition of small amounts of CoO [73]. All this is proof for a complex, multifactorial behavior. It could be influenced by compositional changes. Several articles report the loss of oxygen during heating of δ-Bi_2O_3, Zav'yalova and Imamov [74] state the stoichiometry of the δ-phase to be $Bi_2O_{<2.7}$ and Klinkova et al. [75] proposed that the deciding difference between different polymorphs in pure bismuth oxide is the oxygen content. As proof of their hypothesis they showed that a transition from δ-Bi_2O_3 to γ-Bi_2O_3 or a distorted tetragonal structure (fig. 2) could be achieved without cooling, simply by annealing at a constant temperature in vacuum (vacuum acts as a reducing atmosphere). The claim is further supported by the fact that all high temperature forms possess a considerable anionic conductivity, thus a high oxygen mobility in the lattice. Strictly speaking it would mean that the different bismuth oxide structures are not true polymorphs, but the structures depending inter alia on the Bi:O ratio.

The common bismuth oxide structures were summarized by Medernach and Snyder [76]. The α-Bi_2O_3 as the stable room temperature phase has a monoclinic structure of P21/c space group with 8 Bi^{+3} and 12 O^{-2} atoms in the unit cell. The lattice parameters are a=5.8444(2) Å, b=8.1574(3) Å, c=7.5032(3) Å, α,γ=90° and β =112.97(1)°. The cubic δ-bismuth oxide has a calcium fluoride (CaF_2) type structure in which 25% of the sites in the oxygen sublattice are vacant. This is the reason for its ionic conductivity [77]. It is an ongoing discussion whether the vacancies are statistically distributed [78]. The unit cell has the dimension a=5.6549(9) Å and contains 4 Bi^{+3} and 6 O^{-2} atoms. In certain cases the bismuth oxide can adopt to the metastable β-phase which has the same structure as the δ-phase, but with ordered oxygen positions [72, 79]. It is described by a tetragonal unit cell with $a=b$=7.7400(6) Å and c=5.6446(6) Å. β-Bi_2O_3 has poor ionic conductivity ($< 10^{-2}\ \Omega^{-1}cm^{-1}$) [78, 80]. γ-Bi_2O_3 has a more complicated structure. As the structure is not relevant for this study it will not be further elaborated.

2.6.2 Evaporation behavior

The evaporation behavior of binary compounds is more complicated than the one of elements, because a number of different gas components with different enthalpies of formation form. The total vapor pressure of the material has to be calculated from an equilibrium containing the condensed matter as well as all the gas components. Specially developed softwares are used for such purposes [81]. There is a dearth of information on the bismuth oxide vapor species. Researchers have reported numerous gas species: Bi, O, BiO, Bi_2O,Bi_2O_2, Bi_2O_3, Bi_3O_3, Bi_3O_4, Bi_4O_4, Bi_4O_6 and Bi_5O_7 [82]. The Bi-O system is complicated by the large number of gas species as well as the inconsistencies among the few studies conducted [83, 84, 85, 86]. All available data is based on mass spectrometric studies. Most of them

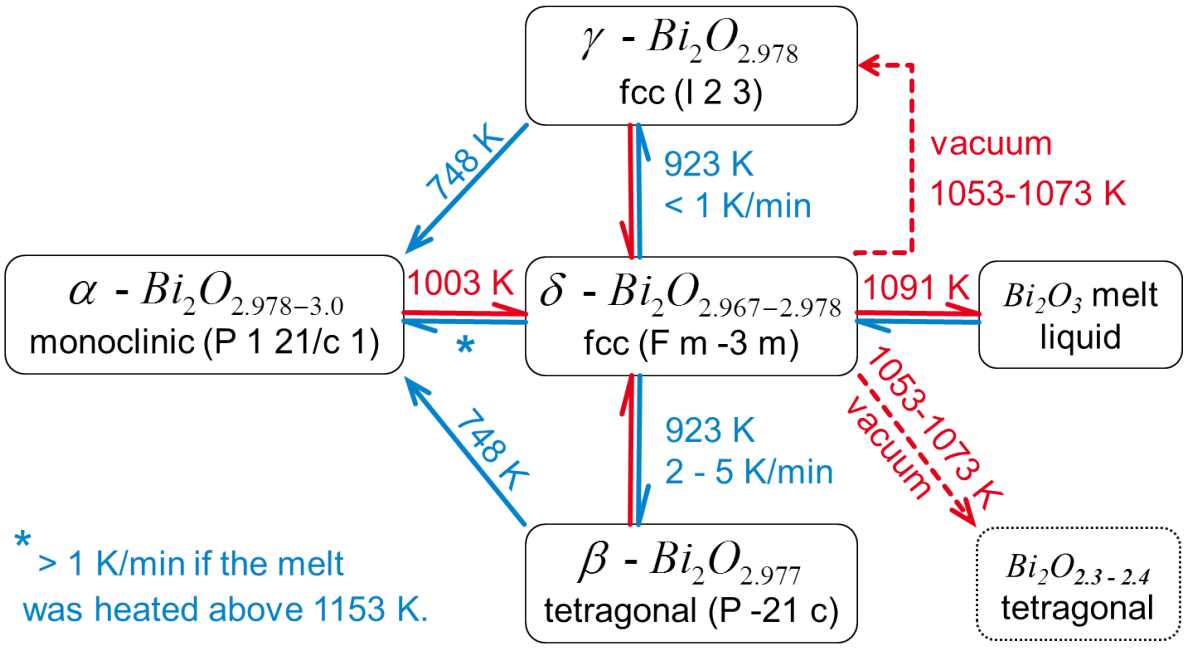

Figure 2: Scheme of bismuth oxide structures. Red arrows indicate heating, blue arrows indicate cooling. The information is a composition from literature values cited in the text, mainly from Mehring [73] and Klinkova et al.[75]. The transitions are reported to depend on multiple factors like maximum heating temperature and cooling rates. The absolute values of the temperatures and rates vary and no guarantee for the quantitative correctness can be given. Elevated temperatures in vacuum atmosphere can also provoke transitions (dashed arrows). Oxygen contents are from Klinkova et al..

where performed with a Knudsen cell. Starting in an initial vacuum the sample can establish the equilibrium vapor pressures. For mass spectrometric analysis a small stream with representative composition leaks through an opening into the vacuum on the other side without significantly affecting the equilibrium inside the cell. Agreement of these studies is only that the most frequent species are Bi and O by an order of magnitude. Besides, Bi_2O_3 and Bi_4O_6 were measured with considerable intensity in every study. Sidorov et al. discuss that many of the above-named species might form from $(Bi_2O_3)_x$ - for example by dissociative ionization in the mass spectrometer. This could be a reason for inconsistencies between different studies.

Simple thermogravimetric measurements in air at ambient pressure showed that appreciable evaporation begins at 1396 K; i.e. 300 K above the melting point. At 1623 K a constant rate of 0.05 mg/min occurs [87]. Measurable vapor pressures occur at 1223 K. While stable under these conditions bismuth oxide seems relatively unstable under reduced oxygen partial pressures. The $p(O_2)$ for decomposition is 250 Pa at 1835 K and 19.7 Pa at 1623 K [87]. A more recent study of ionic clusters produced by laser vaporization [88] provides insight into the stability of the species under different oxygen partial pressures in the vaporization chamber. Above $p(O_2)$= 300 Pa only bismuth oxides form (mainly $(Bi_2O_3)_x$) where as below $p(O_2)$= 200 Pa Bi_x form almost exclusively. Not only the condensed bulk but also the Bi-O species are only stable under a sufficiently high oxygen partial pressure.

The stoichiometry and the evaporation rate in oxides often change under vacuum. Stoichiometry changes are due to decomposition by reduction reactions which involve $p(O_2)$ on the product side. In this respect Shornikov et al. [89] showed how the vapor pressure of oxides increases when deviating from chemically neutral conditions. The increase of the evaporation rate is said to have a kinetic argument: Fewer collisions with other molecules and instantaneous evacuation of the escaping molecules [90]. Onyama et al. [86] found that composition change also applies to bismuth oxide at 1023 K (δ-phase) in vacuum, while the composition remains unchanged in air. Initially large amounts of oxygen evaporate until the composition $Bi_2O_{2.648}$ for congruent evaporation is reached. A composition of $Bi_2O_{2.92}$ for congruent evaporation was claimed by Mashkin et al. [91]. The statistically distributed oxygen vacancies are the reason for the high oxygen mobility and ionic conductivity in the δ-phase. At the same time it rationalizes why the oxygen content can

be changed so easily [75]. Moreover, notable evaporation takes place in the δ-phase and the evaporation rate further increases in the liquid state [85]. This, too is not the case in air [92, 93]. In summary the multiphase evaporation of bismuth oxide is drastically increased in vacuum, accompanied by stoichiometric changes of the still condensed matter.

2.6.3 Bismuth oxide at the nanoscale

Thin films of bismuth oxide were investigated by Zav'yalova et al. [70, 74]. Due to the confinement other structures were observed and analyzed by XRD at RT. Among them was the metastable β-phase and a distorted form with the stoichiometry $Bi_2O_{2.5}$. More recently Fan et al. [94] showed that β-Bi_2O_3 as well as δ-Bi_2O_3 thin films could be deposited by reactive sputtering of Bi onto NaCl, Si, ZrO_2, quartz and glass substrates with controlled temperature. The films were polycrystalline with an average grain size of $\leq$ 20 nm. While the δ-phase only formed in a narrow temperature window around 473 K, the β- and α-phase were readily achieved at higher temperatures. There are a few letters and reports about synthesized bismuth oxide nanoparticles and needles from different groups [95, 96, 97, 98, 99, 100]. If reported the typical structure was β-Bi_2O_3. Only Han-Xiang et al. also prepared the δ-phase by a vacuum vapor-phase oxidation [101]. Except for XRD no further characterization of the particles took place. Hence no surface energies or other thermodynamic properties of bismuth oxide nanoparticles are known.

3 Size-dependent melting models tested on gold

3.1 Results

Experimentally gold is by far the most investigated material in the field of size-effects and it is popular in other fields of research, too. That is why all necessary material properties are known and numerous size-dependent melting and evaporation temperatures are available thus making gold the ideal test-piece for comparing the models. In the present comparison the latest models by Lee et al. [41] and Sun et al. [5] are included, as well as an extensive compilation of size-dependent melting values from literature. Figure 3 shows the experimental and simulation values for melting gold nanoparticles / clusters in a reciprocal plot which visualizes dependencies from the surface to volume ratio by a straight line. The black, solid line gives the best linear fit to the experimental data indicating unaffected $1/D$ behavior as guide for the eye.

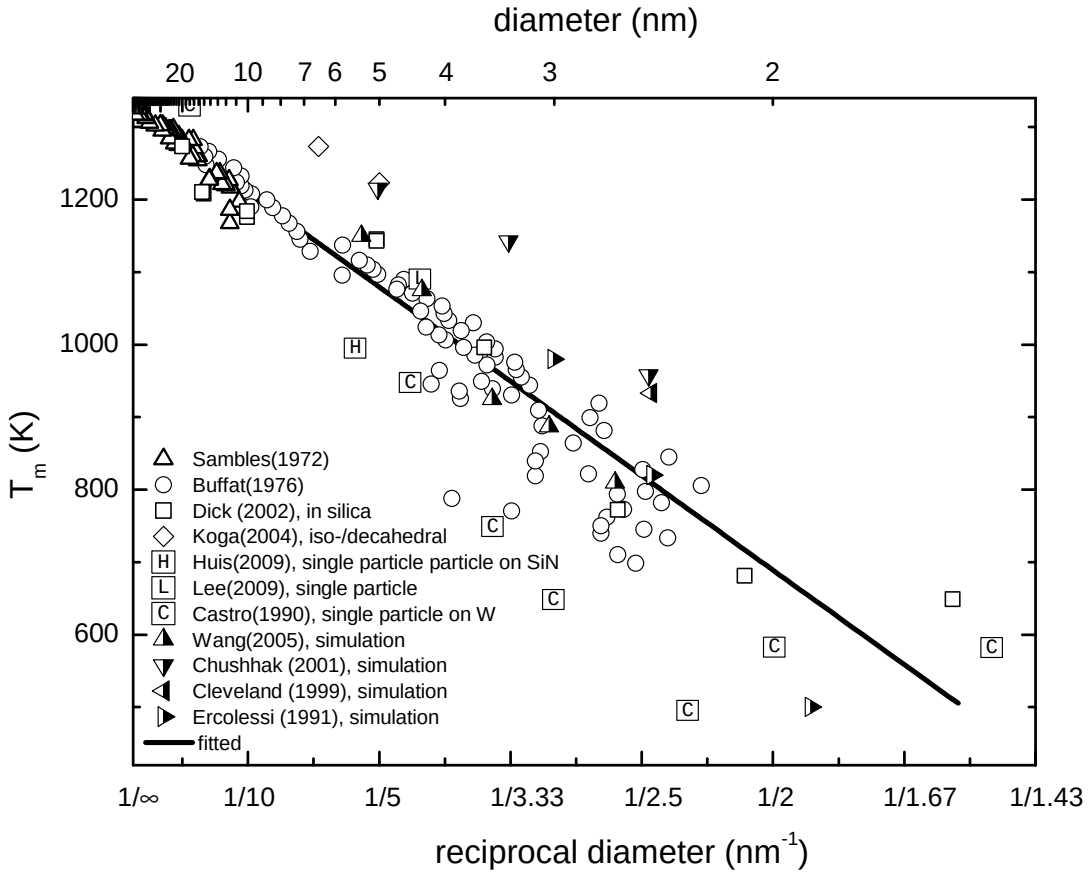

Figure 3: Size-dependent melting of gold nanoparticles down to 1.5 nm. Comparison of experimental values of prominent studies with different techniques, substrate materials or matrix materials as well as simulation values. The best linear fit for Sambles, Buffat, Huis and Lee down to 4 nm indicates "ideal" $1/D$ behavior.

The HOG, HEG, LSM, LNG and BOLS models from chapter 2.3.2 were tested on the basis of the described literature values. To compare the validity of the models they were not fitted using the unknown material properties as fit parameters. In order to compare relative differences, peculiarities and agreement with literature values, the same parameters

Table 1: The values of gold and graphite used for the T_m calculations

property	constant value at T_0	equation for T-dependence	unit	reference
T_0	1337.33		K	[64]
$\triangle_m H$	12552.0	const.	J/mol	[64]
γ_{sv}	1.4	$1.947 - 4.3 \cdot 10^{-4} \cdot T$	J/m^2	[1], [103]
γ_{lv}	1.135	$1.33 - 1.4 \cdot 10^{-4} \cdot T$	J/m^2	[24], [104]
$v_m(s)$	$10.7109 \cdot 10^{-6}$	$10.7 \cdot 10^{-6}(1 + 8.61 \cdot 10^{-5}(T - 1336.15)$	m^3	[105]
$v_m(l)$	$11.3 \cdot 10^{-6}$	$11.3 \cdot 10^{-6}(1 + 6.9 \cdot 10^{-5}(T - 1336.15)$	m^3	[106]
γ_{carbon}	1.000242	$1.174 - 1.3 \cdot 10^{-4} \cdot T$	J/m^2	[107]
Θ(Au(l)-C)	129	const.	deg.	[108]
Θ(Au(s)-C)	127	const.	deg.	[109]
d_0	0.2883	const.	nm	[110, 111]

were applied to each model. The best known values of all necessary parameters, including their linear temperature-dependence, were collected and summarized in table 1. The utilized basic equations of the models are equation no. 23, 24, 26, 27, 28 and 42. The relevant material parameters are the bulk melting temperature T_0, surface energy of the liquid phase in gas γ_{lv}, surface energy of the solid phase in gas γ_{sv}, interfacial energy between the solid and the liquid phase γ_{sl}, interfacial energy between liquid or solid and the carrier substrate γ_{lC} or γ_{sC}, layer thickness t and the molar volume of the liquid and the solid phase $v_m(l)$ and $v_m(s)$. The molar volumes can also be expressed by the molar masses $m_m(l)$, $m_m(s)$ and the respective densities $\rho(l)$, $\rho(s)$, respectively. $\triangle_m H$ is the standard enthalpy of melting and $\triangle_v H$ the standard enthalpy of evaporation. The Gibbs free energy function of solid and liquid gold were taken from the SGTE database reference [102]. Representatively only the experimental values of Buffat and Borel and of Sambles are shown in figures 4 and 5, together with the models of interest. The melting region of the LNG model is shown by a blue, opaque field between the lower and the upper limit. Two calculations from the BOLS model are implemented: The calculation of a particle with the first three atomic layers affected by the surface ($z_3 = 8$), indicated by the solid green line, and only two atomic layers affected ($z_3 = z_{bulk} = 12$). The latter case shows a better fit to experimental data. Figure 4 shows the models with constant parameters. In figure 5 (a) and (b) the linear temperature dependencies of γ_{sv}, γ_{lv}, γ_C, $v_m(l)$, $v_m(s)$, also called 2nd-order effects, are included to show their impact on the curves. $\triangle_m H$ was kept constant and the materials were considered incompressible, so that pressure changes do not have any effect. Following prior treatments, the molar volumes and the surface energies are taken to be linear functions of the temperature.

$$v_m(s,l) = v_m^{\ominus}(s,l)\left(1 + 3\alpha \triangle T\right) \tag{54}$$

$$\gamma = \gamma^{\ominus} + \frac{d\gamma}{dT}\triangle T \tag{55}$$

$v_m^{\ominus}(s,l)$ is the molar volume of the solid (s) or the liquid (l) phase at standard conditions, α is the linear expansion coefficient.

3.2 Discussion

The discussion is introduced by a comparison of the size-dependent melting models for metals (eq. 23, 24, 26, 27, 28) which are tested on gold. As many findings are of general nature they also apply to the subsequent discussions of transforming Bi_2O_3 nanoparticles and help to enlighten the issues of size-dependent melting. Studies by Borel [112], Yaroslav [113], Goswami et al. [114] and Leitner [115] have compared different, mainly thermodynamic models. The influence of changing surface energy was investigated in detail by Lee et al. [104, 108, 109, 116].

Figure *3* shows the values of the famous experiments by Buffat and Borel *[1]* obtained by electron diffraction over a large number of particles and Sambles et al. [24] obtained in TEM evaporation experiments. The values show a certain scattering especially at the smallest sizes (border of experimental feasibility), but correspond well and the trend indicates a linear $1/D_p$ behavior for the entire size range. Looking only at the data of Sambles et al., as Lee et al. *[41]* did, one could interpret a deviation from this linearity below 12 nm (see fig. 5 on page 32(b)). But all the other data show that this is misleading and the linearity roughly holds down to approx. 2nm. The values from Dick et al. [117] were obtained from gold nanoparticles encapsulated by silica. Their different values and behavior demonstrate the effect of a varying interface (free energy). Such changes can be especially strong at an interface between a faceted nanoparticle and a crystalline matrix because of misfits between two lattices. In other materials, like lead, this effect can even lead to superheating instead of melting point reduction [118, 119]. The reasons are on the one hand, that γ_{sv} changes to a different interfacial energy and on the other hand that the heterogeneous nucleation of melt can be suppressed at the solid interface. Noteworthy is also that Castro et al. [120] performed their experiments on tungsten and Huis et al. [121] on amorphous silicon nitride membranes instead of carbon substrates. Both substrates seem to promote T_m more strongly than carbon. This is due to the different interfacial energies and contact angles. Lee et al. [41] showed and discussed in 2007 that if the contact angle is large and the interaction energy is low (C-Au: 129°, 0.45 eV), T_m is hardly affected by the substrate. If, on the other hand the contact angle becomes smaller than 90° and the interaction is stronger (W-Au: 63° [122], 3 eV [120]), the influence can be considerable. The main reason for this is a geometric one: The particle shape changes from a quasi spherical particle at 180° to a thin film at 0°, thus increasing the surface/volume ratio. As this ratio, in turn, is the driving force for melting point depression, T_m decreases with decreasing contact angle.

While most experiments measured an average T_m of many particles, Lee et al. [2] and Huis et al. [121] tracked melting of a single, separate gold nanoparticle in-situ in a TEM (figure *3,* alphabetic data points). This provided valuable insights into the process of a melting particle: The particles melted abruptly (5 nm at 1100 K on C and 1000 K on SiN) without any visible amorphous, liquid surface. Lee et al. observed the disappearance of one atomic layer of C after the particle had evaporated. They inferred that carbon was solved in molten gold, as solubility is commonly much higher in the liquid state. In that respect a contaminating influence by the metallic tungsten film or the glassy SiN film cannot be ruled out, especially since bulk gold generally alloys very well with other metals. But the phase diagrams of W-Au and Si-Au do not show any intermetallic phases and solid solutions. Moreover cycling between melting and solidification was possible without any change of T_m which also supports the presumption that no compositional changes took place. Huis et al. recorded rapid structural switching of a single 5 nm gold nano crystal 5 K below T_m. This interesting observation is an example for the different thermodynamics of nanoparticles which are well explained by molecular dynamics (MD) simulations [123, 124]: Instead of singular transition temperatures, regions of coexistence occur around T_m where both states can be adapted and switching between these states will happen in a fluctuational way.

The smallest sizes in figure *3* were measured by Castro et al. and Dick et al. - both not on carbon. Castro et al. have another data point at $D = 1.2$ nm, $T_m = 582$ K which is outside the plot range of figure 3. These points indicate that below approximately 2 nm the continuous size-dependence of T_m seems to stop and a T_m varying around a mean value seems to establish. The same observation was made by Bachels et al. [125] on free tin particles and clusters. Buffat and Borel explained their scattering and leveling off below 2.5 nm (not shown in fig. *3*) with variations of the integrated intensities of the diffraction patterns and corrected these values. But in the light of the new insights it could be possible that they have the same origin as the other three results. While an influence by the substrate or matrix cannot be ruled out in the first two studies, the more compelling reason is that the regime of smoothly changing properties ends here and clusters with structures obeying different laws of stability than the thermodynamic ones occur. Hence for gold the continuous regime ends at approx. 2 nm. Also recent simulation studies indicated that with a decreasing cluster size, transformation of the melting modes may occur at a critical size [31]. An earlier simulation study by Ercolessi et al. [126] predicted that the enthalpy of melting would decrease and vanish at a critical cluster size $D = 2.1$ nm. Such a disappearance of $\triangle_m H$ definitely marks a boundary below which melting can not be described as a process of an ensemble of atoms, anymore. This means that thermodynamics is not applicable below this size.

Current understanding of Au clusters

While properties of clusters are not in the scope of this work, Koga et al. [127] revealed astonishing facts about the structures of gold up to 18 nm which make the discussion of cluster structures worthwhile. The favored structure of gold clusters containing from hundreds up to a few thousand atoms is a truncated decahedral structure. An icosahedral structure is highly favored kinetically and therefore observed frequently. There is a variety of other possible cluster structures and twinned particles also appear. Which ones are found probably depends sensitively on the conditions of formation and the environment [124]. In Kogas's study they showed that the structure of particles grown from vapor-condensation was not the usual fcc gold structure, but a mixture of icosahedral and decahedral morphologies. Morphology populations showed that these structures were exclusively present up to at least 18 nm. Only annealing above the bulk melting temperature (1373 K) could change the majority of the 18 nm clusters to fcc while the proportion of decahedral clusters (and icosahedral clusters below 5 nm) still linearly increased to 100% at 6 nm. Below 6 nm still none were crystalline. If the constellation after the melt-freeze process is seen as equilibrium state, Koga's results show that below approx. 20 nm other gold structures than fcc can be stable. As this size range clearly intersects with the linear melting regime of Au particles, the finding smears out the distinction of nanoparticles and clusters by structural differences. Moreover, it evokes the question how justified the assumption of constant bulk-like properties in thermodynamic models is. On the other hand the variety of possible structures can be interpreted in the way that energy differences between them are small [126] which in turn would justify the use of average values for the properties approximated by the bulk values. The property in question is above all the solid surface energy γ_{sv}. It intrinsically depends only on the state of the surface atoms. As their average can - to a certain extent - be expected to be similar on the surface of a bulk, a fcc nanoparticle and an icosahedral cluster, it is plausible that an average γ_{sv} can approximately describe all three structures. The simulation values plotted in figure 3 on page 25 [128, 113, 129, 126] scatter from study to study which can be attributed to a limited quantitative accuracy of simulations in general as well as differences in the applied methods, geometric constructions and electronic states. On the whole, simulation values are in accordance with experimental measurements. Supported by the measured values of decahedral clusters by Koga et al., one can assume the higher values of Chusahk and Bartell [113] and of Cleveland et al. [129] could be, because other cluster structures were simulated.

MD simulations on gold clusters (1-3 nm) give information about the process of melting on an atomic level. Findings are that no surface melting occurs on the {111} facets of the icosahedral structure which are favored by the fcc crystal, too. An observed rounding of edges and corners is attributed to a pre-melting of the low-coordinated atoms which spreads out into the ordered facets as the temperature comes close to the melting. Other facets do show surface melting down to a critical size where the melting temperature is lower than the surface diffusion temperature [126, 128, 130]. Simulations on clusters of other materials like lead and nickel definitely did show continuous surface melting [131] and so simulations confirm that surface melting in nanoparticles follows similar rules. Thus it depends on the material and on the surface plane.

All this shows that even for a elementary model system like gold the situation gets very complex at the nanoscale and many factors are responsible for the final size-dependent melting point.

Comparison of models

On the basis of the discussed literature, values different models from chapter 2.3.2 will now be compared. The comparison starts with using constant parameters (fig. 4). This helps to overview the causes of differences between the models. In a second step the effect of 2nd-order effects, e.g. linear temperature dependencies will be taken into account for explaining their impact on the curves (fig. 5).

Most models assume a melting mechanism and derive a melting point depression based on this conception and classical thermodynamics. In figure 4 all thermodynamic models except the LSM describe a straight line. This is because the only size-dependent influence is the surface to volume ratio entering the equations by $A/V \propto 1/D$. In general the models are all derived in the same way (see chap. 2.3.2) with the basic form being the Gibbs-Thomson equation (Yellow line,

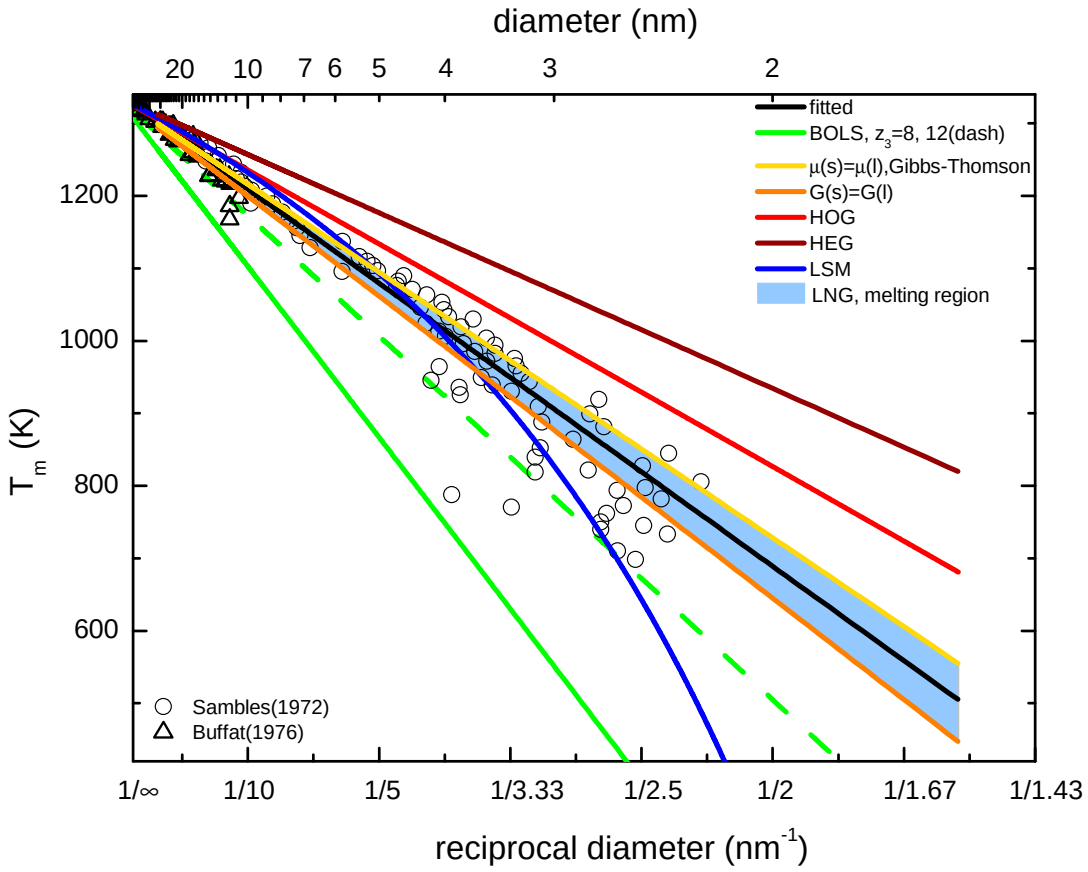

Figure 4: Size-dependent melting of gold nanoparticles. comparison of outstanding thermodynamic and atomistic models. BOLS with m=1. The LNG model defines a melting region within which particles melt in a fluctuational way. It's upper and lower limits are simply equality of the chemical potentials and Gibbs free energies, respectively. HOG takes the difference of the molar volumes into account. HEG further differs between surface area and contact area to the substrate. LSM with t = 0.5 nm which is usually a sheer fit parameter to vary the down-bending of the curve. At $t = 0$ LSM is equal to HOG.

eq. 23). The result from equaling the Gibbs free energies (orange line, eq. 26) differs only because of the factor 3 instead of 2. The main difference for the HOG (red line) is that the difference in molar volumes $v_m(s)$ and $v_m(l)$ is considered leading to equation 24. As $(v_m(l)/v_m(s))^{2/3} < 1$ this leads to a reduced melting point depression. The bigger the difference $v_m(l) - v_m(s)$ the smaller the melting point depression. The main difference for the HEG (dark red line) is that it additionally considers the shape and interface changes of the particle lying on a substrate. For the melting point the differences $\gamma_{sv} - \gamma_{lv}$ and $\gamma_{sc} - \gamma_{lc}$ are relevant. As the second term is always smaller than the first one when the Young equation is used it follows that an interface area reduces the melting point depression. Additionally the shape changes the ratio of surface and interface area. The consequence is that HEG predicts even higher melting temperatures than HOG.

Turning to the LSM model the effect of a layer with constant thickness has to be discussed. The change from a solid-vapor to a solid-liquid + liquid-vapor interface introduces an additional, constant term in equation 28 and 29 which results in a decrease of the slope in the reciprocal diagram. But the deciding difference is the layer thickness t in the denominator of the main fraction $\triangle\gamma_{sl}/r - t$. For large particles $r \gg t$ and the influence is marginal. For ever smaller sizes the influence of t grows causing the net size in the denominator to be smaller and thus accelerating the melting point depression with decreasing size. Evidently the model brakes down at $r = t$. The LSM has been criticized for its aphysical description of an intermediate state of melting by equations for equilibria and especially for the ad hoc

definition of the surface layer to achieve a better fit to observed data [36, 113]. Another model involving the occurrence of a liquid surface layer is the LNG model. Using dynamic nucleation theory it describes the mechanism of melting and rationalizes the occurrence of a liquid surface layer, as well as a range of temperatures over which melting takes place in a fluctuational way. But even if the model makes qualitatively correct predictions and is correct in implying a lower melting point than the HOG model, it is quantitatively not better in reproducing experimental results than other models. This is because the equations for the upper and lower limit are the most basic thermodynamic equations which were discussed above (orange and yellow lines). These equations do not bear any other meaning than the HOG model. So in contrast to LSM, LNG is not able to predict any significantly non-linear $1/D$ behavior. Additionally, the calculation of the actual nucleation and growth transition is a laborious, iterative process which has to be performed for every particle size separately. This is rarely done (also not in this work), especially, because it only refines T_m between the upper and lower limit. Vanfleet et al. [45] calculated the melting temperature of Pb particles but without comparison to experimental values. Similar to the Young-Laplace equation in thermodynamics, the nucleation theory was developed for nucleation from the liquid or the vapor. Switching the process direction the melt has to nucleate from a solid which is much less accurately described by mean, isotropic properties (see also chapter 2.1). Moreover the nucleation and growth has to follow a direction radially from the surface to the core now.

The bond-order-length-strength (BOLS) model is discussed in the end since both, the concept and the trace of the curve are fundamentally different. The change of T_m is described by coordination imperfection and relaxation in the surface region. Other surface effects like reconstruction or re-ordering are not part of the model. The only material parameters necessary for the BOLS are the average bond distance in gold (0.2883 nm) and the bulk melting temperature for proportional scaling between the thermal energy and temperature. The parameter $m = 1$ signifies a proportional change of bond energy with the coordination imperfection c_i. This is indirectly the same as the assumption of a linear relationship between A/V ratio and T_m as found in the thermodynamic models. $m = 2, 3, ...$ signifies a quadratic, cubic, etc. relation which would cause the curve to bend upwards (weaker melting point depression for smaller sizes). Such an effect was discussed by Farell and Van Siclen [67] for directional, covalent bonds in C, Ge and Si. The imperfection c_i depends on the coordination number (eq. 36) and is constant in the second and third layer. In the first layer the coordination number is size-dependent with $z_1 = 4(1 - (0.75/(r\, d_0^{-1})))$. So it changes reciprocally with the size. This would be indirectly the same as the assumption of a size-dependent decrease of the surface energy

$$\gamma_{sv} \propto 1/r \tag{56}$$

which also causes upwards-bending (see fig. 4, dashed line). This topic is discussed in the section “Influence of size-dependent parameters” on page 34 for the thermodynamic models. In summary, there is the surface layer with a c_i that changes with size and two intermediate layers between the surface and the bulk which possesses a constant c_i (fig. 4, solid line). The dashed line symbolizes the case where the third layer is already bulk-like. Simulation results show, that at least for gold, the latter case is the more suitable one[132]. The contribution of the first 3 atomic layers are additively combined. This is why the size-dependent influence of the first layer can be seen more clearly in the dashed, than in the solid line. In BOLS the core is assumed to be entirely unaffected by the particles size and possesses ideal bulk properties. But as elaborated in the section “Influence of size-dependent parameters” on page 34 the surface pressure or surface stress can cause lattice changes. Such changes are significant below 3 nm in gold. In that case the bond distance and strength (d_0 and E_B) will change in the core and the assumption that size-changes are exclusively contributed by the surface would not apply anymore. This is the same argument as in chapter 2.1 for γ. So deviations from real melting values can be expected below 3 nm.

Agreement with experimental data

The Gibbs-Thomson equation (yellow line, upper limit in LNG) derived from equality of the chemical potentials, and equation 26 (orange line, lower limit of the LNG) derived from equality of the Gibbs free energies, are closest to the best fit (black line). Interestingly, these are the most basic equations without any corrections for volume differences between

the phases (HOG) and shape and interface changes when lying on a carrier substrate (HEG). How can this be explained? The curves sensitively depend on the chosen parameter values. The plots in figures *4, 5* are based on the best known values (table 1). But to give an example to show the difficulty γ_{sv} is elaborated. All thermodynamic models require (directly or indirectly) this parameter. The used value is 1.4 J/m^2 [1]. A study by Lee et al. [104] showed that the actual, anisotropic value can be in a range of ±10 % due to reasons explained in chapter 2.1. With $\gamma_{sv} = 1.4\ [J/m^2] \pm 10\,\%$ every model can be matched easily to the data - of course with different γ_{sv} values as the relative differences remain. Normally the models are matched to experimental results by adapting one or more unknown material parameters like γ_{sv}. The accuracy of other parameters is better. γ_{lv} for example is reported to have an error of only ±0.5 % SE (since it can be well accessed by evaporation and contact angle measurements). With regard to this the conclusion is not that the Gibbs Thomson equation actually is the best model. The result rather shows that within the possible accuracy of material parameters at the nanoscale all models are valid. Even though they are based on different premises. A distinction as to which model is the most accurate one is not possible.

For gold, as the present example, the path of the data points is close to linear. If at all, one could interpret slightly lower T_m values around 2.5 nm and a leveling off below 2 nm where the continuous regime seems to end. For other materials like e.g. lead and tin clear deviations from linearity towards lower melting temperatures have been observed [133, 134]. Such a deviation can not be explained with most curves in figure 4, except the LSM. As this non-linear $1/D$ behavior correlates with the observation of surface melting in the bulk, as well as in nanoparticles, it seems reasonable that the deviation is in fact due to a liquid surface layer. Vice versa the previous paragraph showed that no typical surface melting takes place on gold nanoparticles and {111} surfaces. Consistently the size-dependent melting of gold is better described by a model not presuming any pre-molten surface like Gibbs-Thomson, $G(s) = G(l)$, HOG and HEG. So one can distinguish between (at least) two different melting mechanisms. Depending on which one applies to the sample in question one can use either the LSM or one of the other models.

The fit of the BOLS model with $z_3 = 12$ is as good as the thermodynamic models. Initially the BOLS model proposed to use three surface layers with $z_2 = 6$ and $z_3 = 8 - 12$. But $z_3 = 8$ gives the severe overestimation of the solid green line. According to a MD simulation by Weihong et al. [132] the bond changes are restricted to 1.5 bond distances on the surface. Thus, it is justified to use only two instead of three surface layers. Nevertheless, the coordination number values are only based on achieving a best fit for several materials [53]. So even if this model was claimed to dispense with adjustable bulk parameters and only rely on the bulk bond energy of a material, a general adaption enters via these z_i values. Sometimes they actually were used for fitting [135]. An excellent fit would result for $z_2 = 8$ and $z_3 = 12$ which would correspond quite well with the $1.5 \cdot d_0$ from the MD simulation.

Influence of temperature-dependent parameters

The 1st-order approximation in equation 21 can be extended to a second order one, as done by Buffat and Borel [1]. What follows are linearly temperature- and pressure dependent parameters as listed in equations 54 and 55 and table 1. One should not mistake temperature-dependent and size-dependent changes of parameters. As both have an influence on the melting behavior they are sometimes confused. Temperature-dependent changes describe the variation of the bulk property, like γ_{sv}, at different temperatures. For example $\gamma_{sv}(T)$ is described by the function $1.947 - 4.3 \cdot 10^{-4} \cdot T\ [J/m^2]$. So it linearly decreases at rising temperatures. T_m is affected by this function of temperature, as the value of $\gamma_{sv}(T)$ in e.g. equation 24 on page 13 is variable, now. But $\gamma_{sv}(T)$ remains a bulk property, which can be determined by measuring bulk samples. On the other hand, size-dependent properties are defined as changes which happen on the nanoscale due to finite-size effects. So if γ_{sv} measured in a nanoparticle at RT would differ from γ_{sv} measured on a bulk sample at RT it would be a real size-dependent change. Ergo, by definition, $\gamma_{sv}(D)$ is no bulk property anymore. For the explained reasons using temperature- and / or size-dependent properties is an alternative to the LSM in order to achieve non-linear $1/D$ curves.

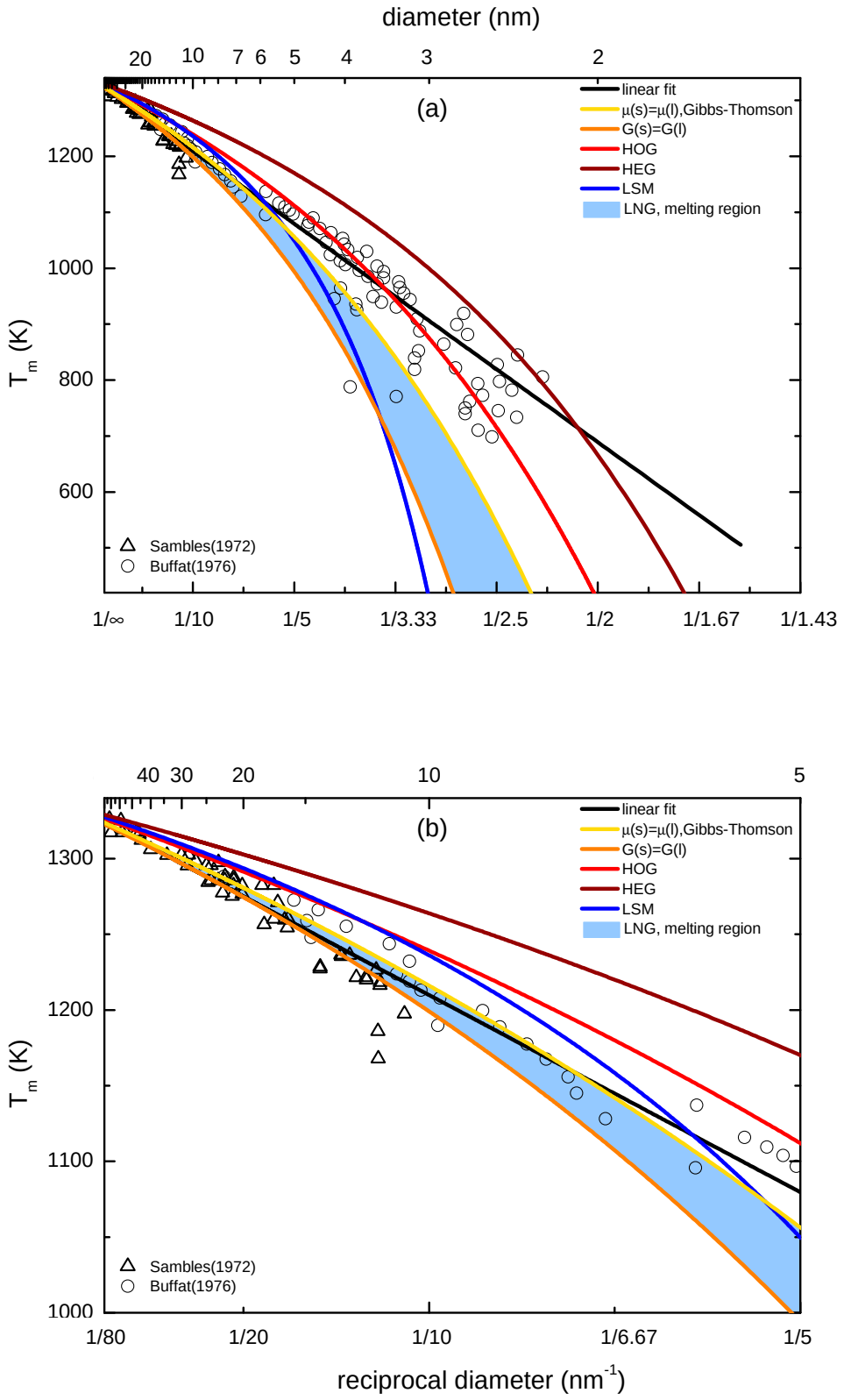

Figure 5: Size-dependent melting of gold nanoparticles. Comparison of outstanding thermodynamic models with temperature-dependence of ν_m and γ taken into account (table 1 on page 26). Different temperature dependencies of the solid and liquid phase cause a bending of the curves alike the effect of a liquid layer in LSM. The close-up in (b) shows more details of the continuous regime's important region between 80 and 5 nm.

Molar volume

Concerning the molar volumes the difference

$$\partial v_m(s)/\partial T - \partial v_m(l)/\partial T \tag{57}$$

is relevant for a change in T_m. As $\partial v_m(s)/\partial T$ is larger than $\partial v_m(l)/\partial T$ it follows $v_m(s) - v_m(l)$ is smaller at lower temperatures which corresponds to a decrease of melting point depression. Thus, this effect causes the T_m curve to bend upwards. Between 3.5 and 12.5 nm the volume changes amount -4.5 to -0.8 %.

Surface energy

For the surface energies the same relation as for molar volumes,

$$\partial \gamma_{sv}/\partial T - \partial \gamma_{lv}/\partial T \tag{58}$$

applies. Here $\partial \gamma_{sv}/\partial T$ is smaller than $\partial \gamma_{lv}/\partial T$. So $\gamma_{sv} - \gamma_{lv}$ is larger at lower temperatures which corresponds to an increase in melting point depression. Thus, this effect causes the T_m curve to bend downwards. The magnitude of energy change is 15 to 50 % in the size range from 12.5 to 3.5 nm which is much larger than for the volume. Therefore, the curve ultimately bends downwards and the depression is increased for lower melting temperatures, e.g. smaller sizes. This can be seen in figure 5. Now the curves of all models are bent - the one of the LSM even stronger than before. When the whole range of sizes (fig. 5 (a), 5(b) and fig. 4) is considered one can conclude that the data points are described better by linear models with constant parameters than by the same models incorporating temperature-dependent parameters which cause a bending of the curves. With the bending the values are over-estimated in the beginning and underestimated in the end with an intersection between 3 and 10 nm. Such an intersection in the middle of the data points clearly indicates a wrong curve shape to match the data. Lee et al. [41] who also incorporated temperature-dependent parameters in their HEG model came to another conclusion. They compared the model only to the experiments by Sambles [24] down to 10nm and found a good agreement between model and experiment. Yet, if a wider size range and more data is considered this statement can not be confirmed.

Enthalpy of melting

Following previous works the enthalpy of melting was considered to be constant in the models as changes are supposed to be small.

$$\triangle_m H = (s_0(l) - s_0(s)) \cdot T_0 = \triangle s_0 \cdot T_0 \tag{59}$$

$\triangle_m H$ signifies the entropy jump between the solid and the liquid phase for a melting bulk at T_0. The melting entropy is related to the vibrational component only [136]. At lower melting temperatures of nanoparticles the lattice vibrations are smaller. But as again the difference between the change in the solid and in the liquid

$$\frac{\partial s_0(l)}{\partial T} - \frac{\partial s_0(s)}{\partial T} = (C_p(l) - C_p(s))/T \tag{60}$$

is decsive and as the vibrations are independent of the aggregate state, $\triangle_m H$ is indeed temperature invariant. Taking the example of the tabulated Gibbs free energies of gold [102] one ends up with

$$\frac{\partial G_0(s)}{\partial T} - \frac{\partial G_0(l)}{\partial T} = const.$$

So the slope difference is not a function of temperature. A visual hint is, that a non-constant value would produce a bend curve for the HEG model in figure 4. This is obviously not the case, so $\triangle_m H$ is temperature-independent.

Additionally to changes of parameter values when the melting temperature is depressed, real size-dependent shifts are possible, too. It is experimentally very difficult to detect such changes as on the nanoscale most traditional methods fail and bulk samples can not be used. Therefore, more theoretical considerations than experimental values exist. As in the previous chapter the size-dependencies of the parameters υ_m, $\gamma_{s\upsilon}$ and $\triangle_m H$ as well as Θ will be treated.

Molar volume

As described in chapter 2.1 a capillary pressure is exerted onto the interior of a small droplet (eq. 2) but as a liquid is, in a good approximation, incompressible this does not change $\upsilon_m(l)$. On the other hand $\upsilon_m(s)$ depends on the surface stress $\sigma_{s\upsilon}$. Mays et al. [12] used the SDLP method to determine lattice parameters as well as a mean $\sigma_{s\upsilon}$ of gold particles between 3.5 and 12.5 nm from electron diffraction. $\sigma_{s\upsilon}$ was $1.175 \pm 0.2\,N/m$ which is lower than the value used in table 1. The calculated volume change in this size range is -0.8 to -0.2 % which is around one quarter of the temperature-dependent changes of $\upsilon_m(s)$. In cluster structures below 3 nm the changes become stronger. Volume reduction of 4 to 17 % are possible between 3 and 0.8 nm size [63, 110]. As the effect of temperature induced and surface stress induced volume changes on T_m is the same, the stress effect was neglected in the curves of figure 5. Incorporating the dependence would further gradually decrease the slope (e.g. curve upwards). Still the effect would be small compared to the influence by $\gamma_{s\upsilon}$ acting counter wise.

Surface energy and surface stress

While υ_m can be calculated from the accurately determined lattice parameters, $\gamma_{s\upsilon}$ is not directly accessible by any method. If the size-dependent melting curve levels off instead of declining more rapidly, this could be explained by a size-dependent decrease of $\gamma_{s\upsilon}$. Tolman derived an equation for liquids in 1949 that shows a decrease of surface free energy with decreasing size [137]. In solids different models also predict a decrease of $\gamma_{s\upsilon}$ with decreasing size which is more or less proportional to $1/D$. At 5 nm particle size the predicted difference to the bulk value is 10 to 15 %.

Very few experimental studies exist. Lu et al. [138] observed a decrease of the total excess grain enthalpy relative to the grain size with decreasing size in selenium. They concluded that $\gamma_{s\upsilon}$ decreases with size. By measuring the size-dependent change of lattice parameters, as done in numerous cases (see review [13, table 1 and 2]) $\sigma_{s\upsilon}$ and $\gamma_{s\upsilon}$ can be calculated via the SDLP method for every measured size. Zhang et al. [15] were the first to employ this consequently to measure the size-dependent change of γ for solid nanoparticles (TiO_2) down to 4.1 nm. σ and γ increased down to 12 nm and then decreased again in a band of $\pm 20\,\%$ around approx. $0.9\,J/m^2$. This is not in accordance with the theoretical models. No definite explanation for this complex behavior is known, yet. Diehm et al [139, 13] simulated σ of GaN at different sizes and observed a deviation from the $1/D$ proportionality below approx. 3 nm. The reported reason was the contribution of edge and corner sites for example by means of line stresses of the edges.

As size-dependent changes and the error for measuring γ are in the same magnitude it is difficult to judge the validity but it is likely that the surface energy changes somewhere below approx. 10 nm. Such an effect is also incorporated in the atomistic BOLS model. For further reading see refs. [20, 60, 140]. The difference between $\gamma_{s\upsilon}$ and $\sigma_{s\upsilon}$ was explained in chapter 2.1.

Enthalpy of melting

Lai et al. measured the size-dependent melting point and enthalpy of melting for tin nanoparticles between 5 and 50 nm by nanocalorimetry [134] and observed a reduction of $\triangle_m H$. Several MD simulation studies of various metals have shown a continuously decreasing $\triangle_m H$ as well [128, 126, 141]. Reason for this decrease is that the thickness of the disordered or pre-molten atoms near the surface maintain a quite constant thickness of 1-3 atomic layers. No entropic energy has to be provided to remove them from the lattice order. The entropy increase at T_m only happens for atoms in the ordered, crystalline core. For large particles the surface portion is negligibly small and

$$\triangle_m H = \triangle S/N \cdot T_m \tag{61}$$

appears constant. Yet, when the size of the particles reaches similar dimensions as the disordered surface the fraction of surface atoms is not small anymore. So for an appreciable amount of atoms no entropic energy is needed. If still the full number of atoms in the particle, N, e.g. the full outer dimensions without subtraction of the surface region are used in equation 61 then $\triangle S$ divides over too many atoms and appears smaller than it actually is. The problem is a geometric effect similar to the one in the LMS model. Only the crystalline core-atoms should be considered; not the ones in the vicinity of the surface. If that is done $\triangle_m H$ is in fact not size-dependent. Lai et al. gave an approximate function for the core size-dependence $\triangle_m H$ within the terminology of the LSM model:

$$\triangle_m H(r) = \triangle_m H_0 \left(1 - \frac{t}{r}\right)^3 \tag{62}$$

where $\triangle_m H_0$ is the molar enthalpy of melting of the bulk. If $\triangle_m H$ deviates considerably or abruptly from such a trend, real size-dependent changes could be expected. Turnier predicted $\triangle_m H_0$ to be independent of size in small nuclei [142, 143]. A true change of $\triangle_m H$ can only happen when the bonding order in the lattice changes, hence when more or less entropic change takes place from the solid to the liquid aggregate state. This would be equivalent to a change in the Gibbs free energy of the solid, crystalline volume ($V/v_m\mu_0 = G_0$ in equation 9). This could be the case when the interior of nanoparticles and clusters gets affected by the surface (for example by surface stress). As discussed for the molar volume such an effect seems to be significant below 3 nm for gold particles.

The cause of the internal changes arises from the surface. This is important when considering the different definitions of surface energy: When surface energy only incorporates energies located at the surface, then the lattice changes have to be attributed to the volume. Hence it would be correct to talk about a change of G_0 and $\triangle_m H$ in the particle volume. The definition of surface energy in the way it is measured by calorimetry is the one of an excess surface free energy, though (see chap. 2.1). Now the volume stress (work) has to be counted as part of the surface excess because it is intrinsically related to the presence of the surface. For this scenario the only noted change would be for γ_{sv}, not for μ_0. So it appears that changes of the particle core by surface stress might be an issue. Therefore, it would be interesting to know how strong the change of the surface excess free energy, caused by σ_{sv}, actually is. Weissmüller made a continuum mechanic estimation for free nanoparticles and nanostructured materials [144]. Using material data for gold from Mays et al. [12] renders a change of the excess surface free energy between 3.5 and 12.5 nm of 0.004 to 0.001 J/m^2; a negligible change. So no matter to which quantity these changes are attributed to, the influence is minimal and can be neglected for the continuous regime.

Contact angle

In the HEG model which takes the particle-substrate interface into account the contact angle plays a role. In the model Θ is considered to be constant. But in fact Murai et al. [145] showed that the contact angle of liquid Sn and Bi particles, supported by a substrate, is not only material-, but also size-dependent for $D < 20\,nm$. This indicates a more complicated substrate to particle interface behavior and thus a more complicated surface/interface area to volume ratio. Hendy et al. [146] discussed in their model that only when the contact angle of the solid and the liquid phase are almost equal the size-dependent melting on a carrier film is comparable to the melting of free, unsupported particles. Lee et al. [41] discussed that the apparent contact angle could also be decreased for nanoparticles on a substrate due to heterogeneous evaporation (rates). But they concluded that size-dependent changes of the contact angle by a few degrees have a negligible influence on T_m.

Conclusion about models

Literature about experiments and simulation has shown that the present model system, gold, does not exhibit continuous surface melting. It is therefore sensible to describe such a behavior with a direct solid to liquid transition as in the Gibbs-Thomson, HOG ore HEG model which predict a linear $1/D$ dependence of T_m. Consistently the path of the gold melting points is almost linear in the reciprocal plot. Other materials are proven to exhibit surface melting. For such materials the slope decreases in the $1/D$ plot due to simple geometric consequences and it makes sense to use the LSM or another

model with a liquid surface layer for their description [147, 148]. In gold nanoparticles, where the surface melting as additional complication can be excluded it seems like bulk-values *do* can be extrapolated down to very small sizes (∼3-4 nm). Temperature and size-dependent changes, tough often used in literature to obtain better fits, do not play a major role. This is in accordance with experiences from nucleation theory where the behavior can be calculated with the assumption of bulk parameters as well [28]. The uncertainty of several parameters in the thermodynamic models, above all $\gamma_{sv}$with ±10 %, generates an uncertainty in the slopes of the straight lines (or curve in case of LSM). Within the given accuracy all models suitable for the non-surface-melting case of gold are valid. In such cases the simplest solution should be preferred. So we recommend to use the simplest model equation (like eq. 23 or 26) if the measured data show linear $1/D$ behavior.

$$T_m = T_0 \left(1 - \frac{C(\gamma_{sv} - \gamma_{lv})v_m}{\triangle_m H\, r}\right) \tag{63}$$

A correction factor C is used for minimizing the difference between model and experiment. It would include all unknown deviations of v_m, γ, $\triangle_m H$, effects from shape, substrate, orientation, non-uniformity and experimental uncertainty. If there is a clear deviation from linearity at small sizes the use of a model with a non-zero, but constant surface thickness can be attempted.

$$T_m = T_0 \left(1 - \frac{C}{\triangle_m H}\left(\frac{\triangle\gamma_{sl}\, v_m(s)}{r-t} - \frac{\gamma_{lv}\left(v_m(s) - v_m(l)\right)}{r}\right)\right) \tag{64}$$

If the fitted value of the thickness t is reasonable, which means between one bond length and ∼ 2nm, this can be seen as the valid melting model. If the thickness is zero or almost zero, this approaches the equation 63 again.

The degree of scattering and deviation shows that a deduction of interfacial properties like γ_{sv} or the liquid-layer thickness by applying one of the model equations to the experimental data can only be accepted with a high uncertainty. While there are several theories about the size-dependence of γ_{sv} the accuracy of the data makes it impossible to derive any conclusions solely from the melting curves. From the current state of science they have to be rather seen as one source of the uncertainty.

4 Experimental and theoretical framework

This chapter contains not only the description of the experimental procedures. It also incorporates special experimental techniques and devices. Derivations of new formulas, necessary for evaluation and discussion of results in the following chapters, are presented as well.

4.1 Synthesis of Bismuth Oxide nanoparticles

The particles were chosen to be synthesized by an aerosol-based evaporation-condensation process with a size-fractioning method.

The setup

The schematic representation of the synthesis setup can be seen in figure 6. Gas streams of 1.3 l/min N_2 and 0.13 l/min O_2, both with a purity of 99.99999 %, were mixed and lead through the setup. In a first tube furnace (1253 - 1373 K) high purity (99.999%) Bi_2O_3 powder was evaporated from a zirconia crucible. Flowing with the carrier gas the vapor cooled down rapidly and nanoparticles nucleated from the over saturated gas. In a second tube furnace the aerosol were annealed at lower temperatures (803 K) to receive spherical, monocrystalline particles. Passing through an ionizing radioactive source the particles were charged - usually with a single electron charge. Within the analysis chamber of a differential mobility analyzer (DMA[149]) charged particles were attracted to a negatively biased center electrode, while being dragged along by the carrier gas. Particles for which the electrical force balances the drag force pass through a collection slit. In this way a narrow size-fraction was separated from the initial distribution. The mobility equivalent diameter (EMD) based hereon is equal to the geometric diameter when the particles are singly charged and spherical. Yet, losses caused a reduction of the particle concentration in the specific fraction by one to two orders of magnitude. The conditioned aerosol could then be either deposited by electrostatic precipitation (ESP) of charged particles [150] or characterized by a scanning mobility particle sizer (SMPS). Particles were always characterized before and after a deposition process. For deposition times of many hours additional samples were taken in-between. A SMPS consists of an ionization source, a DMA, a condensation particle counter (CPC) and a controlling unit (PC). While stepping through the voltage range of the DMA the CPC enumerates the number of particles passing through the detector per unit volume in each size-fraction. So a fractioned size - concentration distribution is measured. From the data the size-distribution function, mean, mode and geometric standard deviation, σ_{GSD}, were calculated. The experimental system used in this study consisted of a electrostatic classifier (Model 3080, TSI Inc.), a differential mobility analyzer (Model 3080n, TSI Inc.) and a condensation particle counter (Model 3025, TSI Inc.). When the SMPS showed the desired size-distribution, the deposition was started. In ESP the inertia and Coulomb forces between particles and negatively biased substrate lead to a defined deposition spot. Typically TEM grids with amorphous silicon nitride (SiN_x) or carbon membranes, but also single crystal wafers and calorimeter chips with a shadow mask were used as deposition targets in this work. For polydisperse samples the deposition time varied between 3 to 50 minutes and for monodisperse samples between 1 and 40 hours depending on the particle size, ESP voltage and deposition target.

The evaporation-condensation process

Friedlander [30] and Stephan et al. [151] describe two processes which can be responsible for the formation of primary particles: coagulation and condensation.

Coagulation is assumed to proceed as follows:

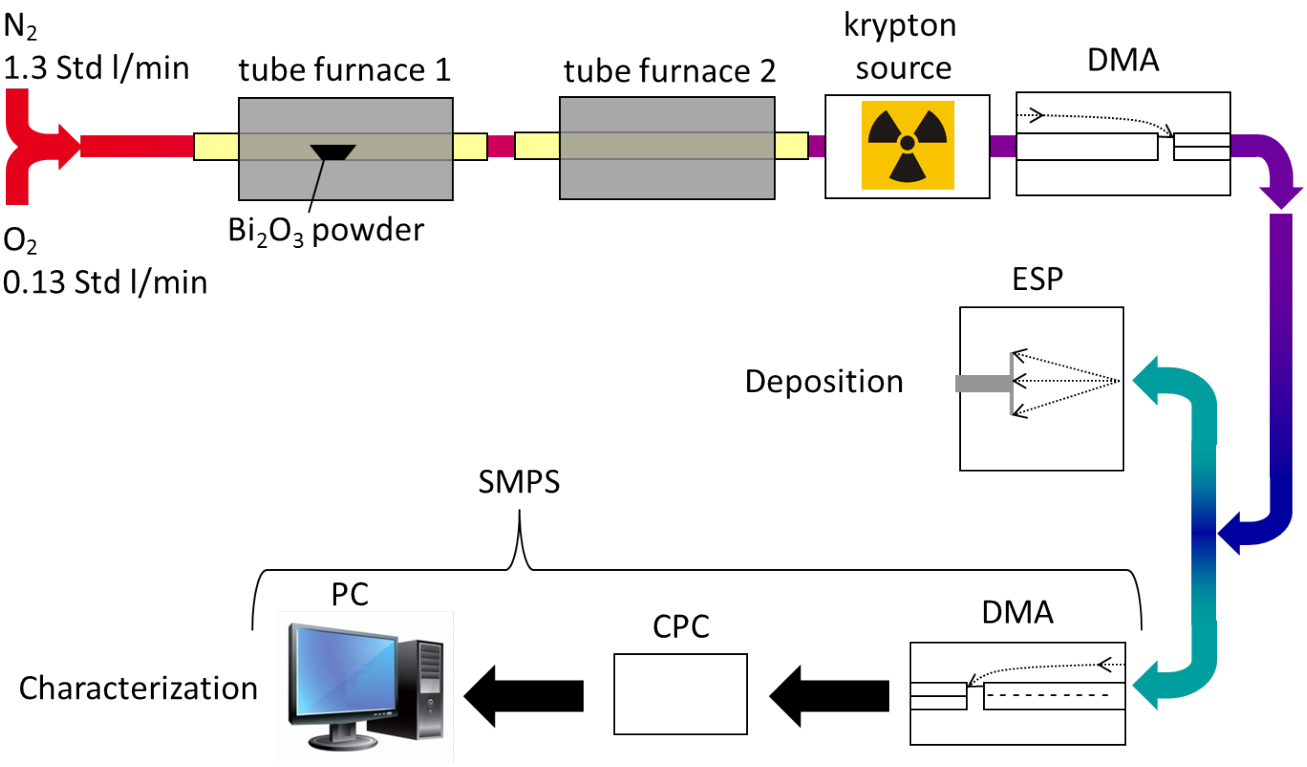

Figure 6: Scheme of the synthesis, deposition and characterization setup.

1. Physical evaporation or chemical reaction provides condensable gas molecules.
2. The molecules form a cloud of stable nuclei.
3. Stable nuclei (liquid or solid) grow by coagulation (collision and coalescence).
4. Coalescence slows down as particle size increases and/or the gases cool.
5. Agglomerate structures start to form because collisions take place without complete coalescence.

The formation of particles by condensation can be described by the following steps:

1. Physical evaporation or chemical reaction provides condensable gas molecules.
2. When a sufficiently over-saturated vapor is reached (by increasing the number of molecules or decreasing T) homogeneous nucleation occurs.
3. Growth of the nuclei to reduce the over-saturation takes place by condensation of molecules at the surface.
4. Condensation slows down as particle size increases and/or the vapor pressure drops.
5. Agglomerate structures start to form because of collisions.

In both mechanisms several of these process steps may go on simultaneously. For example condensable molecules keep on being released from the evaporation crucible and will deposit at the surface of existing particles after the initial surge of particle formation. Which of the two mechanisms controls the gas-to-particle conversion is not absolutely clear. For similar syntheses Polarz et al. reported a combination of initial, homogeneous nucleation of primary particles, followed by collision and imperfect coalescence [152]. Generally speaking formation by collision and coalescence becomes the more likely the higher the concentration of particles is. However, the question of the underlying mechanism is not primarily important for the outcome of the synthesis. Especially because a second furnace was used in which agglomerates sinter to dense, spherical particles [152]. The major drawback of the synthesis methods is its low yield. Not more than a few monolayers of monodisperse particles can be synthesized.

4.2 Characterization of solid Bi_2O_3 nanoparticles

Size calibration

As significant discrepancies between the particle size determined with scanning electron microscopy (SEM), transmission electron microscopy (TEM) and SMPS were identified, a size calibration procedure was launched. Refecence materials RM 8011, RM 8012 and RM 8013 (NIST) on TEM grids with SiN_x membrane were bought. These gold nanoparticles had the nominal sizes of 10, 30 and 60 nm with spherical shape and a very narrow size distribution. They were used for calibration of the SEM and TEM microscope in use. The images were taken under the same conditions and magnifications as (a) in the NIST reports about the reference materials and (b) used for the Bi_2O_3 nanoparticles.

SEM calibration A working distance of 8 mm and different acceleration voltages were used. The images were analyzed with ImageJ software using the implemented threshold automatism to detect the correct particle borders. The projected area data for each numbered particle was converted to an effective spherical diameter in length units (nm) based on the scale. A total of approx. 400 particles were analyzed for each set of parameters at each of the three sizes.

TEM calibration Single particles of the 30 and the 60 nm sample were captured at magnifications from 10k x up to 690k x. The calibration took place in two steps. For high magnifications between 290 kX and 690k x lattice fringes could be seen. As the lattice constant and the corresponding lattice distances of gold are very reliable measures this structural information was used for calibration in the high resolution (HR) regime. A fast Fourier transform (FFT) of the image was used to measure the lattice distance in reciprocal space. The distances of the reflexes were measured, averaged and converted to real space (inverse). These images were analyzed with the FEI software Digital Micrograph. The known distance was used to calibrate the high resolution images and calculate the correct projected area of the particle with 30 and 60 nm nominal size. As second step in the calibration procedure the projected area of the respective particle was determined at all magnifications down to 10k x. As the correct area was known from the HR images a correction function could be determined for lower magnifications. The ECD was caluclated from the area.

DMA calibration As the DMA required airborne particles (aerosols) the reference materials from NIST could not be used. Instead the calibrated microscopes were used to calculate the correct sizes of synthesized Bi_2O_3 nanoparticles which always had been measured by SMPS, too. Hence relating the calibrated sizes from TEM with the sizes obtained in the SMPS gave a correction function. Due to the different size-weighting methods in microscopy and mobility analysis the procedure is only appropriate for spherical particles but could cause errors if the shapes deviate notably from this ideal.

Characterization at room temperature

After synthesis the particles were ex-situ characterized by several methods in order to determine their morphology, crystal structure and purity. Because of the low yield, some experiments requiring larger amounts of sample had to be carried out with a commercially available Bi_2O_3 powder: Bismuth(III) oxide, NanoArc ® , 99.5% from Alfa Aesar Industries (from here on called 'commercial powder') with a stated size of 38 nm. The powder was characterized as well. At room temperature (RT) SEM, TEM, thin film x-ray powder diffraction (XRD), Synchrotron XRD and x-ray photoelectron spectroscopy (XPS) were used.

SEM micrographs were taken as standard for every deposited sample in an JEOL JSM-7500F microscope directly after each synthesis to check the correct size, morphology and deposition density. Additionally, the samples used for heating experiments were characterized in a FEI Tecnai F20 TEM using bright field and high resolution imaging as well as electron diffraction for structure determination. The commercial powder was dispersed in pure ethanol

and treated with an ultrasonic finger for one minute. A drop of the dispersion was let dry on a carrier glass. After sputtering a 15 nm Au-Pd film the samples were investigated with a FEI XL30 FEG SEM.

XRD was carried out on different devices. The small sample amount of the synthesized particles did not allow usual laboratory powder diffraction methods for characterization. Monodisperse particles of 14 nm on a MgO single crystal were characterized with a thin film XRD (Rigaku SmartLab with 9 kW rotating anode) together with E. Hildebrandt and also with a 2D-detector at beamline P02.1 (λ= 0.207309 Å), PETRA III, HASYLAB, Hamburg with M. Hinterstein. From the line profile the isotropic crystallite size was determined [153]. The MgO was chosen because initially heating experiments were anticipated.

XPS was measured on a layer (approx 100 nm thick) of polydisperse bismuth oxide nanoparticles with a mean size of 16.4 nm (σ_{GSD} = 1.45) which were deposited at an ESP voltage of -7 kV for 120 hours ont a silicon <111> wafer. The measurement was performed under high vacuum in the integrated system DAISY-MAT by Corinna Hein, Oberflächenforschung, FB11, TU-Darmstadt. The surface was not cleaned by any sputtering process since this reduced the particles to metallic bismuth under the experimental conditions. As common to electron spectroscopies where the escape depth is only 1-2 nm, the atoms an their chemical binding in the surface region are probed.

Characterization at elevated temperatures

The commercial nanopowder was available in milligram amounts and could be used for high temperature x-ray diffraction (HT-XRD), as well as differential thermal analysis with combined thermogravimetry (DTA-TG) and differential scanning calorimetry (DSC) measurements. For comparison all these experiments were also performed with a high purity Bi_2O_3 micron powder (bismuth(III) oxide, 99.9998%-Bi PURATREM, STREM chemicals).

HT-XRD measurements were carried out with a Bruker D8 diffractometer in Bragg-Brentano geometry with an Anton-Paar HTK 1200N high temperature chamber. The powder was shed onto a platinum foil, slightly compacted and aligned on the sample stage. Two cycles of a temperature ramp of 10 K/min from RT up to 1153 K and back was performed for every sample. A 11° 2Θ window from 25 to 36° was recorded every 15 K with a Super Speed VÅNTEC-1 detector. The measurements were performed in air without gas flow, inert gas (He) at 0.03 std l/min and and technical vacuum (approx. 1 Pa). A test experiment with a hot air blower was performed at the PETRA III beamline P02.1 (λ= 0.207309 Å). Measurements were made stepwise every 10 K, each preceding a holding time of 5 min for equilibration. The average heating rate was ~1 K/min. Rietveld refinement of all patterns was done with the program FullProf [153].

DTA-TG-MS and DSC was measured with different calorimeters. DTA-TG at 300 ml/min gas flow of inert gas (Ar), air and in Ar with a reductive graphite crucible was measured in a Netzsch STA 449 C Jupiter machine from the group dispersive solids, FB11, TU-Darmstadt, operated by Claudia Fasel. The device had an attached mass spectrometer (MS) for analysis of volatile species. DSC was measured under inert gas (Ar) with a gas flow of 20 ml/min in a Netzsch Pegasus 404F. It was operated by Katharina Klinski-Wetzel. The samples were weighted before and after the measurements. All measurements were performed with 10 K/min heating and cooling rates up to 1183 K and usually alumina crucibles were used.

4.3 Evaporation experiments

To analyze the evaporation behavior of the synthesized Bi_2O_3 nanoparticles, a special setup, similar to the one described by Nanda et al. [25, 26, 27] was built up. Behind the synthesis setup in figure 6 an additional tube furnace was positioned which served as evaporation chamber. The monodisperse aerosol of the synthesis flew with 1.43 std l/min through this chamber. For the synthesis the parameters in chapter 4.1 were used to produce initial monodisperse sizes of 47, 29, 17, 8 and 6 nm and for each of these sizes an evaporation experiment was conducted. As depicted in figure

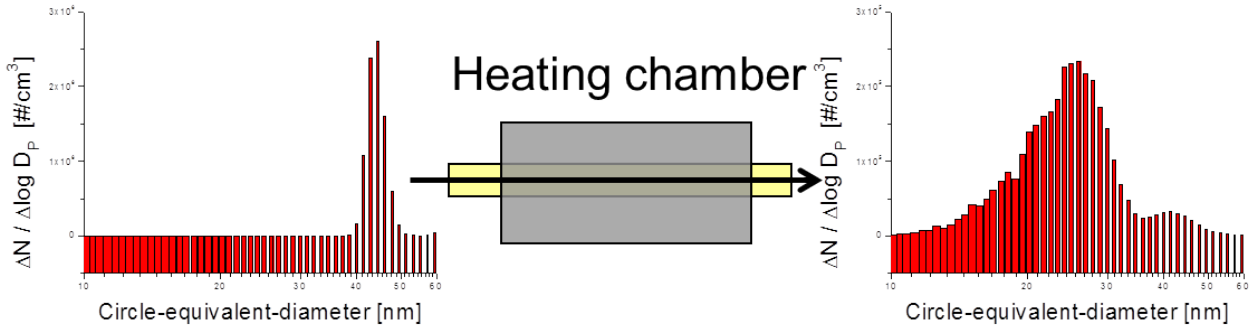

Figure 7: Scheme of the measurement method for analyzing the evaporation behavior. Monodisperse particles were synthesized and transported through a heating chamber as a low concentrated aerosol. The size distribution was sequentially measured before and after the evaporation event. The temperature of the chamber was changed in steps and material properties were derived from the temperature-dependent size change caused by evaporation.

7 the size distribution was measured before and after the chamber. The dwell time in the chamber was calculated to be 2 sec. Stepping through the temperatures between 373 and 1200 K, distributions were recorded and analyzed. Because evaporation causes shrinkage, the changing particle diameter could be used as measure of evaporation rate. An evaluation method was proposed by Nanda et al. [25, 26, 27], but the results were not satisfying. A new method derived from kinetic theory, which simulates the dynamic shrinkage of the nanoparticles in the evaporation chamber was developed. Its mathematical base will now be described..

Evaluation of dynamic evaporation

For analyzing the measured size-changes a model is necessary which relates the size change to the evaporation rate and hence to the physical properties of the particles. Equation 15 was used. The driving force is the pressure difference $p - p_p$ which has to be negative for evaporation because a material can only evaporate if the vapor pressure is higher than the partial pressure in the surrounding atmosphere. For the case of a spherical particle with $v = 1/6\pi D^3$ one can express the change of diameter per unit time as follows:

$$dD = \frac{2v_m(p - p_p)}{\sqrt{2\pi m_m RT}} dt \tag{65}$$

α has been set equal to unity. As diameter is the measured quantity in the DMA this was the equation to work with when simulating the evaporation in the heating chamber with constant temperature. In the case of the experimental setup an initial particle size D was known and the size D_x after a dwell time t in the heating chamber had to be calculated. If the partial pressure driving force $p - p_p$ is constant over time, which is true for large particles, this is simply done by integration.

$$dD_x = D + \int_0^t \frac{2v_m(p - p_p)}{\sqrt{2\pi m_m RT}} dt \tag{66}$$

But for nanoparticles the Kelvin correction has to be applied and equation 65 gets more complicated.

$$D' = \frac{2v_m}{\sqrt{2\pi m_m RT}} (p - p_p \, exp\left[\frac{4v_m \gamma_{lv}}{RT\, D(t)}\right]) \tag{67}$$

As both, $D'(t)$ and $D(t)$ occur, the equation had to be solved as a differential equation. Because of the exponential expression this had to be done numerically in steps for t. In the present case $p_p(T)$ is made up of various gas species of

Bi_2O_3 and was not exactly known in our material system. So the expression was approximated by the Clausius-Clapeyron equation (11, 12) as a mean over all species. Inserted above, this finally gives the equation that had to be solved:

$$D' = \frac{2v_m}{\sqrt{2\pi m_m RT}} \left(p - p_1 \, exp \left[-\frac{\triangle_v H}{R} (\frac{1}{T} - \frac{1}{T_1}) + \frac{4 v_m \gamma_{lv}}{RT \, D(t)} \right] \right) \tag{68}$$

As the concentration of the nanoparticles was low ($< 10^6$ particles/cm^3) and the particles were distributed in fresh, unsaturated gas, the partial pressure in the gas phase, p, was taken to be zero. T_1 and $p_1$are just a pair of values on the P-T curve of the bulk. The unknown material parameters were $\triangle_v H$ and γ_{lv}. These two parameters were determined by fitting the model to the measurement values. The former parameters is a bulk property while the latter is the only one which affects the size-dependence caused by the Kelvin effect. Consequently, the rates of size change were plotted for the 5 initial particle sizes and equation 68 was fitted by adjusting γ_{lv} to match the size-dependent differences between the curves. On the other hand, $\triangle_v H$ was fitted from the slope of a vapor pressure (P-T) curve. The vapor pressure p was received by rearranging equation 68 and stripping off the influence of size by applying the now known γ_{lv}.

4.4 In-situ Transmission Electron Microscopy

The in-situ transmission electron microscope/microscopy (TEM) experiments were carried out at the University of Duisburg-Essen together with R. Theissmann at a FEI Tecnai F20 with a Gatan 652 heatable transfer sample holder for heating up to approx. 1200 K. For preparation of the commercial Bi_2O_3 nanopowder 0.05 g of the powder was mixed with 15 g pure ethanol and dispersed for 1 min with an ultrasonic finger. Directly afterwards a small drop of the dispersion was put onto the TEM grid and let dry. The synthesis and deposition of the monodisperse Bi_2O_3 nanoparticles is described in detail in chapter 4.1 and 5. Most samples were deposited on 15 nm thick, amorphous silicon nitride support films on Si wafers with 0.1 x 0.1 mm windows arranged in a 3x3 array (Ted Pella, Inc.). For testing the influence of substrate materials few samples were deposited on Nickel TEM Grids with a holey 10 nm thick carbon support film. No surfactants were used for any of these preparations to avoid surface contamination. All experiments were performed at a vacuum of approx. 10^{-5} Pa and an acceleration voltage of 200 kV. Before and after every experiment the sample was characterized at room temperature by taking bright field (BF) and selected area electron diffraction (SAED) as well as sometimes high resolution (HR) images. Mainly two types of heating experiments were performed:

Constant heating ramps of 50 K/min and recording of BF movies of single particles (> 50 nm): Only two of these experiments were performed because of the lower information content compared to the other type. Separate, commercial bismuth oxide nanoparticles were chosen: One with 50 nm and one with 100 nm. The latter was connected to a second 50 nm particle by a small neck. Sample position, height and focus were manually controlled to observe the particle during a continuous heating process. The samples were heated until entirely evaporated at 870 and 920 K. For the duration of the whole experiment a video was captured. A tracking algorithm in the video software Adobe Premiere was used during post-processing to compensate the permanent sample drift.

Stepwise heating and recording of SAED and BF images at each step: These were the usual experiments. SAED gave information about the evolving structure and loss of crystallinity at T_{tr} averaged over some thousand particles. The bright field images showed the morphological evolution. Furthermore they were taken without objective aperture in slight under focus so that the superimposed dark field image served as indicator of crystallinity of single particles. The step size was decreased when approaching T_m and heating was stopped 30 - 50 K above that temperature. Subsequent cooling was performed in the same step-wise manner to observe freezing as well. For some samples a second, similar heating cycle was added to melt and freeze the particles a second time. Five samples of different particle sizes were investigated (see chapter 4.1). They are shown in figure 14.

1. 6.4 nm: $\sigma_{GSD} = 1.05$, area fraction = 13.5 %, magnification= 43k x
2. 8.7 nm: $\sigma_{GSD} = 1.05$, area fraction = 4.5 %, magnification= 43k x

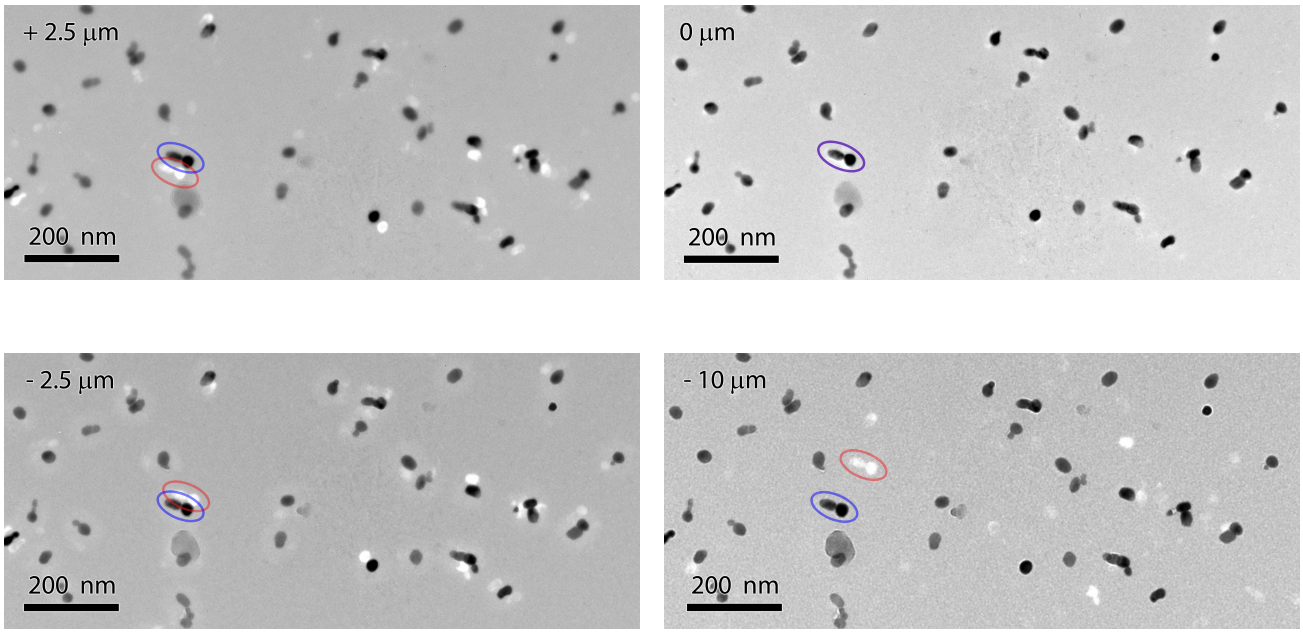

Figure 8: Focal series of BF images taken without objective aperture. The white halos near some particles are caused by diffracted electrons of suitably oriented, crystalline particles. The further one diverges from the focal plane, the more they edge away.

3. 16.0 nm:$\sigma_{GSD} = 1.07$, area fraction = 22.6 %, magnification= 29k x
4. 29.7 nm:$\sigma_{GSD} = 1.09$, area fraction = 3.9 %, magnification= 9.9k x
5. 48.8 nm:$\sigma_{GSD} = 1.18$, area fraction = 2.5 %, magnification= 9.9k x

The population densities (expressed as occupied area fraction) were a result of the synthesis conditions and the deposition time. The density had to be low enough that no significant particle interaction could take place during heating. For further analysis the integrated intensity of the rotational average of each SAED images was calculated which gave diffraction patterns similar to common powder diffractograms. These patterns were analyzed with the software FullProf [154] for phase identification.

A special feature were the BF images taken without objective aperture. Normally the aperture is inserted to intercept diffracted beams and allow the transmitted beam to form the image. This is commonly done as it reduces the effect of aberrations and thus improves contrast and resolution. On the other hand, no structural information is present in such images. Leaving away the objective aperture and slightly defocussing the image leads to micrographs like in figure 8. Particles with a proper orientation to the beam can cause diffraction. Thus, the bright halos, caused by diffracted electrons are a clear indication for crystallinity of a particle; sudden disappearance means loss of crystallinity. A defocus is necessary for the halo to shift and stand out more clearly against the particle's BF image. The effect of diffraction contrast is also nicely visible: Diffracting particles appear darker due to a reduction of intensity of the direct beam.

5 Synthesis and solid state transitions of Bi_2O_3 nanoparticles

In this chapter all topics concerning the solid state of the bismuth oxide nanoparticles are subsumed: from the synthesized particles, to the characterization at RT, and up to the solid state transformations.

5.1 Results

5.1.1 Particle size and shape

The exterior appearance of the solid Bi_2O_3 nanoparticles is in the center of this section. First the correct sizes are determined by calibration of the microscopes and SMPS with help of reference materials. Afterwards the size distributions and morphologies of the as-synthesized, monodisperse Bi_2O_3 nanoparticles are shown.

Size calibration

While the results of the calibration procedure will not be further discussed throughout this work, it is important because all mentioned particle sizes were determined as described in this section.

SEM

The JEOL JSM-7500F was correctly calibrated for micrometer sizes. The procedure was meant to determine errors when investigating particles at the nanoscale. The micrographs taken at 10 kV acceleration voltage were found to give the best particle to background contrast and thus were mainly used for the calibration with the gold reference nanoparticles from NIST. The limited resolution of a SEM only allows to determine the particle border to a certain degree of accuracy [155]. Furthermore, the contrast between carrier film and gold particles was bad which turned out to be a problem for determining the correct particle border during image analysis. So an uncertainty of the final value of up to ± 1 nm has to be assumed. From the observations at different sizes, magnifications and acceleration voltages it can be concluded that the evaluated CED depends on several imperfections of the images caused by beam-particle interaction: Darkening of the image by carbon contamination [156], charging and particle-background-contrast. These effects come into play during image analysis. The present device seemed to be calibrated well and the calibration error of the imaging unit itself seemed to be minor compared to the problems during postprocessing. The determined average particle sizes are listed in table 2 together with the reference values and the calculated correction factor. The correction values are also shown in figure 9. The error of $\pm$ 1 nm is of course much more problematic for 10 nm particles than for 30 or 60 nm ones. Combined with the bad contrast and the decreasing particle-beam interaction the deviation from the reference value increases for smaller particles (e.g the correction factor increases).

The particle-carrier contrast was much better for the Bi_2O_3 nanoparticles and so the analyzed size should be more accurate. Optimal pictures are achieved at different settings for the different materials: gold at 10 to 15 kV and Bi_2O_3 at 20 to 30 kV. Although it is generally recommendable to maintain identical conditions, in this case the priority to achieve the best image contrast, because the errors caused by changes of microscope settings are smaller than the ones caused by evaluating bad micrographs. When only one material is under investigation it should always be done at the same settings (especially the same acceleration voltage). Because of the general uncertainty and the obvious differences in imaging of Au and Bi_2O_3 nanoparticles, the correction function was not used for Bi_2O_3. Generally a particle has to be represented by $\geq$ 1000 pixels, otherwise the digital resolution becomes the limiting factor. This approximate threshold value also applied for the TEM micrographs.

Table 2: Comparison of the stated and measured CED of the three gold reference samples RM 8011, RM 8012 and RM 8013 given in nanometers [nm].

nominal size	reference value for SEM	measured size	deviation	correction factor
10	9.9±0.1	7.6	2.3	1.34
30	26.9±0.1	24.8	2.1	1.08
60	54.9±0.4	53.5	1.4	1.03

TEM

First, the results about the HR calibration are presented. The calibration at lower magnifications is based on this. The lattice-constant of the gold (fcc) unit cell is 0.4072 nm, resulting in {111} lattice-plane distance of 0.2351 nm. While the exact direction of view on the particles could not be determined in the HR images (fig. 10), the plane distance of most dominant reflexes was close to the {111} value, while any other possible planes like {200} or {220} had considerably lower values which would result in unrealistic calibrations. All {111} reflexes in the 30 and 60 nm particles were averaged to give a value of 0.236 nm. The standard deviation from this value is ±0.008 nm and the standard uncertainty of the mean is 0.002 nm. Hence the correction factor for magnifications between 490 and 590k x is 0.996 ± 0.034. For example a particle measured with 10 nm at 590k x would have an actual CED of 9.96 ± 0.34 nm from this part of the analysis.

Second the deviation at lower magnifications was determined. The relative deviation from the initial value at 590k x can be seen in figure 11, together with the relative values of the {111} lattice plane distance which were determined in the first step at HR. Down to 145k x the values fluctuated by± 3.5 % which was within the error and only the correction factor, 0.996, was applied. Between 145k x and 100k x the deviation suddenly dropped to -28 %. This is because of a clearly erroneous calibration which caused disagreements in comparing sizes of Bi_2O_3 and was the motivation for the calibration of the microscopes. Thus, an offset value of +28.19 % at ≤ 100k x was necessary. At very low magnifications the particles were only small spots in the micrographs and were imaged by less than ∼1000 pixels. In this range an error occurs due to the digital resolution of a particle. A function to describe the relative deviation f (in %) for magnifications ≤ 100k x was fitted

$$f = 23.8129\, e^{-\frac{x}{16.64261}} - 34.257 + 0.0654x \tag{69}$$

Where x is the magnification [k x]. It followed a correction function for magnifications ≤ 100k x,

$$D = 0.996\, D_{TEM} \left(1 + \frac{f + offset}{100}\right) \tag{70}$$

D_{TEM} is the measured size and $offset$ is the offset value at $x \leq$ 100k x. Above 100k x the values fluctuated by ± 3.5 % which is within the error and no correction function but only the correction factor, 0.996, was applied. The threshold error in ImageJ software for determining the particle border was tested to be ±0.3 nm. It is quite independent of the magnification until the digital resolution limit was reached. Additionally, the propagated error from the lattice plane distance gave ± 3.8 %. It finally followed an error of

$$0.3 + 0.038\, D_m \tag{71}$$

When comparing SEM and TEM, it became clear that in the size region of interest the uncertainty of SEM is much larger than the one of TEM. This can be attributed to the generally higher resolution of TEM. Furthermore, TEM seemed to be less affected by different material properties (e.g. Au vs. Bi_2O_3). So TEM was better suited, especially if the particle-substrate contrast in SEM was not ideal. Higher accuracy can be achieved in SEM by applying special calibrations and performing simulation calculations [155] for every investigated material, but this is accompanied with a very high

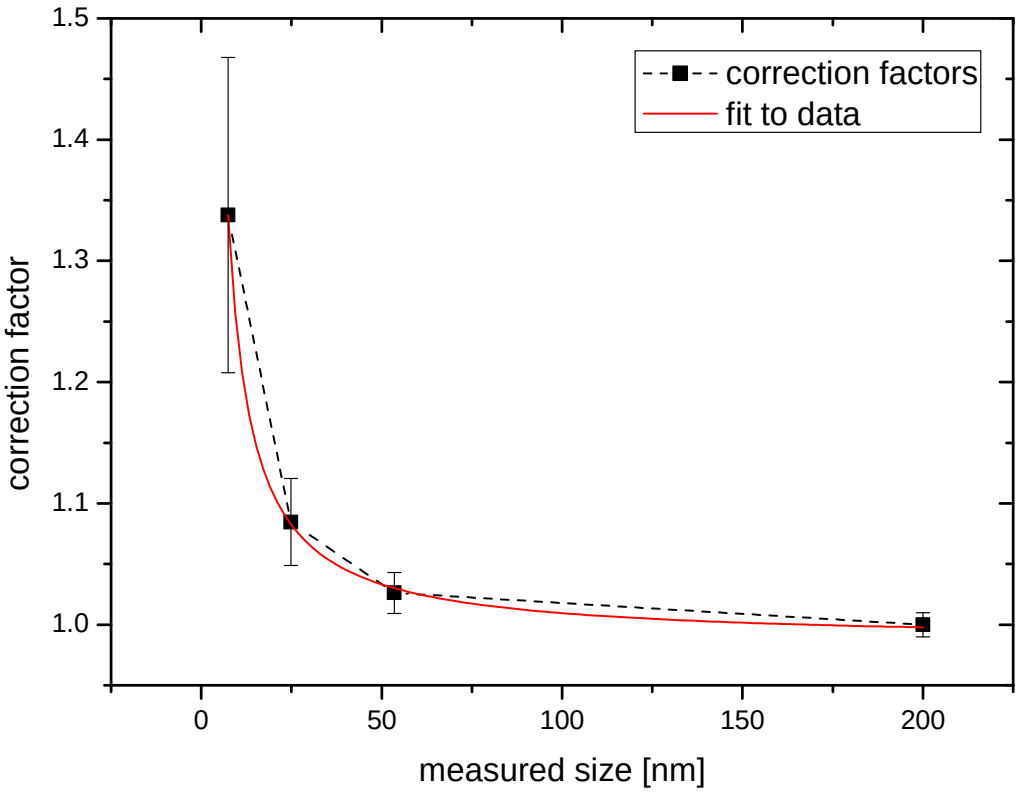

Figure 9: Correction factor for the JEOL JSM-7500F SEM plotted over particle size. The deviation from the reference value increases strongly for smaller particles. Among other things this is because an uncertainty of the particle border of 1 nm is a greater relative error for smaller particles. The value at 200 nm was made up to get a convergence to 1 above the nanoscale.

expenditure. Consequently, unless otherwise mentioned, all sizes given from now on will be calibrated sizes from TEM. As example five sizes of selected Bi_2O_3 nanoparticles, which will be used throughout this work, were calculated and listed in table 3. The higher correction value in this table compared to the SEM correction factor in table 2 is because the systematic offset of 28.19 % was added. The sizes of the 30 nm and 50 nm particles were measured at non-ideal, low magnifications (see fig. 11) where the digital resolution worsens the accuracy. This general problem applies for SEM as well.

DMA

Since the DMA needed an aerosol as measurement medium, the Bi_2O_3 nanoparticles at the sizes given in table 3 were used as calibrant. The corrected mean CED from TEM were compared with the mean values from the corresponding DMA measurement which is shown in figure 12. The deviation of the DMA is a systematic, linear one. The linear fit gave the correction function

$$D = 0.70054\, D_{DMA} - 1.03465\ [nm] \tag{72}$$

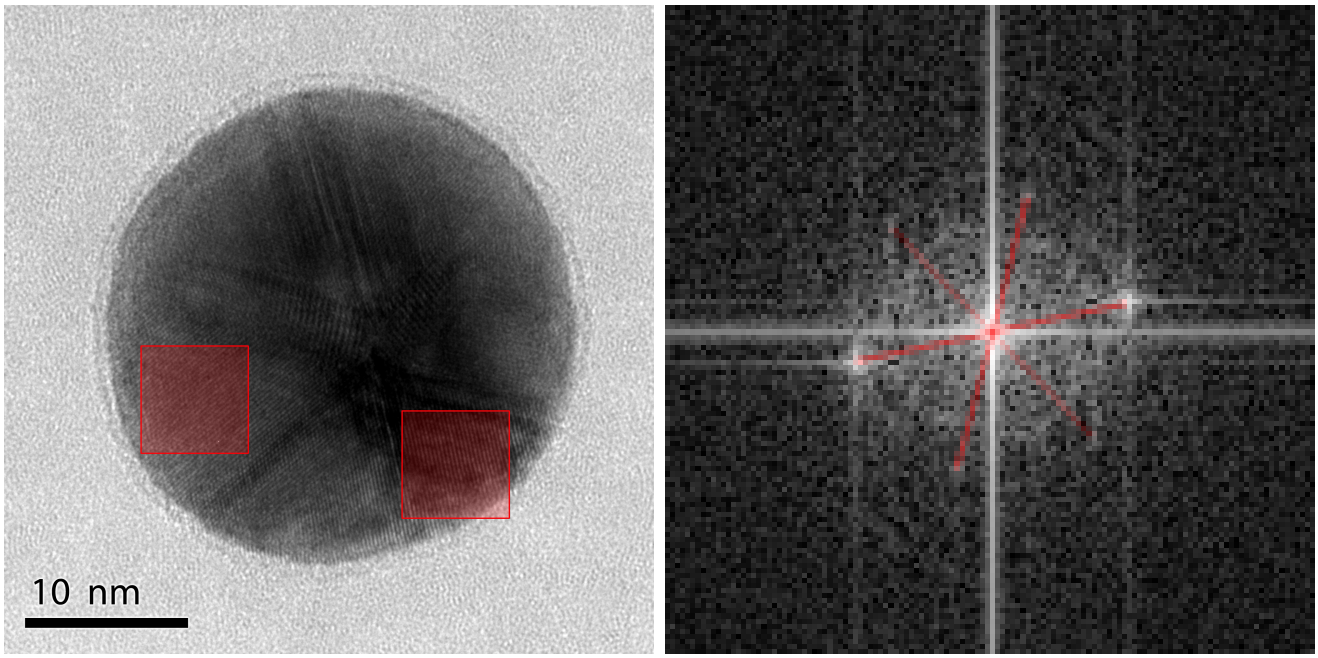

Figure 10: Size calibration at HR: Regions with clear lattice fringes which have approximately the lattice plane distance of {111} (marked red in figure (a)) were Fourier transformed. The distances in the FFT (fig. (b)) were measured and averaged to give the measured lattice plane distance.

Table 3: Selected sizes of Bi_2O_3 nanoparticles which will be important throughout this work.

nominal size	measured mean size in TEM	magnification	correction	corrected mean size
6	6.5	43k x	-29.65 %	6.4±0.5
9	8.8	43k x	-29.65 %	8.7±0.6
15	16.1	29k x	-28.19 %	16.0±0.8
30	27.5	9.9k x	-20.47 %	30±1.5
50	45.5	9.9k x	-20.47 %	49±2.2

Morphology of Bi_2O_3 nanoparticles

The synthesis setup in figure 6 produced polydisperse size distributions. Their mode could be shifted by increasing the furnace temperature. Examples of such initial distributions can be seen in figure 13 (black columns). With the attached DMA set to a certain voltage and applying a sheath gas flow 10 times as high as the actual gas flow through the system, size distributions as depicted by the red columns were achieved. These narrow distribution had a σ_{GSD} of 1.05 to 1.1 which is close to a monodisperse size. For example the distributions of a 6.4, 16.0 and 48.8 nm sample had a full width half maximum (FWHM) of 0.75, 2.0 and 10 nm. So at larger mean sizes, the distributions widened a bit. Typical samples at different sizes and their size distributions from SMPS can be seen in figure 14. The particles up to 30 nm were almost spherical in shape with a circularity of > 0.8. Only the largest size distribution showed partially sintered, aspherical shapes. Larger particles obviously required higher sintering temperatures, so that 803 K was too low at the given dwell time of 2 seconds in the furnace to fully densify these particles. In the micrograph of the 29.7 nm sample one can see some non-spherical particles composed of small primary particles. Apparently such agglomerates have the same mobility as the spherical particles with 30 nm diameter. The agglomerates were not considered in the TEM size analysis and calibration.

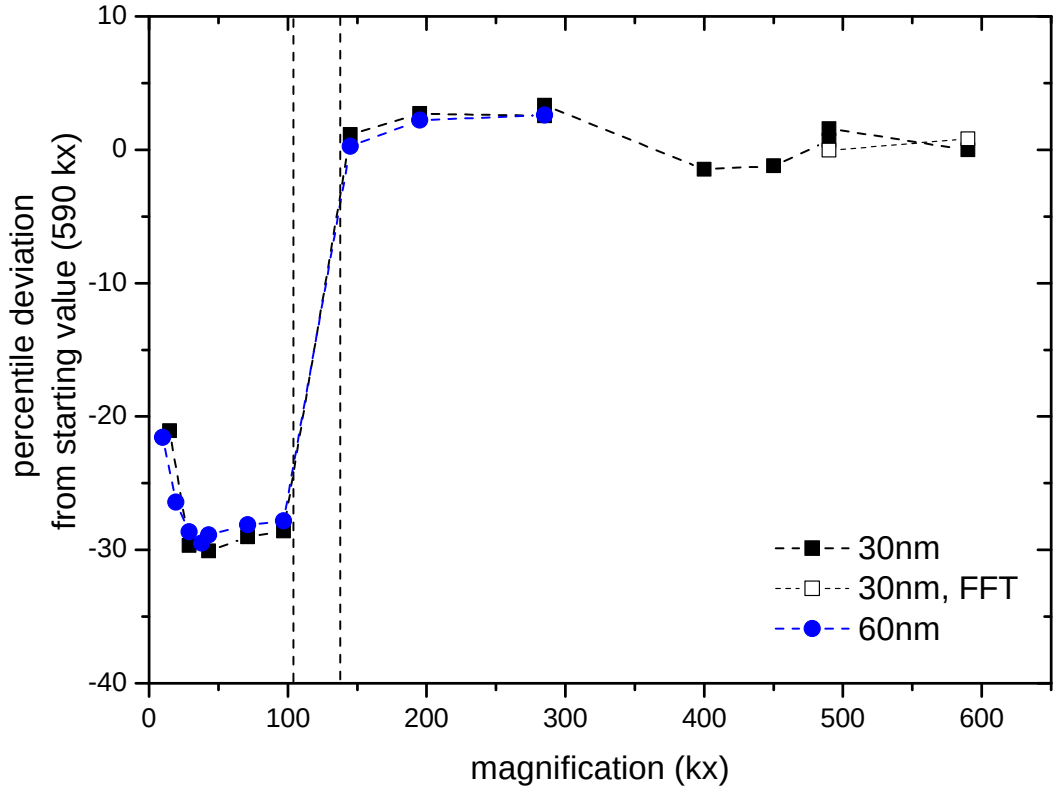

Figure 11: The relative deviation from the sizes at HR (490 - 590k x) at different magnifications is shown. Down to 145k x only slight fluctuations within ± 3.5 % can be found. A clearly erroneous calibration below 100k x is evident from the sudden drop between 145 and 100k x. The increase at the lowest magnifications, 20 and 10k x, is caused by insufficient digital resolution of the particles.

The commercial powder was dispersed, sputtered and investigated in the SEM (fig. 15b on page 53). It shows to be composed of hard and soft agglomerated primary particles with a mean size of approx. 50 ± 7 nm and also a broader distribution of the primary particles. This average size was also confirmed by XRD (see next section). Due to the strong agglomeration and overlapping in the SEM micrographs a more accurate determination was not possible.

5.1.2 Particle characterization at room temperature

Most importantly the crystalline structure and purity of the particles was determined. The structure was analyzed by diffraction with x-ray radiation from the Synchrotron source PETRA III. Figure 15a shows a diffractogram together with the results from the Rietveld refinement. The structure of the analyzed 30 and 14 nm particles was clearly the metastable β-Bi_2O_3 structure with $a=b=0.775$ nm and $c=0.567$ nm. From line broadening the isotropic crystallite size was determined to be 13.9 nm for the sample with nominal size of 15 nm. As this accords well, the particles had to be monocrystalline. The particle volume an thus the diffracting volume decreases with r^3. As consequence the signal decreases drastically and the coherently diffracting regions become too small for conventional Rietveld analysis. This is why smaller particle sizes could not be measured with XRD. But such particles had the same appearance in the HR micrographs in figure 16 and SAED patterns in TEM. The HR images also showed a faceted shape and lattice fringes whose d-spacing could usually be attributed to the 201 and 220 planes of β-Bi_2O_3. No amorphous surface region could be observed.

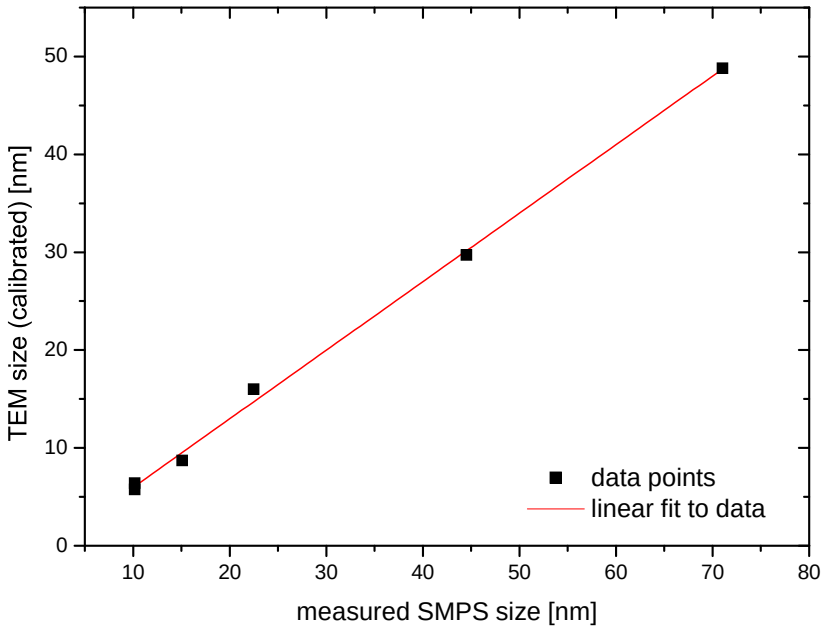

Figure 12: Calibrated mean size from TEM over measured mean size from SMPS for 5 different Bi_2O_3 samples. The straight line is a linear fit giving the correction function for SMPS sizes (eq. 72).

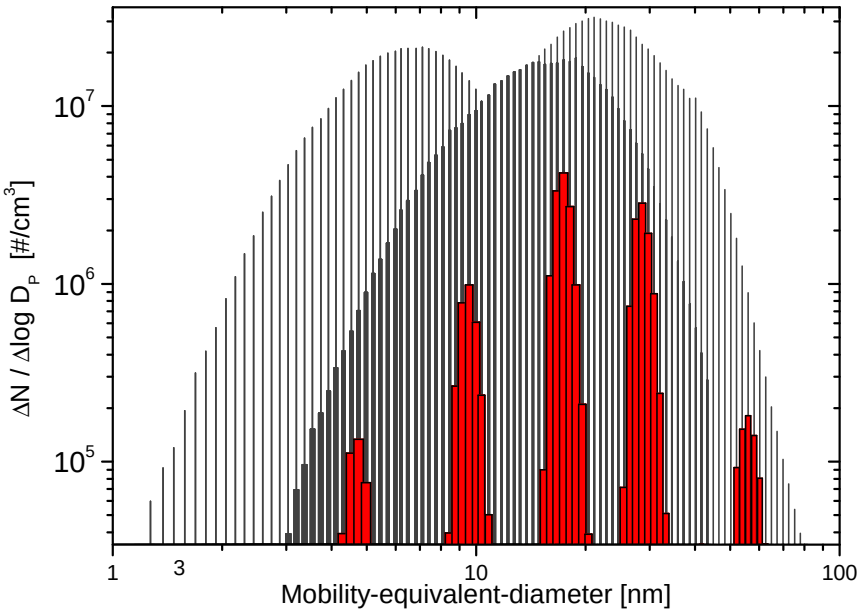

Figure 13: Size-distribution directly after synthesis chamber measured with SMPS. The gray columns in the background are typical polydisperse distributions from the evaporation-condensation process at 1253, 1293 and 1373 K evaporation temperature. From this initial distribution a narrow size fraction could be separated by a DMA (red columns). The size-separation process reduces the concentration by up to 2 orders of magnitude.

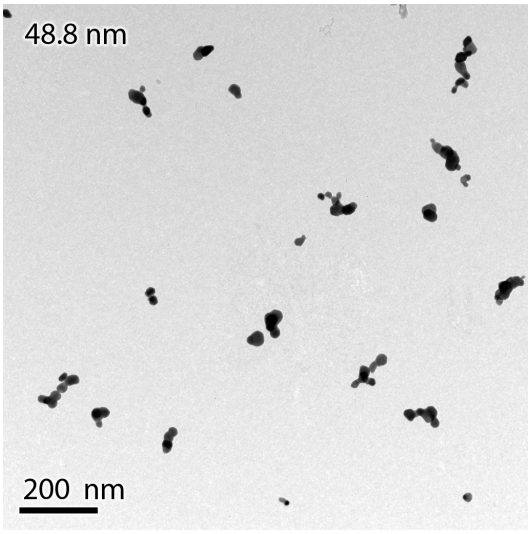
48.8 nm
200 nm

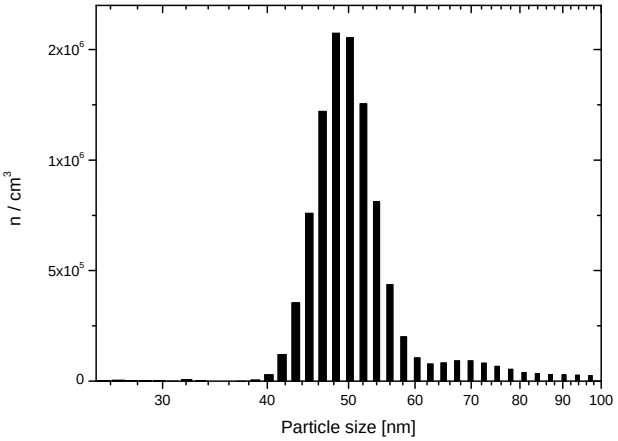
2x10^6
1x10^6
5x10^5
0
n / cm^3
30
40
50
60
70
80
90
100
Particle size [nm]

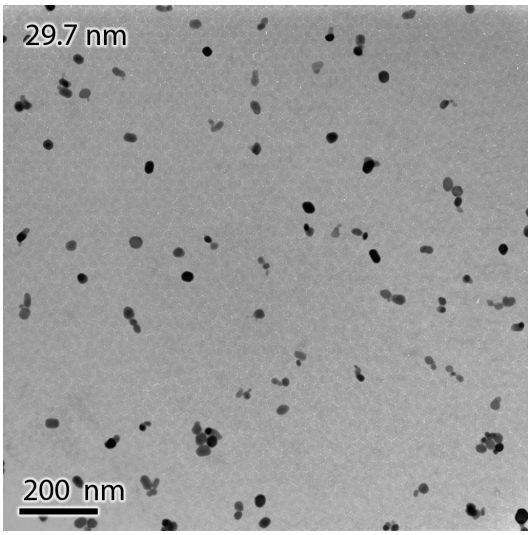
29.7 nm
200 nm

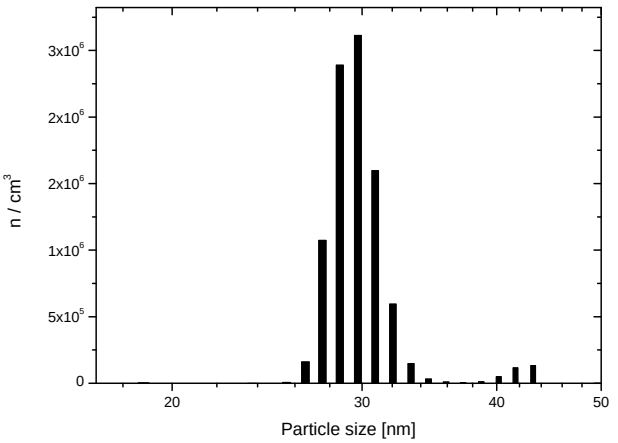
3x10^6
2x10^6
2x10^6
1x10^6
5x10^5
0
n / cm^3
20
30
40
50
Particle size [nm]

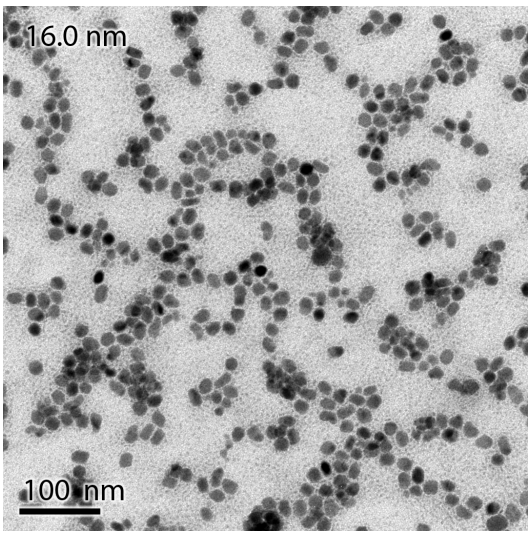
16.0 nm
100 nm

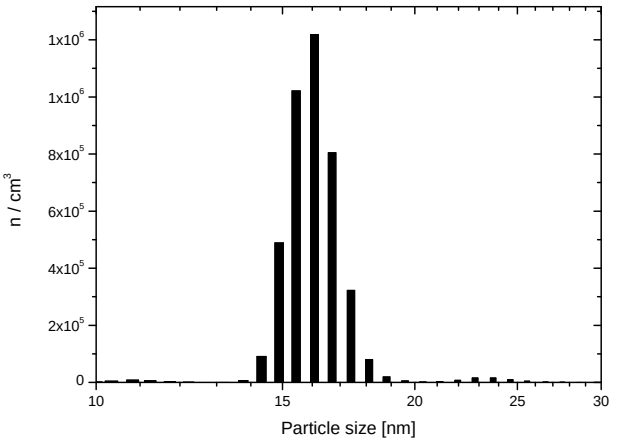
1x10^6
1x10^6
8x10^5
6x10^5
4x10^5
2x10^5
0
n / cm^3
10
15
20
25
30
Particle size [nm]

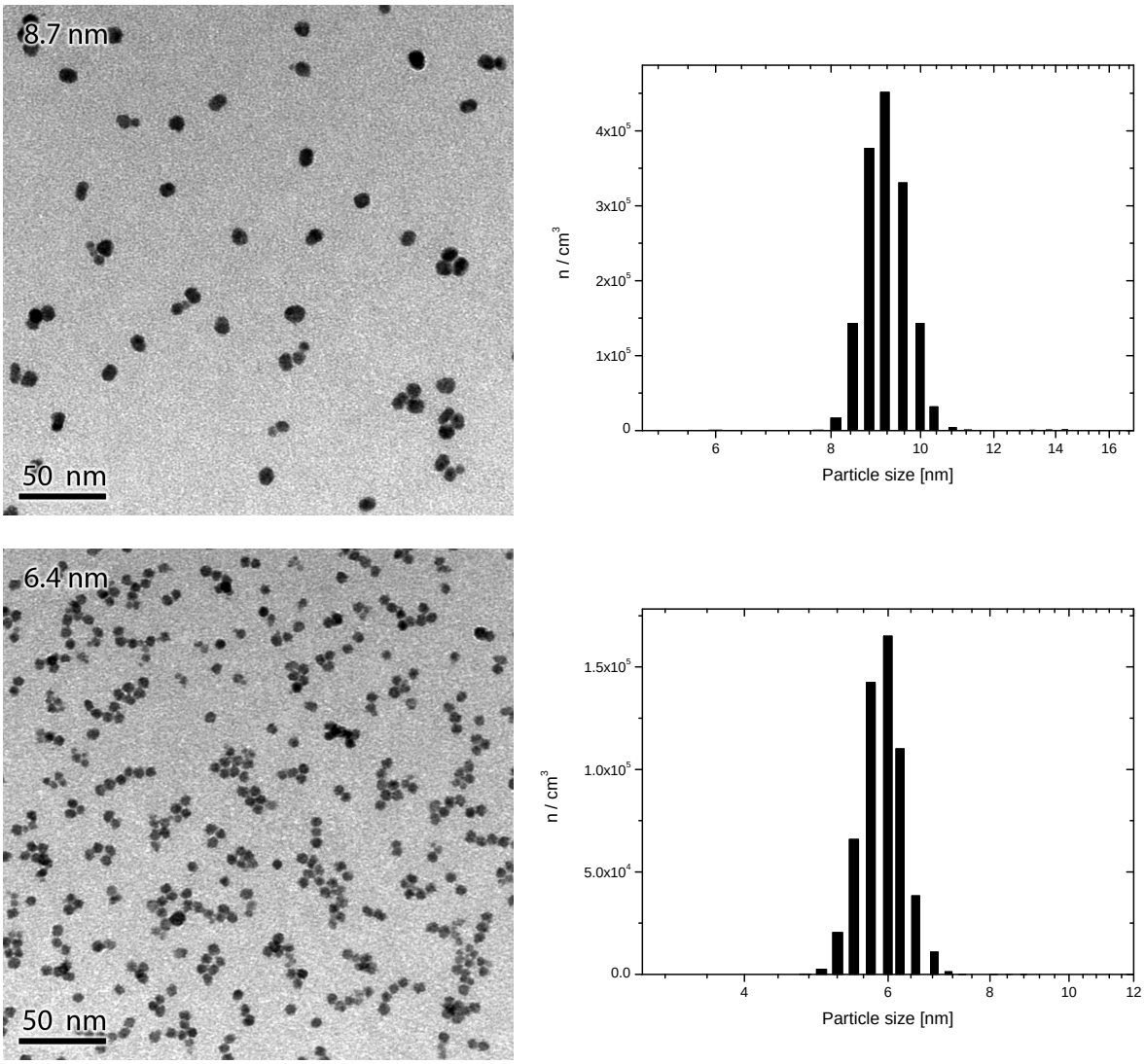

Figure 14: Representative micrographs and corresponding histograms from SMPS of 5 sizes which were also used in the in-situ TEM experiments. The samples up to 16.0 nm consist of primary particles only. In the two biggest sizes coagulation and agglomeration leads to less spherical, polycrystalline shapes.

The XPS spectrum of the same 14 nm particles on a Si wafer showed no impurities. Only emission lines of Bi, O and C were found (fig. 18(a)). The Bi4f doublet was not split, so bismuth only existed in one oxidation state. Sputtering in the vacuum chamber of the XPS caused the Bi4f doublet to split because of formation of metallic Bi. The C-line is inevitable in samples which were exposed to ambient conditions and can not be cleaned by sputtering. A shoulder at higher binding energies can be observed in the detail view of the O1s peak (fig. 18(b)). It is attributable to OH^- and CO_3^{2-} groups adsorbed on the surface in addition to the O^{2-} state in bismuth oxide [80]. The integrated intensities, weighted with the respective atomic sensitivity factor gave the average Bi:O ratio of the probed volume: 0.635. This corresponds to a molecular formula of $Bi_2O_{3.15}$. This over-stoichiometric amount of oxygen is caused by the incorporation of oxygen from the adsorbed surface species which do not belong to the bismuth oxide.

For some experiments in this chapter a commercial Bi_2O_3 nanopowder was used. The diffraction pattern in figure 15b also shows β-Bi_2O_3 with $a=b=0.7737$ nm and $c=0.5635$ nm. The average grain size determined from line broadening was 50 nm. This was in accordance with the mean size from SEM: 50 $\pm$ 7 nm. A few weak reflexes indicated small amounts of another phase which is not α-, β-, γ-, δ- or any other reported Bi_2O_3 polymorph but bismuth hydroxide ($Bi(OH)_3$).

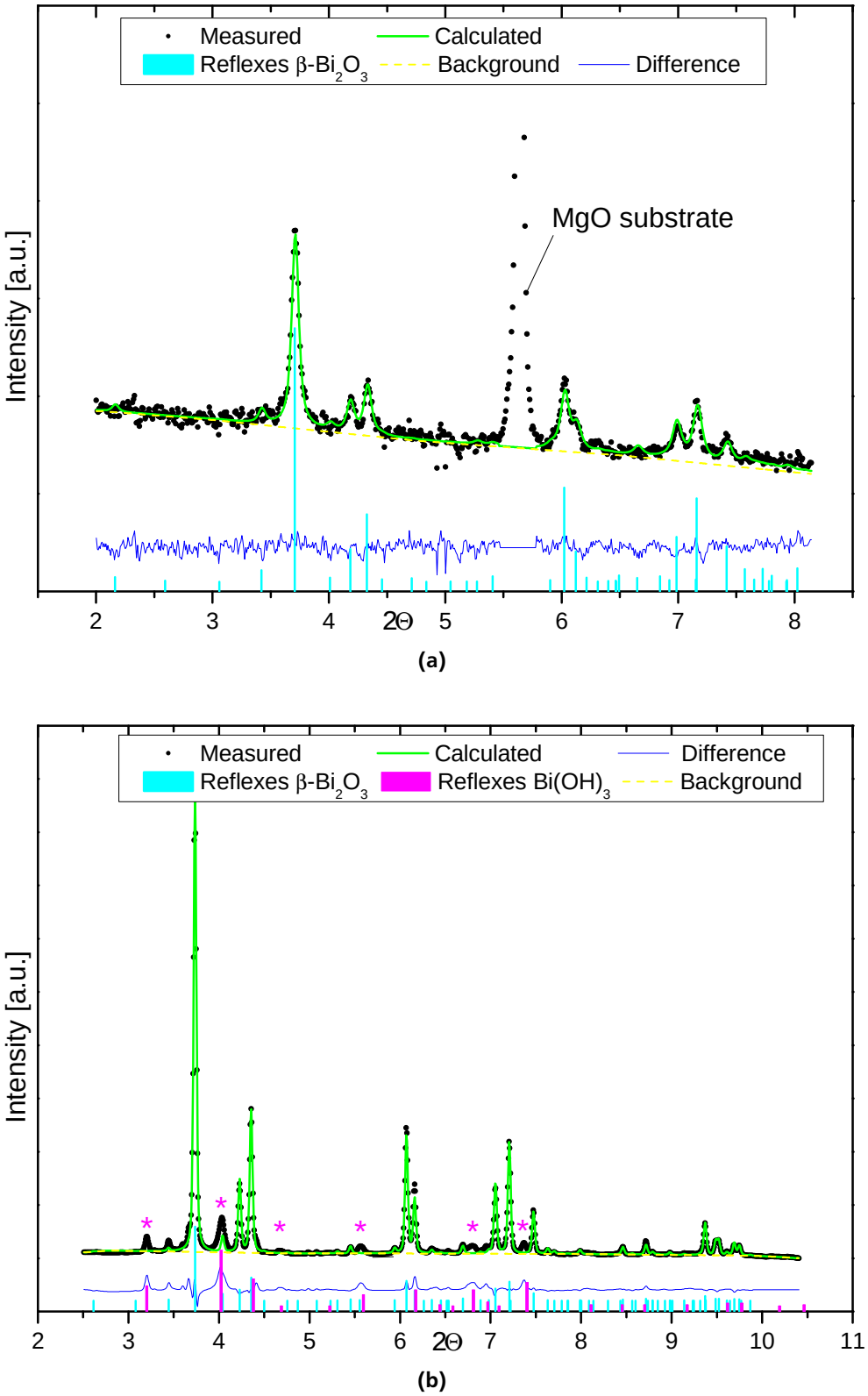

Figure 15: X-ray diffractograms and Rietveld refinements measured at PETRA III, beamline P02.1 (λ= 0.207309 Å) in air. (a) 14 nm bismuth oxide nanoparticles on a MgO single crystal. The structure is β-Bi_2O_3 and no additional phases could be detected. (b) The structure of the commercial nanopowder is β-Bi_2O_3. The stars indicate reflexes of bismuth hydroxide which is a result of aging under ambient conditions.

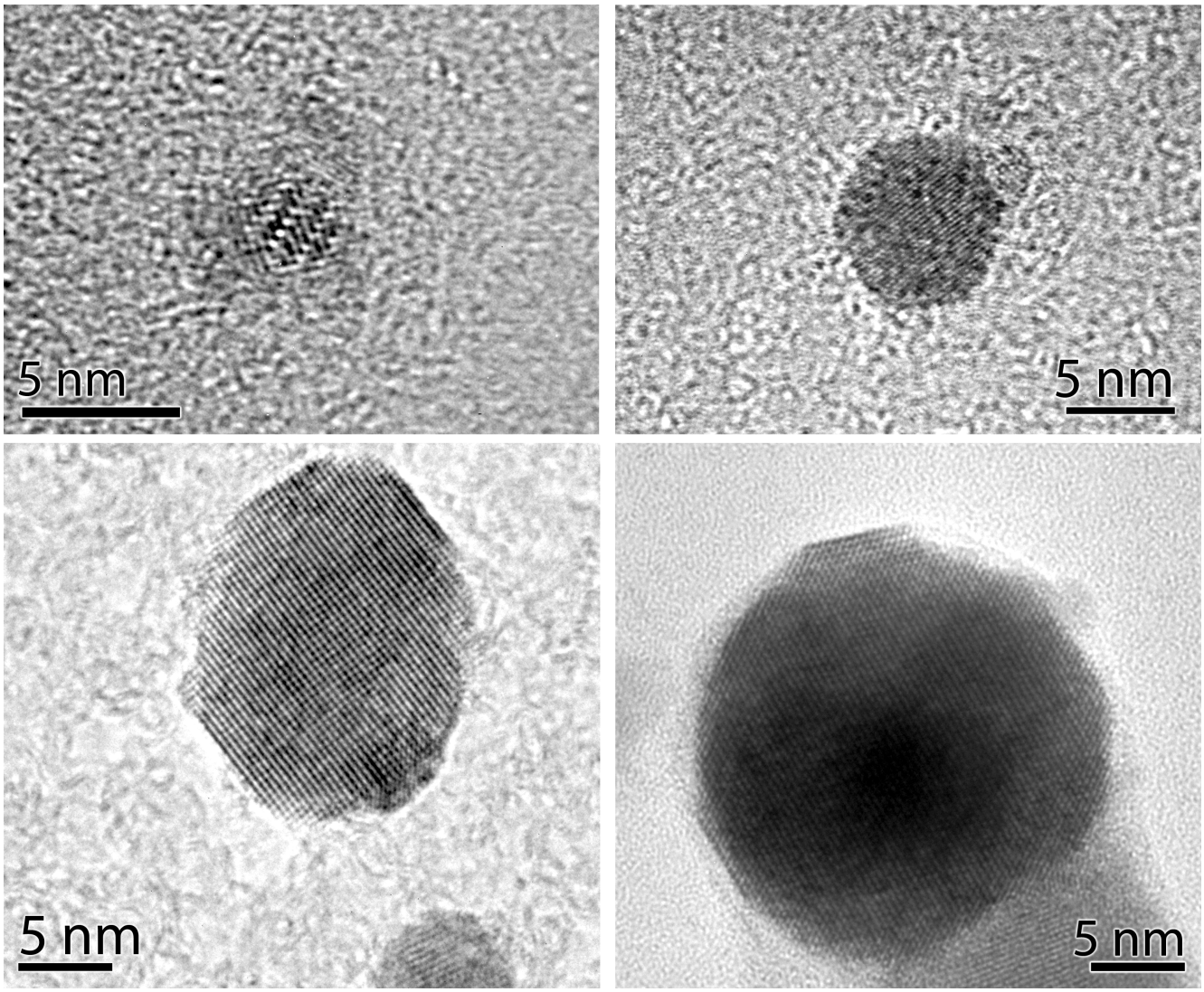

Figure 16: HR TEM images of different bismuth oxide nanoparticles. Lattice fringes and faceting are proof of their (mono)crystalline character. The identifiable d-spacings were from the 201 or 220 planes of β-Bi_2O_3.

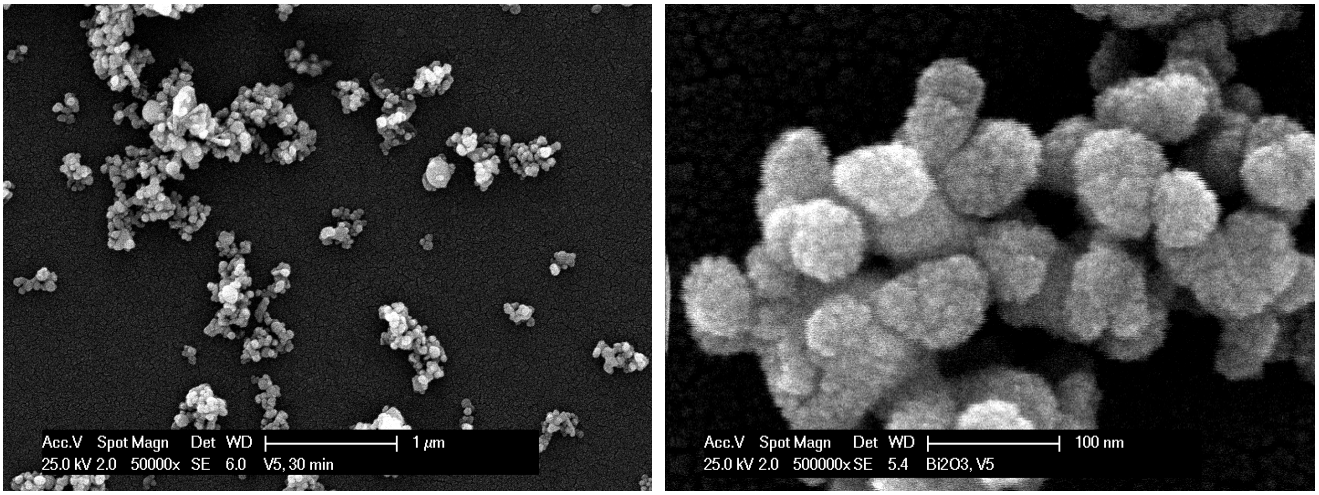

Figure 17: SEM micrographs of the commercial Bi_2O_3 nanopowder. (a) In the overview the agglomerates are visible. (b) The HR image shows the primary particles. The rough surface is caused by the sputtered AuPd film.

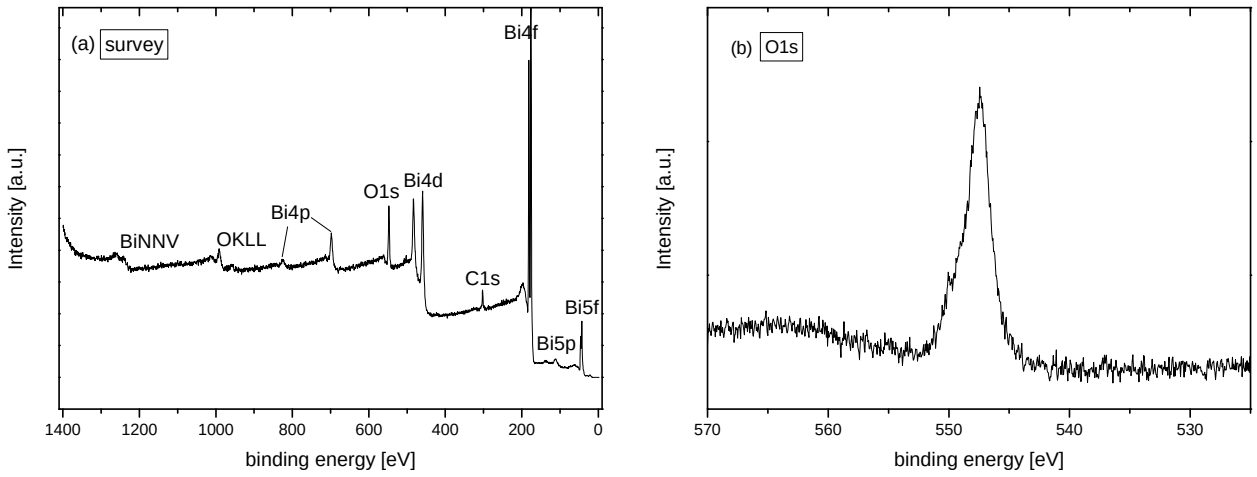

Figure 18: XPS spectrum of 14 nm bismuth oxide nanoparticles on a Si single crystal, measured at DAISY-MAT in vacuum. Only bismuth, oxygen and carbon were found (a). In the O1s peak a shoulder at higher binding energies was measured (b).

For analyzing the high temperature behavior of agglomerated bismuth oxide nanoparticles in the solid state as well as evaporation characteristics, HT XRD and traditional calorimetric measurements were performed in different atmospheres. The commercial nanopowder comparable to the monodisperse particles in the other chapters was used. Serving as bulk reference, a commercial micron-powder (α-Bi_2O_3) was analyzed in the same manner.

DSC and DTA-TG

The endo- and exothermic processes in the samples were measured and compared with DSC. Figure 19(a) shows the first heating cycle of both, the nano- and the micron-powder. The latter shows the two expected peaks of the $\alpha \rightarrow \delta$ transition at 1007 K and melting at 1089 K, whereas the nanopowder undergoes two further exothermic peaks and an endothermic rise in between. Furthermore the melting peak is broadened and the maximum is lower. The $\triangle_m H$ (integrated area) of the nanopowder (15.2 kJ/mol) is larger than the one of the micron-powder (12.9 kJ/mol) and both values lie within the known, broad scattering range [157]. In the second heating cycle (not shown) the nanopowder lacks any additional peaks and shows the common bulk behavior. All transformation temperatures are listed in table 4.

Additionally DTA-TG measurements were performed with the same experimental parameters. But two different atmospheres were used: air and inert gas. Yet, no significant differences could be observed between the atmospheres. Additional information comes from the gravimetric curve and the mass spectroscopy (fig. 19(b)). They show that up to the transition around 733-739 K the sample lost 1.6 % of its mass. The detectable main gas species have masses of m = 12, 16, 30, 32, and 44 which can be attributed to C, O, C_2H_6/CH_2O, O_2 and CO_2, respectively. The small transition at 584 K is accompanied by a peak in m = 12, 30 and 44 and the larger transition at 733 K correlates with peaks in m = 16, 30, and 32. Beyond 750 K no mass loss occurs anymore. Possible heavy species like Bi(g) (m = 209) could not be measured by the spectrometer.

HT XRD

As complementary method high temperature XRD was performed which gave structural information, as well as insight into the evolution of the mean grain size. Additionally the XRD could also be performed in actively pumping vacuum ($\sim$ 1Pa), not only in air and inert gas. The same previously characterized commercial nanopowder and also the same heating rate was used so that the transition temperatures could be compared, even if kinetic processes played a role. The 12° window recorded every 15 K (e.g. fig. 20) was evaluated to observe structural changes. In this way it was confirmed that the transitions around 1000 K and around 1075 K are indeed the $\alpha \rightarrow \delta$ and the $\delta \rightarrow l$ (melting) transitions. As the nanopowder resided in the metastable β-phase at RT, an additional transformation from the β- to the α-phase was measured at 725 $\pm$ 15 K. This coincides with the exothermic transition in DSC and DTA. The evolution of the average, volume weighted, crystallite size was traced by analyzing the line profile broadening which gave insights into the sintering of the particles. Figure 21 shows the particle growth in the different atmospheres at increasing temperatures. Starting at an initial size of 50 nm growth set in around 630 K. From there on the size rapidly increased up to the $\beta \rightarrow \alpha$ transformation. In vacuum the transformation temperature was higher and the crystallites grew larger. The experiment with the hot air blower at the PETRA III beamline provided few results because the temperature was badly calibrated and non-uniform over the sample even though slow heating ramps and long holding times were chosen. Still it showed unambiguously that at the transition temperature the particles had reached a size of $\gg$ 100 nm which is much more than the sizes in figure 21.

A summary of all transition temperatures is given in table 4. Several facts are remarkable: The $\beta \rightarrow \alpha$ transition was approx. 35$\pm$5 K higher in vacuum compared to the transitions at ambient pressure. On the other hand, the $\alpha \rightarrow \delta$ transition was roughly 30 K lower in vacuum. The shape of the melting peak in the calorimetric curves was much broader and lower for the nanopowder and the onset temperatures tended to be lower. Generally the scattering of the melting temperature and enthalpy of melting are large for Bi_2O_3. Still the melting point seemed to be shifted by approx. -30 K in vacuum- independent of the initial size.

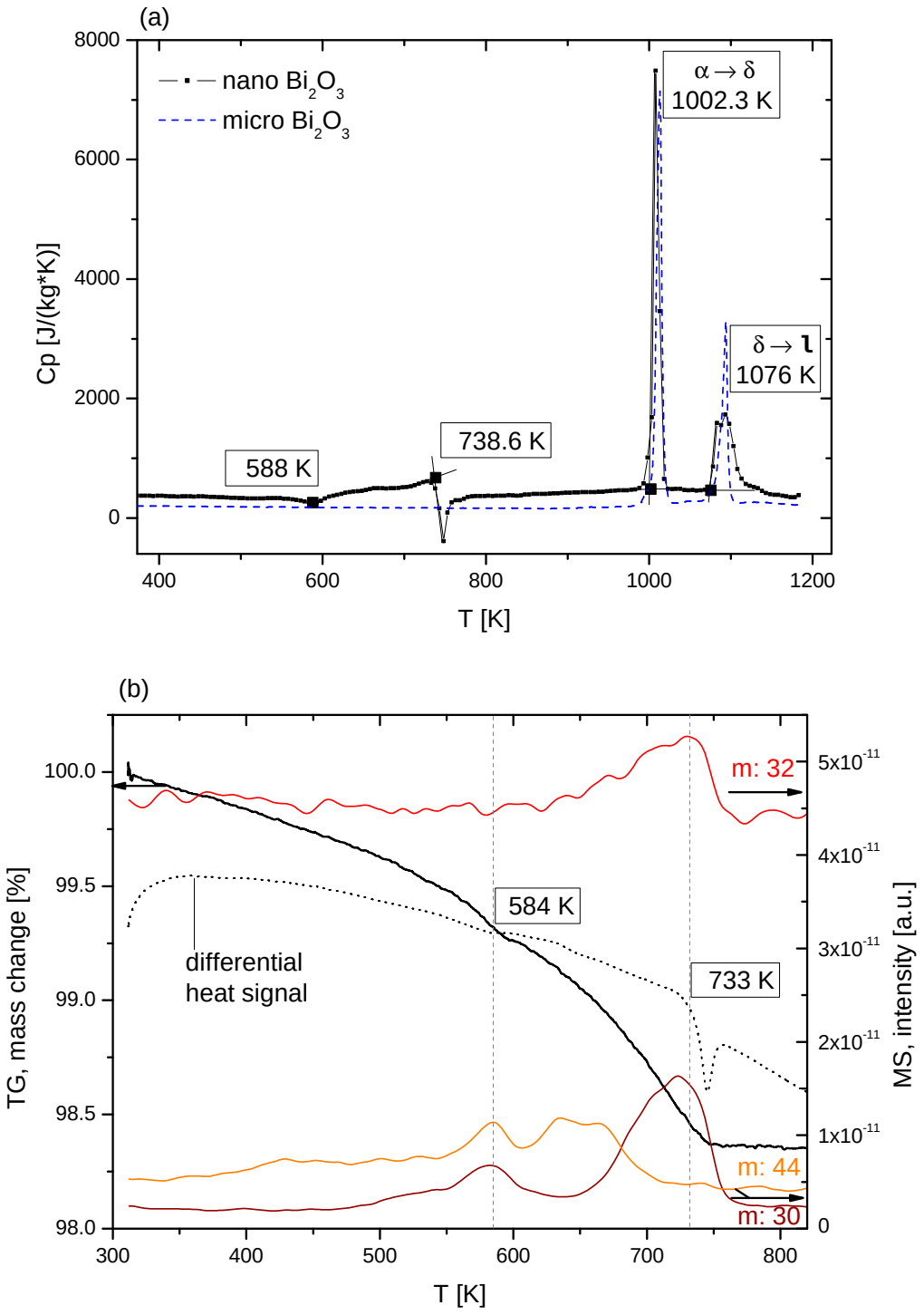

Figure 19: (a) DSC measurement of Bi_2O_3 nano- and micron-powder in argon at ambient pressure. Nanopowder: Minimum at 588 K and exothermic event at 738.6 K, endothermic $\alpha \rightarrow \delta$ phase transition at 1002.3 K and melting at approximately 1076 K. Micron-powder: The powder resides in the α-phase at RT and no exothermic events occur below 1002 K. (b) DTA-TG and MS measurement of the nanopowder between 300 and 820 K. The gravimetric curve (black) is plotted on the left and the MS signal on the right ordinate. The same transitions could be observed up to 750 K. The sample looses -1.6 % of weight until 750 K and mass spectroscopy measures increased amounts of gas species. For example m = 30, 32 and 44 are shown. After the transition around 733 K mass loss and evaporation stop abruptly. The heat signal and dashed lines are just for orientation.

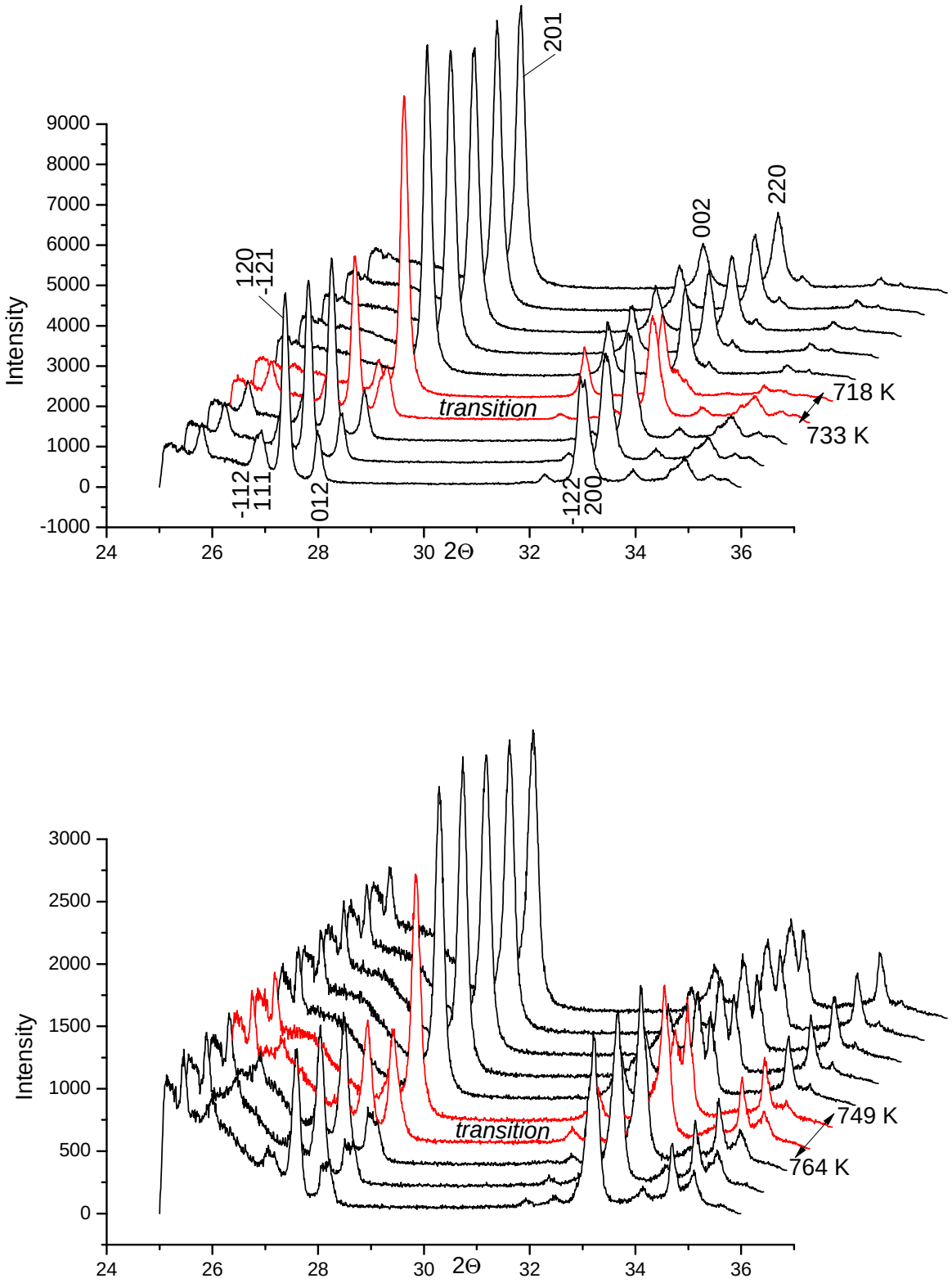

Figure 20: A 12° window with the mayor Bi_2O_3 reflexes during heating at 10 K/min captured in temperature steps of 15 K in (a) inert gas and (b) pumped to ~ 1 Pa from ambient air . The $\beta \rightarrow \alpha$ transition of the commercial Bi_2O_3 nanopowder took place between 717-733 K in air and inert gas and between 749-767 K in vacuum. First the (-111) and (112) reflexes of α-Bi_2O_3 around 29° formed and in the next step also the other reflexes had changed from the β- to the α-structure.

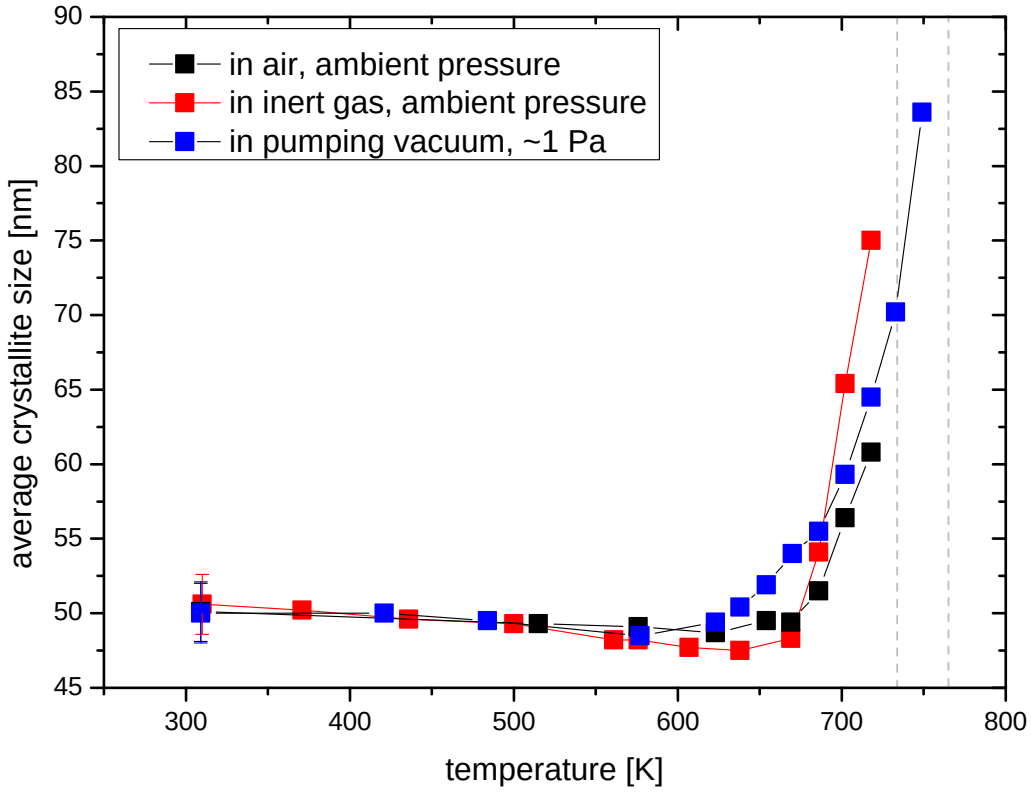

Figure 21: Average, isotropic crystallite sizes calculated from reflex broadening of commercial β-Bi_2O_3 for the patterns shown in figure 20 on the facing page. It indicates grain growth started around 630 K. The crystallites grew until the temperature for the $\beta \rightarrow \alpha$ transition was reached (dashed lines). In vacuum the particles were bigger and the transition occurred later. For illustration: A change from 50 to 70 nm would correspond to a doubling in volume (e.g. coalescence of two 50 nm particles).

Table 4: Temperatures for $\beta \rightarrow \alpha$, $\alpha \rightarrow \delta$ *and* $\delta \rightarrow l$ transitions measured with different methods and in varying atmospheres. The commercial Bi_2O_3 nanopowder (nano) and an ultra pure micron powder (micro) were measured.

transition	atmosphere	powder	method	temperature [K]
	air	nano	DTA	736±2
β	air	nano	XRD	725±15
$\downarrow$	vacuum	nano	XRD	760±15
α	inert gas	nano	DSC	738±2
	inert gas	nano	DTA	733±2
	inert gas	nano	XRD	726±15
	air	nano	DTA	1000±2
	air	nano	XRD	991±15
	air	micro	DTA	1003±2
	air	micro	XRD	991±15
α	vacuum	nano	XRD	959±15
$\downarrow$	vacuum	micro	XRD	959±15
δ	inert gas	nano	DTA	1001±2
	inert gas	nano	DSC	1002±2
	inert gas	nano	XRD	997±15
	inert gas	micro	DSC	1007±2
	inert gas	micro	DTA	1005±2
	air	nano	DTA	1074±9
	air	nano	XRD	1084±15
	air	micro	DTA	1083±2
	air	micro	XRD	1084±15
δ	vacuum	nano	XRD	1052±15
$\downarrow$	vacuum	micro	XRD	1052±15
l	inert gas	nano	DSC	1076±2
	inert gas	nano	DTA	1075±2
	inert gas	nano	XRD	1090±15
	inert gas	micro	DSC	1089±2
	inert gas	micro	DTA	1104±2

5.2 Discussion

The discussion of this chapter intends to combine the results from size and shape determination, RT characterization and high temperature investigation to explain the size-, temperature- and atmosphere-dependent behavior of bismuth oxide nanoparticles in the solid-state regime.

5.2.1 Room temperature

The results show that the synthesized particles are mainly mono-crystalline, mono-disperse and spherical, which is important for the size-dependent studies in the following chapters. High resolution images show that the spherical shape is actually slightly faceted due to the surface planes of the crystallite. At constant temperature in the sintering furnace the largest size, 48.8 nm (fig. 14), was not perfectly densified to spherical particles. A higher sintering temperature or longer sintering time would have been necessary to achieve the same shape like the smaller particles. This demonstrates the influence of size on the coalescence process [30] and is a first hint to the size-dependent behavior of these oxide particles. Otherwise the results of size and size-calibration are unambiguous.

The stable structure of bismuth oxide nanoparticles at RT under oxidizing, inert and slightly reducing (vacuum) conditions is the tetragonal β-structure, which is metastable in the bulk. Interestingly, Jovalekic´ et al. [72] while mainly describing the stabilization of β-Bi_2O_3 at RT by additions of ZrO_2 mention that the Bi-O had to be in a very fine-grained, nanocrystalline state. Moreover quenching, which has been reported as process to stabilize the β-phase [158] tends to produce very fine-grained microstructures. These are possible hints that also in polycrystalline bulk the size of the crystallites plays a role in stabilizing this phase. Generally, size-stabilization is a common process in oxide materials and has been reported for e.g. alumina, zirconia and titania by Navrotsky et al. [18]. Due to the surface contribution the total free energy of the material is altered at the nanoscale; if the contribution gets strong enough high temperature or metastable phases with lower γ_{sv} can become favorable at RT (chap. 2.3). So it can be assumed that the surface energy of β-Bi_2O_3 is considerably lower than the one of the α-phase. But the hypothesis can not be verified since no γ_{sv} values for any bismuth oxide structure are known. Only values for the melt were reported [93].

Moreover, surfaces with their oxygen vacancies or unsatisfied bonds tend to adsorb water and bind hydroxyls, carbonates and/or oxygen to reduce their surface energy (see chap. 2.1) and further stabilize the system. This also seems to be true for bismuth oxide: Under heating in DTA-TG-MS O, O_2, C, CO_2 and some other species are released into the gas phase. Different oxidation states in the O1s peak, an over-stoichiometric amount of oxygen and a C1s line in XPS also indicate the presence of carbon and oxygen containing groups. The spectroscopic study by Barreca et al. [80] discovered a carbonated surface at RT. This is typical for oxides which can form carbonates (e.g. bismutite, $Bi_2O_2CO_3$). The other way round β-Bi_2O_3 is the phase that forms from decomposition of $Bi_2O_2CO_3$. Even on α-Bi_2O_3 surfaces layers of the β form were found after surface-carbonate decomposition. In this context the ordered oxygen vacancies in β-Bi_2O_3 play an important role [80, 71]. So carbonized bismuth oxide and the β-structure seem to be linked; on the surface as well as in the bulk. This makes the β-phase even more favorable for nanomaterials with their large surface area. On the other hand, hydroxylation by aging at RT in humid air is also possible. This can be seen in the diffractogram of the commercial nanopowder (fig. 15b). The same powder could also easily be hydroxylized by ultrasonic treatment in water within minutes. Already in 1964 Levin et al. [158] reported the formation of a bismuth carbonate (bismutite) and an unknown, not described phase as aging effect for micron-powder. But bismutite could not be observed for the nanopowder. While the exact processes are not clear one can conclude that bismuth oxide has a carbonated surface and is reactive under atmospheric conditions. So it should be sealed for storage to avoid compositional changes.

5.2.2 Solid state transitions

When discussing the heating experiments, it is important to recall that compacted, agglomerated powders and no independent particles were used. Hence, the particles have two kinds of interfaces: Surfaces in contact with the surrounding gas and grain boundaries between neighboring particles. This alters the total surface/interface energy compared to free

particles. By heating such samples, sintering will begin prior to melting and when reaching the melting point a densified, coarse-grained bulk will have formed. Such experiments are not helpful for investigating melting and evaporation behavior of nanoparticles but only to learn about solid-state properties of agglomerated nanopowders. By combining the findings from the calorimetric and the diffraction measurements one gets a consistent picture of the phase transitions of agglomerated bismuth oxide nanopowder. The only transition related to nanomaterials is the $\beta \rightarrow \alpha$ transition. So this is the only one important in the context of this work. The usual solid state bulk transitions are listed in table 4 but will not be discussed here and the atmospheric influences on melting and evaporation of nanoparticles are discussed in the respective chapters of this work.

Two unexplained peaks exist in the caloric curve of figure 19(a). Both of them are considerably lower than any observed melting temperature in this work (more details about melting will follow in chapter 7.1). Therefore, a melting and solidification process as described by Schierning et al. [159] can not be the explanation for the alternating exo- and endothermic events. The first minimum is at 588 K. No structural changes were observed but the mass decreased strongly in this region, accompanied by a rise of the C, CO_2 and C_2H_6/CH_2O concentrations. A lowered sample mass corresponds to a smaller signal in DSC. So a sudden mass loss leads to a falling signal, which could erroneously be interpreted as exothermic process. The following region of a steadily rising DSC signal includes the region of particle growth (fig. 21) which is usually preceded by neck formation and densification. These first sintering stages could not be detected by XRD. Hence, the observed rise is due to sintering of the sample. It is accompanied by further evaporation of more strongly bound oxygen and carbon containing species. This can lead to an elevated signal, too.

At T_{tr} = 738 K the phase transformation from the β-phase of the nanoparticles to the bulk α-phase takes place. This transition can only occur in the nanopowder and its summarized features are:

1. The peak has the typical shape of an exothermic phase transformation (fig. 19(a)).
2. The crystallite growth increases rapidly up to the point of phase transition, yet different sizes and temperatures were measured in different atmospheres (fig. 21).
3. A slower heating rate produces larger particles at T_{tr} (section 5.1.3 on page 56).
4. β-Bi_2O_3 remains stable up to the melting point in free nanoparticles between 7 and 50 nm (chap. 7).
5. Along with mass loss O, O_2 and C_2H_6/CH_2O reach their maximum concentration and drop abruptly after the sample has fully transformed (fig. 19(b)).
6. Between 663 and 763 K bulk bismutite switches from decomposition to β-Bi_2O_3 to decomposition to α-Bi_2O_3 [158, 160] and in the same temperature region surface carbonate conversion to pure Bi_2O_3 surfaces takes place [80].

This set of information together with the preceding findings is interpreted in the following paragraph and a graphical explanation is given in figure 22.

β-Bi_2O_3 nanoparticles are stabilized in this form because of a presumably low surface energy making the total free energy lower than the one of α-phase nanoparticles of the same size. The size-dependent chemical potentials change with $1/D$ (eq. 20 in chapter 2.3). At a certain, critical size ($D_c(T)$) where $G(\beta) = G(\alpha)$ the $\beta \rightarrow \alpha$ transition can occur (blue square). Below this size β-Bi_2O_3 is always stable. The ability of β-Bi_2O_3 to bind carbonate groups further lowers the surface energy and acts stabilizing. Therefore the critical size ($D_{c,c}(T)$) for $G(\beta_{carbonated}) = G(\alpha)$ should be larger (orange square). According to the results, particles $\gg$ 100 nm can be stable with a carbonated surface. But ultimately also a carbonated β-Bi_2O_3 particle should transform to α. Above that size α-Bi_2O_3 is always stable. When the nanopowder is heated the particles grow by sintering and enter region (b) of figure 22, where they are only stable because of their carbonated surface. At the temperature of bullet point 6 which corresponds to the measured transition temperature, 735 K, they loose their carbonate layer which increases γ_{sv}. Thus at the given set of T and D they move from the orange to the blue intersection and suddenly $D > D_c$. Consequently, the transformation to the α-phase occurs together with the vaporization of the carbon and oxygen containing species. It also makes plausible how different sizes

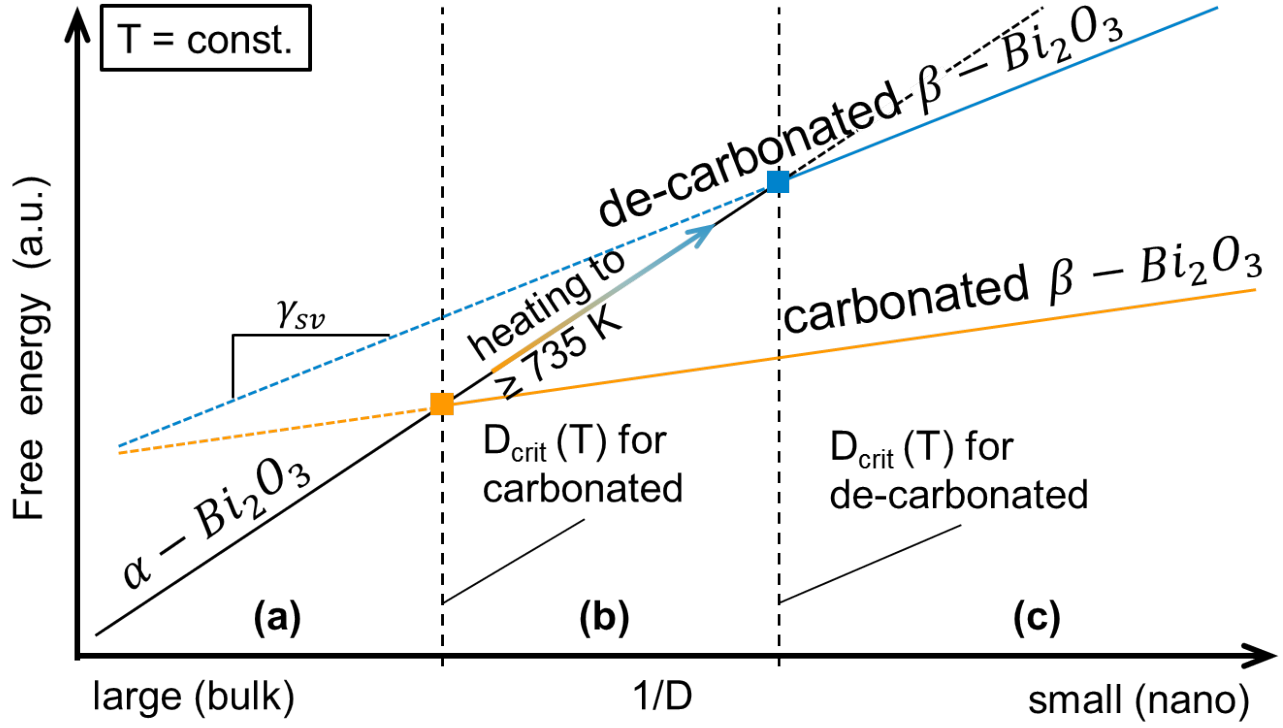

Figure 22: Scheme of the postulated stability diagram at constant T in attempt to explain the $\beta \rightarrow \alpha$ transformation. No units and values are given as it is a qualitative illustration. A phase transformation occurs at $G(\alpha) = G(\beta)$ which depends on the slope of the curves. This in turn depends on the surface energy of the phase. As carbonization decreases γ_{sv}, the critical size is larger for carbonated than for de-carbonated β-Bi_2O_3. In region (a) α-Bi_2O_3 is always the stable form. In the intermediate region (b) β-Bi_2O_3 is stable below and α-Bi_2O_3 above the temperature for de-carbonization (~ 735 K). Region (c) is the absolute stability region of β-Bi_2O_3.

can transform around 735 K. Separate particles in the TEM which are not able to grow remain below D_c and rest in the β-phase until they melt. Apparently, this model is able to explain all observed phenomena but ought to be put on a more sound basis by a systematic, size-dependent/ heating rate-dependent study. The transition temperature in vacuum is higher than in the other two atmospheres. As only HT XRD measurements could be performed in that atmosphere (chap. 4.2), the information is limited. An explanation could be that the lack of heat conduction through the gas causes the actual temperature in the sample to be lower than the measured temperature of the heating stage. In that case the powder would also experience a slower heating rate which could explain the larger size in figure 21 as well. The critical size at RT is an interesting value. According to eq. 43 the correct critical size at RT is smaller than the measured critical size at 738 K, just like the $T_m(r)$ becomes lower for smaller sizes. For a qualitative statement the parameters in eq. 43 would have to be known. After this size-dependent nano-phase to bulk-phase transformation the initial nanopowder behaves like Bi_2O_3 micron-powder with the regular transition temperatures.

6 Evaporation of Bi_2O_3 nanoparticles

Three important issues are treated in this chapter: Firstly, assessment of the improved method to analyze the evaporation behavior of nanoparticles. Secondly, an attempt to understand the vapor system of bismuth oxide. Thirdly, the surface energy and size-dependent evaporation of the nanoparticles.

6.1 Results

The thermodynamic properties γ_{lv} and $\triangle_v H$ were determined by fitting a dynamic evaporation model to the measured size-changes in the evaporation chamber with a dwell time of 2 sec. This took place in an atmosphere of 90 % N_2 and 10 % O_2 at 10^5 Pa. Different initial particle sizes were used and the temperature was raised in steps. As an example figure 23 shows the measured mode of the particle size distribution in an experiment with 47 nm particles. Important for the evaporation is the region behind the dashed line where particle size starts to decrease due to evaporation from the surface. The method described by Nanda et al. [27] gave 1080 K as onset temperature for evaporation. For the analysis method used in this work (chap. 4.3) the experimental shrinkage rate was calculated by

$$\frac{\triangle D}{\triangle t} = \frac{\left|D - D_0\right|}{\triangle t} \tag{73}$$

where $\triangle t$ is the dwell time, D_0 is the initial particle size and D the respective value in figure 23. Both analyses were done for all 5 initial sizes.

In addition to the experiments, calculations of the dynamic evaporation of particles over time were performed at constant temperature. This was done by numerically solving the differential equation 68. Examples of a 6 and a 47 nm particle are shown in figure 24. Owing to the smaller volume the smaller particle has fully evaporated at lower temperatures. Furthermore, the Kelvin effect (eq. 13 on page 10) leads to higher vapor pressures and self-reinforcing evaporation at small sizes, hence bending the curve downwards.

This model was applied to calculate the final sizes depending on γ_{lv} and $\triangle_v H$. The average shrinkage rates according to equation 73 were calculated and compared to the experimental values. The surface energy is responsible for the differences in curving upwards between the 5 sizes in figure 25(a). Therefore, it could be determined by fitting the model to the measurement values (black lines). The average value of $\gamma_{lv} = 0.13 \pm 0.04$ J/m^2 did not fit perfectly to every size. Inaccuracies in the measurement method as well as changes in the material properties could be responsible for that. On the other hand, the onset method by Nanda et al. yielded $\gamma_{lv} = 2.08$ J/m^2 which is unrealistically high. With $\gamma_{lv} = 0.13$ J/m^2, $\triangle_v H$ was determined by a fit to the slope of the vapor pressure curve in figure 25(b), resulting in 185 $\pm$ 15 kJ/mol. Apparently, the little changes in the 6 and 8 nm samples lead to high uncertainties. The dashed line from Sidorov et al. [85] comes from a mass spectrometry (MS) study in 1980 and will be subject of the discussion (chap. 6.2 on page 67).

Evaporation of separate nanoparticles was observed in the TEM. However, rapid cooling directly after melting showed, that the particles were metallic bismuth and had been deprived of all oxygen in the molten state (chap. 7). Some further hints about evaporation of agglomerated and sintered nano- and micron-powder in different atmospheres were revealed by calorimetric and HT XRD experiments. One DTA-TG experiment with nanopowder in a carbon crucible was performed in inert gas. It did not show any changes in the transition temperatures, but mass loss started after the $\alpha \rightarrow \delta$ transition and increased drastically after melting (fig. 26). A droplet of bulk Bi was left after the experiment, so the entire oxygen had evaporated from the sample. HT XRD in vacuum showed similar results: From a rapidly diminishing reflex intensity after the $\alpha \rightarrow \delta$ transition and bismuth reflexes after re-crystallization, one can assume that the same reduction and

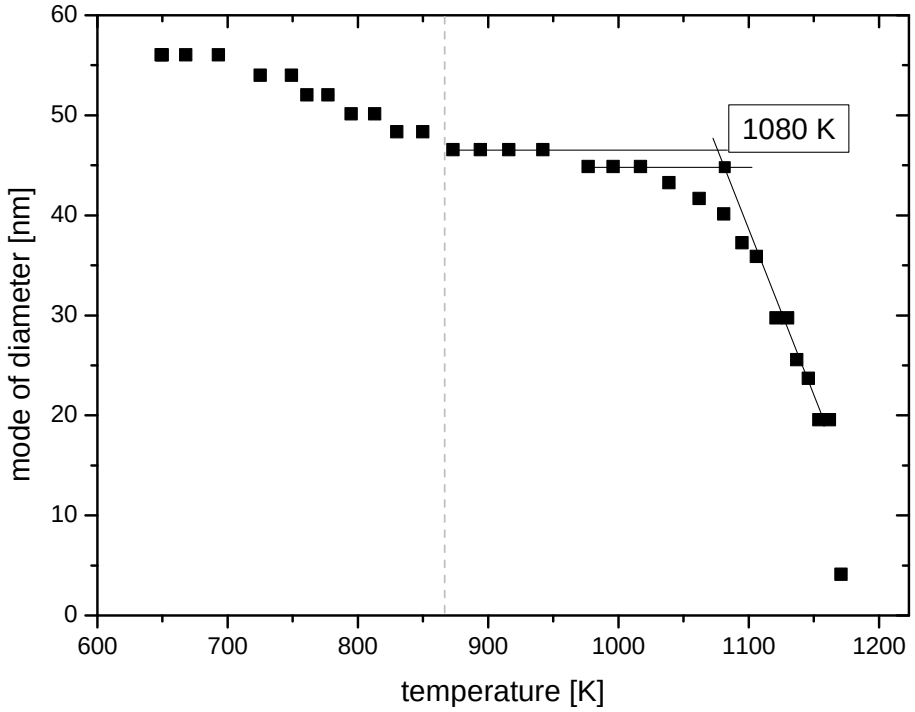

Figure 23: Example of evaporating Bi_2O_3 nanoparticles with an initial size of 56 nm in 10 % O_2, 90 % N_2 at 10^5 Pa. This curve is special because there are two regions of size-change (divided by the dashed line). Usually the size remains constant up to the onset of evaporation. Here the first drop at 700 K comes from sintering of the agglomerated particles to dense shapes. The second region is caused by evaporation. The cross-over of the two tangential lines marks the defined onset-temperature for evaporation according to the method described by Nanda et al. [27].

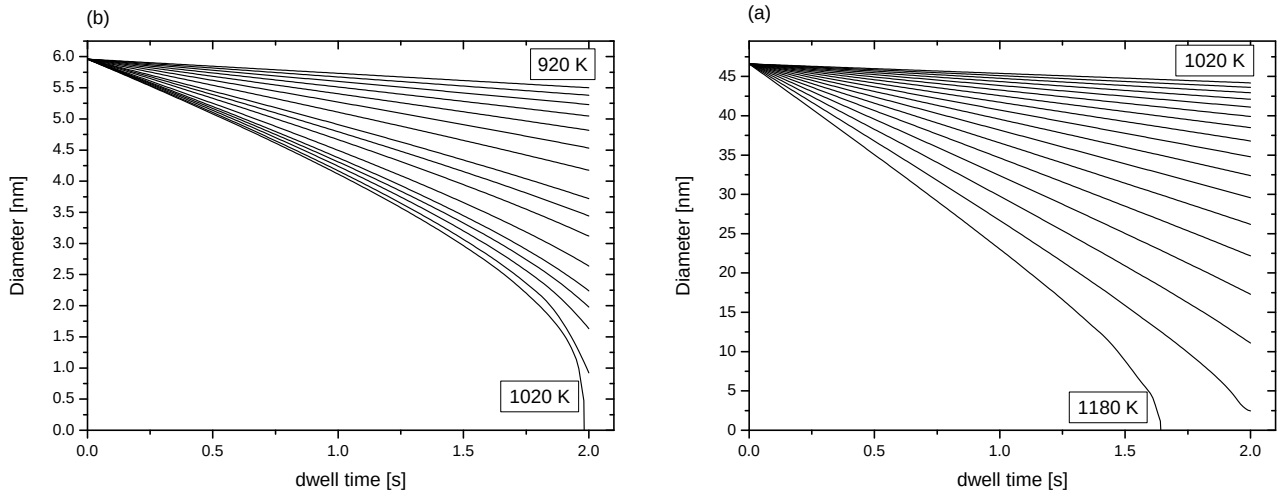

Figure 24: Calculated shrinkage caused by evaporation of a particle with 6 nm (a) and 47 nm (b) initial size. During the dwell time in the evaporation chamber the particles shrink. From top to bottom the temperature is raised and shrinkage increases non-linearly with T. The bending of the curves is caused by the Kelvin effect at small sizes which self-reinforces the evaporation. The measurement setup can only measure the initial and final size at 0 and 2 seconds, not the process in-between.

evaporation process took place in vacuum. No such mass loss and material changes happened in air and inert gas at ambient pressure up to 1180 K.

6.2 Discussion

Important points to treat in this discussion are (1) if the measurement method and the analysis method are suitable to probe the evaporation behavior of inorganic nanoparticles, (2) how the bulk vapor pressure and $\triangle_v H$ of bismuth oxide behaves with changing temperature and atmosphere and (3) if the Kelvin equation with γ_{lv} can be applied to the evaporation of (bismuth) oxide nanoparticles.

Size-dependent evaporation method

Two processes lead to size changes in figure 23. Between 700 and 900 K the large agglomerates (fig. 14, 48.8 nm) change their shape to dense, spherical particles. While this does not change the volume it goes along with a reduction of the mobility equivalent diameter measured in the DMA. The shape change could happen by diffusion or even a melt-crystallization event, but a sheer size measurement can not differ those mechanisms. Merely, melting could be expected to cause a more abrupt size change at the melting temperature instead of a stretched transition. In the second region above 900 K evaporation sets in. As temperature has a $e^{-1/T}$ influence on the evaporation rate, the size changes ever faster at increasing temperature until the particles fully evaporate within the dwell time in the heated region. This dynamic process is reduced to an onset-temperature by the evaluation method of Nanda et al. which resembles the analysis of thermodynamic phase transformations in calorimetric measurements. The determined value of γ_{lv} was unrealistically high and as recognized by others [9] this generally seems to be the case for this onset method. In this work the evaluation of the data via a fit of the dynamic evaporation process gave more realistic values. Though, the theory requires the particles to be much smaller than the mean free path in the aerosol for the kinetic theory to apply. A further advantage of this evaluation is that the surface energy can be determined for each size separately, if the vapor pressure function of a material is known exactly. Thus, size-dependent changes of γ_{lv} could be measured. This was not possible in this work, because the bismuth oxide vapor in air is not known. It had to be approximated by the Clausius-Clapeyron equation with $\triangle_v H$ as additional fit parameter. Independent of the evaluation method, the measurement has some advantages. Firstly, free particles without influence of a substrate or a matrix are measured. Secondly, different atmospheres can be used - most important for oxides: also ambient-like conditions. The measurement sensitively depends on an accurate determination of the initial and final particle size. In this work the sizes were calibrated with TEM (chap. 5.1.1). The fact that the temperature distribution in the heating chamber is only approximated by the maximum value in the middle also induces some error. Both problems could be reduced by a specifically adapted setup.

Vapor pressure of bismuth oxide

The evaporation behavior of oxides in general is complicated and not sufficiently understood in many cases, including bismuth oxide. The focus of this work was not to investigate the temperature- and atmosphere-dependent gas species of the bismuth oxide vapor - other methods such as a special Knudsen-Cell MS would be necessary for that. However, a certain understanding is necessary since the peculiarities of nanoparticles are always based on the bulk properties. No sufficient or even quantitative answer to the multi-component vapor of bismuth oxide can be given here, but an attempt is made to interpret the observations consistently. Experimental-wise this section is important to receive a proper baseline for analyzing the size-dependent behavior in a second step.

A number of facts about evaporation of bismuth oxide seem important:

1. Under atmospheric pressure Bi_2O_3 is stable at least up to 1350 K [87].
2. If the oxygen partial pressure is high enough, almost exclusively oxidic gas components are present - mainly $(Bi_2O_3)_x$. Below approx. 200 Pa mainly metallic Bi_x components form (at least from laser vaporization) [88].

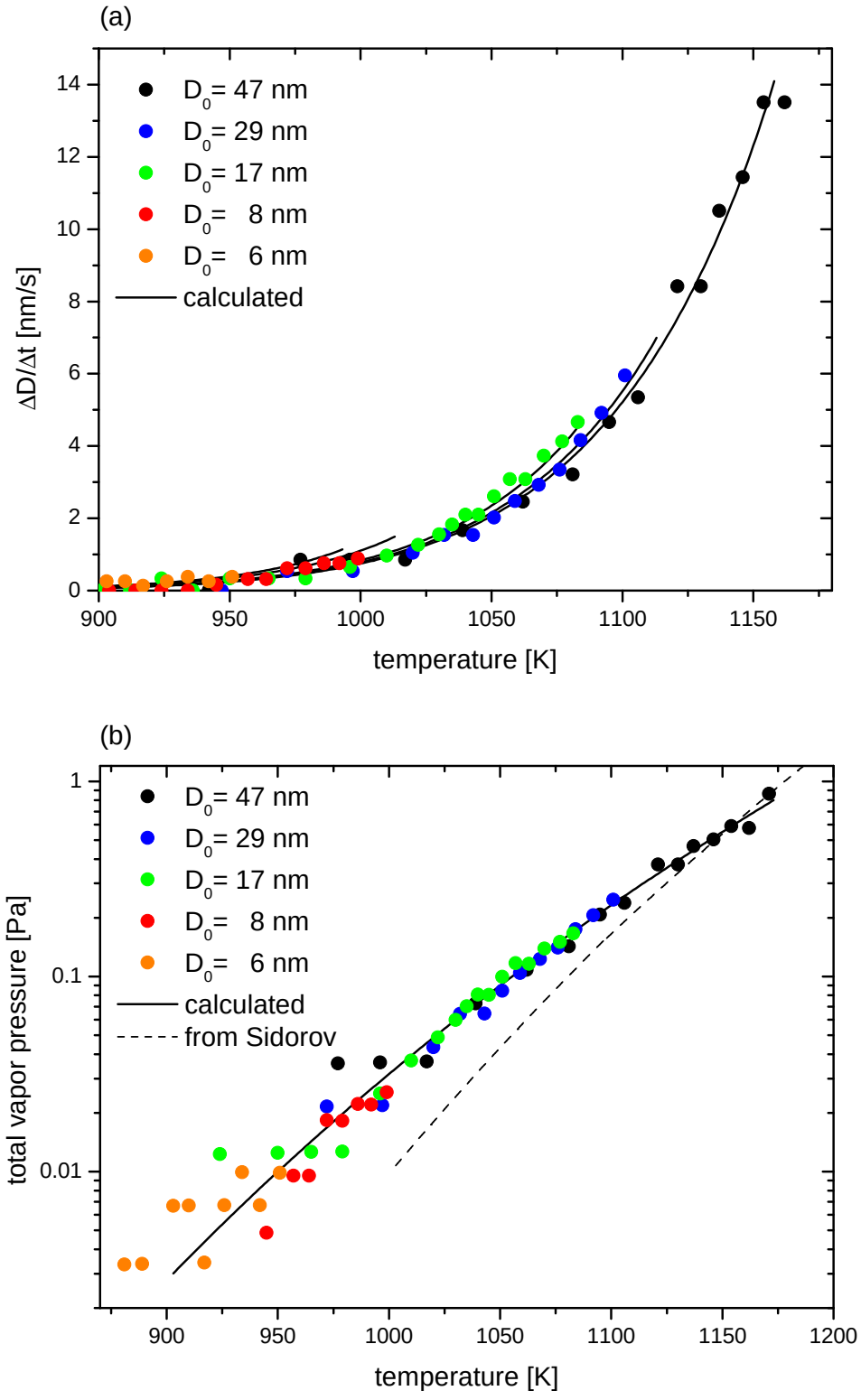

Figure 25: (a) Evaporation rate given as rate of diameter change with a dwell time, $\triangle t$, of 2 sec. Different colors are different initial particle sizes. The black lines indicate the simultaneous fit to extract γ_{lv} as the only unknown parameter that causes size-dependent changes. The fit gave an average γ_{lv} = 0.13 $\pm$ 0.04 J/m^2. (b) Vapor pressure curve of bulk Bi_2O_3 determined from dynamic evaporation calculation of Bi_2O_3 nanoparticles. The slope renders a $\triangle_v H$ of 185 $\pm$ 15 kJ/mol averaged over all species. The dashed line is a function for the total vapor pressure from a Knudsen-Cell MS study [85].

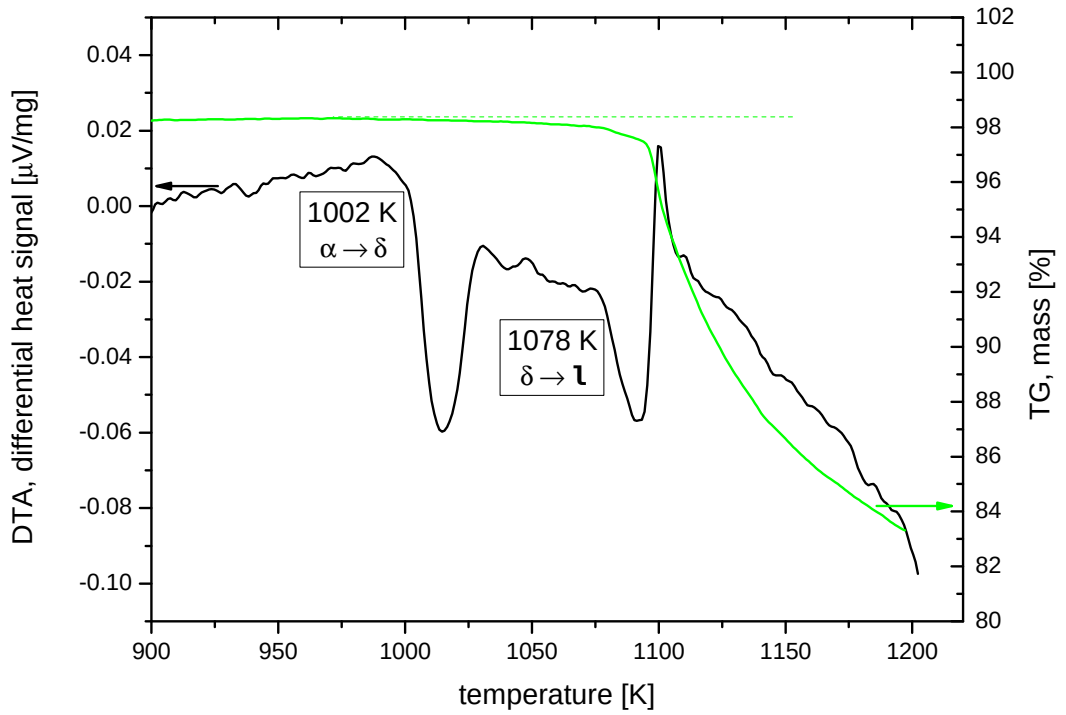

Figure 26: DTA-TG measurement of bismuth oxide nanopowder in a carbon crucible under inert gas. The $\alpha \rightarrow \delta$ and melting transition temperatures are unchanged, but a mass loss sets in after the transformation into the δ-phase and drastically increased in the molten state.

3. In the MS studies [83, 84, 85, 91] the only or dominant species were always Bi and O_2 and the most recent study reported massive oxygen loss in the beginning of the each Knudsen-Cell experiment - even in the solid state [86].

4. Under vacuum, e.g. at low total and oxygen partial-pressure, liquid and solid δ-Bi_2O_3 are not stable. Mainly oxygen evaporates. Probably the high oxygen mobility enables its easy escape. The composition for congruent evaporation in the solid state is oxygen deficient [87, 86, 75, 91].

The results of this work (chap. 6.1) support this summary of literature. Moreover, they show that liquid bismuth oxide reacts to metallic bismuth under moderately reducing conditions. Therefore, it seems clear that the Knudsen-Cell MS studies investigated a non-stoichiometric bismuth oxide. The following basic evaporation / decomposition reactions can be conceived.

$$Bi_2O_3(s,l) \rightarrow (Bi_2O_3)_x(g) \tag{74}$$

$$Bi_2O_{3-x}(s,l) \rightarrow 2Bi(g) + (3-x)/2\,O_2 \tag{75}$$

The reduction reaction 75 depends on the oxygen partial pressure and is therefore increased in vacuum. On the other hand, the congruent evaporation 74 does not have any $p(O_2)$ dependence. This explains, why mainly Bi and O_2 were measured with MS and $(Bi_2O_3)_x$ was dominant at higher oxygen partial pressures. Conclusively, one can assume that the total vapor pressure and composition reported in MS studies will differ from the state in the ambient conditions of the experiment in this work.

The dashed vapor pressure curve in figure 25(b) comes from a MS study by Sidorov et al. [85] and the solid line is the average, total vapor pressure of this work - approximated by the Clausius-Clapeyron equation. The enthalpy of evaporation of Sidorov et al. is higher (approx. 245 kJ/mol) which can be explained by the compositional difference discussed above. The enthalpies of sublimation/evaporation of Bi_2O_3 (reaction 74) and Bi_4O_6 are 277/237 kJ/mol and 234/156 kJ/mol, respectively. The enthalpy of reaction 75 with stoichiometric Bi_2O_3 is 976/946 kJ/mol. The values for the formation of oxidic species are in the same region as the measured 185 ± 15 k/mol, which indicates molecular evaporation of bismuth oxide under ambient-like conditions. MS measures the thermodynamically stable forms of the gases effusing from the Knudsen-Cell (chap. 2.6.2 on page 21). Therefore, it is possible that molecular $(Bi_2O_3)_x$ evaporates in the cell, on the surface and decomposes to Bi and O later on. This was already adumbrated by Sidorov et al.. The vapor pressures from this work are higher than Sidorov's values. Apart from the mentioned sources of error and compositional differences it is possible that this is caused by the assumption $p = 0$ in equation 68. If $p > 0$ this would decrease p_s proportionally.

Another observation is that the rate of evaporation is significantly higher in vacuum. A low oxygen partial pressure at constant total pressure in pure inert gas does not have this effect. Consequently, the absolute pressure and / or the actively pumping vacuum are responsible for the increased rate. Reference [90] proposes an argument of kinetic hindrance: Because of fewer collisions under low pressure the molecules can escape more easily. An actively pumping vacuum keeps the partial pressure above the surface constantly low. The evaporation rate is higher, the lower p, because the driving force for evaporation is $p - p_s$. Hence, the active vacuum prevents equilibration ($p = p_s$) and thus keeps the rate of evaporation at a maximum value. These two explanations do not exclude each other and probably both contribute.

Kelvin equation and surface energy

After the general evaporation behavior of bismuth oxide its size-dependence on the nanoscale will be discussed now. Under constant molar volume it results solely from the surface energy γ_{lv} in the Kelvin equation (13). The measured average value of 0.13 ± 0.04 J/m^2 is lower than the only reported literature value of 0.217 J/m^2 at 1123 K. This was measured by Fujino et al. with the ring method [93]. They also reported a linear temperature dependence of $\partial\gamma/\partial T$ = -2.1·10^{-5} J m^{-2}K^{-1}. At 1023 K, the average temperature for evaporation of the nanoparticles, γ_{lv} would be 0.219 J/m^2. For such a large difference measurement errors discussed in the previous sections are one possible explanation. Assuming a correct measurement the other reason is that different properties are probed by the two methods. The ring method measures the maximum force when a platinum ring detaches from the surface of liquid bismuth oxide. It probes the surface stress which is a purely mechanical property. On the other hand, surface energy is defined as the excess energy occurring due to the existence of a surface. Generally, surface stress and surface energy are said to be the same in a liquid (chap. 2.1) because they can not withstand shear stress. This statement however, is based on theoretical considerations only. γ_{lv}, as it is determined with the presented method, comes directly from evaporation of gas components on the nanoparticles' surface. Thus, it is a measure of how hard it is to remove these molecules or atoms from the surface. This is a different process than the above definition of an excess state. Ouyang et al. treat this topic with an own model for γ_{sv} and γ_{lv} [9]. In this light it is possible that the different values occur, because different surface-related properties are probed with the different methods. Due to lack of better knowledge or ambiguous nomenclature they are described by the same term.

Closer inspection of figure 25(a) shows that γ_{lv} = 0.13 J/m^2 underestimates the curvature for large particles and overestimates the curvature of small particles. Within the evaporation model this is explained by a variable γ_{lv}. A temperature-dependence, as well as a size-dependence would be possible. According to Eötvös rule for the temperature-dependence of γ_{lv}, it increases with decreasing temperature. This would cause a trend opposite to the observed direction. A size-dependence of γ_{lv} with the correct trend was predicted by Toleman [137]. So a size-dependence of γ_{lv} would be possible. But the uncertainty of the present measurement with the unknown vapor-pressure function does not allow definite statements. Instead, the differences of the values are included in the error of ±0.04 J/m^2. Within this uncertainty the Kelvin effect is valid for the evaporation of bismuth oxide nanoparticles.

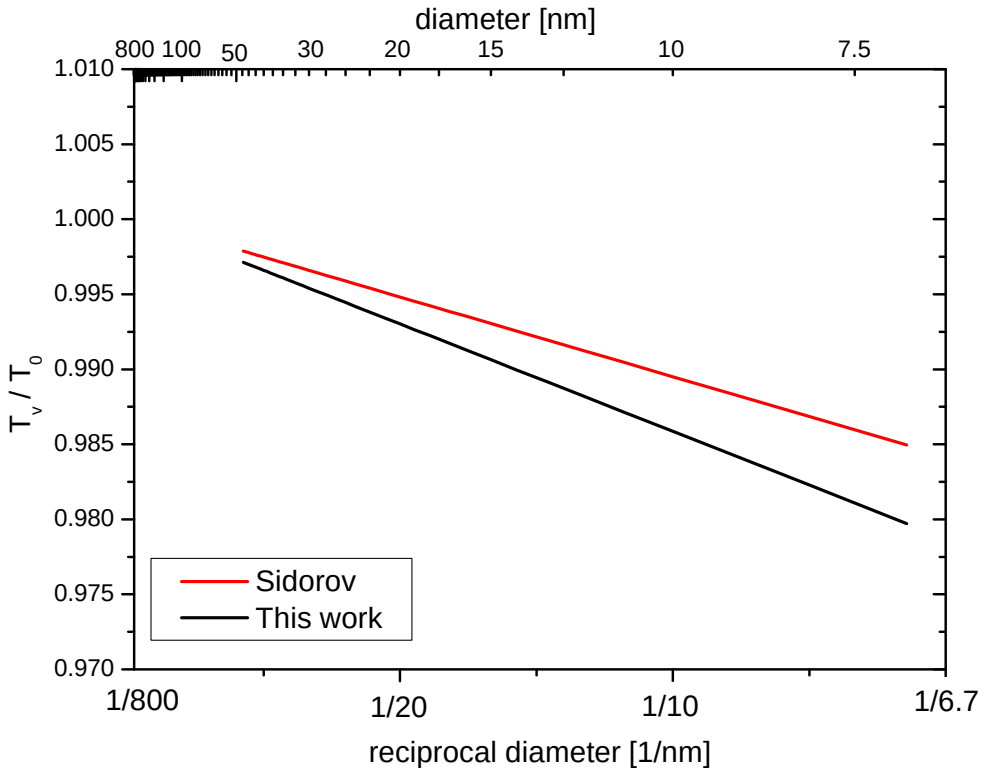

Figure 27: 2D T-D phase diagram showing isobar lines of the normal pressure. γ_{sv} = 0.13 J/m^2 was used with two different vapor pressure functions, one from this work and one from Sidorov et al. [85]. The boiling temperatures are normalized to the bulk value and only plotted for the size region of the investigated particles.

The determined values of γ_{lv} and $\triangle_v H$ were used to calculate the size-dependent normal vapor pressure function. From equations 12 and 13 T_v was calculated as follows:

$$T_v = \frac{\triangle_v H - 4\gamma_{lv} v_m / D}{\triangle_v H / T_1 - R ln\left(p_v / p1\right)} \tag{76}$$

T_v and p_v belong to the boiling point and T_1 and p_1 come from a known P-T point in figure 25(b). The T_v-D plot can be seen in figure 27. The lines are isobares for normal pressure. Because of the different vapor pressure functions of Sidorov et al. and this work, leading to different bulk boiling temperatures the isobars were normalized to the bulk value. In both cases γ_{lv} = 0.13 J/m^2 was used. As T_v changes proportionally to $1/D$ and γ_{lv}, a line with the slope proportional to γ_{lv} results in a reciprocal plot. Because of the low value of γ_{lv} the size-effect of boiling point reduction is small. This statement holds, independent of the vapor pressure function.

In summary, the method of measuring and simulating the shrinkage rate to analyze the surface energy of bismuth oxide works, but a specifically developed setup could enhance the results considerably. Problematic was the unknown and complicated equilibrium of numerous bismuth oxide gas species, which becomes even more complicated under reductive vacuum conditions. Still, the Kelvin equation itself is valid and an average value of 0.13 ± 0.04 J/m^2 was determined for the surface energy of liquid particles between 6 and 47 nm. Due to the low value the boiling point depression is weak.

7 Melting of Bi_2O_3 nanoparticles

The results concerning melting of Bi_2O_3 nanoparticles were mainly obtained by in-situ TEM heating experiments. There is a possibility that these results are not described by a size-dependent melting point reduction but by a size-dependent chemical reaction. For that reason the model for a size-dependent reactions from chapter 2.4 on page 19 will be relevant. Additionally results and findings from the previous chapters will enter the discussion.

7.1 Results

7.1.1 Bismuth oxide nanoparticles

Typical images of particle distributions as they were used for the heating experiments are shown in figure 14. Figure 28 shows SAED images together with the corresponding bright field images as they were captured for each sample at each temperature. These images were selected from a group of images of the 29.7 nm sample to present the most significant changes. The bright field images gave insight into morphology changes during heating and cooling while the diffraction images were used for phase identification and to observe the loss of crystallinity at the melting transition. For that purpose diffractograms were calculated from the rotational intensity as shown in figure 29 as a waterfall graph for some relevant temperatures between room temperature and several degrees above the transformation temperature. The structure was β-Bi_2O_3. The signal intensity was too weak and the adjustments were not optimized for more detailed analyses like evolution of lattice constants or even profile matching. During heating the signal intensity gradually decreased until it vanished eventually. Approaching the transformation temperature the diffraction halos in BF started to disappear. For each particle the change was an abrupt switching from crystalline to non-crystalline. These switchings took place over a temperature range of approx. 30 to 40 K and correlated with the vanishing diffraction intensity in SAED. As combined transformation criterion any diffraction reflex had to be vanished in the diffraction pattern as well as any diffraction halo had to be disappeared in the bright field images. For the illustrated example the melting temperature was analyzed to be 783 K. The other samples transformed at:

1. 6.4 nm: 483 K
2. 8.7 nm: 525 K
3. 16.0 nm: 673 K
4. 29.7 nm: 783 K
5. 48.8 nm: 810 K

For testing the influence of other substrate materials one experiment was performed with 16.0 nm particles on a 10 nm carbon substrate instead of SiN_x. Carbon is known to act as a reducing agent. But the analyzed melting temperature of 678 K agreed well with the value on SiN_x substrate. A striking observation was that approx. 20 K (29 nm sample) or approx. 50 K (8 nm sample) below the transformation temperature the SAED pattern degraded by e-beam illumination. This started after a period of several seconds and after several minutes the sampled region appeared less crystalline or even amorphous. Adjacent regions which were not illuminated still showed crystallinity, though. Hence images close to the transformation temperature were always taken at “fresh” spots of the sample. Waiting for a long time (up to 15 min.) close to T_{tr} did not change the SAED and BF images, so time did not seem to be relevant as long as the region was not illuminated. During the whole heating procedure the particles were not observed to migrate or rotate on the

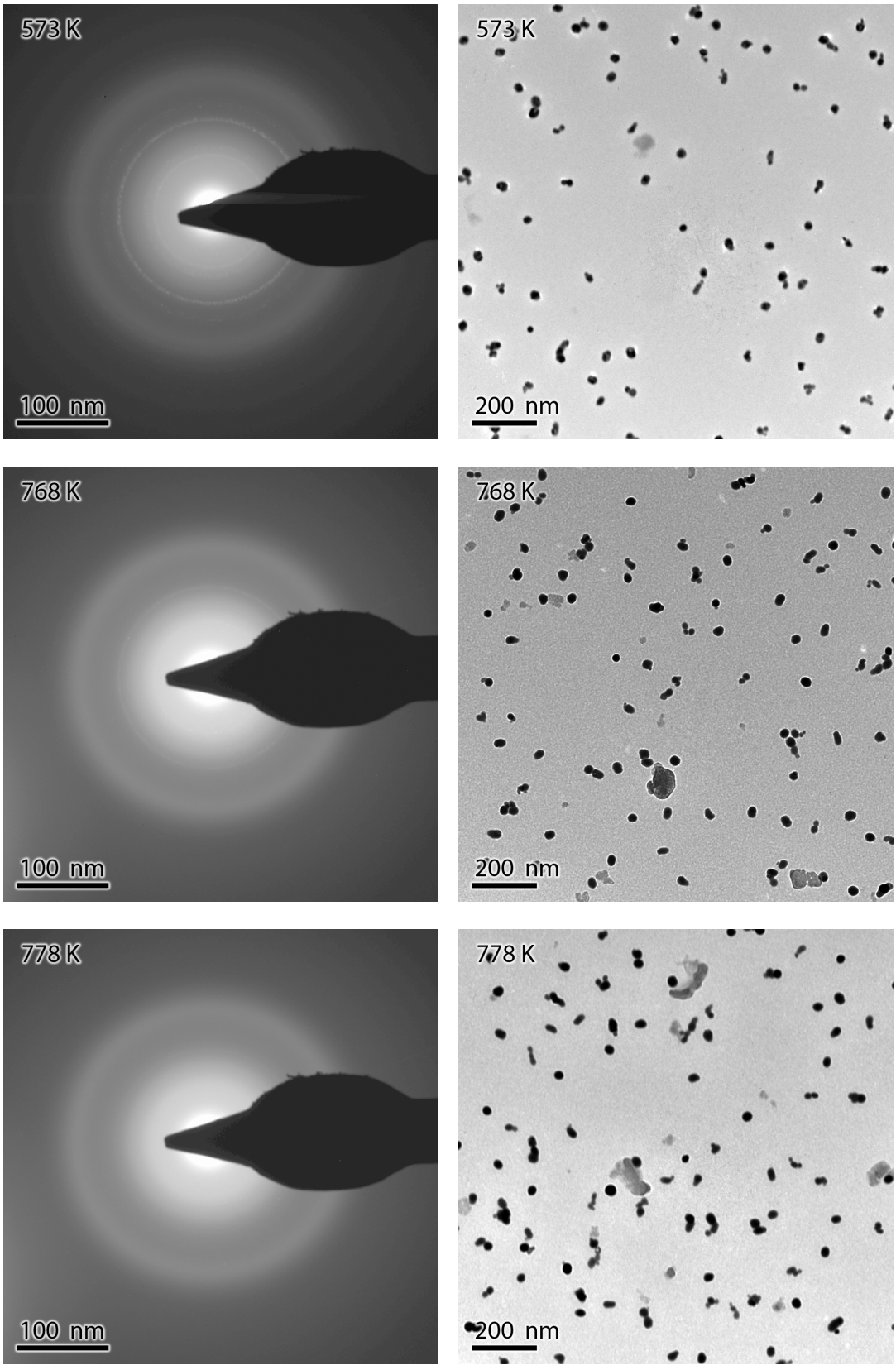

Figure 28: Series of SAED images and corresponding BF images taken without objective aperture. The diffraction rings are well visible at 573 K and numerous particles show diffraction halos. 768 K is very near to the transformation temperature. At 778 K the diffraction rings have completely vanished and no particle shows any diffraction halos anymore.

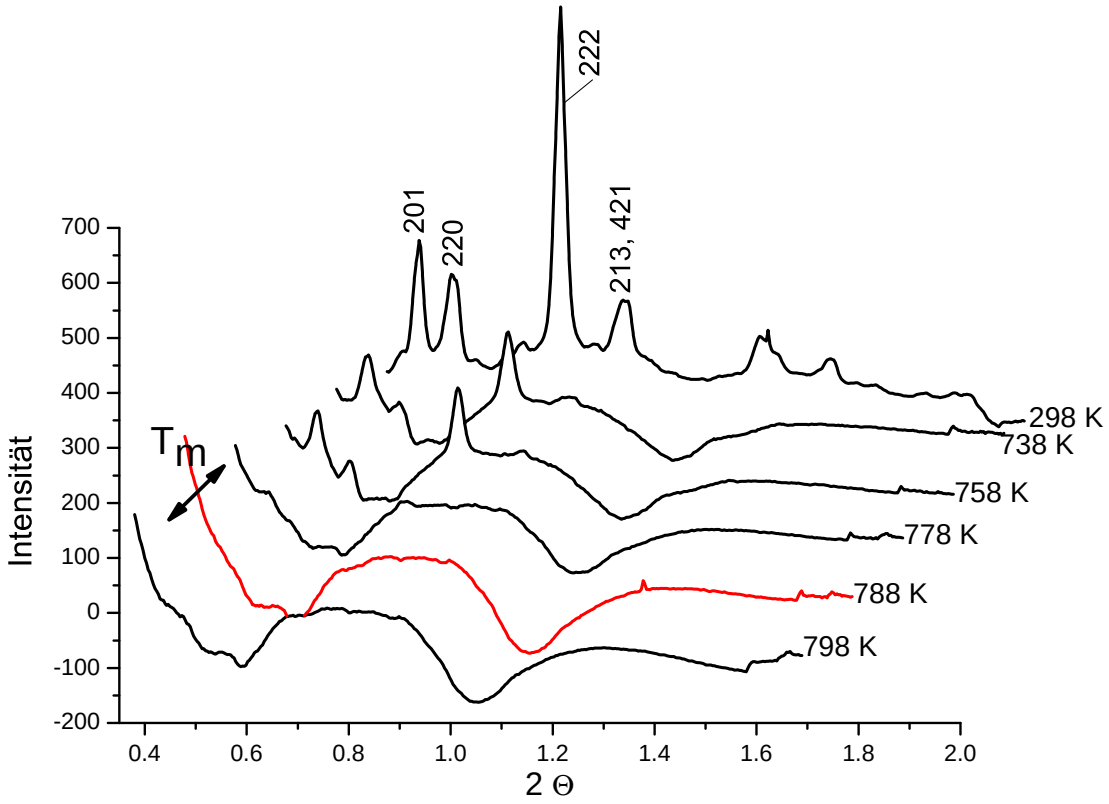

Figure 29: Diffractograms of 29.7 nm Bi_2O_3 nanoparticles from temperature up to T_m. The transition occurred at 783 ± 15 K, when the (222) reflex disappeared and no crystalline particles were visible the imaging mode of the TEM anymore. A standard background pattern was subtracted in this waterfall graph.

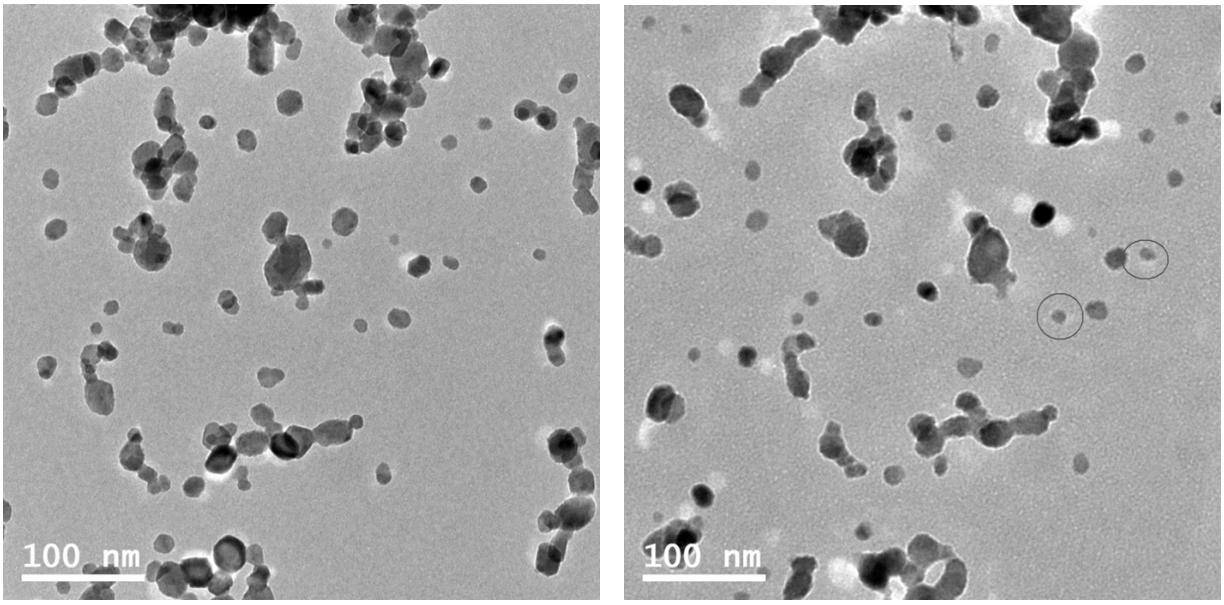

Figure 30: Left: Initial sample before heating (Bi_2O_3). Right: Same sample and spot after the experiment (Bi). Images were taken without objective aperture to have an indicator for crystallinity. No drastic, morphologic changes happened during melting and re-crystallization.

substrate. As can be seen in figure 30, the exterior shape hardly changed during the course of experiment - not even in the second heating cycles. Only the edges had become softer and agglomerates had grown together at the necks. Yet, after a heating cycle the coarser diffraction images and the uniform diffraction halos of former agglomerates showed that inside the exterior shape the matter had coalesced. Some particles appeared darker than others. Those were different ones before and after heating. As this darkening mostly correlated with strong diffraction halos this effect was due to diffraction contrast, but not due to mass contrast. The effect of the e-beam together with temperature steps of 10-20 K near T_{tr} and the error in temperature measurement of approx. 10 K are summarized in an estimated error of 20 - 30 K as indicated by the different error bars in figure 31.

One sample was heated beyond the transformation temperature to observe evaporation. Considerable shrinkage was observed above 770 K for 16 nm particles. This value is only a rough indicator since the magnification was low (29k x), the position on the sample was changed frequently and only the projected area is seen in TEM. The observation of a single 50 nm and a pair of connected 100 + 50 nm bismuth oxide particles during heating ramps (see page 42) lacked the structural information of the above experiments but revealed two important facts: Visible shrinkage due to evaporation was observed roughly at 850 K for both sizes. The movement of matter from one particle to another during tilting of the sample holder was a proof for the liquid state of the matter at 793 K.

An important result from the DTA and HT XRD experiments with the commercial β-Bi_2O_3 nanopowder and α-Bi_2O_3 micron-powder (chapter 5.1.3 on page 56) was that vacuum atmosphere changed the transition temperatures by approx. - 30 $\pm$ 15 K independent of the powder size. Under inert gas atmosphere and in air T_0 corresponded to the literature values. Mass loss in a reducing crucible, indicating evaporation, only started above the regular T_0. Up to the melting point Bi_2O_3 was stable.

Cooling back to room temperature revealed two things. First, the crystallization of the separate particles did not occur until below 398K. Second, analysis of the diffraction patterns of the re-solidified particles revealed that they had become metallic bismuth. As a chemical change occurred along with the transitions the vanishing crystallinity will not be termed “melting” but “transformation” for the time being.

Evaluation of the transformation temperatures as phase transformation

At first, the data was evaluated under the assumption that the particles underwent a regular 1st-order phase transformation from solid to liquid. This hypotheses and the one of a redox - reaction will be treated in the discussion. The size-dependent transformation temperatures are shown in figure 31 plotted reciprocally together with the measured melting temperatures of bismuth nanoparticles and literature values. A least-squares fit of a linear function was performed which is indicated by the black, solid line. The intersection at $1/D = 0$ gave a $T_\infty$of 867 K for the β-Bi_2O_3 phase under the given conditions in the TEM. While the first data points can be fitted by a straight line very well, the smaller sizes, especially the smallest particles with 6.4 nm, accord with the line within the borders of the error range. This might be a hint for a deviation from linearity.

The basic HOG model (eq. 24 on page 13 and 63 on page 36) was applied to test the validity of the melting curve. T_0 was replaced by T_∞. The particles resided in the β-phase but no enthalpy or free energy of this usually metastable phase is known. Thus the value of the bulk transition from δ-Bi_2O_3, 14.7 kJ/mol [64] was used for $\triangle_m H$. The solid molar volume was calculated from two quantities: (a) The average stoichiometry in bismuth oxide under vacuum conditions [86, 157], $Bi_2O_{2.29}$, and (b) the unit cell volume known from x-ray diffraction characterization (see chapter 5.1.2) of 0.338315 nm^3. The thermal expansion coefficient deduced from HT XRD experiments in vacuum in chapter 5.1.3 is $1.24656 \cdot 10^{-9}$ K^{-1}. The final value for $v_m(s) = 4.72777 \cdot 10^{-5}$ m^3/mol at 673 K which was taken to be the fix point. For the same temperature the liquid molar volume was extrapolated from Hwang et al. [92] to be $5.307 \cdot 10^{-5}$ m^3/mol in air and ambient pressure. The γ_{lv} was analyzed in chapter 6.1 to be γ_{lv}= 0.13 J/m^2 for the particles under investigation. No literature values for γ_{sv} are known, so it was used as a fit parameter to match the black line in figure 31. The resulting value of 0.3 J/m^2 can be judged by comparing with other oxide materials. The value is of course subject to a high uncertainty caused by the propagation of uncertainties of the other estimated parameters. It is a very rough estimate that should not be mistaken as real material property but rather considered as quantity for further discussion. The used

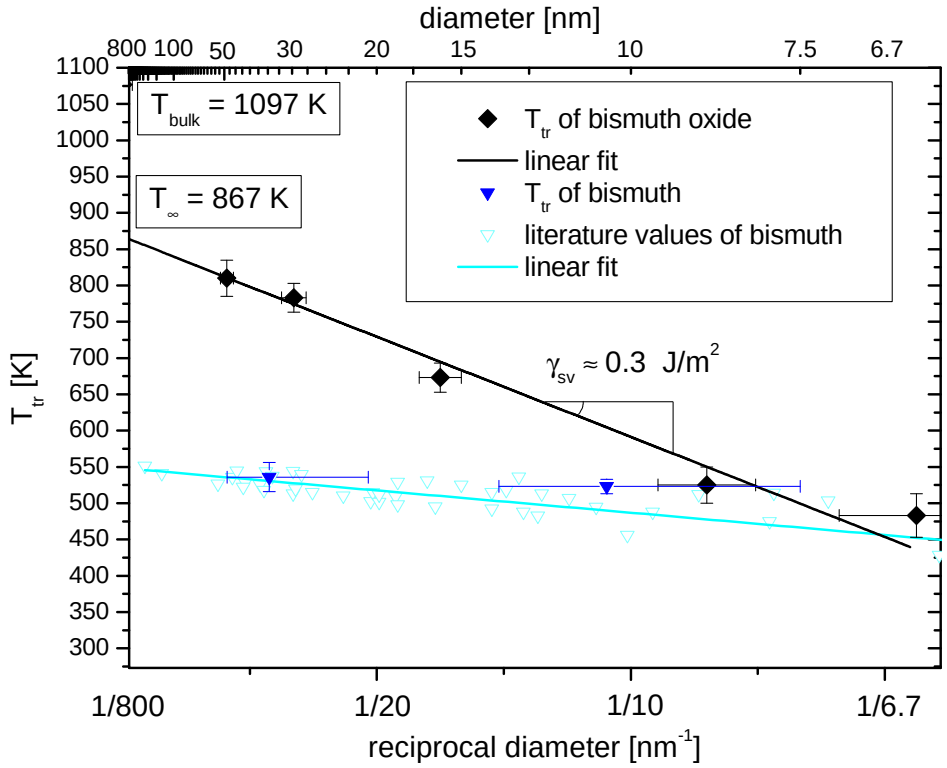

Figure 31: Size-dependent transition temperatures of Bismuth oxide and metallic Bismuth nanoparticles in the in-situ TEM heating experiments. The cyan triangles show literature values of metallic bismuth particles and the blue, filled triangles are values from the second heating cycles of this study (with a broad size distribution). X-error bars are dominated by the size distribution and y-error bars by the transformation region of the particles. The respective best linear fit is shown by solid lines. According to the HOG model the slope of the Bi_2O_3 curve corresponds to a γ_{sv} of approx. 0.3 J/m^2 and the hypothetical T_∞ of β-Bi_2O_3 would be 867 K.

parameters are summarized in table 5 and the validity and accuracy of the chosen values will be discussed in chapter 7.2.1.

Evaluation of the transformation temperatures as reduction reaction

It is important to mention that the transformation took place at temperatures where metallic bismuth is already liquid ($T_0 = 544.55$ K). Hence melting and reduction would be indistinguishable by the applied electron-diffraction method. Therefore the data was also evaluated under the assumption that the particles underwent a full reduction

$$\beta - Bi_2O_3(s) \rightarrow 2\,Bi(l) + \frac{3}{2}O_2(g) \tag{77}$$

This hyopthesis and the one of a pure phase transformation will be compared in the discussion. The size dependent temperature for redox equilibrium was calculated according to equation 53:

$$T = -\frac{3}{2R\,ln(p(O_2))}\left[\triangle_r G_m^\infty(T) + \frac{4}{D}\left(2\,\gamma_{lv}(\mathrm{Bi})\,v_m(\mathrm{Bi}) - \gamma_{sv}(\mathrm{Bi_2O_3})\,v_m(\mathrm{Bi_2O_3})\right)\right] \tag{78}$$

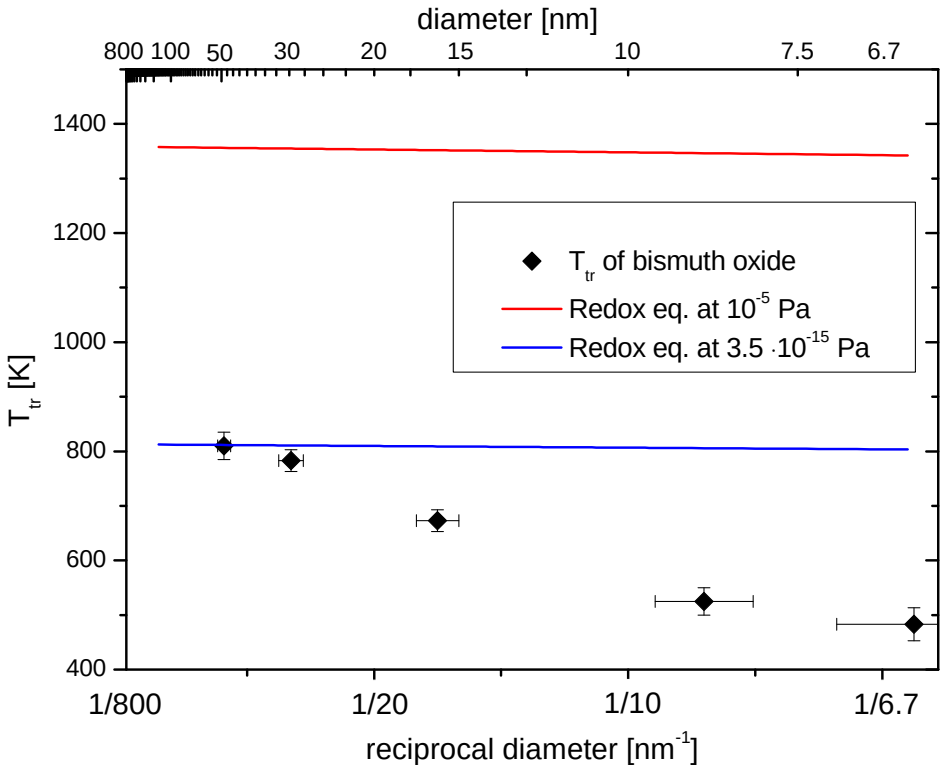

Figure 32: Measured transformation temperatures and calculated size-dependent redox reaction equilibrium of $Bi_2O_3 \rightleftharpoons 2\,Bi + \frac{3}{2}\,O_2$ (calculated at $p(O_2) = 10^{-5}$, $3.5 \cdot 10^{-15}$ Pa). The temperature for equilibrium stability change is much higher than any observed transformation temperature unless the oxygen partial pressure would become as low as 10^{-15} Pa. The size dependence is much weaker than the experimental one.

The required values for the calculation can be found in tables 5 and 6. As bulk Bi_2O_3 does not reside in the β-phase no values for $\triangle_r G(T)^\infty$ are known. But several functions for the bulk phases can be found in literature [157] and the function of Kameda et al. [161, 162] for the δ-Bi_2O_3 was used. The oxygen partial pressure was approx. 10^{-5} Pa. Figure 32 shows that the experimental data could not be matched with reasonable values of $p(O_2)$ and γ_{sv}. The former parameter shifts the intercept with the ordinate and γ_{sv} influences the slope of the line. The $\triangle_r G_m^\infty(T)$ term in equation 78 is large at any temperature and always far above the melting range of bulk and nanosized Bi_2O_3. As the vapor pressure in the denominator is in the logarithm it does not compensate for $\triangle_r G_m^\infty(T)$ - not even for low values in a vacuum chamber. The difference in the round brackets, responsible for the size-dependence, is also small, resulting in a very shallow slope of the line. Ergo, despite a large uncertainty in some parameters the slope of the experimental data could not be rationalized with a size-dependent redox reaction.

7.1.2 Metallic bismuth nanoparticles

When it was clear that metallic bismuth nanoparticles resulted from the first heating cycle, a second heating cycle was used to investigate their melting an re-crystallization behavior as well. As bismuth oxide particles which had been in contact with each other coalesced to bigger units at re-crystallization, the size distribution of the bismuth experiments was much broader and less well characterized. This is reflected by the broad error bars in figure 31. The experiments and analyses were performed in the same way as in the previous section. Figure 33 shows a waterfall graph of diffractograms from ~35 nm particles. The derived melting temperature was 536 K. For the other investigated size, ~ 10.5 nm, the T_m was 523 K. These two values are compared to literature values [163, 164, 165, 133, 166] in figure 31. A least squares fit

Table 5: Properties of bismuth oxide nanoparticles for the calculations.

property	constant value	equation for T-dependence	unit	obtained from/by
T_∞	867	-	K	this work
$\triangle_m H$	14700	const.	J/mol	[64]
γ_{sv}	~0.3	const.	J/m^2	fitted
γ_{lv}	0.13±0.04	const.	J/m^2	this work
$v_m(s)$	$47.28 \cdot 10^{-6}$	$1.24656 \cdot 10^{-9}$	m^3/mol	[86, 157] + this work
$v_m(l)$	$53.07 \cdot 10^{-6}$	$6.7756 \cdot 10^{-9}$	m^3/mol	[106], extrapolated
$\triangle_r G_m^\infty$	-	$549700 - 261.1 \cdot T$	J/mol	[161, 162]

Table 6: Properties of bismuth nanoparticles for the calculations.

property	constant value	equation for T-dependence	unit	reference
T_0	544.55	-	K	[64]
$\triangle_m H$	11296.8	const.	J/mol	[64]
γ_{sv}	0.55	const.	J/m^2	[133]
γ_{lv}	0.375	const.	J/m^2	[133]
$v_m(s)$	$21.32 \cdot 10^{-6}$	const.	m^3/mol	[133]
$v_m(l)$	$20.75 \cdot 10^{-6}$	const.	m^3/mol	[133]

of a linear function was applied to the literature data. The present values show to be in accordance with other literature values. The material properties used for the calculations here and in the discussion are summarized in table 6.

An interesting phenomenon was observed for the crystallization of the Bi nanoparticles. The particles did not start to crystallize until below 380 K. Down to 310 K particles were observed to crystallize abruptly and while fluctuating a trend to lower crystallization temperatures for smaller particles could be observed. The crystallization criterion was mainly the occurrence of diffraction halos in BF. Figure 34 shows a series of BF images with increasing number of crystalline particles during cooling from 397 to 299 K.

7.2 Discussion

7.2.1 Bismuth oxide nanoparticles

The in-situ TEM heating experiments are in the center of this discussion. From their observations it is a fact that a change from solid oxide to a liquid state took place at the respective transformation temperature and that metallic bismuth re-crystallized at cooling. But it is difficult to distinguish between a pure melting transition and a reduction reaction yielding liquid Bi and volatile O_2. In spite of this distinction a solid-liquid transformation occurred and as such it was analyzed by the existing size-dependent melting models.

Size-dependent melting

In figure 31 the melting points coincide reasonably well with the linear fit of the HOG model. As no deviation from linearity is observable for smaller sizes, there is no indication for a liquid surface layer. A peculiarity is the intercept which usually denotes the bulk melting temperature: With 867 K it is 230 K below the usual bulk value. But in contrast to the known metal studies these oxide nanoparticles reside in a different phase than the common bulk structure (β-Bi_2O_3). Therefore, the intercept at T_∞ marks a hypothetical value. Particles larger than the critical size D_c adopt the

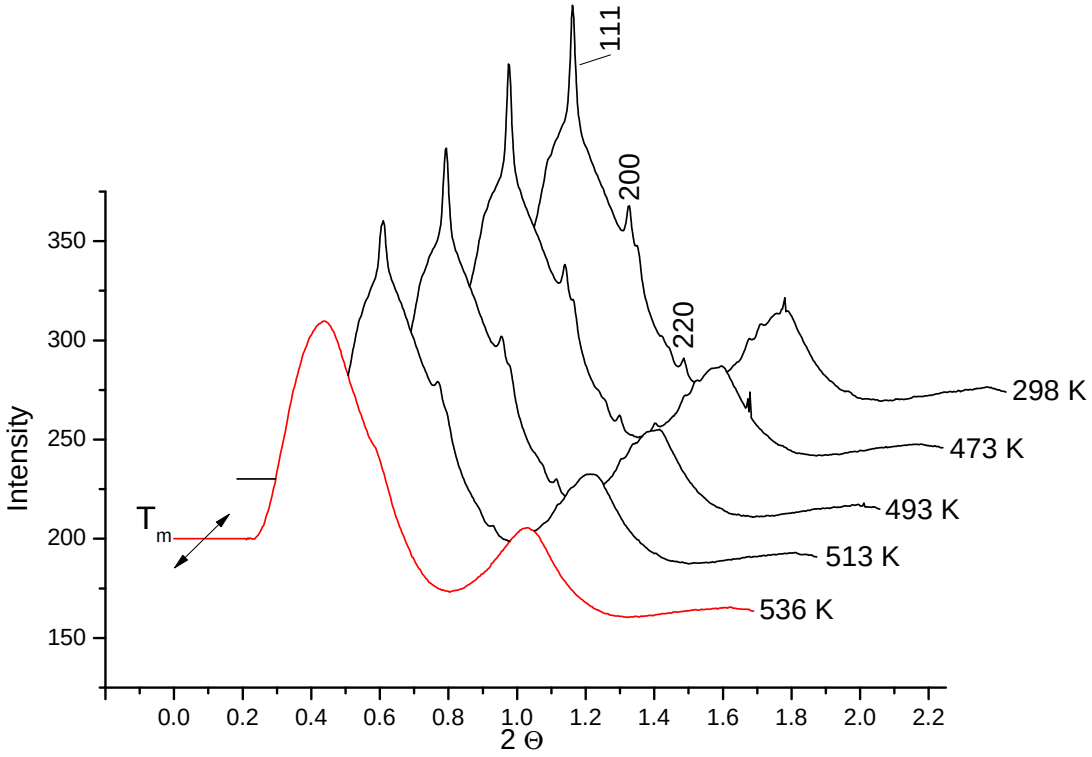

Figure 33: Diffractograms of 35 nm Bi nanoparticles which formed after the first heating cycle with Bi_2O_3. The bulk $T_0(\mathrm{Bi})$ = 545 K. The transition occurred at $T_m(\mathrm{Bi})$ = 536 ± 13 K. The background was not subtracted in this waterfall graph.

usual α-structure (chap. 5.1.3). It can be expected that after this size-dependent change from β to α, the particles will perform the usual bulk transformations to the δ-phase at 1003 K and melt at 1097 K. Hence T_∞ would be equal to T_0 for particles larger than the critical size and a jump in the size-dependent melting curve would occur. As there is not any bulk counterpart no reference values for the $\beta \rightarrow l$ transformation exist. This is also true for most other thermodynamic parameters required for the models. Therefore maximal and minimal values for the parameters $\triangle_m H$, $\upsilon_m(l)$, $\upsilon_m(s)$ and $\gamma_{l\upsilon}$ will be estimated to show the widest possible range of the common fit parameter $\gamma_{s\upsilon}$. The chosen value for $\triangle_m H$ is the one of the bulk $\delta \rightarrow l$ transformation. It served as a lower limit because the β-structure with its lower symmetry will have a higher enthalpy of melting. The literature values for $\triangle_m H$ scatter strongly [167]. Still, an upper limit would be the combined change $\triangle_{tr} H(\alpha \rightarrow \delta) + \triangle_m H(\delta \rightarrow l) = 29.8 + 14.7 = 44.5$ kJ/mol [64]. The solid molar volume could be as high as $52.9 \cdot 10^{-6}$ m^3/mol due to changes in Bi:O ratio up to stoichiometric Bi_2O_3 and a higher thermal expansion coefficient reported by Levin et al. [158] ($3.57707 \cdot 10^{-09}$ K^{-1}). As liquid bismuth oxide tends to reduce to bismuth under vacuum conditions $\gamma_{l\upsilon}$ of liquid bismuth, 0.375 J/m^2, can be estimated as an upper limit. The lowest value of 0.217 J/m^2 was found for bulk Bi_2O_3 in air at 1123 K [93]. A sensible value of $\gamma_{s\upsilon}$ was 0.3 J/m^2, but minimum and maximum values could be between 0.25 and 0.75 J/m^2. The main cause of uncertainty is the enthalpy of melting. Nevertheless, 0.3 J/m^2 as well as the relative difference between $\gamma_{l\upsilon}$ and $\gamma_{s\upsilon}$ are plausible values when compared to the surface energies of e.g. solid titania nanoparticles (0.6 to 1.0 J/m^2[15]) and liquid titania (0.38 J/m^2[168]). According to these values it is plausible that a physical phase transformation occurred.

A number of other arguments point to a melting transformation, rather than a chemical reaction:

1. The reflexes of the bismuth oxide structure remained up to the melting point and the transformation was observed to be abrupt for the individual particles. This shows that no gradual decay or reduction took place.

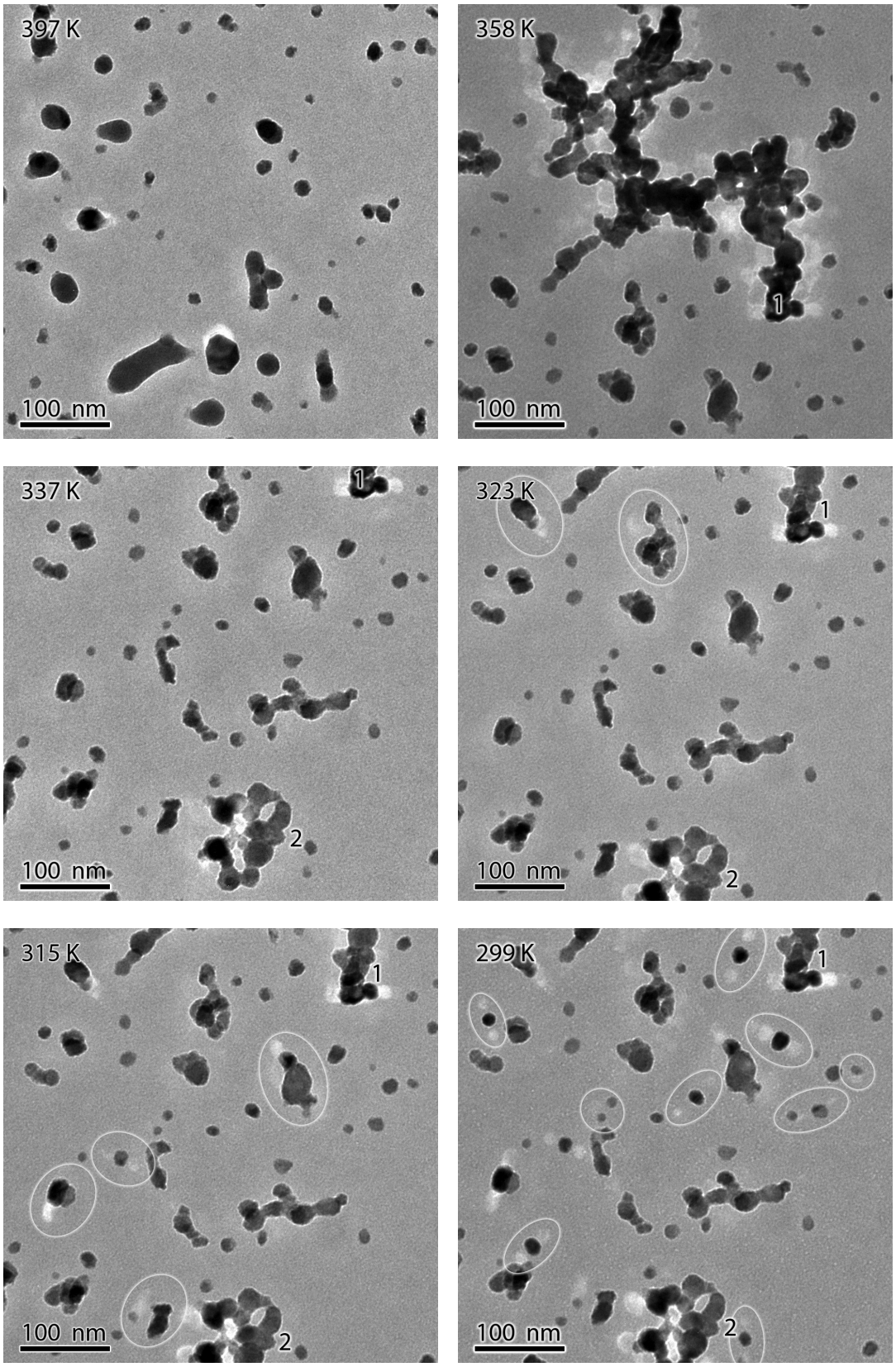

Figure 34: Series of BF images without objective aperture during cooling a polydisperse Bi sample. At 397 K the first two crystalline particles were observed. Then the biggest structure no. 1 was found crystalline (358 K). Shortly after no. 2 crystallized (337 K). Afterwards ever smaller particles became crystalline. Each freezing processes occured instantly within the observable time resolution. For orientation the two big particles no. 1 and 2 are always numbered, and particles which freshly crystallized at the respective temperature are circled.

2. The high temperature XRD experiments (chapter 5.1.3) show basically the same behavior, whether they were performed in air or vacuum. Differences were a general shift of the melting temperature and a notable evaporation rate in vacuum - both independent of initial particle size and both caused by stoichiometric changes due to oxygen loss (chap. 2.6).

3. A preliminary investigation of bismuth oxide nanoparticles on a NiO-film was performed for the chip calorimeter, which will be described in chapter 9.3. It indicates that melting occurs in a similar temperature range (window of 100 K) under ambient conditions.

Supporting information can also be found in literature:

1. Takahashi et al. [169, 170] performed electromotive force (emf) measurements in electrochemical cells with varying $p(O_2)$ up to 973 K (solid, α-Bi_2O_3). They found that bulk bismuth oxide can be reduced to Bi if the partial pressure drops below the equilibrium partial pressure at a certain temperature (eq. 48 and 52 on page 19) but is stable as long as $p(O_2)$ is above that value. These equilibrium partial pressures are very low as calculated and shown in the next section.

2. It is known that in contrast to its solid form bismuth oxide melts are highly reactive and possess a low thermodynamic stability under non-oxidizing conditions [171, 172, 173].

In the light of this additional information one can conclude that the process is primarily a melting process which is followed by oxygen loss in the liquid phase, just like in the bulk. But also in analogy to the bulk a shift of T_m by the reducing conditions is quite possible. This shift is probably due to stoichiometry changes, caused by incongruent evaporation (chap. 2.6.2 and 6.2).

The particles in the biggest samples show clear agglomerate nature and asphericity. This raises the question whether such shape changes alter the transition temperature. The topic has often been discussed and used as one point of criticism about the thermodynamic melting models which all assume a spherical crystallite shape. Chang et al. [174] conceived experiments where aluminum needles with different apex angles were melted and thus curvature and molten volume could be changed independently. Their results showed that the over-all melting temperature only depends on the surface to volume ratio and not on the curvature. The present results confirm this finding as the melting of the 29.7 and 48.8 nm particles would be drastically reduced if the local curvature had been of importance. The 29.7 nm sample seems to be exactly in line with the two smaller sizes. Because of the smaller size and volume of the agglomerates in this sample they diffract much less and thus do not influence the analyzed T_m. They were not considered for the determination of the average size, neither (chap. 5.1.1). On the other hand T_m of the 48.8 nm sample seems a bit lower than expected, though still within the error range. This also accords with the predictions: All particles consist of agglomerated and coalesced primary ones. They deviate strongly from a perfect spherical shape. So the surface to volume ratio is increased and thus T_m should be lower.

Although still within the error range, the smallest particle size seems to deviate slightly from linearity. So definite conclusions can not be drawn and more measurements at even smaller sizes would be necessary. Still this potential deviation can not be ascribed to geometric reasons- especially because the value is higher instead of lower. In analogy to the findings about gold nanoparticles in the previous chapter the end of the continuous regime could be reached at 6.4 nm. Another explanation could be that the reduced and bismuth-rich surface region causes a convergence to the melting curve of bismuth as the influence of a more oxidic core diminishes.

The phenomenon that the molten particles do not form larger droplets but on the contrary, the exterior shape hardly changes has been observed in metallic nanoparticles, too [175]. No explanation has been found in literature. A possible reason could be strong adhesion forces or even a superficial chemical bonding with the substrate. Lee et al. [2] observed the dissolution of one atomic layer of carbon in molten Au on the particle-substrate interface. The influence of dissolved carbon is discussed in the respective article. Additionally, the produced deepening could have a mechanical effect: It could keep the particle in position and hinder free movement which is necessary for coalescence of droplets.

The high vacuum and the focused electron beam are conditions under which the experiments were carried out. Their influences on T_m will be discussed now. The results were also treated assuming a size-dependent reduction reaction. This most extreme case would have rendered the treatment of the data as a phase transformation obsolete. But figure 32 shows that neither the temperature range nor the size-dependence qualify to explain the experimental data. Nevertheless there are observations which provide evidence for shifts in the free energies of redox reactions of Bi_2O_3 (chap. 2.4): First, ultrasonic dispersion of nanoscale Bi_2O_3 (commercial powder) was easily hydroxylated to bismuth hydroxide (checked by XRD) and even storing in water at RT could change the powder within a few days, while both was not possible with usual micron Bi_2O_3 powder. Second, the in-situ TEM experiments with separated nanoparticles produced pure, metallic bismuth, while similar HT XRD experiments with milligram amounts of bismuth oxide resulted in unidentified, but not fully reduced phases even though the maximum temperatures were much higher (bulk Bi_2O_3 can be reduced to Bi under low oxygen pressures , though [176]). Also Irmawati et al. [177] showed that Bi_2O_3 needles with a thickness in the nanoscale could be reduced more easily than broader ones. So it is probable that the calculated size-dependent change of the redox equilibrium in figure 32 exists, like the ones calculated by Navrotsky et al. [61] for other oxide nanoparticles.

Turning back to the melting transition, it already became clear in chapter 5 about the solid-state transformations that an actively pumping vacuum atmosphere has a considerable influence on the incongruent-evaporation rate which in turn affects the stoichiometry of the oxide. Nanoparticles were observed to be more affected because of the high surface area from which evaporation can take place. If the stoichiometry is altered several scenarios can explain deviations from the reference melting temperature. The calculated phase diagram by Risold et al. [157] predicts a monotectic point of 1061 K for Bi-O melts with an oxygen content < 0.6 (stoichiometric Bi_2O_3). Within the error of the HT XRD measurements this value agrees with the experimental $T_0 = 1052 \pm 15$ K in vacuum (this work). In this case the value would be independent of size and a general offset of approx. -25 K would occur as soon as oxygen-deficiency occurs in the oxide. From a thermodynamic point of view, loss of oxygen by evaporation will inevitably change the chemical potential of bulk, as well as of nanoparticles. Thus the phase equilibrium (transition) temperature (where $\mu(s) = \mu(l)$) would shift. Due to the defects in the structure, the chemical potential must be higher and the transition temperature would be decreased which accords with the observations.

Another observed influence is the electron beam. Sample heating has often been discussed as an influence in TEM studies, especially for organic samples [178]. Electrons passing through the sample loose a certain amount of energy along the path. A heat transfer model can be established, if one assumes that the entire energy is dissipated by heat. The heating effect in the irradiated region, which is in thermal contact with the surrounding, can thus be calculated. Yet, the conclusion normally is that the sample is only heated by a few degrees. Calculating the temperature rise under typical experimental conditions of the present work according to [179, 180] results in a maximum of +6 K in the center of the irradiated region. A problem are particles with a small and bad thermal contact to the substrate: It is possible that the amount of heat generated inside the particle, Q, can not flow off properly due to the high thermal interface resistance. This leads to superheating of the particle. The temperature of a particle can be calculated by

$$\triangle T = \frac{Q h_c}{k \pi r_c^2} \tag{79}$$

$\triangle T$ is the temperature increase of the particle compared to the supporting substrate, $h_c = 2$ nm and $r_c = 0.5$ nm are the presumed thickness and radius of the contact through which the heat flows in one dimension. The thermal conductivity of the interface region is $k = 1$. The temperature increase depends strongly on the size of the contact region. The presented worst-case calculation for particles in the range between 5 and 30 nm gave $\triangle T \approx 10^{-3}$ K which is negligibly small. This is because in the small particle volume only little heat is generated. Only if the particles became larger than 100 nm and the contact size remained, the temperature would rise more than 1 K and above 500 nm the rise would exceed 10 K. The reports by Howe, Yokota et al. [181, 182] which reported temperature increments of 50 up to 200 K referred to big particles (around 1μm), with small contact area and current densities 2-3 orders of magnitude higher

than the ones which were used in the present experiments. $\triangle T$ was reported to be proportional to the current density . Egerton and Malac [156] reviewed several other damage processes of electron beams on organic and inorganic samples. Mechanisms eligible for affecting the bismuth oxide sample are:

Electron beam sputtering: High angle elastic scattering of incident electrons by the Coulomb field of the nuclei can displace atoms/ions. The low-bound atoms at the surface can be detached by this mechanism. In analogy to ion beam bombardment this process is called sputtering. The required threshold energy for displacement is much lower for low-Z elements. So surface oxygen would be preferentially sputtered by this mechanism.

Radiolysis: Energy input by inelastic scattering (energy exchange of incident electrons with valence and core electrons) indirectly causes displacement of lattice ions. The processes is increased at higher temperatures. In the case of metal oxides, radiolysis is believed to occur via the Knotek-Feibelman mechanism [183] creating neutral or positive oxygen nuclei which are repelled by the surrounding metal ions and ejected into the vacuum. The process continues until the material becomes sufficiently conducting to screen the positive oxygen ions. Since the mass loss occurs mainly close to the surface of the specimen, it is also known as electron-stimulated desorption.

Both mechanisms would deplete the surface region from oxygen. Furthermore, the large number of electrons provided by the electron beam can facilitate any reduction process. One can conclude that the electron beam further supports the oxygen depletion of bismuth oxide and therefore also plays a role in shifting the melting point.

Whether the vacuum atmosphere or the damage by the electron beam is the dominant influence or, what is more probable, if it is a combination of both effects can not be concluded here. But there are several causes for shifting T_0 and T_m at hand and it is very likely that the size-dependent melting curve is offset compared to one under oxidizing conditions. The phase transformations of Bi_2O_3 nanoparticles which were measured under different atmospheres showed a decrease of approx. -30 K in vacuum. So this might be a hint to the approximate range within which T_0 and T_m shift due to atmosphere induced stoichiometric changes. But the measurements were not preformed on separated nanoparticles, so the value could also be higher. As this offset changes T_∞ the difference between T_0 and T_∞ could have two causes now: The described size-stabilized β-phase as well as the influence by the experimental conditions in the TEM. Moreover, the surface region is depleted of oxygen, hence the γ_{sv} will be altered since surface reduction and oxygen vacancy formation are known to change the surface regions of oxides [19]. It is even conceivable that a metallic surface layer forms.

Conclusion

To conclude this part of the discussion it was shown that most likely a melting transformation of bismuth oxide was observed without indications for a pre-molten liquid surface layer. But as the harsh conditions in the TEM change the stoichiometry of the sample and probably deplete the surface of oxygen, the quantitative values of the size-dependent melting curve are altered compared to oxidizing conditions without an electron probe. Measurements with a sensitive chip calorimeter in different atmospheric conditions, as described in chapter 9.2 and 9, would be ideal to test this supposition and also exclude the influence of a highly energetic probe beam.

The obtained values for melting point depression of bismuth oxide nanoparticles are stronger than the effect for any known metal (fig. 35). The reason is twofold. For one thing, T_∞ is drastically reduced compared to T_0 which is caused by the elevated ground state of the nanoparticles in the metastable β-phase and probably by the conditions in the TEM which tend to deplete bismuth oxide of oxygen. For another, the size-dependence is stronger because of a bigger $\triangle\gamma$.

7.2.2 Melting and crystallization of metallic bismuth nanoparticles

The results about melting bismuth nanoparticles in the second heating cycles are unambiguous. The accordance with other literature values in figure 31 is good and it was shown that bismuth, which does not exhibit surface melting in the bulk, can be fit by phase-equilibrium models like the Gibbs-Thomson equation, HOG and HEG. The effect of melting point depression is weak in bismuth because it is one of the few materials where the density of the liquid state is higher than

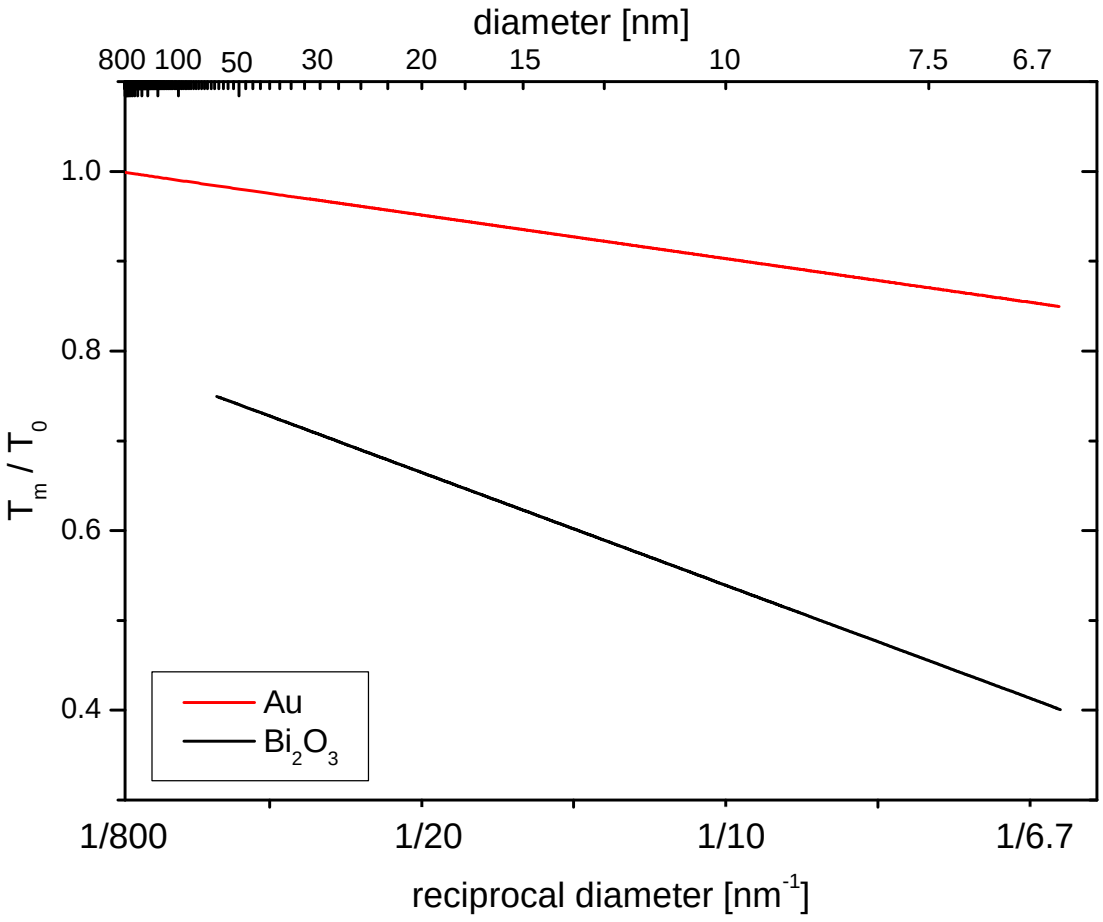

Figure 35: Comparison of the relative size-dependent melting point reduction between gold and bismuth oxide. The curves were calculated with the HOG model on the basis of experimental values form this work and literature values. The Bi_2O_3 curve was only plotted for the ascertained size range. Causes for the stronger depression in Bi_2O_3 are (a) an offset of the T_∞value and (b) a steeper slope.

in the solid state. Furthermore $\triangle\gamma$ is small. The experiments also show that the experimental method is functional and that the particles are pure, so only small amounts of residual oxygen could have remained after the reduction process in the melt.

The crystallization of molten Bi nanoparticles can be explained by nucleation theory as done e.g. by Sheng et al. [184]. The theory is very similar to the size-dependent liquid-nucleation-growth (LNG). In contrast to superheating for melting, undercooling is common for crystallization. A liquid is a very homogeneous state with small, local fluctuations. Therefore only few nucleation sites exist - preferentially at solid-liquid interfaces (heterogeneous nucleation). These sites are counted in sites per volume or sites per surface area [184]. Especially in free particles or particles with a small contact area to the substrate the probability for nucleation is further reduced. As nanoparticles are small, $\leq$1 nucleation sites per particle exists according to classical theories. To form a critical nucleus for crystallization the free energy (nucleation) barrier has to be overcome. The higher the degree of undercooling, $\triangle T$, the lower this barrier and thus the higher the likelihood of nucleation. The size dependent free energy which ultimately changes the melting temperature of nanoparticles changes the free energy barrier in the same way. Hence melting point and freezing temperature of nanoparticles are related via the following formula:

$$\triangle T = \triangle T_0 + \alpha \triangle T_m \tag{80}$$

$\triangle T_0$ is the degree of undercooling in the bulk, α is a proportionality factor between 0 and 1 and $\triangle T_m = T_m - T_0$ is the melting point depression. This means smaller particles, with lower melting point also have a proportionally lower freezing temperature. This was validated by the DSC experiments of Sheng et al. [184]. The present results also confirm this phenomenon as bigger shapes had the tendency to crystallize at a higher temperature than smaller ones. Still freezing is a statistical process and only around 100 particles were examined in the TEM. The freezing temperature range tends to be lower which could be ascribed to the relatively free particles in this study compared to the embedded ones of Sheng et al.

8 Stability diagram of Bi_2O_3 nanoparticles

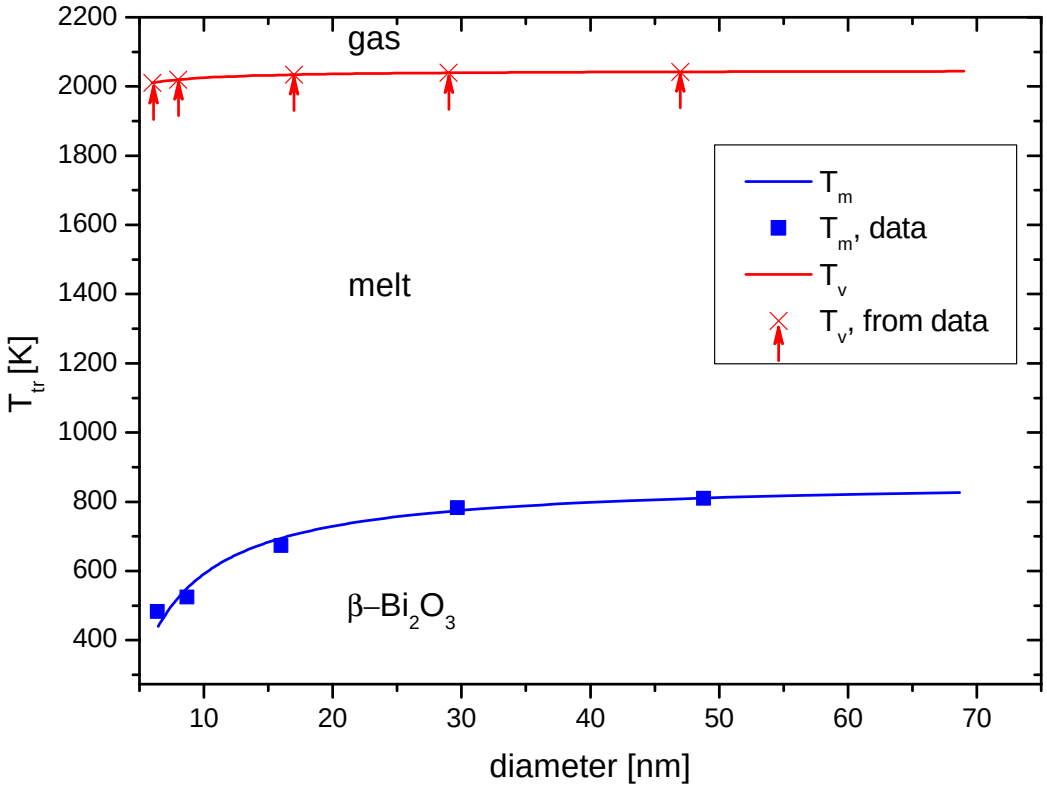

Figure 36: Size-dependent melting and boiling temperatures of bismuth oxide nanoparticles. The blue points are measured melting temperatures in the TEM and the blue line comes from the HOG melting model. The red crosses with arrow are the particle sizes used to measure and calculate evaporation at lower temperatures. From that data their theoretical boiling point was extrapolated (red line).

All findings from the experimental chapters about size-dependent phase transformations of Bi_2O_3 nanoparticles (chap. 4 to 7) are brought together in this chapter to form a schematic, size-dependent stability diagram for bismuth oxide.

The in-situ heating experiments in the TEM performed on 5 particle sizes (6, 9, 14, 30 and 49 nm) showed a very strong melting point depression which is in accordance with a $1/D$ melting behavior. However the high vacuum and the electron beam are no chemically neutral conditions for oxides. Hence, a shift of the absolute values of the melting temperatures was discussed in chapter 7. The HOG model was fitted to the data points in the reciprocal plot of figure 31 and 35 on page 85. The same curve was plotted in figure 36 over D together with the data points. They are represented as a blue line and blue squares, respectively. These curves were calculated with the criterion $\mu(s) = \mu(l)$. They represent the boundary line between the region of stability of the solid β-phase and the melt.

The combined measurement and calculation of the dynamic evaporation was performed on 5 initial sizes as well (6, 8, 17, 29 and 47 nm). The resulting size-dependent boiling temperature was discussed in chapter 6 and plotted in figure 27 on page 71. Since the evaporation rate at the actual boiling point would be much too high, the vapor pressure curve

was determined between 850 and 1175 K. With Clausius-Clapeyron equation (12) this curve was extrapolated to the boiling point. A $\triangle_v H$ of 250 kJ/mol [85] was used for this purpose. The main problem of the evaporation experiments was the unknown, complicated evaporation behavior of bismuth oxide. Its vapor consists of many different gas species whose vapor pressures depend on temperature and atmosphere. The curve of figure 27 on page 71 has been reproduced in figure 36. The red line is the calculated line according to equation 76 on page 71 and the arrows mark the initial particle sizes which were used to determine the vapor pressure at lower temperatures. The line is the boundary between the liquid and the gaseous state.

In chapter 5 a phase transformation from the β-phase (nano-phase) to the α-phase (bulk-phase) was measured in compacted nanopowder. Since the β-phase is only stable as nano-phase, this is a size-dependent solid-state phase transformation which takes place at a set size and temperature. Possibly it follows the size-dependence of equation 43 on page 18 [56]. However, the critical size is influenced by surface-adsorbates: β-Bi_2O_3 tends to form a carbonized surface layer which stabilizes the phase. Not much is known about the transformation, except that it ultimately takes place around 735 K where the bismuth carbonates decompose. On the other hand, if particles are separated and are not given the possibility to grow (like in the TEM experiments) they retain their β-structure until they melt.

The schematic stability diagram is shown in figure 37. The melting and boiling information from figure 36 is reproduced. Additionally, the solid-state transformation from the nano-phase to the bulk-phase is shown, and the transformations of bulk Bi_2O_3 are plotted as horizontal (size-independent) lines in the macro-scale region. Squares and arrows indicate measured sizes. Regions where the stability boundary is unknown are marked with dashed lines. The region between the nanoscale and the macro-scale is not explained. The boiling temperature of the bulk, $T_{v,0}$, is known with a high inaccuracy. Consequently $T_v(r)$, which is based on this value, is uncertain as well. The path of the solid-state transition, marked with T_{tr}, is unknown. The curve was drawn assuming a $1/D$ dependence as proposed in equation 43 on page 18. The axes are not scaled since the absolute values of the phase transitions are subject to the mentioned uncertainties (see also respective chapters). All size-dependent phase transformations of this work are summarized in this scheme. Because of the pronounced polymorphism of bismuth oxide further phase transformations depending on the oxygen-content and the atmosphere are possible.

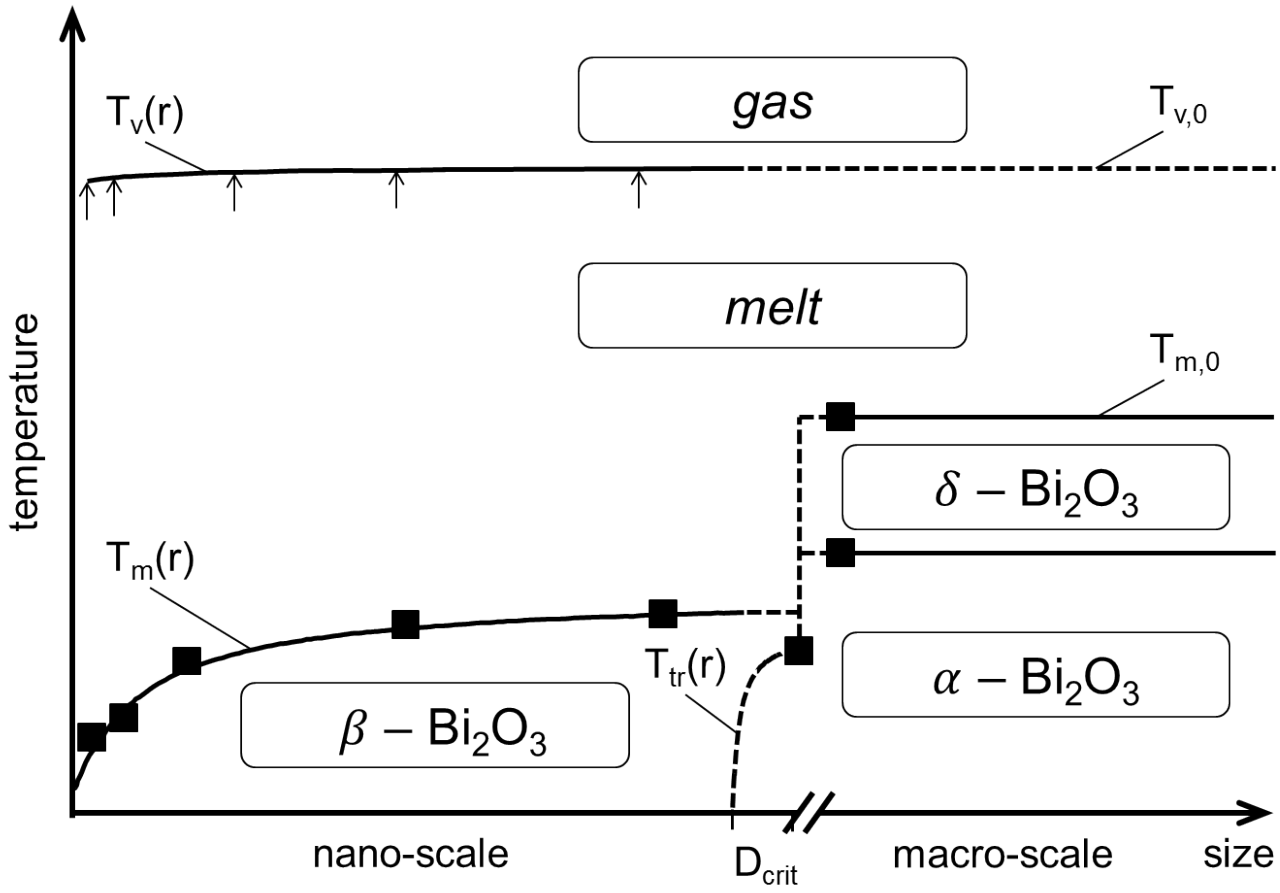

Figure 37: Schematic T-D stability diagram of Bi_2O_3. The dashed lines indicate unknown lines and regions. The squares and arrows are measured values in this work and the break in the abscissa marks the change from the makro-scale to the nano-scale.

9 High temperature chip calorimetry

The growing interest in nanomaterials and their properties calls for new methods to characterize them. One such tool is chip calorimetry, also called membrane-based calorimetry, thin-film calorimetry or nanocalorimetry [185, 186, 187, 188]. It is the equivalent to traditional calorimetric devices for milligram amounts of sample and enables the study of thermodynamic properties of nanoscale structures and materials. Such very small devices are produced with photo-lithographic methods as used in microsystem technology. A heated area in the micrometer region is created by Joule heaters on a very thin membrane (usually of amorphous silicon nitride) of 10 to 200 nm thickness. Temperature sensors are either thermocouples or resistance thermometers. Compared to classical calorimeters the small thermal mass increases the sensitivity and also the applicable heating and cooling rates by orders of magnitude [189, 190, 191]. But the currently available production processes were not developed for operation at elevated temperatures (in the temperature range above approx. 773 K). Oxidation and diffusion processes and reactivity become sufficiently fast to cause damage during the course of measurements. Merely the use of a high vacuum could prevent this for some applications [192, 193] which is counterproductive when investigating atmosphere sensitive materials like oxides. As in the case of traditional calorimeters, a chip calorimeter that operates at high temperatures in various atmospheres and pressures would be highly desirable.

Such a device was developed in this project. The next chapter is a short introduction to the most important parts and the operation mode of the device. The details about the setup and the AC mode can be found in the published work [194]. The recently added fast scanning, power-compensated, differential scanning (Fast DSC) mode is described in detail by Zhuravlev and Schick [195, 196]. Afterwards the preliminary results about the chip calorimeter on the way to a device for measuring melting of Bi_2O_3 and other inorganic compounds under various atmospheres are presented. The results and discussion sections are threefold: First the general functioning of the device up to 1073 K is shown. Afterwards the problematic of particle-substrate interaction is discussed on one, illustrative example. Finally the worked out, but not yet applied solution of a passivating top-layer is presented.

9.1 The device

Chip

The central component of the instrument is the high temperature calorimeter chip, which was specially designed and manufactured by Xensor Integration, NL (Fig. 1 and 2). The version of the chip used in this work was the XI 377. The chips are produced by photo-lithography processes on silicon wafers. Figure 38a shows the few hundred nanometer thick SiN_x cantilever with two highly-doped and meander-shaped polysilicon leads. They serve as Joule heaters in the active area at the tip of the beam. Two heaters are necessary in the AC measuring mode where one heater sets a certain base temperature and the second one is used for temperature modulation (see mode of operation). The heated area measures 90x90 μm^2 and is capped with a SiN_x top layer to prevent oxidation. The design allows free thermal expansion in almost every direction of space, which avoids thermal stress and cracking of the membrane. The temperature is measured by a thermopile consisting of 5 polysilicon thermocouples next to the heaters. In figure 38b two identical cantilevers facing each other are shown. One acts as the reference sensor, the other as the sample sensor in the differential measurements. But if necessary the cantilevers can also be operated independently. The electrical leads, bond pads and bond wires are made of gold. Thus all materials are stable at high temperature. The chip is bonded on an alumina carrier plate with platinum-palladium-gold alloy leads and contact pads. The pads are used to connect the chip in the measurement chamber.

Mobile measurement chamber

To work with atmosphere-sensitive samples a vacuum tight, mobile measurement chamber with electrical feed feedthroughs was developed (fig. 39). It allows loading and mounting of the chips inside a glove box and the subsequent transfer to the calorimeter setup without exposure to air. A compact high-temperature contact unit establishes the electrical contacts to two calorimeter chips easily and reversibly without any tools [197]. To withstand high temperatures the entire chamber as well as the contact unit and the electrical connections are built exclusively of alumina, platinum and quartz. The chamber can be placed inside a split tube furnace and the setup incorporates a vacuum pump as well as devices for gas flow- and pressure control. In summary the chamber features the following:

- Oxygen or moisture sensitive samples can be kept under controlled atmosphere at all times even if they have to be prepared externally.
- Gas atmosphere (any non-corrosive gas), pressure (from 0.1 mbar to 1 bar), gas flow (from 1E-5 to 1000 mbar l/s) and ambient temperature (from RT to 1373 K) can be controlled during the experiments.

Mode of Operation

The main mode of operation was modulated or AC calorimetry [198, 199]. A fast, modulated temperature or heating current is superimposed onto the constant or slowly changing bath temperature. The alternating signal at known frequency makes the use of Lock-In amplifiers possible which can extract small signals from noisy background, thus providing a very high sensitivity. AC calorimetry is especially useful for determining the heat capacity as function of temperature, to monitor time dependent processes and to detect reversible phase transitions with very high sensitivity [200]. The technique of AC calorimetry has been applied to chip calorimetry by Huth et al. who presented the first differential AC chip calorimeter in 2005 [201]. Additionally the software and electronics for power compensated DSC, called fast DSC [195, 196], were added to the setup later. While the sensitivity is worse by approximately one order of magnitude it is an extremely fast technique. Heating rates of 10^5 K/sec are well possible. Thanks to that, exchange of heat and matter with the environment can be minimized and experiments at quasi-adiabatic conditions can be performed. Also rate dependent phenomena and chemical reactions can be resolved and investigated [189, 190, 191, 193]. Moreover enthalpies of transition or reaction, e.g $\triangle_m H$, are directly deducible from the area under the curve.

9.2 Experiments

9.2.1 Temperature calibration procedure

The aim was to calibrate the thermopile signal and to determine the maximum operating temperature of the chips in AC mode. The measurements were performed at 80 Hz with a continuously changing base temperature of 10 K/min (temperature scans). The RMS heating power increased from 50 µW at room temperature (RT) to 65 µW at 1053 K. This resulted in a temperature oscillation amplitude and offset below one Kelvin. Furthermore, the operation was tested in air, argon, nitrogen, helium and a forming gas mixture of Ar - H_2 with 10 vol% H_2. All gases were of high purity ($\leq$ 10 ppm impurities) at a pressure of 1 bar. Preceding each measurement, an annealing treatment of the chip at 723 K in the split tube furnace and an on-chip heating ramp (10 K/min) above the planned maximum temperature of the experiment was performed. The following high purity substances (according to ITS 90 [202, 203, 204]) were used for temperature calibration: Indium, zinc, aluminum and a silver (71.9 wt%) – copper (28.1 wt%) eutectic alloy with the respective melting points Tm of 429.75 K, 692.68 K, 933.47 K and 1052.78 K. Micrometer sized particles were scratched off the freshly ground bulk substances. They were pressed flat between two alumina plates and one particle was placed on a heated area of the chip. The other area was left empty and differential measurements were performed. The particles adhered strongly to the surface of the chips after the heat treatment. Hence, the chips could not be cleaned and used for multiple runs of different substances.

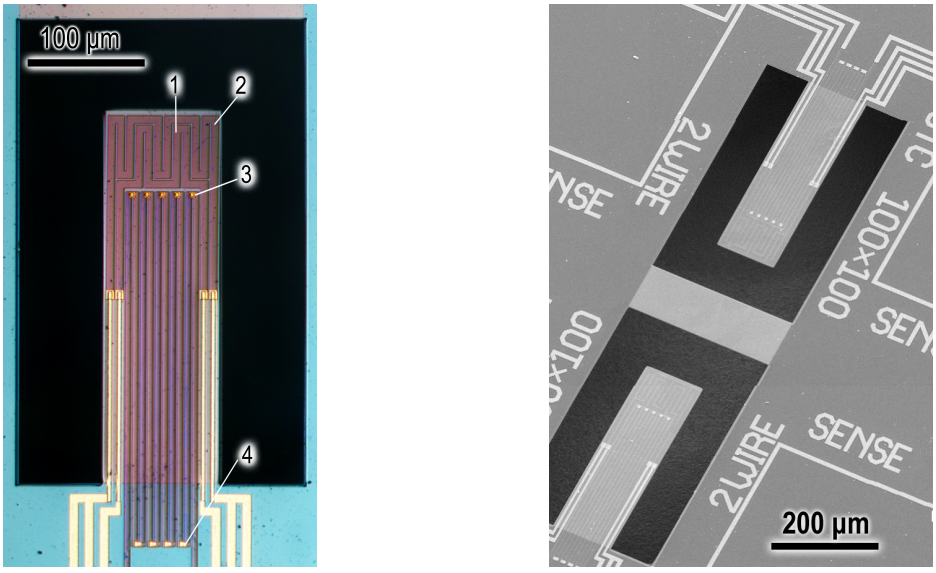

(a) (b)

Figure 38: (a) Light microscope image of a used XI-377 cantilever. The membrane material is a low-stress SiN_x that was etched away around the cantilever. The two meander shaped leads (1) and (2) on the front area are the polysilicon AC heater and DC heater, respectively . The golden dots in the middle, next to the heaters (3) are the 5 hot junctions of the thermocouples. The cold junctions (4) are positioned in the area with thick silicon wafer substrate. The chip was cycled 96 times to 973 K with 10 K/min. (b) SEM micrograph of two facing cantilevers. One serves as reference sensor, the other as sample sensor. The close spacial proximity increases the probability of similar characteristics and same affection by fluctuations. This is important for the differential measurement. Through the holes in the membrane the ceramic ground plate can be seen.

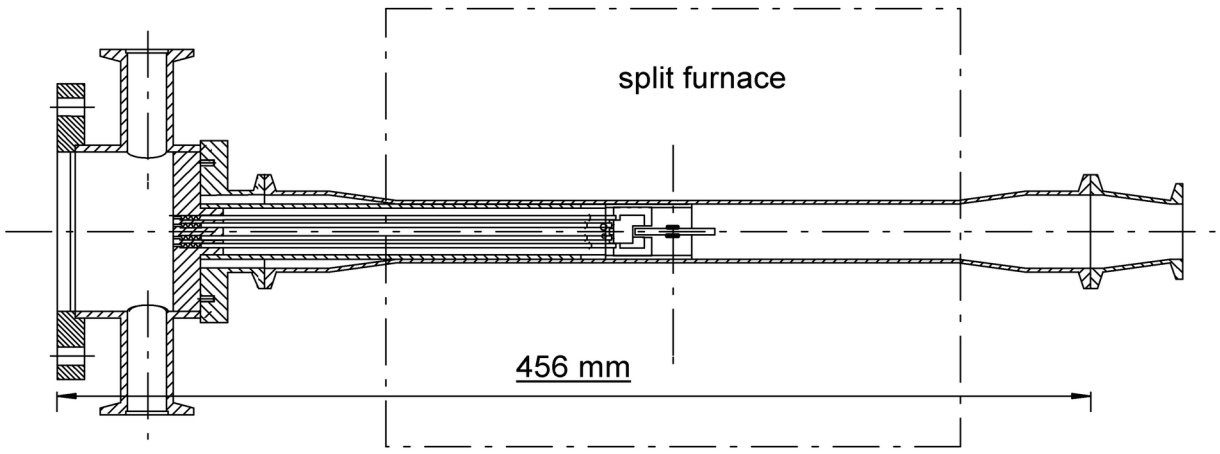

Figure 39: Mobile measurement chamber with HT pressure contact. It is 46 cm long and can be sealed and carried to the setup. There it is attached to a vacuum system for atmosphere control. The electrical feed troughs are at the left end. The chips are positioned in the middle of a split tube furnace to set certain ambient temperatures.

9.2.2 Heating of Bi_2O_3 nanoparticles

Preliminary investigations with the own AC chip calorimeter and a fast DSC in the laboratories of C. Schick at the University of Rostock by E. Zhuravlev showed that bismuth oxide penetrates the SiN_x top layer of the chips and destroys them. Therefore, an experiment with a sputtered gold film between the chip and the nanoparticles was performed.

A laser cut shadow mask of stainless steel with a 100x100 μm^2 window was positioned over the active area at the tip of the cantilever (fig. 38a). An approx. 35 nm thick gold film was sputtered with a Balzers SCD 050 sputter coater. In the calorimeter three identical annealing cycles with 10 K/min up to 1073 K in argon gas at 1 bar were performed until no changes of the measurement curve occurred anymore. Afterwards polydisperse bismuth oxide nanoparticles with a mean size of 16.4 nm ($\sigma_{GSD} = 1.45$) were deposited via ESP with -7 kV for 20 minutes using the same shadow mask. This resulted in a < 10 % fraction of a monolayer. In the calorimeter the chamber was purged and evaporated with argon before the actual experiment. 6 identical cycles with 10 K/min up to 1053 K were run. Between the first and the second cycle the sample was transferred to the SEM to investigate changes.

9.2.3 Development of a passivation layer

As a consequence of the findings of the two previous sections the need for a passivation layer to avoid sample-substrate interaction at high temperatures arose. Consequently the reactivity of bismuth oxide nanopowder with numerous high temperature-stable inorganic compounds was tested in solid state reactions and subsequent XRD analyses. Zirconia (ZrO_2), magnesia (MgO) and nickel oxide (NiO) did not form any mixed or unknown phases up to 1173 K. Phase diagrams confirmed this. For the reason of technical availability NiO was chosen. A process was developed to deposit a thin NiO layer in the active area of the chips. Sputtering techniques were used and the produced layers were examined with high resolution SEM (JEOL 7600 with hot emitter) and a thin film x-ray diffractometer (Rigaku SmartLab with 9 kW rotating anode). The XRD measurements and improvements were made together with E. Hildebrandt (Dünne Schichten, FB11, TU-Darmstadt). The process is far from beeing optimized. Attempting to achieve crack-free and as thin layers as possible would be desirable for the sensitivity of the chip.

The starting structure were 1x1 cm^2 pellets of Si wafer (no chip) with the same SiN_x thin film (approx. 1 μm thick) as used for the Xensor chips. They were cleaned in an ultrasonic bath in acetone, double-distilled water and ultra-pure ethanol; each for ten minutes. Afterwards and directly before starting the sputtering process they were blown off with dry air. An intermediate platinum layer for good adhesion between SiN_x and NiO was found to be necessary. So a Pt layer of 100 nm was sputtered (could probably be thinner) in a Balzers SCD 050 sputter coater with argon gas. Afterwards the sputter chamber was opened and the target was changed to Ni. Then a 30 nm thick NiO layer (checked with XRD) was reactively sputtered by inserting a small amount of air at the beginning of the process. The Pt+NiO structure was annealed in argon gas up to 773 K and afterwards in air up to 1073 K with heating ramps of 3 K/min. Finally, polydisperse bismuth oxide nanoparticles with a mean size of 16.4 nm ($\sigma_{sd} = 1.45$) were deposited via ESP with -0.5 kV for 1.5 hours resulting in a < 10 % fraction of a monolayer.

After the production one sample was in turn investigated in the SEM and heated to 623 K, 723 K, 823 K and 873 K. It was tried to observe morphologic changes of the Bi_2O_3 nanoparticles which could hint to melting of the particles on the substrate or a reaction with the substrate.

9.3 Results

High temperature calibration

The different melting points were used as calibration temperatures. To do so the peak onset of the amplitude was constructed by intersecting an extrapolated background curve and a tangent to the flank of the melting peak. Such a construction can be seen in figure 40(a) for a single-beam measurement. This thermopile voltage marks the melting point

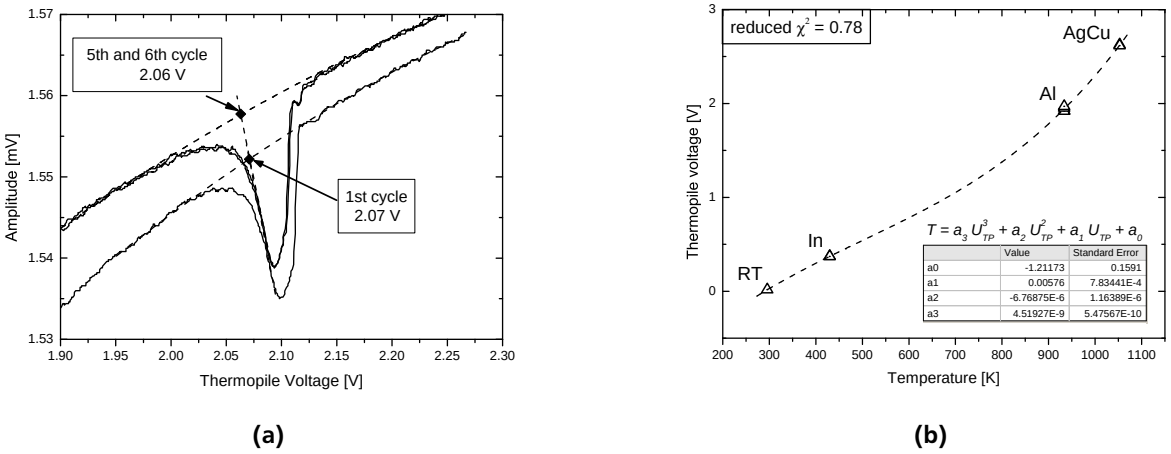

Figure 40: (a) Amplitude of the complex thermopile signal is shown for the melting events of an aluminum particle in argon gas at 1 bar. It was measured with a single cell (not differentially) 6 times in a row. The dashed lines were used for determination of the melting point: The intersection between the extrapolated ground curve and the tangent to the flank of the melting peak gives the onset point of the event.The shape of the melting peaks changes but the onset of the transition is quite constant after the first heating cycle where good thermal contact between membrane and sample is established. The variation of 10 mV equals approximately 2 K. (b) Calibration Curve in forming gas. Δ symbolizes the calibration points at 297 K and the melting points of indium, aluminum and silver-copper eutectic which were taken from several differential measurements. $--$ is the calibration function which resulted from the fit of a 3rd order polynomial equation to these points. It gives the conversion between temperature and thermopile voltage. The function and its fit parameters are also shown.

of the respective substance and assigning this to the known reference temperature one receives a plot as shown by the scattered points in figure 40(b). Finally the calibration function was received by fitting a 3rd order polynomial function to the measured points which is shown as a dashed line in the same figure together with the function and the values of the fitting parameters a_0 to a_3. There is no further physical meaning to these parameters. As every scanning experiment was performed at the same rate of 10 K/min, no rate-dependent calibration was necessary. According to this curve, the chips can be operated at least up to 1093 K.

While this general calibration procedure is routinely applicable, difficulties during the actual measurements occurred at high temperatures. Independent of the atmosphere the melting of indium was unproblematic and reproducible in any atmosphere. For the other tested metals deterioration due to oxidation was an important issue. Especially the small size of the samples gives rise to a substantial error by the formation of a surface-oxide layer. If oxidation occurs the melting peaks shift and shrink with every cycle. Aluminum could only be melted reproducibly in inert and forming gas atmosphere. A typical measurement is shown in figure 40(a). The calibration substance with the highest melting point of 1052.78 K is silver-copper eutectic alloy. It could only be melted in forming gas. A gradual change of T_0 with every cycle was observed. A more detailed discussion in a publication by the author [194] explained that this drift was due to compositional changes in the silver-copper alloy and not due to the device itself. The lack of good calibration points above 933 K (melting of aluminum) required the use of this alloy.

Reaction with SiN_x membrane

Other recommended phase transformations between 933 and 1273 K are the solid-solid transformations of barium carbonate ($BaCO_3$) at 1079 K, strontium carbonate ($SrCO_3$) at 1197 K, the freezing of sodium chloride (NaCl) at 1075.168 K [202, 205] and the melting point of bismuth oxide (Bi_2O_3) at 1098 K. All substances have been tested. In all cases the material reacted with the underlying SiN_x membrane and the silicon heaters and/or the thermocouples. The exact com-

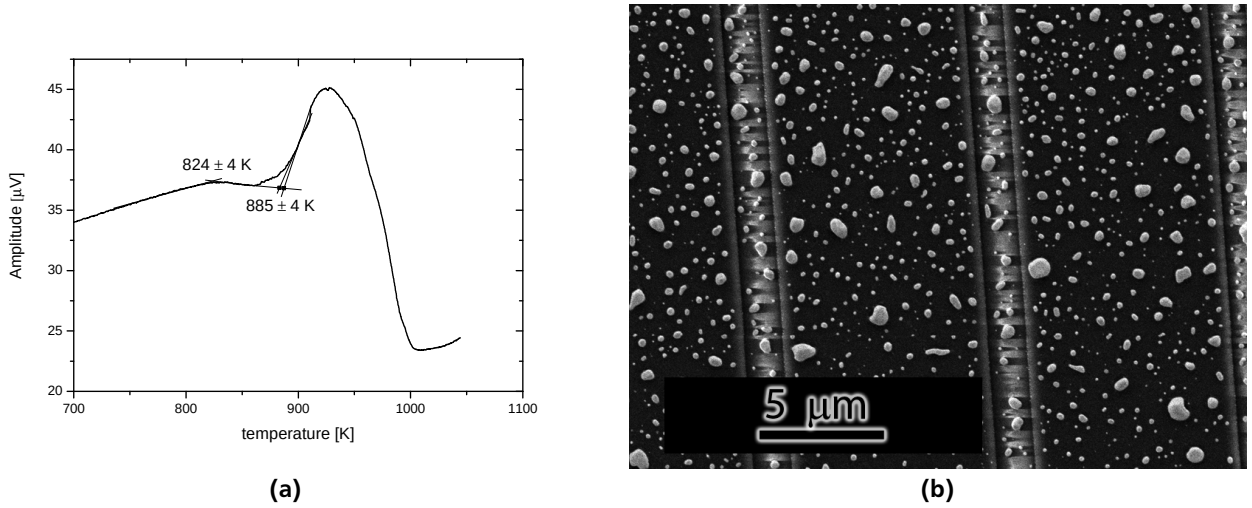

Figure 41: (a) First heating cycle of the calorimetric curve of Bi_2O_3 nanoparticles on a gold thin film. The unit of the ordinate is the amplitude of the oscillating temperature signal, which is directly related to the heat capacity of the sample. (b) Au-Bi-O balls formed during reaction of bismuth oxide nanoparticles with the gold thin film at 885 K in the first heating cycle.

position of the amorphous SiN_x in the Xensor devices is unknown, but a high Si and a low N content are expected. The use of other top layer materials instead of SiN_x promises to extend the applicability range considerably. At the moment the theoretical, physical limitation of an empty device is the melting point of gold at 1337 K.

As a first test a gold layer was sputtered and annealed on top of pre-annealed chip and polydisperse Bi_2O_3 nanoparticles (mode = 16 nm) were deposited in the active region of the chip. The occupied area fraction was < 10 % and no particle interaction was possible. The amplitude of the complex thermopile signal in the first heating cycle is shown in figure 41a. The curve levels off at 824 K and the onset of the subsequent peak is at 885 K. Ex-situ investigation in the SEM showed that the homogeneous gold film had reacted with the bismuth oxide nanoparticles to form balls between several hundred nm and 1 µm (fig. 41b). The composition was not further investigated. The signal of further cycles were identical and did not show any other events. No C_p calibration was performed and so the C_p of the sample was not evaluated.

Protective NiO top-layer

From the previous results the need for a passivating, protective top-layer is evident. The process described in the experimental part yielded the NiO layers in figure 42 which were stable at least up to 1073 K and probably higher. Small cracks and inhomogeneities were observed which probably could be reduced by optimizing the production process. In spite of that the cracks were only $\leq$ 20 nm thick. So an investigation of separated Bi_2O_3 nanoparticles was possible. The deposited particles on the described Pt + NiO on top of the Si-SiN_x pellets can be seen in figure 43 (a). Ex-situ SEM investigation after heating to 623, 723, 823 and 873 K showed that between 723 and 823 K (fig. 43 (b) and (c)) pronounced changes in the particle shape and distribution occurred. No repetitions of this experiment were made yet, and the results have to be considered as preliminary.

9.4 Discussion

The functioning of the high temperature chip calorimeter with the current XI-377 chips was shown up to 1093 K. From several calibration substances above 930 K it became clear that a suitable inert top layer on the chip has to be chosen and the atmosphere must be adjusted according to the material under investigation. For metals residual oxygen in the chamber has to be minimized by using a high vacuum. For oxides a high total pressure and oxygen partial pressure re-

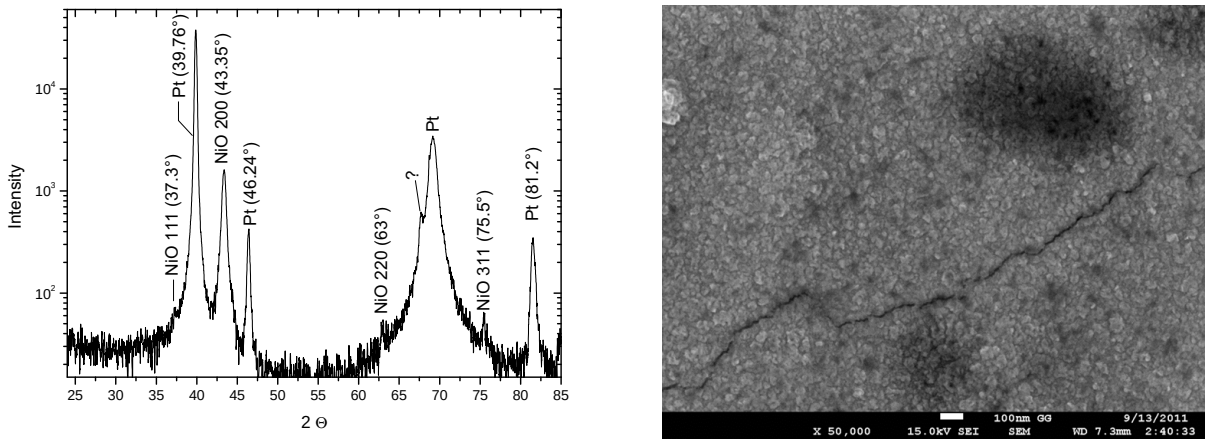

Figure 42: Thin film XRD pattern and SEM micrograph of annealed NiO protection layer with Pt adhesion layer underneath. They were sputtered on top of the approx. 1 μm thick SiN_x layer as also used for the Xensor calorimeter chips. No other phases than pure Pt and pure NiO were observed. The micrograph shows some inhomogeneities as well as thin cracks after annealing.

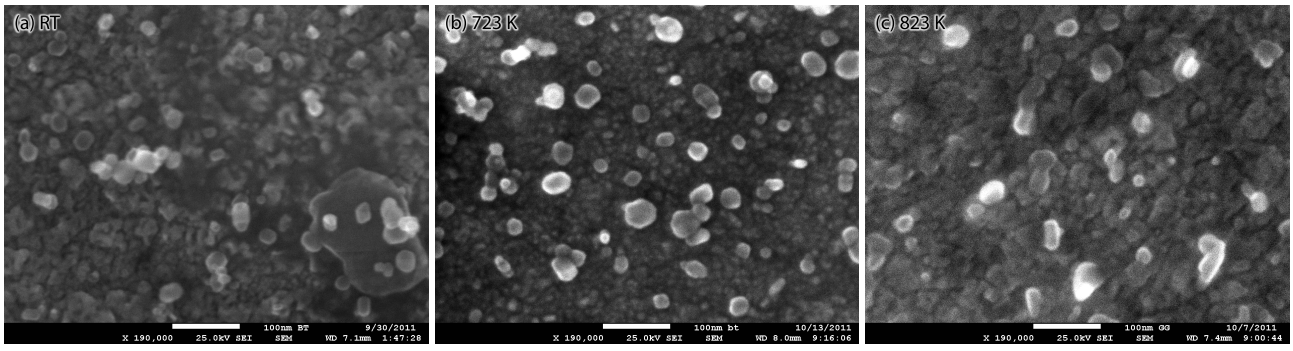

Figure 43: Preliminary experiment with 16 nm monodisperse Bi_2O_3 on sputtered NiO thin film in the initial state at RT (a), after heating to 723 K (b) and 823 K (c). The small particles disappeared and the big particles changed their shape between 723 and 823 K.

duces evaporation [29]. Furthermore this work has demonstrated that an actively pumping vacuum drastically increases the evaporation rate of bismuth oxide. For bismuth oxide neither the SiN_x of the chips nor gold has proven to be suitable as top layer material.

As the bismuth melt is known to be very reactive it is possible that the two distinct features of the measured reaction in figure 41 can be split into melting of the particles at the leveling-off temperature (824 K) and beginning reaction at the onset of the large peak (885 K). But this interpretation is speculative because it is not based on any proof. The temperature would be 150 K higher than the measured transition temperature in the TEM for similar mode of the size distribution. Furthermore, the preliminary calorimeter tests were carried out with a polydisperse, broad size distribution as depicted in figure 13 (gray columns). So the melting of the smaller particles which contribute less to the over-all measurement signal might as well have taken place at temperatures below 824 K.

The proof of concept for a passivation layer between the SiN_x and the Bi_2O_3 nanoparticles has been successful. The layer of Pt + NiO is stable at high temperatures and the nanoparticles seems to melt and evaporate without interacting or even destroying it. Unfortunately the concept could not be applied to actual chip calorimetry measurements, yet. Still, the changes in figure 43 between 723 and 823 K might indicate that melting of large bismuth oxide particles (approx. 40 - 60 nm) and evaporation of smaller (approx. 10 - 20 nm) took place in that temperature region. This is a hint that despite ambient pressure and inert gas atmosphere, size-dependent melting of Bi_2O_3 occurs at similar temperatures like in the in-situ TEM experiments. But these results and thus the conclusions have not been validated. From TEM experiments it is known that comparing the morphology before and after heating is not a good criterion to judge whether nanoparticles have melted or not.

In summary no definite statements can be given at the current state of research with the chip calorimeter. But once working, the possibilities are manifold and would contribute to complete the picture of size-, and atmosphere-dependent phase transitions in (bismuth) oxide nanoparticles. It would also add valuable thermodynamic information about the phase transitions.

10 Conclusion

The aim of nanoscience is the change and utilization of material properties by adapting the size and shape of nano-objects. To achieve this one has to be able to produce a material in various sizes and understand its size-dependent behavior to be finally able to tune its properties in the desired way for application. While size-dependent changes of the melting and boiling point as well as other phase transformations are known for metals no systematic study on inorganic compounds, like oxides, has been conducted yet. The aim of this work was to demonstrate a size-dependence of melting and other phase transformations in size-selected, spherical bismuth oxide particles. The size-dependence was compared with known models developed for metallic nanoparticles. Several experimental methods were tested and used.

Preceding the experiments a review of the existing size-dependent melting models tested on the well investigated material gold yielded information on their applicability: (1) There are pronounced differences in the proportionality factors of the $1/D$ dependence. Determining material properties like γ_{sv} by fitting models to the data is thus not accurate. (2) Temperature- and size-dependent material properties cause a deviation from $1/D$ dependence. They are often used to improve the fit to data even though the values' absolute uncertainty is larger than the magnitude of change. For gold no measurable dependence on temperature or size could be observed. (3) A maximum melting point reduction is achieved by a material which has a large $\triangle\gamma = \gamma_{sv} - \gamma_{lv}$, a large $v_m(l)/v_m(s)$ and a small $\triangle_m H$.

As the first experimental step pure, spherical, monodisperse and monocrystalline particles were synthesized in different sizes. They showed the phenomenon of a size-stabilized phase transformation: At RT they were all stable in the tetragonal β-form which is known as a metastable high temperature phase in the bulk. The surface of the particles was carbonated which reduces the surface energy and thus further stabilizes the β-phase.

To avoid coarsening during heating, separated particles in a low-concentrated aerosol or deposited on a substrate were used. The sample volume was therefore very small which posed high requirements on the experimental methods. Such works with metals rely almost exclusively on electron probe methods - especially BF and SAED in a TEM. With regard to spacial resolution they are superior to any other method and strong beam-sample interaction provides the necessary sensitivity to measure scattered particles. On the other hand the strong electron beam requires a high vacuum. While this is no problem for metals, oxides and other compounds can be unstable under such conditions. Especially at high temperatures the vacuum can lead to destabilization, reduction and evaporation. Bismuth oxide showed to be a 'good' example for this: The evaporation rate was increased and liquid nanoparticles could be reduced to metallic bismuth. Presumably the high oxygen mobility and the shift of the redox-equilibrium are responsible for that.

In this work several complementary methods were used to investigate the different phase transitions of bismuth oxide nanoparticles. In the solid state regime the use of traditional DSC, DTA-TG-MS and HT XRD with milligram amounts of a commercial nanopowder was possible. A nano-phase (β) → bulk-phase (α) transition was observed which was preceded by crystal growth and evaporation of O and C containing species. An interpretation was proposed that successfully explains all observations: A sudden destabilization takes place due to the loss of the stabilizing, carbonized surface, but only above a critical size. Scattered nanoparticles without the possibility of growth stayed below that size and thus remained in the β-structure up to their melting point.

For the size-dependent melting and evaporation experiments 5 monodisperse sizes between 7 and 50 nm were synthesized. In-situ heating experiments were conducted in the TEM. They revealed a size-dependent melting behavior with a strong melting point reduction (-55 % at 7 nm) which has two causes: For one thing, the material is in the β-phase which causes an offset in the theoretical bulk melting temperature of -230 K. For another, a strong size-dependency was observed from which an approximate solid-surface energy of 0.3 J/m^2 was determined. Yet, the conditions in the TEM could cause a lowering of the transition temperatures compared to chemically neutral conditions. Everything indicates that no stable, liquid surface layer forms prior to melting. In spite of the covalent-ionic bonds in this oxide material the qualitatively same size-dependence shows like in metals without surface-melting. But the magnitude of depression is much larger.

For evaporation an aerosol of the monodisperse particles was heated in a chamber with defined dwell time. A method was established which used a combined measurement and modeling of the dynamic evaporation process. An advantage of this method is that it measures free particles under atmosphere-like conditions without the use of a highly energetic probe beam. It could be shown that the Kelvin equation is valid for liquid Bi_2O_3. Thus, the vapor pressure also changes with a $1/D$ dependence. Caused by the low liquid-surface energy of 0.13 J/m^2 it is much weaker than for melting.

Based on all findings in this work a schematic size-stability diagram was drawn in figure 37 on page 89. This is comparable to a pressure-temperature phase diagram in the bulk. The axes are not scaled since the absolute values of the phase transitions are subject to uncertainties caused by the mentioned changes depending on atmosphere and experimental conditions. All size-dependent phase transformations of this work are summarized in this scheme. Because of the pronounced polymorphism of bismuth oxide further phase transitions depending on the oxygen-content and the atmosphere are possible.

11 Outlook

This work has shown several size-dependent phase transitions in bismuth oxide. On the other hand it also became clear that stoichiometric changes and even reduction can occur depending on the oxygen partial pressure and absolute pressure of the atmosphere. An important next step for validation of the transition temperatures (especially for melting) would be a systematic investigation in different atmospheres. The chip calorimeter would be well suited for this purpose. This device has already been developed and built. It combines several advantages for the investigation of atmosphere-sensitive nanomaterials: It is operable under various atmospheres including air, inert gas and vacuum. It also dispenses with a highly energetic probe beam. It also features a mobile measurement chamber to keep samples under controlled atmospheres at all times. Sensitivities in the pico-Joule/Kelvin range and heating rates of 10^5 K/sec allow measuring small nanoparticles under quasi-adiabatic conditions. The operability of the device up to 1093 K and the functioning of a passivating NiO layer were already shown. Another progress in experimental methods would be to build a specially designed setup for size-dependent evaporation. This method has been proven to be successful and can be even more powerful when the vapor pressure function of a material is exactly known. Such a setup would improve measurement accuracy considerably. Also, a size dependent analysis of γ_{lv} as well as measurements of the size-dependent melting temperature like it was shown for clusters by [206, 207] and indirectly seen in figure 23 could be possible.

Bismuth oxide itself has a non-trivial behavior in vacuum and during evaporation. This is not well understood which is also true for many other oxides. A better understanding and calculation of the multiphase equilibrium would be helpful for any high temperature application and vacuum processes. Furthermore surfaces play a decisive role for evaporation and for properties of nanomaterials. Since they are responsible for most changes at the nanoscale a better understanding of surface structures, or at least knowledge of the average surface energy from independent methods are important. Adsorbates, atmosphere and temperature have a decisive impact on these properties and should be considered, too. Such knowledge would allow a better assessment of models and the size-dependent properties could be determined much more accurately.

12 Acknowledgements

I thank Sonja for all her love, patience and support which made this possible and also my parents for their continuous encouragement. I also thank my supervisor and mentor Olivier Guillon very much. A great part of the experimental work took place in collaboration with the “Nanostrukturtechnik” (NST) group of Prof. Roland Schmechel and apl. Prof. Einar Kruis at the University Duisburg-Essen. Here I am especially grateful to Gabi Schierning and Ralf Theissmann. Without their invaluable help and support the experimental work would not have been possible. But I would also like to thank all the other NST members. While building up the chip calorimeter I received a lot of advice from Christoph Schick, Heiko Huth and Evgeny Zhuravlev from the Polymer Physics group at the University of Rostock. Emil Aulbach and Michael Weber were a great help for the measurement chamber and the electronics. Developing the passivation layer for the chip, I worked together with Erwin Hildebrandt. The financial support for the chip calorimeter setup came from the Joint Research Laboratory Nanomaterials, Karlsruhe Institute of Technology, Technische Universität Darmstadt and the state of Hessen as a joint research project together with Prof. Horst Hahn. I’m very grateful for all these supports. Thank also goes to Manuel Hinterstein for the measurements at PETEA III and Prof. Rolf Schäfer for the constructive discussions. Furthermore I thank all the helpers at the Materials Science department of the TU-Darmstadt, especially the ones doing the DSC and DTA measurements. I also thank all the current and former members of the NAW group for the enjoyable working atmosphere. Finally, great thanks goes out to all proof readers: Christoph, Enric, Gabi, Roland, Sonja and Wook. Thank you also to the DFG for funding this Emmy Noether project.

Thank you.

List of symbols

α	Thermal expansion coefficient
ΔS	Entropy differnce between two states
$\dot{\vee}$	Exclusive OR
γ	Specific surface or interface excess free energy
γ_{lC}	Interfacial energy between liquid phase and carrier substrate
γ_{lv}	Surface energy of the liquid phase in gas
γ_{sC}	Interfacial energy between solid phase and carrier substrate
γ_{sl}	Interfacial energy between the solid and the liquid phase
γ_{sv}	Surface energy of the solid phase in gas
μ	Chemical potential
μ^{∞}	Size-independent part of the chemical potential of a nanoparticle
ρ	Density
$\rho(l)$	Density of the liquid phase
$\rho(s)$	Density of the solid phase
σ	Surface or interface stress
σ_{GSD}	Geometric standard deviation
τ	Dimensionality of the sample (BOLS model)
Θ	Contact angle at interfaces or diffraction angle for electron- and x-ray diffraction
$\triangle_m H$	Standard enthalpy of melting
$\triangle_r G$	Gibbs free energy of a reaction
$\triangle_v H$	Standard enthalpy of evaporation
ς_i	i-th layer to total volume ratio (BOLS); or the atomic portion of the i-th atomic shell
a, b, c	Lattice constants
C	Correction factor for fitting the slope of size-dependent melting curves
c_i	Normalized cohesion energy of a surface atom in the i-th layer (BOLS)
d	Bond length of an atom in its usual lattice site (BOLS)
D_{crit}	Critical particle size for phase transition

d_i	Bond length of an atom in the i-th atmoc layer counted from the surface (BOLS)
E	Bulk modulus
E_B	Atomic bond energy in the bulk (BOLS)
E_b	Cohesive energy per bond
E_{coh}	Cohesive energy of a particle
E_m	Energy level required for melting at T_m
E_{therm}	Thermal energy of a particle
G	Gibbs free energy
K_j	The number of atoms lined along the radius of a sphere (BOLS model)
m	Bond nature (BOLS model)
$m_m(l)$	Molar mass of the liquid phase
$m_m(s)$	Molar mass of the solid phase
n	Number of moles in a pure substance or mole fraction in a mixture
P	Pressure
p_p	Corrected vapor pressureat the surface of a small droplet or particle
p_s	Vapor pressure
R	Gas constant, 8.31447 J mol^{-1} K^{-1}
r	Radius
r^*	Critical radius in nucleation theory
s	Entropy
T	Temperature
t	Thickness of the molten surface layer
T_0	Transition temperature of a material in its bulk state (macroscopic dimensions, usual phase)
T_∞	Transition temperature of a phase with macroscopic dimensions
T_m	Melting temperature
T_{tr}	General transition temperature
$v_m(l)$	Molar volume of the liquid phase
$v_m(s)$	Molar volume of the solid phase
$v_m^{\ominus}(s,l)$	Molar volume of the solid or liquid phase at standard conditions
z	Atomic coordination number in a bulk

z_i Atomic coordination number in the i-th atomic layer counted from the surface

SiN_x Amorphous silicon nitride, used for thin films and membranes in microsystem technology

BF Bright field mode in TEM. Transmitted beams form the image.

CPC Condensation particle counter

DMA Differential mobility analyzer

DSC Differential scanning calorimetry

DTA-TG Differential thermal analysis with combined thermogravimetry

EMD Equivalent mobility diameter determined by DMA

emf Eelectromotive force

ESP Electrostatic precipitation

FFT Fast Fourier transform

FWHM Full width half maximum of a peak or a distribution function

HR High resolution electron microscopy.

HT-XRD High temperature x-ray diffraction

MS Mass spectrometer or mass spectrometry

RT Abbr. for room temperature

SAED Selected area electron diffraction mode in TEM to observe diffraction patterns.

SDLP Size-dependent lattice parameter. Method to determine the surface stress in nanoparticles

SEM Scanning electron microscopy

SMPS Scanning mobility particle sizer

XPS X-ray photoelectron spectroscopy

XRD X-ray diffraction

Bibliography

[1] P. Buffat and J. P. Borel, "Size effect on the melting temperature of gold particles," *Physical Review A*, vol. 13, no. 6, p. 2287, 1976. [Online]. Available: http://link.aps.org/abstract/PRA/v13/p2287

[2] J. Lee, J. Lee, T. Tanaka, and H. Mori, "In-situ atomic-scale observation of melting point suppression in nanometer-sized gold particles," *Nanotechnology*, vol. 20, no. 47, p. 475706, 2009.

[3] M. W. Pitcher, S. V. Ushakov, A. Navrotsky, B. F. Woodfield, G. Li, J. Boerio-Goates, and B. M. Tissue, "Energy crossovers in nanocrystalline zirconia," *Journal of the American Ceramic Society*, vol. 88, no. 1, pp. 160–167, 2005. [Online]. Available: http://dx.doi.org/10.1111/j.1551-2916.2004.00031.x

[4] J. B. Rivest, L.-K. Fong, P. K. Jain, M. F. Toney, and A. P. Alivisatos, "Size dependence of a temperature-induced solid-solid phase transition in copper(i) sulfide," *The Journal of Physical Chemistry Letters*, vol. 2, no. 19, pp. 2402–2406, doi: 10.1021/jz2010144. [Online]. Available: http://dx.doi.org/10.1021/jz2010144

[5] C. Q. Sun, "Size dependence of nanostructures: Impact of bond order deficiency," *Progress in Solid State Chemistry*, vol. 35, no. 1, pp. 1–159, 2007. [Online]. Available: http://www.sciencedirect.com/science/article/B6TX3-4K42199-1/2/74f8d866db5f6f4e4a09e0e47b59f811

[6] J. Weissmüller, "Thermodynamics of nanocrystalline solids," in *Nanocrystalline Metals and Oxides, Selected Properties and Applications*, ser. Electronic Materials: Science and Technology, P. Knauth and J. Schoonman, Eds. Kluwer Academic Publishers, 2002, vol. 7, ch. 1, pp. 1–40. [Online]. Available: http://www.springer.com/chemistry/electrochemistry/book/978-0-7923-7627-9

[7] H. M. Lu and Q. Jiang, "Comment on: Higher surface energy of free nanoparticles," *Physical Review Letters*, vol. 92, no. 17, p. 179601, 2004. [Online]. Available: http://link.aps.org/doi/10.1103/PhysRevLett.92.179601

[8] K. K. Nanda, A. Maisels, F. E. Kruis, H. Fissan, and S. Stappert, "Nanda et al. reply," *Physical Review Letters*, vol. 92, no. 17, p. 179602, 2004, pRL. [Online]. Available: http://link.aps.org/doi/10.1103/PhysRevLett.92.179602

[9] G. Ouyang, X. Tan, and G. Yang, "Thermodynamic model of the surface energy of nanocrystals," *Physical Review B*, vol. 74, no. 19, p. 195408, 2006. [Online]. Available: http://link.aps.org/doi/10.1103/PhysRevB.74.195408

[10] J. Weissmüller and J. W. Cahn, "Mean stresses in microstructures due to interface stresses: A generalization of a capillary equation for solidsss," *Acta Materialia*, vol. 45, no. 5, pp. 1899–1906, 1997, doi: 10.1016/S1359-6454(96)00314-X. [Online]. Available: http://www.sciencedirect.com/science/article/pii/S135964549600314X

[11] R. Shuttleworth, "The surface tension of solids," *Proceedings of the Physical Society. Section A*, vol. 63, no. 5, p. 444, 1950. [Online]. Available: http://stacks.iop.org/0370-1298/63/i=5/a=302

[12] C. W. Mays, J. S. Vermaak, and D. Kuhlmann-Wilsdorf, "On surface stress and surface tension: Ii. determination of the surface stress of gold," *Surface Science*, vol. 12, no. 2, pp. 134–140, 1968, doi: 10.1016/0039-6028(68)90119-2. [Online]. Available: http://www.sciencedirect.com/science/article/pii/0039602868901192

[13] M. Diehm, P. Agoston, and K. Albe, "Size-dependent lattice expansion in nanoparticles: Reality or anomaly?" *Physical Chemistry Chemical Physics*, vol. 14, 2012.

[14] R. L. Snyder, J. Fiala, and H. J. Bunge, *Defect and microstructure analysis by diffraction*, ser. Inernational Union of Crystallography Book Series. New York: Oxford University Press Inc., 1999, iSBN: 0 19 850189 7.

[15] H. Zhang, B. Chen, and J. F. Banfield, "The size dependence of the surface free energy of titania nanocrystals," *Physical Chemistry Chemical Physics*, vol. 11, no. 14, pp. 2553–2558, 2009. [Online]. Available: http://dx.doi.org/10.1039/B819623K

[16] A. A. Levchenko, G. Li, J. Boerio-Goates, B. F. Woodfield, and A. Navrotsky, "TiO_2 stability landscape: Polymorphism, surface energy, and bound water energetics," *Chemistry of Materials*, vol. 18, no. 26, pp. 6324–6332, 2012/06/20 2006, doi: 10.1021/cm061183c. [Online]. Available: http://dx.doi.org/10.1021/cm061183c

[17] C. Herring, “Some theorems on the free energies of crystal surfaces,” *Physical Review*, vol. 82, no. 1, pp. 87–93, 1951, pR. [Online]. Available: http://link.aps.org/doi/10.1103/PhysRev.82.87

[18] A. Navrotsky, “Energetics of oxide nanoparticles,” *International Journal of Quantum Chemistry*, vol. 109, no. 12, pp. 2647–2657, 2009. [Online]. Available: http://dx.doi.org/10.1002/qua.21981

[19] M. V. Ganduglia-Pirovano, A. Hofmann, and J. Sauer, “Oxygen vacancies in transition metal and rare earth oxides: Current state of understanding and remaining challenges,” *Surface Science Reports*, vol. 62, no. 6, pp. 219–270, 2007, doi: 10.1016/j.surfrep.2007.03.002. [Online]. Available: http://www.sciencedirect.com/science/article/pii/S0167572907000295

[20] J. Lee, M. Nakamoto, and T. Tanaka, “Thermodynamic study on the melting of nanometer-sized gold particles on graphite substrate,” *Journal of Materials Science*, vol. 40, no. 9, pp. 2167–2171, 2005. [Online]. Available: http://dx.doi.org/10.1007/s10853-005-1927-6

[21] D. V. Talapin, A. L. Rogach, A. Kornowski, M. Haase, and H. Weller, “Highly luminescent monodisperse cdse and CdSe/ZnS nanocrystals synthesized in a hexadecylamine-trioctylphosphine-oxide-trioctylphospine mixture,” *Nano Letters*, vol. 1, no. 4, pp. 207–211, 2012/07/03 2001, doi: 10.1021/nl0155126. [Online]. Available: http://dx.doi.org/10.1021/nl0155126

[22] G. Anoop, T. S. Mark, and W. Hartmut, “Luminescent colloidal dispersion of silicon quantum dots from microwave plasma synthesis: Exploring the photoluminescence behavior across the visible spectrum,” *Advanced Functional Materials*, vol. 19, no. 5, pp. 696–703, 2009. [Online]. Available: http://dx.doi.org/10.1002/adfm.200801548

[23] W. L. K. Thomson, “On the equilibrium of vapour at a curved surface of liquid,” *Phil. Mag.*, vol. 42, pp. 448–452, 1871.

[24] J. R. Sambles, “An electron microscope study of evaporating gold particles: The kelvin equation for liquid gold and the lowering of the melting point of solid gold particles,” *Proceedings of the Royal Society of London. Series A, Mathematical and Physical Sciences (1934-1990)*, vol. 324, no. 1558, pp. 339–351, 1971. [Online]. Available: http://dx.doi.org/10.1098/rspa.1971.0143

[25] K. K. Nanda, F. E. Kruis, and H. Fissan, “Evaporation of free PbS nanoparticles: Evidence of the kelvin effect,” *Physical Review Letters*, vol. 89, no. 25, p. 256103, 2002. [Online]. Available: http://link.aps.org/doi/10.1103/PhysRevLett.89.256103

[26] K. K. Nanda, A. Maisels, F. E. Kruis, H. Fissan, and S. Stappert, “Higher surface energy of free nanoparticles,” *Physical Review Letters*, vol. 91, no. 10, p. 106102, 2003. [Online]. Available: http://link.aps.org/doi/10.1103/PhysRevLett.91.106102

[27] K. K. Nanda, A. Maisels, and F. E. Kruis, “Surface tension and sintering of free gold nanoparticles,” *The Journal of Physical Chemistry C*, vol. 112, no. 35, pp. 13 488–13 491, 2008, doi: 10.1021/jp803934n. [Online]. Available: http://dx.doi.org/10.1021/jp803934n

[28] H. Reiss, P. Mirabel, and R. L. Whetten, “Capillarity theory for the "coexistence" of liquid and solid clusters,” *The Journal of Physical Chemistry*, vol. 92, no. 26, pp. 7241–7246, 1988, doi: 10.1021/j100337a016. [Online]. Available: http://dx.doi.org/10.1021/j100337a016

[29] R. H. Lamoreaux and D. Hildebrand, “High-temperature vaporization behavior of oxides ii. oxides of Be, Mg, Ca, Sr, Ba, B, Al, Ga, Ti, Si, Ge, Sn, Pb, Zn, Cd, and Hg,” *Journal of Physical and Chemical Reference Data*, vol. 10, no. 3, pp. 419 – 443, 1987. [Online]. Available: http://www.nist.gov/srd/reprints.htm

[30] S. K. Friedlander, *Smoke, Dust, and Haze: fundamentals of aerosol dynamics*, 2nd ed. New York: Oxford University Press, 2000.

[31] Q. S. Mei and K. Lu, “Melting and superheating of crystalline solids: From bulk to nanocrystals,” *Progress in Materials Science*, vol. 52, no. 8, pp. 1175–1262, 2007, doi: 10.1016/j.pmatsci.2007.01.001. [Online]. Available: http://www.sciencedirect.com/science/article/pii/S0079642507000023

[32] J. W. Christian, “Solidification and melting,” in *The Theory of Transformations in Metals and Alloys*. Oxford: Pergamon, 2002, ch. 14, pp. 623–701, doi: 10.1016/B978-008044019-4/50019-2. [Online]. Available: http://www.sciencedirect.com/science/article/pii/B9780080440194500192

[33] B. Pluis, D. Frenkel, and J. F. van der Veen, "Surface-induced melting and freezing ii. a semi-empirical landau-type model," *Surface Science*, vol. 239, no. 3, pp. 282–300, 1990, doi: DOI: 10.1016/0039-6028(90)90231-V. [Online]. Available: http://www.sciencedirect.com/science/article/B6TVX-46SWVK8-HR/2/50dc022356284bab4124281306dc1921

[34] A. Rühm, H. Reichert, W. Donner, H. Dosch, C. Gruetter, and J. Bilgram, "Bulk and surface premelting phenomena in α-gallium," *Physical Review B*, vol. 68, no. 22, p. 224110, 2003. [Online]. Available: http://link.aps.org/doi/10.1103/PhysRevB.68.224110

[35] J. W. M. Frenken, P. M. J. Maree, and J. F. van der Veen, "Observation of surface-initiated melting," *Physical Review B*, vol. 34, no. 11, pp. 7506–7516, 1986, pRB. [Online]. Available: http://link.aps.org/doi/10.1103/PhysRevB.34.7506

[36] P. R. Couchman and W. A. Jesser, "Comments on melting mechanism for crystalline species," *Philosophical Magazine*, vol. 35, no. 3, pp. 787–790, 1977. [Online]. Available: <Go to ISI>://A1977DA72400018

[37] U. Tartaglino, T. Zykova-Timan, F. Ercolessi, and E. Tosatti, "Material surfaces and nanosystems close to the melting temperature," *Journal of Materials Science*, vol. 40, no. 9, pp. 2141–2147, 2005, 10.1007/s10853-005-1905-z. [Online]. Available: http://dx.doi.org/10.1007/s10853-005-1905-z

[38] P. Pawlow, "Über die Abhängigkeit des Schmelzpunktes von der Oberflächenenergie eines Festkörpers," *Zeitschrift fuer physikalische Chemie*, vol. 65, no. 545, p. 36, 1909.

[39] ——, "Über den Einfluss der Oberfläche einer festen Phase auf die latente Wärme und die Temperatur des Schmelzens," *Colloid and Polymer Science*, vol. 7, no. 1, pp. 37–39, 1910, 10.1007/BF01503961. [Online]. Available: http://dx.doi.org/10.1007/BF01503961

[40] M. Takagi, "Electron-diffraction study of liquid-solid transition of thin metal films," *Journal of the Physical Society of Japan*, vol. 9, no. 3, p. 359, 1956.

[41] J. Lee, T. Tanaka, J. Lee, and H. Mori, "Effect of substrates on the melting temperature of gold nanoparticles," *Calphad*, vol. 31, no. 1, pp. 105–111, 2007, doi: DOI: 10.1016/j.calphad.2006.10.001. [Online]. Available: http://www.sciencedirect.com/science/article/B6TWC-4M87BRN-1/2/a54d22809fd5185844da0eebd1469837

[42] H. Reiss and I. B. Wilson, "The effect of surface on melting point," *Journal of Colloid Science*, vol. 3, no. 6, pp. 551–561, 1948. [Online]. Available: http://www.sciencedirect.com/science/article/B759F-4CXCV04-S2/2/2b8ea3e5ef225428189c95f5ace1dbbe

[43] A. E. Curzon, "The use of electron diffraction in the study of (1) melting and supercooling of thin films; and (2) magnetic crystals." Ph.D. dissertation, University of London, London, 1959-60.

[44] K. J. Hanszen, "Theoretische Uuntersuchungen über den Schmelzpunkt kleiner Kügelchen - ein Beitrag zur Thermodynamik der Gernzflächen," *Zeitschrift für Physik*, vol. 157, no. 5, pp. 523–553, 1960. [Online]. Available: <Go to ISI>://A1960WN77700001

[45] R. R. Vanfleet and J. M. Mochel, "Thermodynamics of melting and freezing in small particles," *Surface Science*, vol. 341, no. 1, pp. 40–50, 1995, doi:10.1016/0039-6028(95)00728-8. [Online]. Available: http://www.ingentaconnect.com/content/els/00396028/1995/00000341/00000001/art00728 http://dx.doi.org/10.1016/0039-6028(95)00728-8

[46] P. R. Couchman and W. A. Jesser, "Thermodynamic theory of size dependence of melting temperature in metals," *Nature*, vol. 269, no. 5628, pp. 481–483, 1977, 10.1038/269481a0 10.1038/269481a0. [Online]. Available: http://dx.doi.org/10.1038/269481a0

[47] C. Q. Sun, Y. Wang, B. K. Tay, S. Li, H. Huang, and Y. B. Zhang, "Correlation between the melting point of a nanosolid and the cohesive energy of a surface atom," *Journal of Physical Chemistry B*, vol. 106, no. 41, pp. 10 701–10 705, Oct 2002. [Online]. Available: <Go to ISI>://000178548600025

[48] C. Q. Sun, H. L. Bai, S. Li, B. K. Tay, and E. Y. Jiang, "Size-effect on the electronic structure and the thermal stability of a gold nanosolid," *Acta Materialia*, vol. 52, no. 2, pp. 501–505, 2004, doi: 10.1016/j.actamat.2003.09.033. [Online]. Available: http://www.sciencedirect.com/science/article/pii/S1359645403005676

[49] L. Pauling, "Atomic radii and interatomic distances in metals," *Journal of the American Chemical Society*, vol. 69, no. 3, pp. 542–553, 1947, doi: 10.1021/ja01195a024. [Online]. Available: http://dx.doi.org/10.1021/ja01195a024

[50] V. M. Goldschmidt, "Krystallbau und chemische Zusammensetzung," *Berichte der deutschen chemischen Gesellschaft (A and B Series)*, vol. 60, no. 5, pp. 1263–1296, 1927. [Online]. Available: http://dx.doi.org/10.1002/cber.19270600550

[51] K. K. Nanda, S. N. Sahu, and S. N. Behera, "Liquid-drop model for the size-dependent melting of low-dimensional systems," *Physical Review A*, vol. 66, no. 1, Jul 2002. [Online]. Available: <Go to ISI>://000177200800074

[52] W. H. Qi, M. P. Wang, M. Zhou, X. Q. Shen, and X. F. Zhang, "Modeling cohesive energy and melting temperature of nanocrystals," *Journal of Physics and Chemistry of Solids*, vol. 67, no. 4, pp. 851–855, 2006. [Online]. Available: http://www.sciencedirect.com/science/article/B6TXR-4J4HH8X-2/2/dffb2010e7710e0c155570c1bed16fbc

[53] C. Q. Sun, L. K. Pan, Y. Q. Fu, B. K. Tay, and S. Li, "Size dependence of the 2p-level shift of nanosolid silicon," *The Journal of Physical Chemistry B*, vol. 107, no. 22, pp. 5113–5115, 2003, doi: 10.1021/jp0272015. [Online]. Available: http://dx.doi.org/10.1021/jp0272015

[54] C. Q. Sun, H. L. Bai, B. K. Tay, S. Li, and E. Y. Jiang, "Dimension, strength, and chemical and thermal stability of a single C-C bond in carbon nanotubes," *The Journal of Physical Chemistry B*, vol. 107, no. 31, pp. 7544–7546, 2012/07/09 2003, doi: 10.1021/jp035070h. [Online]. Available: http://dx.doi.org/10.1021/jp035070h

[55] Q. Sun, C. M. B. Li, H. L., and E. Y. Jiang, "Melting point oscillation of a solid over the whole range of sizes," *Nanotechnology*, vol. 16, no. 8, p. 1290, 2005. [Online]. Available: http://stacks.iop.org/0957-4484/16/i=8/a=051

[56] A. Suresh, M. J. Mayo, W. D. Porter, and C. J. Rawn, "Crystallite and grain-size-dependent phase transformations in yttria-doped zirconia," *Journal of the American Ceramic Society*, vol. 86, no. 2, pp. 360–362, 2003. [Online]. Available: http://dx.doi.org/10.1111/j.1151-2916.2003.tb00025.x

[57] A. Navrotsky, "Energetic clues to pathways to biomineralization: Precursors, clusters, and nanoparticles," *Proceedings of the National Academy of Sciences of the United States of America*, vol. 101, no. 33, pp. 12 096–12 101, 2004. [Online]. Available: http://www.pnas.org/content/101/33/12096.abstract

[58] Y. Ma, R. H. Castro, W. Zhou, and A. Navrotsky, "Surface enthalpy and enthalpy of water adsorption of nanocrystalline tin dioxide: Thermodynamic insight on the sensing activity." *Journal of Materials Research*, vol. 26, no. 7, pp. 848–853, 2011. [Online]. Available: http://journals.cambridge.org/abstract_S088429141000097X

[59] F. Xu, W. Zhou, and A. Navrotsky, "Cadmium selenide: Surface and nanoparticle energetics." *Journal of Materials Research*, vol. 26, no. 5, pp. 720–725, 2011. [Online]. Available: http://journals.cambridge.org/abstract_S0884291411000203

[60] R. Andrievskii and A. Khachoyan, "Role of size-dependent effects and interfaces in physicochemical properties of consolidated nanomaterials," *Russian Journal of General Chemistry*, vol. 80, no. 3, pp. 555–566, 2010. [Online]. Available: http://dx.doi.org/10.1134/S1070363210030370

[61] A. Navrotsky, C. Ma, K. Lilova, and N. Birkner, "Nanophase transition metal oxides show large thermodynamically driven shifts in oxidation-reduction equilibria," *Science*, vol. 330, no. 6001, pp. 199–201, 2010. [Online]. Available: http://www.sciencemag.org/content/330/6001/199.abstract

[62] G. Guenther, G. Schierning, R. Theissmann, R. Kruk, R. Schmechel, C. Baehtz, and A. Prodi-Schwab, "Formation of metallic indium-tin phase from indium-tin-oxide nanoparticles under reducing conditions and its influence on the electrical properties," *Journal of Applied Physics*, vol. 104, no. 3, p. 10, Aug 2008. [Online]. Available: <Go to ISI>://000258493900138

[63] J. T. Miller, A. J. Kropf, Y. Zha, J. R. Regalbuto, L. Delannoy, C. Louis, E. Bus, and J. A. van Bokhoven, "The effect of gold particle size on Au-Au bond length and reactivity toward oxygen in supported catalysts," *Journal of Catalysis*, vol. 240, no. 2, pp. 222–234, 2006, doi: 10.1016/j.jcat.2006.04.004. [Online]. Available: http://www.sciencedirect.com/science/article/pii/S0021951706001205

[64] Scientific Group Thermodata Europe (SGTE), *Thermodynamic Properties of Elements, Ac to C60*, ser. Landolt-Boernstein - Group IV Physical Chemistry, Numerical Data and Functional Relationships in Science and Technology. Springer Berlin / Heidelberg, 2002, vol. 19A1, ISBN: 3540653279. [Online]. Available: http://dx.doi.org/10.1007/10652891_4

[65] A. N. Goldstein, C. M. Echer, and A. P. Alivisatos, "Melting in semiconductor nanocrystals," *Science*, vol. 256, no. 5062, pp. 1425–1427, 1992, 10.1126/science.256.5062.1425. [Online]. Available: http://www.sciencemag.org/cgi/content/abstract/256/5062/1425

[66] X. Kuang, G. Carotenuto, and L. Nicolais, "A review of ceramic sintering and suggestions on reducing sintering temperatures," *Advanced Performance Materials*, vol. 4, no. 3, pp. 257–274, 1997, 10.1023/A:1008621020555. [Online]. Available: <Go to ISI>://A1997XV25400001

[67] H. H. Farrell and C. D. Van Siclen, "Binding energy, vapor pressure, and melting point of semiconductor nanoparticles," vol. 25, 2007, pp. 1441–1447. [Online]. Available: http://dx.doi.org/10.1116/1.2748415

[68] N. Kumada, N. Kinomura, P. M. Woodward, and A. W. Sleight, "Crystal structure of Bi_2O_4 with β - Sb_2O_4 -type structure," *Journal of Solid State Chemistry*, vol. 116, no. 2, pp. 281–285, 1995, doi: 10.1006/jssc.1995.1214. [Online]. Available: http://www.sciencedirect.com/science/article/pii/S0022459685712145

[69] M. Jansen, "Darstellung von wasserfreiem $KBiO_3$," *Z. Naturforsch.*, vol. 32 b, pp. 1340–1, 1977.

[70] A. Zav'yalova, R. Imamov, and Z. Pinsker, "Crystal structure of hexagonal BiO," *Kristallografiya*, vol. 10, p. 480, 1965.

[71] X. L. Chen and W. Eysel, "The stabilization of β-Bi_2O_3 by CeO_2," *Journal of Solid State Chemistry*, vol. 127, no. 1, pp. 128–130, Nov 1996. [Online]. Available: <Go to ISI>://A1996WA80200019

[72] J. Cedomir, M. Zdujic, D. Poleti, L. Karanovic, and M. Mitric, "Structural and electrical properties of the $2Bi_2O_3$-$3\,ZrO_2$ system," *Journal of Solid State Chemistry*, vol. 181, no. 6, pp. 1321–1329, 2008, doi: 10.1016/j.jssc.2008.02.038. [Online]. Available: http://www.sciencedirect.com/science/article/pii/S0022459608001199

[73] M. Mehring, "From molecules to bismuth oxide-based materials: Potential homo- and heterometallic precursors and model compounds," *Coordination Chemistry Reviews*, vol. 251, no. 7-8, pp. 974–1006, 2007, 0010-8545 doi: DOI: 10.1016/j.ccr.2006.06.005. [Online]. Available: http://www.sciencedirect.com/science/article/B6TFW-4K6645T-3/2/cbb47463820e7cad5fba0e5d5d4f47f2

[74] A. A. Zav'yalova and R. M. Imamov, "Special features of the crystal structure of bismuth oxides," *Journal of Structural Chemistry*, vol. 13, no. 5, pp. 811–814, 1973. [Online]. Available: http://dx.doi.org/10.1007/BF00738892

[75] L. Klinkova, V. Nikolaichik, N. Barkovskii, and V. Fedotov, "Thermal stability of Bi_2O_3," *Russian Journal of Inorganic Chemistry*, vol. 52, no. 12, pp. 1822–1829, 2007. [Online]. Available: http://dx.doi.org/10.1134/S0036023607120030

[76] J. W. Medernach and R. L. Snyder, "Powder diffraction patterns and structures of the bismuth oxides," *Journal of the American Ceramic Society*, vol. 61, no. 11-12, pp. 494–497, 1978. [Online]. Available: http://dx.doi.org/10.1111/j.1151-2916.1978.tb16125.x

[77] M. Yashima and D. Ishimura, "Crystal structure and disorder of the fast oxide-ion conductor cubic bi2o3," *Chemical Physics Letters*, vol. 378, no. 3-4, pp. 395–399, 2003, doi: 10.1016/j.cplett.2003.07.014. [Online]. Available: http://www.sciencedirect.com/science/article/pii/S0009261403012958

[78] S. Hull, S. T. Norberg, M. G. Tucker, S. G. Eriksson, C. E. Mohn, and S. Stolen, "Neutron total scattering study of the δ and β phases of Bi_2O_3," *Dalton Transactions*, no. 40, pp. 8737–8745, 2009. [Online]. Available: http://dx.doi.org/10.1039/B910484B

[79] S. K. Blower and C. Greaves, "The structure of β-Bi_2O_3 from powder neutron diffraction data," *Acta Crystallographica Section C*, vol. 44, no. 4, pp. 587–589, 1988. [Online]. Available: http://dx.doi.org/10.1107/S0108270187011661

[80] D. Barreca, F. Morazzoni, G. A. Rizzi, R. Scotti, and E. Tondello, "Molecular oxygen interaction with Bi_2O_3: a spectroscopic and spectromagnetic investigation," *Physical Chemistry Chemical Physics*, vol. 3, no. 9, pp. 1743–1749, 2001. [Online]. Available: http://dx.doi.org/10.1039/B009482J

[81] G. Eriksson, "Thermodynamic studies of high-temperature equilibria. XII. SOLGASMIX, a computer program for calculation of equilibrium compositions in multiphase systems." *Chemica Scripta*, vol. 8, pp. 100–103, 1975.

[82] S. C. Marschman and D. C. Lynch, "Review of the Bi and Bi-O vapor systems," *The Canadian Journal of Chemical Engineering*, vol. 62, no. 6, pp. 875–879, 1984. [Online]. Available: http://dx.doi.org/10.1002/cjce.5450620620

[83] O. M. Uy and J. Drowart, "Mass spectrometric determination of the dissociation energies of the molecules BiO, BiS, BiSe and BiTe," *Transactions of the Faraday Society*, vol. 65, pp. 3221–3230, 1969. [Online]. Available: http://dx.doi.org/10.1039/TF9696503221

[84] C. K. Kazenas, D. M. Chizhikov, Y. U. Tsvetkov, and M. V. Olshevskii, "Mass spectrometric study of bismuth oxide vaporization," *Doklady Akademii Nauk SSSR*, vol. 207, pp. 354–355, 1972.

[85] L. N. Sidorov, I. Minayeva, E. Z. Zasorin, I. D. Sorokin, and A. Y. Borshchevskiy, "Mass-spectrometric investigation of gas-phase equilibria over bismuth trioxide," *High Temperature Science*, vol. 12, no. 3, pp. 175–196, 1980. [Online]. Available: <Go to ISI>://A1980KN21000002

[86] E. Oniyama and P. G. Wahlbeck, "Phase equilibria in the bismuth-oxygen system," *The Journal of Physical Chemistry B*, vol. 102, no. 22, pp. 4418–4425, 1998. [Online]. Available: http://pubs.acs.org/doi/abs/10.1021/jp980166a

[87] R. Metz, C. Machado, M. Elkhatib, J. J. Counioux, H. Delalu, and K. Alabdullah, "Stabilité thermique de composés intervenants au cours du frittage des varistances ZnO, Thermal stability of compounds in ZnO varistor sintering," *Silicates industriels*, vol. 66, no. 1-2, pp. 15–22, 2001.

[88] J. Opitz-Coutureau, A. Fielicke, B. Kaiser, and K. Rademann, "Antimony and bismuth oxide cluster ions," *Physical Chemistry Chemical Physics*, vol. 3, no. 15, pp. 3034–3041, 2001. [Online]. Available: <Go to ISI>://000170012900012

[89] S. Shornikov, "Effect of redox conditions on the evaporation of oxide melts in the CaO-MgO-FeO-Al_2O_3-SiO_2 system," *Geochemistry International*, vol. 46, no. 7, pp. 724–729, 2008. [Online]. Available: http://dx.doi.org/10.1134/S0016702908070069

[90] Z. Z. Fang, Ed., *Sintering of Advanced Materials*. Woodhead Publishing in Materials, 2010, ISBN: 978 1 84569 562 0. [Online]. Available: http://www.woodheadpublishing.com/en/book.aspx?bookID=1570

[91] K. N. Marushkin and A. S. Alikhanyan, "Mass-spectrometry investigation of oxides gomogeneity range," *Doklady Akademii Nauk*, vol. 329, no. 4, pp. 452–454, 1993. [Online]. Available: <Go to ISI>://WOS:A1993LR07300019

[92] C. Hwang, S. Fujino, and K. Morinaga, "Density of Bi_2O_3-B_2O_3 binary melts," *Journal of the American Ceramic Society*, vol. 87, no. 9, pp. 1677–1682, 2004. [Online]. Available: <Go to ISI>://000224192900010

[93] S. Fujino, C. Hwang, and K. Morinaga, "Surface tension of PbO-B_2O_3 and Bi_2O_3-B_2O_3 glass melts," *Journal of Materials Science*, vol. 40, no. 9, pp. 2207–2212, 2005, 10.1007/s10853-005-1934-7. [Online]. Available: http://dx.doi.org/10.1007/s10853-005-1934-7

[94] H. T. Fan, S. S. Pan, X. M. Teng, C. Ye, G. H. Li, and L. D. Zhang, "δ-Bi_2O_3 thin films prepared by reactive sputtering: Fabrication and characterization," *Thin Solid Films*, vol. 513, no. 1-2, pp. 142–147, 2006, doi: 10.1016/j.tsf.2006.01.074. [Online]. Available: http://www.sciencedirect.com/science/article/pii/S0040609006002549

[95] C. C. Huang, I. C. Leu, and K. Z. Fung, "Fabrication of δ-Bi_2O_3 nanowires," *Electrochemical and Solid-State Letters*, vol. 8, no. 4, pp. A204–A206, 2005. [Online]. Available: http://esl.ecsdl.org/content/8/4/A204.abstract

[96] K. Latha, L. Jin-Han, and M. Yuan-Ron, "Synthesis of bismuth oxide nanostructures by an oxidative metal vapour phase deposition technique," *Nanotechnology*, no. 29, p. 295605, 2007. [Online]. Available: http://stacks.iop.org/0957-4484/18/295605

[97] W. Dong and C. Zhu, "Optical properties of surface-modified Bi_2O_3 nanoparticles," *Journal of Physics and Chemistry of Solids*, vol. 64, no. 2, pp. 265–271, 2003, doi: 10.1016/S0022-3697(02)00291-3. [Online]. Available: http://www.sciencedirect.com/science/article/pii/S0022369702002913

[98] B. Yang, M. Mo, H. Hu, C. Li, X. Yang, Q. Li, and Y. Qian, "A rational self-sacrificing template route to β-Bi_2O_3 nanotube arrays," *European Journal of Inorganic Chemistry*, vol. 2004, no. 9, pp. 1785–1787, 2004. [Online]. Available: http://dx.doi.org/10.1002/ejic.200300966

[99] L. Maedler and S. E. Pratsinis, "Bismuth oxide nanoparticles by flame spray pyrolysis," *Journal of the American Ceramic Society*, vol. 85, no. 7, pp. 1713–1718, 2002. [Online]. Available: http://dx.doi.org/10.1111/j.1151-2916.2002.tb00340.x

[100] F. Gao, Q. Lu, and S. Komarneni, "Protein-assisted synthesis of single-crystal nanowires of bismuth compounds," *Chemical Communications*, no. 4, pp. 531–533, 2005. [Online]. Available: http://dx.doi.org/10.1039/B413584A

[101] H.-X. Hu, K.-q. Qiu, and G.-f. Xu, "Preparation of nanometer δ- and β-bismuth trioxide by vacuum vapor-phase oxidation," *Transactions of Nonferrous Metals Society of China*, vol. 16, no. 1, pp. 173–177, 2006. [Online]. Available: http://www.sciencedirect.com/science/article/B82XX-4JG3RW9-13/2/2e442013bbba0c8c52fa7289177be7e2

[102] A. T. Dinsdale, "SGTE data for pure elements," *Calphad*, vol. 15, no. 4, pp. 317–425, doi: DOI: 10.1016/0364-5916(91)90030-N. [Online]. Available: http://www.sciencedirect.com/science/article/B6TWC-48CWY4X-9M/2/78112cc6c4cef36ef1f38fc75c5ecaf3

[103] L. E. Murr, *Interfacial Phenomena in Metal and Alloys*. Addison-Wesley Publishing Company, 1975, vol. 8. [Online]. Available: http://dx.doi.org/10.1002/piuz.19770080108

[104] J. Lee, M. Nakamoto, and T. Tanaka, "Thermodynamic study on the melting of nanometer-sized gold particles on graphite substrate," *Journal of Materials Science*, vol. 40, no. 9, pp. 2167–2171, 2005, 10.1007/s10853-005-1927-6. [Online]. Available: http://dx.doi.org/10.1007/s10853-005-1927-6

[105] W. M. Haynes, Ed., *CRC Handbook of Chemistry and Physics*, 91st ed. CRC Press, 2010.

[106] T. Iida and R. I. Guthrie, *The Physical Properties of Liquid Metals*. Oxford University Press, USA, 1993.

[107] S. K. Rhee, "Critical surface energies of Al_2O_3 and graphite," *Journal of the American Ceramic Society*, vol. 55, no. 6, pp. 300–303, 1972. [Online]. Available: http://dx.doi.org/10.1111/j.1151-2916.1972.tb11289.x

[108] J. Lee, T. Tanaka, K. Seo, N. Hirai, J.-G. Lee, and H. Mori, "Wetting of Au and Ag particles on monocrystalline graphite substrates," *Rare Metals*, vol. 25, no. 5, pp. 469–472, 2006, doi: 10.1016/S1001-0521(06)60086-7. [Online]. Available: http://www.sciencedirect.com/science/article/pii/S1001052106600867

[109] J. Lee, H. Ishimura, and T. Tanaka, "Anisotropy of wetting of molten Au on differently oriented α-Al_2O_3 single crystals," *Scripta Materialia*, vol. 54, no. 7, pp. 1369–1373, 2006, doi: 10.1016/j.scriptamat.2005.12.006. [Online]. Available: http://www.sciencedirect.com/science/article/pii/S1359646205008316

[110] A. Pinto, A. R. Pennisi, G. Faraci, G. D'Agostino, S. Mobilio, and F. Boscherini, "Evidence for truncated octahedral structures in supported gold clusters," *Physical Review B*, vol. 51, no. 8, pp. 5315–5321, 1995. [Online]. Available: http://link.aps.org/doi/10.1103/PhysRevB.51.5315

[111] X. Zhang, J.-l. Kuo, M. Gu, X. Fan, P. Bai, Q.-G. Song, and C. Q. Sun, "Local structure relaxation, quantum trap depression, and valence charge polarization induced by the shorter-and-stronger bonds between under-coordinated atoms in gold nanostructures," *Nanoscale*, vol. 2, no. 3, pp. 412–417, 2010. [Online]. Available: http://dx.doi.org/10.1039/B9NR00326F

[112] J. P. Borel, "Thermodynamical size effect and the structure of metallic clusters," *Surface Science*, vol. 106, no. 1-3, pp. 1–9, 1981. [Online]. Available: http://www.sciencedirect.com/science/article/B6TVX-46TY224-SW/2/6f7cc4979436aa1ecd5ea75e27832d65

[113] Y. G. Chushak and L. S. Bartell, "Melting and freezing of gold nanoclusters," *The Journal of Physical Chemistry B*, vol. 105, no. 47, pp. 11 605–11 614, 2001, doi: 10.1021/jp0109426. [Online]. Available: http://dx.doi.org/10.1021/jp0109426

[114] G. Krishna Goswami and K. Kar Nanda, "Thermodynamic models for the size-dependent melting of nanoparticles: Different hypotheses," *Current Nanoscience*, vol. 8, no. 2, pp. 305–311, doi:10.2174/157341312800167731. [Online]. Available: http://www.ingentaconnect.com/content/ben/cnano/2012/00000008/00000002/art00020 http://dx.doi.org/10.2174/157341312800167731

[115] J. Leitner, "Melting point of nanoparticles," *Chemicke Listy*, vol. 105, no. 3, pp. 174–185. [Online]. Available: <Go to ISI>://WOS:000288820200004

[116] J. Lee, H. Ishimura, and T. Tanaka, "Novel method determining contact angle of liquid au on solid al2o3 single crystal (0001) surface at 1373k," in *Advanced Structural and Functional Materials Design, Proceedings*, ser. Materials Science Forum, Y. Umakoshi and S. Fujimoto, Eds., 2006, vol. 512, pp. 309–312, international Symposium on Advanced Structural and Functional Materials Design NOV 10-12, 2004 Osaka, JAPAN. [Online]. Available: <Go to ISI>://000237250000053

[117] K. Dick, T. Dhanasekaran, Z. Zhang, and D. Meisel, "Size-dependent melting of silica-encapsulated gold nanoparticles," *Journal of the American Chemical Society*, vol. 124, no. 10, pp. 2312–2317, 2002, doi: 10.1021/ja017281a. [Online]. Available: http://dx.doi.org/10.1021/ja017281a

[118] H. W. Sheng, "Superheating and melting-point depression of Pb nanoparticles embedded in Al matrices," *Philosophical Magazine Letters*, vol. 73, no. 4, pp. 179–186, 2012/06/15 1996, doi: 10.1080/095008396180812. [Online]. Available: http://dx.doi.org/10.1080/095008396180812

[119] K. Chattopadhyay, V. Bhattacharya, K. Biswas, M. Luysberg, K. Tillmann, and T. Weirich, "Melting and solidification of alloys embedded in a matrix at nanoscale," in *EMC 2008 14th European Microscopy Congress 1 to 5 September 2008, Aachen, Germany*. Springer Berlin Heidelberg, 2008, ch. I2.6, pp. 461–462. [Online]. Available: http://dx.doi.org/10.1007/

[120] T. Castro, R. Reifenberger, E. Choi, and R. P. Andres, "Size-dependent melting temperature of individual nanometer-sized metallic clusters," *Physical Review B*, vol. 42, no. 13, p. 8548, 1990. [Online]. Available: http://link.aps.org/abstract/PRB/v42/p8548

[121] M. A. van Huis, N. P. Young, G. Pandraud, J. F. Creemer, D. Vanmaekelbergh, A. I. Kirkland, and H. W. Zandbergen, "Atomic imaging of phase transitions and morphology transformations in nanocrystals," *Advanced Materials*, vol. 21, no. 48, pp. 4992–4995, 2009. [Online]. Available: http://dx.doi.org/10.1002/adma.200902561

[122] N. Eustathopoulos and D. Pique, "Calculation of solid-liquid-vapour contact angles for binary metallic systems," *Scripta Metallurgica*, vol. 14, no. 12, pp. 1291–1296, 1980, doi: 10.1016/0036-9748(80)90181-7. [Online]. Available: http://www.sciencedirect.com/science/article/pii/0036974880901817

[123] A. Proykova and R. S. Berry, "Insights into phase transitions from phase changes of clusters," *Journal of Physics B-Atomic Molecular and Optical Physics*, vol. 39, no. 9, pp. R167–R202, 2006. [Online]. Available: <Go to ISI>://WOS:000238319900003

[124] R. S. Berry and M. S. Boris, "Phase transitions in various kinds of clusters," *Physics-Uspekhi*, vol. 52, no. 2, p. 137, 2009. [Online]. Available: http://stacks.iop.org/1063-7869/52/i=2/a=R02

[125] T. Bachels, H.-J. Guentherodt, and R. Schaefer, "Melting of isolated tin nanoparticles," *Physical Review Letters*, vol. 85, no. 6, p. 1250, 2000, copyright (C) 2007 The American Physical Society Please report any problems to prola@aps.org PRL. [Online]. Available: http://link.aps.org/abstract/PRL/v85/p1250

[126] F. Ercolessi, W. Andreoni, and E. Tosatti, "Melting of small gold particles: Mechanism and size effects," *Physical Review Letters*, vol. 66, no. 7, pp. 911–914, 1991. [Online]. Available: http://link.aps.org/doi/10.1103/PhysRevLett.66.911

[127] K. Koga, T. Ikeshoji, and K.-i. Sugawara, "Size- and temperature-dependent structural transitions in gold nanoparticles," *Physical Review Letters*, vol. 92, no. 11, p. 115507, 2004. [Online]. Available: http://link.aps.org/doi/10.1103/PhysRevLett.92.115507

[128] Y. Wang, S. Teitel, and C. Dellago, "Melting of icosahedral gold nanoclusters from molecular dynamics simulations," *The Journal of Chemical Physics*, vol. 122, no. 21, pp. 214 722–16, 2005. [Online]. Available: http://dx.doi.org/10.1063/1.1917756

[129] C. L. Cleveland, W. D. Luedtke, and U. Landman, "Melting of gold clusters," *Physical Review B*, vol. 60, no. 7, pp. 5065–5077, 1999. [Online]. Available: http://link.aps.org/doi/10.1103/PhysRevB.60.5065

[130] N. Wang, "Melting, solidification and sintering/coalescence of nanoparticles," Ph.D. dissertation, Ohio State University, 2010. [Online]. Available: http://rave.ohiolink.edu/etdc/view?acc_num=osu1284476300

[131] Y. Qi, T. Cagin, W. L. Johnson, and W. A. Goddard Iii, "Melting and crystallization in Ni nanoclusters: The mesoscale regime," *The Journal of Chemical Physics*, vol. 115, no. 1, pp. 385–394, 2001. [Online]. Available: http://dx.doi.org/10.1063/1.1373664

[132] W. Qi, B. Huang, and M. Wang, "Bond-length and -energy variation of small gold nanoparticles," *Journal of Computational and Theoretical Nanoscience*, vol. 6, no. 3, pp. 635–639, 2009, doi:10.1166/jctn.2009.1085. [Online]. Available: http://www.ingentaconnect.com/content/asp/jctn/2009/00000006/00000003/art00027 http://dx.doi.org/10.1166/jctn.2009.1085

[133] G. L. Allen, R. A. Bayles, W. W. Gile, and W. A. Jesser, "Small particle melting of pure metals," *Thin Solid Films*, vol. 144, no. 2, pp. 297–308, 1986. [Online]. Available: http://www.sciencedirect.com/science/article/B6TW0-46T4RFJ-8W/2/e345724a1ba07026e26a170f40e4d917

[134] S. L. Lai, J. Y. Guo, V. Petrova, G. Ramanath, and L. H. Allen, "Size-dependent melting properties of small tin particles: Nanocalorimetric measurements," *Physical Review Letters*, vol. 77, no. 1, pp. 99–102, Jul 1996. [Online]. Available: <Go to ISI>://A1996UU47500026

[135] C. Q. Sun, L. K. Pan, Y. Q. Fu, B. K. Tay, and S. Li, "Size dependence of the 2p-level shift of nanosolid silicon," *The Journal of Physical Chemistry B*, vol. 107, no. 22, pp. 5113–5115, 2003, doi: 10.1021/jp0272015. [Online]. Available: http://dx.doi.org/10.1021/jp0272015

[136] S. Xiong, W. Qi, Y. Cheng, B. Huang, M. Wang, and Y. Li, "Universal relation for size dependent thermodynamic properties of metallic nanoparticles," *Physical Chemistry Chemical Physics*, vol. 13, no. 22, pp. 10 652–10 660, 2011. [Online]. Available: http://dx.doi.org/10.1039/C0CP90161J

[137] R. C. Tolman, "The effect of droplet size on surface tension," *The Journal of Chemical Physics*, vol. 17, no. 3, pp. 333–337, 1949. [Online]. Available: http://dx.doi.org/10.1063/1.1747247

[138] K. Lu and N. X. Sun, "Grain-boundary enthalpy of nanocrystalline selenium," *Philosophical Magazine Letters*, vol. 75, no. 6, pp. 389–395, Jun 1997. [Online]. Available: <Go to ISI>://WOS:A1997XB91800008

[139] M. Diehm, "Finite-size effects in oxide nanoparticles," Master's thesis, TU Darmstadt, Darmstadt, March 2010 2010.

[140] S. Xiong, W. Qi, Y. Cheng, B. Huang, M. Wang, and Y. Li, "Modeling size effects on the surface free energy of metallic nanoparticles and nanocavities," *Physical Chemistry Chemical Physics*, vol. 13, no. 22, pp. 10 648–10 651, 2011. [Online]. Available: http://dx.doi.org/10.1039/C0CP02102D

[141] Y. Shibuta and T. Suzuki, "A molecular dynamics study of the phase transition in bcc metal nanoparticles," *The Journal of Chemical Physics*, vol. 129, no. 14, pp. 144 102–10, 2008. [Online]. Available: http://dx.doi.org/10.1063/1.2991435

[142] R. F. Tournier, "Presence of intrinsic growth nuclei in overheated and undercooled liquid elements," *Physica B: Condensed Matter*, vol. 392, no. 1-2, pp. 79 – 91, 2007. [Online]. Available: http://www.sciencedirect.com/science/article/pii/S0921452606017868

[143] R. F. Tournier and E. Beaugnon, "Texturing by cooling a metallic melt in a magnetic field," *Science and Technology of Advanced Materials*, vol. 10, no. 1, p. 014501, 2009. [Online]. Available: http://stacks.iop.org/1468-6996/10/i=1/a=014501

[144] J. Weissmüller, J.ller, "Comment on: Lattice contraction and surface stress of fcc nanocrystals," *The Journal of Physical Chemistry B*, vol. 106, no. 4, pp. 889–890, 2012/06/20 2002, doi: 10.1021/jp013381r. [Online]. Available: http://dx.doi.org/10.1021/jp013381r

[145] J. Murai, T. Marukawa, T. Mima, S. Arai, K. Sasaki, and H. Saka, "Size dependence of the contact angle of liquid clusters ofBi and Sn supported on SiO_2, Al_2O_3, graphite, diamond and AlN," *Journal of Materials Science*, vol. 41, no. 9, pp. 2723–2727, 2006. [Online]. Available: http://dx.doi.org/10.1007/s10853-006-7875-y

[146] S. C. Hendy, "A thermodynamic model for the melting of supported metal nanoparticles," *Nanotechnology*, vol. 18, no. 17, p. 175703, 2007. [Online]. Available: http://stacks.iop.org/0957-4484/18/i=17/a=175703

[147] R. Kofman, P. Cheyssac, A. Aouaj, Y. Lereah, G. Deutscher, T. Ben-David, J. M. Penisson, and A. Bourret, "Surface melting enhanced by curvature effects," *Surface Science*, vol. 303, no. 1-2, pp. 231–246, 1994, doi: DOI: 10.1016/0039-6028(94)90635-1. [Online]. Available: http://www.sciencedirect.com/science/article/B6TVX-46SWVYP-1KT/2/65bbb43b1903e77a161d0e055c927726

[148] H. Sakai, "Surface-induced melting of small particles," *Surface Science*, vol. 351, no. 1-3, pp. 285–291, 1996. [Online]. Available: <Go to ISI>://A1996UM63400031

[149] D. Hummes, "Entwicklung eines Differentiellen Mobilitäts-Analysators zur Bereitstellung von monodispersen Partikeln im Nanometergrössenbereich," PhD, Pro Universitate Verlag, Sinzheim, 1997, iSBN: 3-932490-21-5.

[150] M. Rouenhoff and F. Kruis, "Nanoparticle film formation by means of an electrostatic precipitator, abstract t012a01," *European Aerosol Conference 2009, Karlsruhe*, 2009.

[151] P. Stephan, K. Schaber, S. Karl, and F. Mayinger, *Thermodynamik, Grundlagen und technische Anwendungen*, 15th ed., ser. Band 2: Mehrstoffsysteme und chemische Reaktionen. Heidelberg: Springer, 2010, vol. 2.

[152] S. Polarz, R. Abhijit, M. Michael, H. Simon, S. Detlef, S. Lars, B. Gerd, E. K. Frank, and D. Matthias, "Chemical vapor synthesis of size-selected zinc oxide nanoparticles," *Small*, vol. 1, no. 5, pp. 540–552, 2005, 10.1002/smll.200400085. [Online]. Available: http://dx.doi.org/10.1002/smll.200400085

[153] J. Rodriguez-Carvajal and T. Roisnel, "Line broadening analysis using fullprof*: Determination of microstructural properties," in *European Powder Diffraction Epdic 8*, ser. Materials Science Forum, Y. Andersson, E. J. Mittemeijer, and U. Welzel, Eds., 2004, vol. 443-4, pp. 123–126, 8th European Powder Diffraction Conference MAY 23-26, 2002 Uppsala, SWEDEN. [Online]. Available: <Go to ISI>://WOS:000189421300025

[154] R. A. Young and D. B. Wiles, "Profile shape functions in rietveld refinements," *Journal of Applied Crystallography*, vol. 15, no. 4, pp. 430–438, 1982. [Online]. Available: http://dx.doi.org/10.1107/S002188988201231X

[155] E. Buhr, N. Senftleben, T. Klein, D. Bergmann, D. Gnieser, C. G. Frase, and H. Bosse, "Characterization of nanoparticles by scanning electron microscopy in transmission mode," *Measurement Science and Technology*, vol. 20, no. 8, p. 084025, 2009. [Online]. Available: http://stacks.iop.org/0957-0233/20/i=8/a=084025

[156] R. F. Egerton, P. Li, and M. Malac, "Radiation damage in the TEM and SEM," *Micron*, vol. 35, no. 6, pp. 399–409, 2004, doi: 10.1016/j.micron.2004.02.003. [Online]. Available: http://www.sciencedirect.com/science/article/pii/S0968432804000381

[157] D. Risold, B. Hallstedt, L. J. Gauckler, H. L. Lukas, and S. G. Fries, "The bismuth-oxygen system," *Journal of Phase Equilibria*, vol. 16, no. 3, pp. 223–234, Jun 1995, iSI Document Delivery No.: TT793 Times Cited: 33 Cited Reference Count: 61. [Online]. Available: <Go to ISI>://A1995TT79300004

[158] E. M. Levin and R. S. Roth, "Polymorphism of bismuth sesquioxide .i. pure bi2o3," *Journal of Research of the National Bureau of Standards Section a Physics and Chemistry*, vol. A 68, no. 2, p. 189, 1964. [Online]. Available: <Go to ISI>://A19646957B00004

[159] G. Schierning, R. Theissmann, H. Wiggers, D. Sudfeld, A. Ebbers, D. Franke, V. T. Witusiewicz, and M. Apel, "Microcrystalline silicon formation by silicon nanoparticles," *Journal of Applied Physics*, vol. 103, no. 8, 2008. [Online]. Available: <Go to ISI>://WOS:000255456200144

[160] E. M. Levin and R. S. Roth, "Polymorphism of bismuth sesquioxide .2. effect of oxide additions on polymorphism of bi2o3," *Journal of Research of the National Bureau of Standards Section a-Physics and Chemistry*, vol. A 68, no. 2, pp. 197–, 1964. [Online]. Available: <Go to ISI>://A19646957B00005

[161] K. Kameda and K. Yamaguchi, "Activity measurements of liquid Pb - Ti alloys by an emf method using a zirconia electrolyte," *Journal of the Japan Institute of Metals*, vol. 55, no. 9, pp. 951–956, 1991. [Online]. Available: <Go to ISI>://WOS:A1991GG94500007

[162] K. Kameda, K. Yamaguchi, and T. Kon, "Activity of liquid Ti-Bi alloys measured by an emf method using zirconia electrolyte," *Journal of the Japan Institute of Metals*, vol. 56, no. 8, pp. 900–906, 1992. [Online]. Available: <Go to ISI>://WOS:A1992JL06200006

[163] C. J. Coombes, "The melting of small particles of lead and indium," *Journal of Physics F: Metal Physics*, vol. 2, no. 3, pp. 441–449, 1972.

[164] S. J. Peppiatt, "Melting of small particles .2. bismuth," *Proceedings of the Royal Society of London Series a-Mathematical Physical and Engineering Sciences*, vol. 345, no. 1642, p. 401, 1975. [Online]. Available: <Go to ISI>://A1975AS18800009

[165] V. P. Skripov, V. P. Koverda, and V. N. Skokov, "Size effect on melting of small particles," *Physica Status Solidi (a)*, vol. 66, no. 1, pp. 109–118, 1981. [Online]. Available: http://dx.doi.org/10.1002/pssa.2210660111

[166] E. A. Olson, M. Y. Efremov, M. Zhang, Z. Zhang, and L. H. Allen, "Size-dependent melting of Bi nanoparticles," *Journal of Applied Physics*, vol. 97, no. 3, 2005. [Online]. Available: <Go to ISI>://000226778300071

[167] R. Ganesan, T. Gnanasekaran, and R. S. Srinivasa, "Determination of standard molar gibbs free energy of formation of Bi_2O_3 over a wide temperature range by EMF method," *The Journal of Chemical Thermodynamics*, vol. 35, no. 10, pp. 1703–1716, 2003, doi: 10.1016/S0021-9614(03)00158-7. [Online]. Available: http://www.sciencedirect.com/science/article/pii/S0021961403001587

[168] N. Ikemiya, J. Umemoto, S. Hara, and K. Ogino, "Surface tensions and densities of molten Al_2O_3, Ti_2O_3, V_2O_5 and Nb_2O_5," *ISIJ International*, vol. 33, no. 1, pp. 156–165, 1993.

[169] T. Takahashi, T. Esaka, and H. Iwahara, "Conduction in Bi_{203}-based oxide ion conductors under low oxygen pressure. I. Current blackening of the Bi_{203}- Yz_{03} electrolyte," *Journal of Applied Electrochemistry*, vol. 7, no. 4, pp. 299–302, 1977. [Online]. Available: http://dx.doi.org/10.1007/BF01059169

[170] ——, "Conduction in Bi_{203}-based oxide ion conductors under low oxygen pressure. II. Determination of the partial electronic conductivity," *Journal of Applied Electrochemistry*, vol. 7, no. 4, pp. 303–308, 1977. [Online]. Available: http://dx.doi.org/10.1007/BF01059170

[171] G. Gattow and H. Schröder, "Über Wismutoxide. III. Die Kristallstruktur der Hochtemperaturmodifikation von Wismut(III)-oxid," *Zeitschrift für anorganische und allgemeine Chemie*, vol. 318, 1962.

[172] K. Z. Fung, H. D. Baek, and A. V. Virkar, "Thermodynamic and kinetic considerations for Bi_2O_3-based electrolytes," *Solid State Ionics*, vol. 52, no. 1-3, pp. 199–211, 1992. [Online]. Available: http://www.sciencedirect.com/science/article/B6TY4-46MTS6M-73/2/3160abffe8aaabed5b59421842fb924d

[173] D. F. Lupon, J. Merker, and F. Schoelz, "Zur korrekten Verwendung von Platin in RFA-Labors," in *5. Anwendertreffen Röntgenfluoreszenz- und Funkenemissionsspektrometrie*. Dortmund: W. C. Heraeus GmbH and Co. KG, 1998, p. 17.

[174] J. Chang, E. Johnson, T. Sakai, and H. Saka, "Finite size melting of spherical solid-liquid aluminium interfaces," *Philosophical Magazine*, vol. 89, no. 7, pp. 595–604, 2009, doi: 10.1080/14786430902720952. [Online]. Available: http://dx.doi.org/10.1080/14786430902720952

[175] Z. L. Wang, "Transmission electron microscopy of shape-controlled nanocrystals and their assemblies," *The Journal of Physical Chemistry B*, vol. 104, no. 6, pp. 1153–1175, 2000, doi: 10.1021/jp993593c. [Online]. Available: http://dx.doi.org/10.1021/jp993593c

[176] P. Shuk, H. D. Wiemhofer, U. Guth, W. Gopel, and M. Greenblatt, "Oxide ion conducting solid electrolytes based on Bi_2O_3," *Solid State Ionics*, vol. 89, no. 3-4, pp. 179–196, 1996. [Online]. Available: http://www.sciencedirect.com/science/article/B6TY4-3VT9GGT-1/2/0a3155eedf5251b7bad631666cb982ea

[177] R. Irmawati, M. N. Noorfarizan Nasriah, Y. H. Taufiq-Yap, and S. B. Abdul Hamid, "Characterization of bismuth oxide catalysts prepared from bismuth trinitrate pentahydrate: influence of bismuth concentration," *Catalysis Today*, vol. 93-95, pp. 701–709, 2004. [Online]. Available: http://www.sciencedirect.com/science/article/B6TFG-4CS4M19-4/1/aa83263d149cabc5c3b1f236a4a66a0f

[178] L. D. Marks, "Experimental studies of small particle structures," *Reports on Progress in Physics*, vol. 57, no. 6, p. 603, 1994. [Online]. Available: http://stacks.iop.org/0034-4885/57/i=6/a=002

[179] H. Zheng, S. A. Claridge, A. M. Minor, A. P. Alivisatos, and U. Dahmen, "Nanocrystal diffusion in a liquid thin film observed by in situ transmission electron microscopy," *Nano Letters*, vol. 9, no. 6, pp. 2460–2465, 2009, doi: 10.1021/nl9012369. [Online]. Available: http://dx.doi.org/10.1021/nl9012369

[180] ——, "Nanocrystal diffusion in a liquid thin film observed by in situ transmission electron microscopy, supplementary material," *Nano Letters*, vol. 9, no. 6, pp. 2460–2465, 2009, doi: 10.1021/nl9012369. [Online]. Available: http://dx.doi.org/10.1021/nl9012369

[181] T. Yokota, M. Murayama, and J. M. Howe, “In situ transmission-electron-microscopy investigation of melting in submicron Al-Si alloy particles under electron-beam irradiation,” *Physical Review Letters*, vol. 91, no. 26, p. 265504, 2003, pRL. [Online]. Available: http://link.aps.org/doi/10.1103/PhysRevLett.91.265504

[182] J. M. Howe, T. Yokota, M. Murayama, and W. A. Jesser, “Effects of heat and electron irradiation on the melting behavior of Al-Si alloy particles and motion of the Al nanosphere within,” *Journal of Electron Microscopy*, vol. 53, no. 2, pp. 107–114, 2004. [Online]. Available: http://jmicro.oxfordjournals.org/content/53/2/107.abstract

[183] M. R. McCartney, P. A. Crozier, J. K. Weiss, and D. J. Smith, “Electron-beam-induced reactions at transition-metal oxide surfaces,” *Vacuum*, vol. 42, no. 4, pp. 301–308, 1991, doi: 10.1016/0042-207X(91)90042-H. [Online]. Available: http://www.sciencedirect.com/science/article/pii/0042207X9190042H

[184] H. W. Sheng, K. Lu, and E. Ma, “Melting and freezing behavior of embedded nanoparticles in ball-milled Al_2O_3 - M (M=In, Sn, Bi, Cd, Pb) mixtures,” *Acta Materialia*, vol. 46, no. 14, pp. 5195–5205, 1998, doi: 10.1016/S1359-6454(98)00108-6. [Online]. Available: http://www.sciencedirect.com/science/article/pii/S1359645498001086

[185] D. W. Denlinger, E. N. Abarra, K. Allen, P. W. Rooney, M. T. Messer, S. K. Watson, and F. Hellman, “Thin film microcalorimeter for heat capacity measurements from 1.5 to 800 K,” *Review of Scientific Instruments*, vol. 65, no. 4, pp. 946–959, 1994. [Online]. Available: http://link.aip.org/link/?RSI/65/946/1

[186] S. L. Lai, G. Ramanath, L. H. Allen, P. Infante, and Z. Ma, “High-speed (10^4 °C/s) scanning microcalorimetry with monolayer sensitivity (J/m^2),” *Applied Physics Letters*, vol. 67, no. 9, pp. 1229–1231, 1995. [Online]. Available: <Go to ISI>://A1995RR04200018

[187] F. Fominaya, T. Fournier, P. Gandit, and J. Chaussy, “Nanocalorimeter for high resolution measurements of low temperature heat capacities of thin films and single crystals,” *Review of Scientific Instruments*, vol. 68, no. 11, pp. 4191–4195, 1997. [Online]. Available: http://link.aip.org/link/?RSI/68/4191/1

[188] D. W. Cooke, K. J. Michel, and F. Hellman, “Thermodynamic measurements of submilligram bulk samples using a membrane-based "calorimeter on a chip”,” *Review of Scientific Instruments*, vol. 79, no. 5, pp. 053 902–10, 2008. [Online]. Available: http://link.aip.org/link/?RSI/79/053902/1

[189] M. Y. Efremov, E. A. Olson, M. Zhang, F. Schiettekatte, Z. S. Zhang, and L. H. Allen, “Ultrasensitive, fast, thin-film differential scanning calorimeter,” *Review of Scientific Instruments*, vol. 75, no. 1, pp. 179–191, 2004. [Online]. Available: <Go to ISI>://000187536500028

[190] M. Y. Efremov, E. A. Olson, M. Zhang, S. L. Lai, F. Schiettekatte, Z. S. Zhang, and L. H. Allen, “Thin-film differential scanning nanocalorimetry: heat capacity analysis,” *Thermochimica Acta*, vol. 412, no. 1-2, pp. 13–23, 2004, doi: DOI: 10.1016/j.tca.2003.08.019. [Online]. Available: http://www.sciencedirect.com/science/article/B6THV-49V7BWR-1/2/206f351a9cfd74f1318df8d08604086d

[191] A. A. Minakov and C. Schick, “Ultrafast thermal processing and nanocalorimetry at heating and cooling rates up to 1 MK/s,” *Review of Scientific Instruments*, vol. 78, no. 7, pp. 073 902–10, 2007. [Online]. Available: http://link.aip.org/link/?RSI/78/073902/1

[192] A. F. Lopeandia and J. Rodriguez-Viejo, “Size-dependent melting and supercooling of ge nanoparticles embedded in a sio2 thin film,” *Thermochimica Acta*, vol. 461, no. 1-2, pp. 82–87, Sep 2007. [Online]. Available: <Go to ISI>://000249227900009

[193] R. K. Kummamuru, L. De La Rama, L. Hu, M. D. Vaudin, M. Y. Efremov, M. L. Green, D. A. LaVan, and L. H. Allen, “Measurement of heat capacity and enthalpy of formation of nickel silicide using nanocalorimetry,” *Applied Physics Letters*, vol. 95, no. 18, 2009. [Online]. Available: <Go to ISI>://000271666800030

[194] G. Guenther, E. Aulbach, H. Hahn, and O. Guillon, “High-temperature chip calorimeter with atmosphere control,” *Thermochimica Acta*, vol. 522, no. 1-2, pp. 77–85, Aug 2010. [Online]. Available: <Go to ISI>://WOS:000294593900012

[195] E. Zhuravlev and C. Schick, “Fast scanning power compensated differential scanning nano-calorimeter: 1. the device,” *Thermochimica Acta*, vol. 505, no. 1-2, pp. 1–13, 2010, doi: 10.1016/j.tca.2010.03.019. [Online]. Available: http://www.sciencedirect.com/science/article/pii/S0040603110001061

[196] ——, "Fast scanning power compensated differential scanning nano-calorimeter: 2. heat capacity analysis," *Thermochimica Acta*, vol. 505, no. 1-2, pp. 14–21, 2010, doi: 10.1016/j.tca.2010.03.020. [Online]. Available: http://www.sciencedirect.com/science/article/pii/S0040603110001073

[197] G. Guenther, E. Aulbach, and O. Guillon, "Vorrichtung betreffend eine lösbare, elektrische Hochtemperatur-Vielfachkontaktierung, EP09170563.2," Germany Patent EP09 170 563.2, 2012.

[198] P. F. Sullivan and G. Seidel, "Steady-state AC-temperature calorimetry," *Physical Review*, vol. 173, no. 3, p. 679, 1968. [Online]. Available: <Go to ISI>://A1968B780700007

[199] Y. Kraftmakher, "Modulation calorimetry and related techniques," *Physics Reports-Review Section of Physics Letters*, vol. 356, no. 1-2, pp. 1–117, Jan 2002. [Online]. Available: <Go to ISI>://000173124600001

[200] A. Maesono and R. P. Tye, "Applications of AC calorimetry and differential phase calorimetry in the measurement of heat capacity and phase transitions," *High Temperatures-High Pressures*, vol. 30, no. 6, pp. 695 – 700, 1998. [Online]. Available: <Go to ISI>://000077880400010

[201] V. Lupascu, H. Huth, C. Schick, and M. Wuebbenhorst, "Specific heat and dielectric relaxations in ultra-thin polystyrene layers," *Thermochimica Acta*, vol. 432, no. 2, pp. 222–228, 2005, doi: DOI: 10.1016/j.tca.2005.04.022. [Online]. Available: http://www.sciencedirect.com/science/article/B6THV-4G4XBN0-1/2/1b13264ad2dd7ef3b6777b98259c0625

[202] R. E. Bedford and et al., "Recommended values of temperature for a selected set of secondary reference points," *Metrologia*, vol. 20, no. 4, p. 145, 1984. [Online]. Available: http://stacks.iop.org/0026-1394/20/i=4/a=003

[203] R. Sabbah, A. Xu-wu, J. S. Chickos, M. L. P. Leitao, M. V. Roux, and L. A. Torres, "Reference materials for calorimetry and differential thermal analysis," *Thermochimica Acta*, vol. 331, no. 2, pp. 93–204, 1999, doi: DOI: 10.1016/S0040-6031(99)00009-X. [Online]. Available: http://www.sciencedirect.com/science/article/B6THV-3WY40MT-1/2/61a96a480a7e9e3e64c4c2d9d72ec6f9

[204] T. P. Jones and J. Tapping, "The determination of the thermodynamic temperatures of thermometry fixed points in the range 660 °C to 1064 °C," *Metrologia*, vol. 25, no. 1, p. 41, 1988. [Online]. Available: http://stacks.iop.org/0026-1394/25/i=1/a=007

[205] K. Kostyrko, M. Skoczylas, and A. Klee, "Certified reference materials for thermal analysis," *Journal of Thermal Analysis and Calorimetry*, vol. 33, no. 1, pp. 351–357, 1988, 10.1007/BF01914623. [Online]. Available: http://dx.doi.org/10.1007/BF01914623

[206] M. F. Jarrold and J. E. Bower, "Mobilities of metal cluster ions: Aluminum and the electronic shell model," *The Journal of Chemical Physics*, vol. 98, no. 3, pp. 2399–2407, 1993. [Online]. Available: http://dx.doi.org/10.1063/1.464167

[207] C. M. Neal, A. K. Starace, and M. F. Jarrold, "Ion calorimetry: Using mass spectrometry to measure melting points," *Journal of the American Society for Mass Spectrometry*, vol. 18, no. 1, pp. 74–81, 2007. [Online]. Available: http://www.sciencedirect.com/science/article/B6TH2-4M0J4KN-1/2/b291f7e8a68e2a64df1745c90af23f81

Curriculum Vitae

Personal Details

First name:	Gerrit
Surname:	Guenther
Date of birth:	11/17/1980
Nationality:	German and Swiss (born in Frankfurt a.M., Germany)

Work Experience

04/07 – 11/12	PhD student and research assistant in the materials science department of the Technical University of Darmstadt, Germany
04/06 – 02/07	Diploma thesis and research assistant in the Institute for Nanotechnology (INT), national research center in Karlsruhe (KIT), Germany

Higher Education

03/02 – 09/06	Study of “Technical Physics” at the University of Applied Sciences Ravensburg-Weingarten Degree: Dipl. Ing. (FH)
04/07 – 12/12	Application exams and dissertation in the materials science department, Technical University of Darmstadt, Degree: Dr. rer. nat. (equivalent to Ph.D.)

Basic Education

07/2000	High school: Main-Taunus-Schule, Hofheim, Germany Degree: Higher education entrance qualification

Languages

German:	Native speaker
English:	Fluent, both written and oral
French:	Advanced
Spanish:	Beginner

Erklärung zur Dissertation

Hiermit versichere ich, die vorliegende Dissertation ohne Hilfe Dritter nur mit den angegebenen Quellen und Hilfsmitteln angefertigt zu haben. Alle Stellen, die aus Quellen entnommen wurden, sind als solche kenntlich gemacht. Diese Arbeit hat in gleicher oder ähnlicher Form noch keiner Prüfungsbehörde vorgelegen.

Darmstadt, February 12, 2013

(G. Günther)